Multifrequency and multiresonance EPR techniques applied to nitroxide radicals and nitroxide-labeled systems

Inaugural dissertation

for the attainment of the title of doctor
in the Faculty of Mathematics and Natural Sciences
at the Heinrich Heine University Düsseldorf

presented by

Anna Irena Nalepa
from Dąbrowa Tarnowska (Poland)

Düsseldorf, September 2015

from the Max Planck Institute for Chemical Energy Conversion
at the Heinrich Heine University Düsseldorf

Published by permission of the
Faculty of Mathematics and Natural Sciences at
Heinrich Heine University Düsseldorf

Supervisor: Prof. Wolfgang Lubitz
Co-supervisor: Prof. Claus Seidel

Date of the oral examination: 28/09/2015

Abstract

Site-directed spin labeling (SDSL) of target proteins with nitroxide radicals in conjunction with electron paramagnetic resonance (EPR) spectroscopy is a powerful method for elucidation of macromolecular structure and conformational dynamics on the molecular level. Moreover, information on the microenvironment properties at the site of the spin label can be inferred from the analysis of the magnetic interaction parameters of the nitroxide. This thesis focuses on the development of high-field/high-frequency EPR methodology for detailed characterization of the local environment. Heterogeneity of this local environment results in distinct nitroxide radical populations. In order to gain insight into the nature of these populations and to correlate them with local environment properties this work is mostly focused on investigation of model systems. Since the spin probe employed in this work is structurally related to the most widely applied nitroxide in structural biology, the MTS ((1-oxyl-2,2,5,5-tetramethylpyrroline-3-methyl)methanethiosulfonate) spin label, the conclusions are valid for SDSL proteins. The following topics are addressed in this work:

i. Comparison of W-band (94 GHz) cw and pulsed EPR techniques to probe distinct populations of a nitroxide spin probe is made. These populations are typically not completely resolved in W-band cw EPR spectra of protonated SDSL systems due to broad EPR lines. This enforces either the necessity of system perdeuteration to decrease the EPR linewidth or to perform cw EPR experiments at even higher magnetic fields/ higher microwave frequencies to increase the spectral resolution. In this work the applicability of a pulsed EPR technique, ELDOR-detected NMR (EDNMR) at a moderately high microwave frequency of 94 GHz, is tested. It is shown that W-band EDNMR is the best-suited EPR technique for the characterization of distinct nitroxide populations. Its advantages include: (i) superior sensitivity as compared to ENDOR (complementary pulsed EPR technique) and (ii) capability to obtain spectral information for protonated systems. These advantages are crucial for the future applications of the EDNMR technique to SDSL systems.

ii. In most protic solvents, including water, several distinct nitroxide radical populations are resolved using W-band EDNMR. Their origin is addressed and it is unequivocally shown that they correspond to different hydrogen-bonding situations of the nitroxide. Moreover, comparison of several protic solvents leads to the conclusion that magnetic parameters of nitroxides are predominantly influenced by the H-bonding situation of the radical. The solvent polarity exerts a minor effect on the nitroxide magnetic parameters. This has to be taken into account for correct interpretation of polarity/proticity profiles obtained in SDSL proteins and in biological membranes.

iii. The influence of the thermal history of the sample on nitroxide radical populations in frozen, aqueous solution is investigated. Using W-band EDNMR it is shown, that annealing of shock frozen samples above the glass transition temperature causes rearrangements of H-bonds between water and nitroxide. This is reflected as a change in the ratio of spin probe populations in which nitroxides are described with different magnetic interaction parameters. Therefore, reproducible sample freezing is required for reliable polarity/proticity profiles obtained at low temperature by X-band (9.4 GHz) cw EPR in biomacromolecules.

iv. The applicability of the W-band EDNMR technique to determine the site-specific water content is shown. The studied paramagnetic probes included: (i) the nitroxide radical, (ii) the nitroxide radical attached to bacterial photosynthetic reaction center (bRC) from *Rhodobacter sphaeroides* R26 and (iii) ionic states of native cofactors in bRC. The admixture of the disaccharide trehalose allows for additional manipulation of the hydration level of the studied systems. The limitations for local water sensing using nitroxides or native paramagnetic centers are specified both for D_2O or $H_2{}^{17}O$ exchange experiments. Importantly, it is demonstrated that W-band EDNMR on nitroxides in conjunction with $H_2{}^{17}O$ water exchange has the potential to provide quantitative information on the site-specific water content in macromolecules.

Zusammenfassung

Die ortsspezifische Spinmarkierung (site-directed spin labeling, SDSL) von Proteinen mit Nitroxidradikalen in Verbindung mit Elektronenspinresonanz (electron paramagnetic resonance, EPR)-Spektroskopie ist eine effiziente Methode zur Aufklärung der makromolekularen Struktur und Konformationsdynamik auf molekularer Ebene. Darüber hinaus können Informationen über Eigenschaften der Mikroumgebung am Ort des Spinlabels aus der Analyse der Parameter der magnetischen Wechselwirkungen des Nitroxids erhalten werden. Die vorliegende Arbeit beschäftgt sich mit der Entwicklung von Hochfeld-/Hochfrequenz-EPR-Methodologien zur detaillierten Charakterisierung der unmittelbaren Umgebung des Radikals. Im Falle einer Heterogenität dieser lokalen Umgebung liegen unterscheidbare Populationen der Nitroxidradikale vor. Um Einblick in die Natur dieser Populationen zu erhalten und diese mit Eigenschaften der lokalen Umgebung zu korrelieren, konzentriert sich diese Dissertation vor allem auf die Untersuchung von Modellsystemen. Da die in dieser Arbeit verwendete Spinsonde strukturell ähnlich zu dem in der Strukturbiologie am häufigsten verwendeten Nitroxid, dem Spinlabel MTS ((1-oxyl-2,2,5,5-tetramethylpyrroline-3-methyl)methanethiosulfonate), ist, sind die hier gezogenen Schlussfolgerungen auch für entsprechende SDSL-Proteine gültig. Folgende Themenbereiche werden in dieser Arbeit behandelt:

i. W-Band (94 GHz) cw und gepulste EPR-Techniken zur Untersuchung unterschiedlicher Populationen einer Nitroxid-Spinsonde werden verglichen. In W-band cw EPR-Spektren protonierter SDSL-Systeme sind diese Populationen üblicherweise nicht komplett aufgelöst aufgrund der breiten EPR-Linien. Dies macht entweder die Perdeuterierung der Probe erforderlich, um die EPR-Linienbreite zu verringern, oder cw EPR-Experimente bei noch höheren Magnetfeldern und Mikrowellenfrequenzen durchzuführen, um die spektrale Auflösung zu erhöhen. In der vorliegenden Arbeit wird eine gepulste EPR-Technik, ELDOR-detektierte NMR (EDNMR) bei einer mittelhohen Mikrowellenfrequenz von 94 GHz, auf ihre Anwendbarkeit hin untersucht. Es wird gezeigt, dass W-band EDNMR die am besten geeignete EPR-Technik zur Charakterisierung unterschiedlicher Nitroxidpopulationen ist. Zu den Vorteilen gehören: (i) ihre höhere Empfindlichkeit verglichen mit ENDOR (komplementäre gepulste EPR-Technik) und (ii) die Möglichkeit, Informationen über protonierte Systeme zu erhalten. Diese Vorteile sind entscheidend für die zukünftige Anwendung der EDNMR-Technik auf SDSL-Systeme.

ii. In den meisten protischen Lösungsmitteln, einschließlich Wasser, können mehrere unterscheidbare Nitroxidradikalpopulationen mittels W-Band EDNMR aufgelöst werden. Bezogen auf ihren Ursprung wird eindeutig gezeigt, dass sie zwei unterschiedlichen Wasserstoffbrücken-Bindungssituationen des Nitroxids zuzuordnen sind. Außerdem führt der Vergleich mehrerer protischer Lösungsmittel zu dem Schluss, dass die magnetischen Parameter des Nitroxids hauptsächlich durch die H-Brücken-Bindungssituation des Radikals beeinflusst werden. Die Polarität des Lösemittels hat einen geringeren Einfluß auf seine magnetischen Parameter. Dies muss zur korrekten Interpretation von Polaritäts-/Protizitätsprofilen, berücksichtigt werden die in SDSL-Proteinen und biologischen Membranen erhalten wurden.

iii. Der Einfluss der thermischen Vorgeschichte der Probe auf die Nitroxidradikalpopulationen in gefrorener wässriger Lösung wird untersucht. Mittels W-Band EDNMR wird gezeigt, dass das

Erwärmen schockgefrorener Proben über die Glasübergangstemperatur eine Neuausrichtung der H-Brücken zwischen Wasser und dem Nitroxid bewirkt. Diese zeigt sich als Veränderung des Verhältnisses der Spinsondenpopulationen, in der Nitroxide mit unterschiedlichen magnetischen Wechselwirkungsparametern beschrieben werden. Daher ist ein reproduzierbares Verfahren beim Einfrieren von Proben notwendig, um verlässliche Polaritäts-/Protizitätsprofile, die bei tiefen Temperaturen mittels X-band (9.4 GHz) cw EPR in Biomakromolekülen erhalten werden, zu erstellen.

iv. Die Anwendbarkeit der W-band EDNMR-Technik zur Bestimmung des ortsspezifischen Wassergehalts wird gezeist. Die untersuchten paramagnetischen Sonden umfassen: (i) das Nitroxidradikal, (ii) das an das bakterielle photosynthetische Reaktionszentrum (bRC) von *Rhodobacter sphaeroides* R26 gebundene Nitroxidradikal und (iii) ionische Zustände nativer Kofaktoren in bRC. Hinzumischen des Disaccharids Trehalose ermöglicht eine zusätzliche Manipulation des Hydrationszustands der studierten Systeme. Die Grenzen der lokalen Wasserdetektion mittel Nitroxiden oder nativer paramagnetischer Zentren werden sowohl für D_2O- als auch $H_2{}^{17}O$-Austauschexperimente spezifiziert. Dabei ist wichtig, dass gezeist wird, dass W-Band EDNMR an Nitroxiden in Verbindung mit $H_2{}^{17}O$-Wasseraustausch das Potential besitzt, quantitative Informationen über den ortsspezifischen Wassergehalt in Makromolekülen zu liefern.

Table of Contents

Abstract iii
Zusammenfassung v
General introduction 1
References 3
EPR theory and methods 5
2.1 Spin Hamiltonian 5
2.1.1 Electron and nuclear Zeeman interactions 5
2.1.2 Hyperfine interaction 7
2.1.3 Nuclear quadrupole interaction 8
2.1.4 Strong and weak coupling between electron and nuclear spins 9
2.1.5 Weak coupling between electron spins 10
2.2 Continuous wave EPR 10
2.3 Pulsed EPR methods 11
2.3.1 Echo-detected EPR spectrum 12
2.3.2 Hyperfine spectroscopy 13
2.4 High-field/high-frequency EPR 16
References 18
EPR spectroscopy on nitroxides 21
3.1 The principle of site-directed spin labeling 21
3.2 cw EPR spectra of nitroxide radicals 22
3.3 Local microenvironment characterization using nitroxides 24
3.4 Local solvent accessibility studies using nitroxides 26
3.5 Distance measurements by EPR using nitroxides 28
References 29
High-field ELDOR-detected NMR study of nitroxide radicals in disordered solids: towards characterization of heterogeneity of microenvironments in spin-labeled systems 35
4.1 Introduction 35
4.2 Materials and methods 37
4.3. W-band cw EPR and EDNMR on nitroxide radical in 2-propanol 43
4.4. W-band EDNMR spectral resolution in increasingly protonated systems 46
4.5 Comparison of W-band EDNMR spectra in ^{14}N- and ^{15}N-labelled nitroxides 48
4.6 Comparison of W-band EDNMR and ENDOR sensitivity 50
4.7 Discussion and conclusions 52
References 54
Investigation of nitroxide spin labels H-bonded to different solvent molecules using 244 GHz cw EPR and W-band ENDOR and EDNMR 57
5.1 Introduction 57
5.2. Materials and methods 59
5.3 244 GHz cw EPR on nitroxide dissolved in various solvents 61
5.4 W-band EDNMR on nitroxide radical dissolved in various protic solvents 65

5.5 W-band ENDOR on nitroxide spin probes dissolved in various protic solvents 68
5.6 Discussion 76
References 77
Annealing induced nitroxide H-bond network rearrangement studied using W-band cw EPR and EDNMR 81
6.1 Introduction 81
6.2 Materials and methods 83
6.3 Influence of annealing on the H-bond network of nitroxide spin probes dissolved in glycerol and D_2O/glycerol mixtures 84
6.4 Annealing induced rearrangement of the H-bond network around the nitroxide spin label in spin-labeled T4-lysozyme 90
6.5 Conclusions and outlook 92
References 93
Investigation of local water exchange processes in photosynthetic reaction centers (bRCs) of *Rhodobacter sphaeroides* R26 embedded in trehalose matrices 97
7.1 Introduction. 97
7.2 Material and methods 100
7.3 Results and discussions 102
7.3.1 Kinetics of water diffusion within R1/trehalose glass 102
7.3.2 Water accessibility of R1/trehalose glasses at different RH 106
7.3.3 Water accessibility of SL-RC/trehalose glass at different RH 108
7.3.4 Local water accessibility in the vicinity of native cofactors in RCs embedded in trehalose. 109
7.3.5 W-band EDNMR and Davies ENDOR on RC/trehalose equilibrated with $H_2{}^{17}O$ 109
7.4 Conclusions 115
References 117
Preparation of cysteine-34-nitroxide spin-labeled human α_1-microglobulin 123
8.1 Introduction 123
8.2 Materials and Methods 124
8.3. Preparation of $\alpha_1 m^{AM}$ 127
8.4 Preparation of $\alpha_1 m^{N-O\bullet}$ 129
8.5 Determination of the molar extinction coefficient of $\alpha_1 m^{AM}$ and $\alpha_1 m^{N-O\bullet}$ 130
8.6 Mass spectrometric analysis 131
8.7 Determination secondary structure elements by CD spectroscopy 132
8.8 Quantification of the degree of spin labeling in $\alpha_1 m^{N-O\bullet}$ preparations 133
8.9 Conclusions 133
References 134
Summary and outlook 139
Acknowledgements 139
Curriculum Vitae 139

Chapter 1

General introduction

Electron paramagnetic resonance (EPR), also known as electron spin resonance (ESR), is a spectroscopic method to study systems with at least one unpaired electron, either naturally present or artificially incorporated into a biomacromolecule. Since the first EPR experiment performed by Zavoisky [1], both continuous wave and pulsed EPR techniques have been successfully developed and established, providing unique electronic and local geometric structures [2]. While most compounds carrying unpaired electrons are chemically reactive, stable paramagnetic species can also be synthesized and introduced into system under study as spin probes or spin labels. Nitroxide radicals are an important class of such molecules, yielding information on the system under study. This information ranges from local environment characteristics to long-range structural information based on distance constraints [3]. Nevertheless, X-ray crystallography and NMR spectroscopy are still the main techniques capable of determining the structures of biological macromolecules like proteins and nucleic acids at atomic resolution [4;5]. X-ray structures can exhibit high resolution, but large and stable protein crystals are required in which the protein is lined up in a regular lattice. Therefore, distortion of the structure by crystal packing effects cannot be excluded. Moreover, only the static protein structure is obtained by conventional X-ray crystallography, while at the same time mobile structural parts like surface loops often fail to be resolved. In many cases it proves difficult or even impossible to find sets of crystallization conditions that would stabilize each of the individual states involved in the function of a protein. However, recent developments of picosecond time-resolved X-ray crystallography offers a promising methodology to visualize in real time the conformational evolution of proteins [6;7]. NMR is often providing atomic-level structures as accurate as those determined by X-ray diffraction [8]. Since NMR makes use of protein solutions, information on dynamics of flexible loops and on domain motion is accessible. The structure determination by NMR is based on the analysis of numerous spin-spin interactions between nuclei, i.e. the nuclear Overhauser effect (NOE). The interpretation requires sequence-specific assignment of the many hundred to several thousand NMR peaks from a protein [9]. This approach is therefore efficient only when the structure of a small or intermediate size protein has to be solved, but for larger macromolecules it becomes challenging or even impossible. Therefore, structure determination by NMR is mostly limited to proteins with molecular weights less than ca. 60 kDa, but still provides a viable alternative for structure determination if a protein cannot be crystallized.

Alternative characterization techniques that can be applied to proteins in native-like environments are probe-based techniques including the pulsed EPR technique PELDOR (pulsed electron-electron double resonance) [10;11] and Förster resonance energy transfer (FRET) [12;13] methods. They can provide long-range distance constraints to support the modelling of structure from many available short distances obtained using NMR. But often they are used as stand-alone tools to study conformational changes of macromolecules. Both techniques are able to provide information on

"problematic" structures such as flexible, less ordered regions and they are not limited by a high molecular weight of the system.

FRET relies on the distance dependent non-radiative energy transfer between a donor and an acceptor fluorophore that occurs if the fluorophores are in close proximity and their emission/excitation spectra overlap [14]. The range of donor-acceptor pairs commercially available allows distance measurements in the range of 25–60 Å, extending up to 100 Å in favorable cases [15]. Apart from the high intrinsic sensitivity of fluorescence-based experiments, FRET can be performed on freely diffusing molecules in solution. In PELDOR, long-range structural information is mainly extracted from dipole-dipole interaction of two spatially separated electron spins. In the most widely used approach, when a pair of nitroxide spin labels is incorporated into the protein, distance constraints in the range of 18 to 60 Å can be routinely obtained using PELDOR [16]. The information content of a single sample is limited but at the same time very specific because solvent and protein matrix are usually diamagnetic and do not contribute to the PELDOR signal.

Both fluorescence labels and nitroxide spin labels exhibit conformational flexibility due to the structure of the linker by which they are attached to the protein. This property minimizes the influence of the label side chain on the biomacromolecule conformation, but also increases the uncertainty in the interpretation of the distance with respect to the protein backbone, especially when measuring short distances. For the current *in silico* spin labelling programs, the conformation of the spin label in the local environment of the attachment site is predicted by methods based on calculated spin label rotamer libraries [17-19]. This results in an average error of the predicted distances of about 3 Å. Further reducing the error in interpreting spin-spin distances is crucial for limiting the number of additional EPR experiments that are in turn required to decrease the number of structural models satisfying EPR-derived distance constraints [20]. Unraveling of the contribution of specific spin label rotamers to the heterogeneity of observed distances requires additional considerations of the specific interactions of the nitroxide radical with its local environment, since these will influence the occupancy of the individual spin label rotamer states. Supplementary experimental data on the extent of specific interactions between nitroxide radicals and local environment are necessary to provide clues concerning possible improvements of *in silico* spin labeling methods.

However, up-to-date no systematic studies on the extent of H-bond formation between nitroxide radicals and various proton donor groups exist. In this work these specific interactions are therefore investigated in more detail using high-field/high-frequency EPR techniques. We have used various simplified model systems related to the most common H-bond donor groups present in spin-labeled proteins. Magnetic parameters of nitroxides are known to be influenced by both proticity, i.e. availability of H-bond donor groups, and polarity of its local environment. The specific interactions will often result in a heterogeneity of magnetic parameters, but are not easily experimentally accessible. Hence, to apply them as indicators of H-bond formation between nitroxide and nearby proton donor groups, development of proper experimental methodology is necessary. For that purpose, the applicability of the pulsed EPR method, ELDOR-detected NMR (EDNMR) at W-band (94 GHz) was evaluated in detail, as described in Chapter 4. It specifically allows to obtain the magnetic interaction parameter hyperfine coupling constant, A_{zz}, for the nitroxide radical. Its capability to differentiate between different H-bonding situations of nitroxide radical was further tested using various protic solvents and compared with results of 244 GHz cw EPR experiments as

shown in Chapter 5. The interaction of nitroxide radicals with water molecules, which is expected to be the predominant interaction for solvent exposed spin labels, was studied in detail in Chapter 6. The emphasis is put on defining what role the cryoprotectant and the sample freezing rate play in determining the nitroxide spin probe populations. The specific interaction between nitroxide radicals and water molecules is further employed in testing the applicability of W-band EDNMR for determining site-specific solvent accessibility using the photosynthetic bacterial reaction center from *Rhodobacter sphaeroides* as test system, as described in Chapter 7. Finally, in Chapter 8, the preliminary biochemical results for obtaining a nitroxide spin-labeled variant of human α_1-microglobulin protein are presented.

References

[1] E. Zavoisky *The paramagnetic absorption of a solution in parallel fields*. J. Phys.-USSR **1944,** 8, 377-380.

[2] A. Schweiger, G. Jeschke *Principles of pulse electron paramagnetic resonance*, Oxford University Press, Oxford, 2001.

[3] G.I. Likhtenshtein, J. Yamauchi, S. Nakatsuji, A.I. Smirnov, R. Tamura *Nitroxides. Applications in chemistry, biomedicine and materials science*, Wiley-VCH Verlag, Weinheim, 2008.

[4] B. Rupp, V.V. Kirshnan *Macromolecular structure determination: comparison of X-ray crystallography and NMR spectroscopy*. eLS **2012,** 1-13.

[5] H. van den Bedem, J.S. Fraser *Integrative, dynamic structural biology at atomic resolution - it's about time*. Nat. Methods **2015,** 12, 307-318.

[6] F. Schotte, J. Soman, J.S. Olson, M. Wulff, P.A. Anfinrud *Picosecond time-resolved X-ray crystallography: Probing protein function in real time*. J. Struct. Biol. **2004,** 147, 235-246.

[7] R. Neutze *Opportunities and challenges for time-resolved studies of protein structural dynamics at X-ray free-electron lasers*. Philos. Tr. Soc. B **2014,** 369, 20130318.

[8] K. Wüthrich *NMR studies of structure and function of biological macromolecules (Nobel lecture)*. Angew. Chem. Int. Edit. **2003,** 42, 3340-3363.

[9] T.K. Hitchens, G.S. Rule *Fundamentals of protein NMR spectroscopy (focus on structural biology)*, Springer, Berlin, 2005.

[10] A.D. Milov, A.B. Ponomarev, Yu.D. Tsvetkov *Electron-electron double resonance in electron spin echo: Model biradical systems and the sensitized photolysis of decalin*. Chem. Phys. Lett. **1984,** 110, 67-72.

[11] M. Pannier, S. Veit, A. Godt, G. Jeschke, H.W. Spiess *Dead-time free measurement of dipole-dipole interactions between electron spins*. J. Magn. Reson. **2000,** 142, 331-340.

[12] L. Stryer, R.P. Haugland *Energy transfer: A spectroscopic ruler*. Proc. Natl. Acad. Sci.USA **1967,** 58, 719-726.

[13] S. Kalinin, T. Peulen, S. Sindbert, P.J. Rothwell, S. Berger, T. Restle, R.S. Goody, H. Gohlke, C.A.M. Seidel *A toolkit and benchmark study for FRET-restrained high-precision structural modeling*. Nat. Methods **2012,** 9, 1218-1225.

[14] Th. Förster *10th Spiers Memorial Lecture. Transfer mechanisms of electronic excitation*. Discuss. Faraday Soc. **1959,** 7-17.

[15] B. Schuler *Single-molecule FRET of protein structure and dynamics - a primer*. J.Nanobiotechnology **2013,** 11, (Suppl 1)-S2.

[16] G. Jeschke *DEER distance measurements on proteins*. Annu. Rev. Phys. Chem. **2012,** 63, 419-446.

[17] Y. Polyhach, E. Bordignon, G. Jeschke *Rotamer libraries of spin labelled cysteines for protein studies*. Phys. Chem. Chem. Phys. **2011,** 13, 2356-2366.

[18] G. Hagelueken, R. Ward, J.H. Naismith, O. Schiemann *MtsslWizard: In silico spin-labeling and generation of distance distributions in PyMOL*. Appl. Magn. Reson. **2012,** 42, 377-391.

[19] N.S. Alexander, R.A. Stein, H.A. Koteiche, K.W. Kaufmann, H.S. Mchaourab, J. Meiler *RosettaEPR: Rotamer library for spin label structure and dynamics*. PLOS One **2013,** 8, e72851.

[20] K. Sale, L. Song, Y.-S. Liu, E. Perozo, P. Fajer *Explicit treatment of spin labels in modeling of distance constraints from dipolar EPR and DEER*. J. Am. Chem. Soc. **2005,** 127, 9334-9335.

Chapter 2

EPR theory and methods

In this chapter the theoretical basis of electron paramagnetic resonance (EPR) spectroscopy is presented. The chapter is organized as follows: In the first part spin Hamiltonian terms relevant for studies of nitroxide radicals are introduced. In section 2, the basics of EPR operation in cw mode is described. In section 3, pulsed EPR methods used in this work are introduced. Finally, in section 4, the advantages of high-field/high-frequency EPR are outlined.

2.1 Spin Hamiltonian

The energies of states of a paramagnetic system comprising an effective electron spin S and *m* nuclei with nuclear spins I_k (k=1,…, m) can be described by using the concept of the spin Hamiltonian operator [1;2]. The following terms in the static spin Hamiltonian describe the interactions of the electron and nuclear spins among themselves (couplings) and interaction with an external magnetic field, $\vec{\boldsymbol{B}}_{\mathbf{0}}$ [3]:

$$\hat{\mathrm{H}}_{\mathrm{S}} = \hat{\mathrm{H}}_{\mathrm{EZ}} + \hat{\mathrm{H}}_{\mathrm{HF}} + \hat{\mathrm{H}}_{\mathrm{NZ}} + \hat{\mathrm{H}}_{\mathrm{NQ}} + \hat{\mathrm{H}}_{\mathrm{ZFS}} + \hat{\mathrm{H}}_{\mathrm{NN}} \qquad \text{Eq. (2.1)}$$

These terms, in the listing order, correspond to: the electron Zeeman interaction, the hyperfine interactions between the electron spin and the *m* nuclei with nuclear spins I_k, the nuclear Zeeman interaction, the nuclear quadrupole interaction (for nuclei with I > ½), the zero-field splitting H_{ZFS} (for S > ½) and the spin-spin interactions between pairs of nuclear spins. $\hat{H}_S$ is called the spin Hamiltonian, since apart from phenomenological interaction parameters it contains only spin coordinates that are described by the electron and nuclear spin vector operators, $\hat{S}$ and $\hat{I}_k$, respectively, where $\hat{\mathrm{S}} = [\hat{\mathrm{S}}_{\mathrm{x}}, \hat{\mathrm{S}}_{\mathrm{y}}, \hat{\mathrm{S}}_{\mathrm{z}}]$ and $\hat{\mathrm{I}}_{\mathrm{k}} = [\hat{\mathrm{I}}_{\mathrm{x,k}}, \hat{\mathrm{I}}_{\mathrm{y,k}}, \hat{\mathrm{I}}_{\mathrm{z,k}}]$. In the following, the discussion of spin Hamiltonian terms is limited to magnetic interactions relevant for the presented work. The detailed theoretical description can be found in comprehensive textbooks, for example [1;3;4].

2.1.1 Electron and nuclear Zeeman interactions

The electron Zeeman interaction is the interaction of the magnetic moment, $\vec{\boldsymbol{\mu}}$, associated with the electron spin S, and an external static magnetic field, $\vec{\boldsymbol{B}}_{\mathbf{0}}$. The spin Hamiltonian describing the electron Zeeman interaction is given by:

$$\hat{\mathrm{H}}_{\mathrm{EZ}} = \frac{\beta}{\mathrm{h}} \vec{\mathbf{B}}_{\mathbf{0}} \mathrm{g}_{\mathrm{e}} \hat{\mathbf{S}} \qquad \text{Eq. (2.2)}$$

where β is the Bohr magneton, $\vec{\mathbf{B}}_{\mathbf{0}}$ the static magnetic field vector, g_e is equal to 2.0023 is the g-value of the free electron, *h* is the Planck constant and $\hat{\boldsymbol{S}}$ the electron spin vector operator.

For the free electron (S = ½), the presence of a static magnetic field results in a splitting into two energy levels that are otherwise degenerate in the absence of $\vec{\boldsymbol{B}}_{\mathbf{0}}$. These energy levels correspond to

two electron spin states, i.e. the electron spin projection oriented parallel or anti-parallel to the magnetic field vector, $\vec{\boldsymbol{B}}_{\mathbf{0}}$, as is shown in Fig. 2.1.

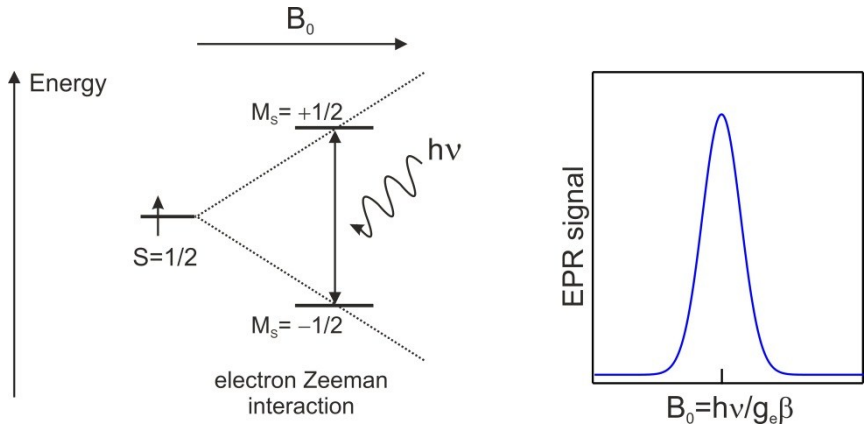

Figure 2.1 *Energy level splitting for S=1/2 spin system in an external magnetic field* $\vec{\boldsymbol{B}}_{\mathbf{0}}$ *due to electron Zeeman interaction. The transition between two energy levels can be induced by irradiation at microwave (mw) frequency, ν, which matches their energy difference. On the right, the resulting EPR absorption spectrum is shown.*

The energies for the two spin states are given by the eigenvalues of $\hat{H}_{EZ}$ and are characterized by the spin quantum numbers $M_s = \pm ½$:

$$E(M_s) = g_e \beta B_0 M_s \qquad \text{Eq. (2.3)}$$

The energy difference between two spin states is given by:

$$\Delta E = h\nu = g_e \beta B_0 \qquad \text{Eq. (2.4)}$$

As follows from Eq. 2.4, this energy difference increases in a linear manner with increasing $\vec{\boldsymbol{B}}_{\mathbf{0}}$ strength.

For the unpaired electron spin confined in the molecular orbital, the effective field $\vec{\boldsymbol{B}}_{\boldsymbol{eff}}$ is usually the superposition of external and additional inner fields related to the symmetry of the molecule. These inner fields are transmitted to the electron spin by the spin-orbit coupling, i.e. the interaction of the EPR-observable electronic ground state with excited states, leading to admixture of the excited state orbital angular momentum, $\vec{L}$ [4]. Hence, the spin Hamiltonian describing the electron Zeeman interaction for a bound electron changes to:

$$\hat{H}_{EZ} = \frac{\beta}{h}\vec{\mathbf{B}}_{\mathbf{eff}} g_e \hat{\mathbf{S}} = \frac{\beta}{h}\vec{\mathbf{B}}_{\mathbf{0}}\mathbf{g}(\theta,\varphi)\hat{\mathbf{S}} \qquad \text{Eq. (2.5)}$$

where **g** is a 3x3 matrix that encodes the orientation-dependent Zeeman interaction, and θ, φ are the polar angles describing the direction of the magnetic field with respect to the molecular g-matrix axis system. However, for organic radicals the deviation of the g values from g_e is usually small.

The **g** matrix can be converted by rotation into a form in which all non-diagonal elements are equal to 0, i.e. the so called principal axes representation:

$$\mathbf{g} = \begin{bmatrix} g_{xx} & 0 & 0 \\ 0 & g_{yy} & 0 \\ 0 & 0 & g_{zz} \end{bmatrix} \qquad \text{Eq. (2.6)}$$

with g_{xx}, g_{yy} and g_{zz} being the principal values of **g**.

If the magnetic field is directed along one of the principal axes, the resonant field is obtained by inserting the corresponding principal value into Eq. 2.4. For an arbitrary $\vec{\boldsymbol{B}}_{\mathbf{0}}$ orientation, described by θ and φ, the following expression is inserted into the resonance condition:

$$g(\theta,\varphi)^2 = g_{xx}^2 \cdot \sin^2\theta \cdot \cos^2\varphi + g_{yy}^2 \cdot \sin^2\theta \cdot \sin^2\varphi + g_{zz}^2 \cdot \cos^2\theta \qquad \text{Eq. (2.7)}$$

which includes the direction cosines between $\vec{\boldsymbol{B}}_{\mathbf{0}}$ and the principal axes of the **g** matrix.

In analogy to the electron spin, the nuclear spin **I** is quantized in an external magnetic field. As a result, a nuclear Zeeman splitting into (2I+1) energy levels takes place for a given nuclear quantum number I, see Fig. 2.2. Since this interaction is much smaller, as compared to the electron spin interaction, the splitting can usually be neglected in the EPR spectrum. The spin Hamiltonian describing the nuclear Zeeman interaction is given by:

$$\hat{H}_{NZ} = -\frac{\beta_n}{h}\vec{\mathbf{B}}_{\mathbf{0}} g_n \hat{I} \qquad \text{Eq. (2.8)}$$

where g_n is the nuclear g-factor that depends on the nucleus, β_n is the nuclear magneton and $\hat{\boldsymbol{I}}$ the nuclear spin vector operator.

Importantly, due to the field dependence of both electron and nuclear Zeeman interactions their contribution to the spin Hamiltonian may be varied by changing the $\vec{\boldsymbol{B}}_{\mathbf{0}}$ strength.

2.1.2 Hyperfine interaction

The presence of m nuclei with nuclear spins $I_k>0$, e.g. proton (I=½) or the ^{14}N isotope of nitrogen (I=1), in the vicinity of an unpaired electron spin will produce a local magnetic field that is sensed by the unpaired electron in addition to the externally applied magnetic field. The resulting interaction between magnetic moments associated with the electron spin S and nuclear spin I_k is called the hyperfine interaction. It is represented in the spin Hamiltonian by term:

$$\hat{H}_{HF} = \sum_{k=1}^{m} \hat{\mathbf{S}}\mathbf{A_k}\hat{I}_k \qquad \text{Eq. (2.9)}$$

where A_k is the hyperfine interaction matrix for given nuclei with spin I_k.

The hyperfine interaction comprises the isotropic and anisotropic parts that have their origin in different physical mechanisms.

The isotropic contribution to the hyperfine matrix is due to so-called Fermi contact interaction. It is a quantum effect and occurs when finite electron spin density resides at the nucleus, i.e. usually when the *s* orbitals contribute to the molecular orbital. However, the spin density at the nucleus can also be induced through a spin polarization mechanism, resulting in a non-zero Fermi contact interaction in systems with unpaired electrons in orbitals other than *s* [5].

The energy of the Fermi contact interaction in the spin Hamiltonian is described by:

$$\hat{H}_{FC} = \left(\frac{2}{3}\right)\frac{\mu_0}{h} g\beta g_n \beta_n |\psi(0)|^2 \hat{\mathbf{S}}\hat{\mathbf{I}} = a_{iso}\hat{\mathbf{S}}\hat{\mathbf{I}} \qquad \text{Eq. (2.10)}$$

where $|\psi(0)|^2$ is the probability density of the unpaired electron at the nucleus.

The second mechanism is the classical dipole-dipole interaction between the magnetic moments associated with the electron and nuclear spins. This interaction depends on the relative orientation of the magnetic moments and is, therefore, anisotropic. The spin Hamiltonian term describing the energy of this interaction is given as:

$$\hat{H}_{DD} = \frac{1}{4\pi}\frac{\mu_0}{r^3 h} g\beta g_n \beta_n \left[\hat{\mathbf{S}}\hat{\mathbf{I}} - \frac{3}{r^2}(\hat{\mathbf{S}}\mathbf{r})(\hat{\mathbf{I}}\mathbf{r})\right] = \hat{\mathbf{S}}\mathbf{T}\hat{\mathbf{I}} \qquad \text{Eq. (2.11)}$$

where μ_0 is the permeability of the vacuum and r is the distance between the two spins.
Within the point dipole approximation (spin densities considered to be located at single point in space) the hyperfine interaction matrix, **A**, separated into isotropic and anisotropic contributions, is expressed as:

$$A = \begin{bmatrix} A_\perp & 0 & 0 \\ 0 & A_\perp & 0 \\ 0 & 0 & A_\parallel \end{bmatrix} = a_{iso} + \begin{bmatrix} -T & 0 & 0 \\ 0 & -T & 0 \\ 0 & 0 & 2T \end{bmatrix} \qquad \text{Eq. (2.12)}$$

where T is equal to:

$$T = \frac{1}{4\pi}\frac{\mu_0}{r^3 h} g\beta g_n \beta_n \qquad \text{Eq. (2.13)}$$

In this principal axes representation, i.e. only diagonal terms are present, the dipolar interaction matrix **T** is symmetric and traceless. Consequently, for fast rotational motion of the molecule in solution, the anisotropic part is averaged out and only isotropic hyperfine interactions can be measured.

2.1.3 Nuclear quadrupole interaction

For nuclei with spin I>½, e.g. ^{14}N or ^{2}H, the charge distribution is non-spherical and is described by the electric nuclear quadrupole moment, Q. The interaction of this electric quadrupole moment of the nucleus with the electric field gradient is called nuclear quadrupole interaction. In the principal axes representation, the spin Hamiltonian describing the energy of this interaction is written as:

$$\frac{\hat{H}_{NQ}}{h} = \hat{\mathbf{I}}\mathbf{P}\hat{\mathbf{I}} = P_x\hat{I}_x^2 + P_y\hat{I}_y^2 + P_z\hat{I}_z^2 = \frac{e^2qQ}{4I(2I-1)h}[3I_z^2 - I(I+1) + \eta(I_x^2 - I_y^2)] \qquad \text{Eq. (2.14)}$$

where **P** is the traceless nuclear quadrupole tensor, eq is the electric field gradient and $\eta = \frac{P_x - P_y}{P_z}$ is the asymmetry parameter of the charge distribution with $|P_{zz}| \geq |P_{yy}| \geq |P_{xx}|$ and $0 \leq \eta \leq 1$. The largest principal value of the quadrupole tensor is given by:

$$P_z = e^2qQ/2I(2I-1)h \qquad \text{Eq. (2.15)}$$

To characterize the nuclear quadrupole interaction, usually the parameters e^2qQ/h and η are presented.

The resulting energy level diagram for a nitroxide radical, i.e. a spin system with S=½, I=1, that includes all magnetic interactions described above, is shown in Fig. 2.2.

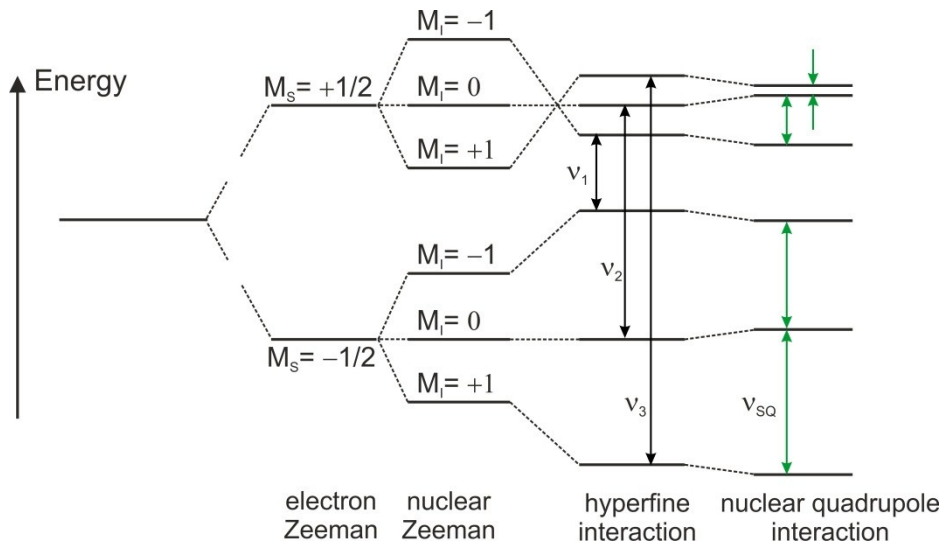

Figure 2.2 *Energy level diagram for an S=½, I=1 spin system with ν_n>0, A>0, P<0 and $|A/2| > |\nu_n|$, where ν_n is the nuclear Larmor frequency. The allowed EPR (ΔM_S=±1 and ΔM_I=0) and NMR (ΔM_S=0 and ΔM_I=±1) transitions are marked with black and green arrows, respectively.*

2.1.4 Strong and weak coupling between electron and nuclear spins

Since the magnetic field which is set up at the nucleus depends both on the external magnetic field $\vec{\boldsymbol{B}}_{\boldsymbol{0}}$ (nuclear Zeeman interaction) and on the hyperfine coupling with the electron spin (the 'hyperfine field'), the nuclear spin is quantized along the sum of these two contributions. Depending on which contribution is the dominant one, one has to consider the weak coupling or the strong coupling case. The electron spin energy level schemes for both cases are presented in Fig. 2.3 for a simple spin system with S=½, I=½. This system has two nuclear transitions with frequencies $\nu_n \pm \frac{A}{2}$, where ν_n is the nuclear Larmor frequency and A the hyperfine coupling constant. In the weak coupling case, i.e. when $|\nu_n| > |\frac{A}{2}|$, the doublet is centered at $|\nu_n|$ and split by $|A|$. In the strong coupling case, i.e. $|A| > |2\nu_n|$, the doublet is centered at $|A/2|$ and split by $2|\nu_I|$. Importantly, if the nuclear Zeeman and hyperfine interaction are of the same order of magnitude, the hyperfine field at the nucleus perpendicular to the external field ($\vec{\boldsymbol{B}}_{\boldsymbol{0}}$ directed along z direction) can no longer be neglected. It contributes a pseudosecular interaction $B = \sqrt{A_{zx}^2 + A_{zy}^2}$ in the xy plane. The nuclear frequencies are then given (in angular frequency units) by [3]:

$$\omega_\alpha = \sqrt{\left(\omega_n + \frac{A}{2}\right)^2 + \frac{B^2}{4}} \qquad \text{Eq. (2.16)}$$

$$\omega_\beta = \sqrt{\left(\omega_n - \frac{A}{2}\right)^2 + \frac{B^2}{4}}$$

This pseudosecular contribution causes a tilt of the effective field from the z direction of the external magnetic field. As a consequence, the excitation of the electron spin will exert an influence on the nuclear spin state. Therefore, forbidden EPR transitions, where both M_s and M_I change (ΔM_S=±1 and ΔM_I=±1), become partially allowed. These non-secular terms affect not only the nuclear transition frequencies but also the transition probabilities and thus the intensities of the ENDOR lines.

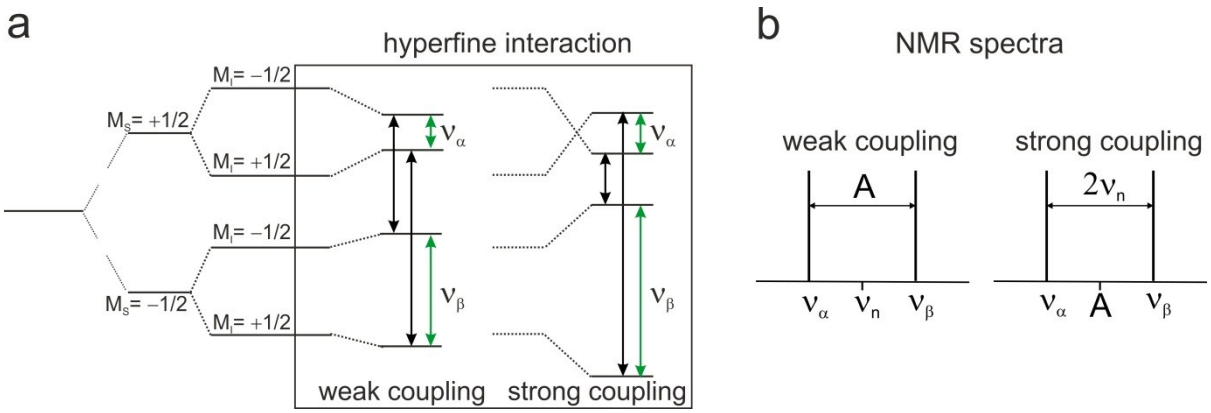

Figure 2.3 *(a) Energy level diagram for an S=½, I=1 spin system with $\nu_n > 0$ and $A > 0$ in the weak and strong coupling case. The allowed EPR and NMR transitions are marked with black and green arrows, respectively. (b) Corresponding NMR spectra observed for the two energy level diagrams in (a).*

2.1.5 Weak coupling between electron spins

A system of two weakly coupled unpaired electrons with spins S_1 and S_2, can be conveniently described by two single-spin Hamiltonians and additional terms, which arise from the coupling:

$$\hat{H}_S(S_1, S_2) = \hat{H}_S(S_1) + \hat{H}_S(S_2) + \hat{H}_{exch} + \hat{H}_{dd} \qquad \text{Eq. (2.17)}$$

The last two terms characterize the contributions due to spin exchange $\hat{H}_{exch}$ and dipole-dipole coupling, $\hat{H}_{dd}$.

The exchange coupling described with $\hat{H}_{exch}$, occurs when two paramagnetic species are close enough for the orbitals of the two spins to overlap, allowing the unpaired electrons to be exchanged. In liquid solutions, the Heisenberg exchange interaction is mainly governed by the collisions of paramagnetic species that lead to temporary, strong overlap of orbitals.

The dipole-dipole interaction between two electrons can be treated analogous to the dipolar coupling between the electron and nuclear spin (see Chapter 2.1.2). The contribution of the dipole-dipole interaction to the spin Hamiltonian has the form:

$$\hat{H}_{dd} = \frac{1}{4\pi}\frac{\mu_0}{r_{12}^3 h} g_1 g_2 \beta^2 \left[\hat{\mathbf{S}}_1 \hat{\mathbf{S}}_2 - \frac{3}{r_{12}^2}(\hat{\mathbf{S}}_1 \mathbf{r_{12}})(\hat{\mathbf{S}}_2 \mathbf{r_{12}})\right] \qquad \text{Eq. (2.18)}$$

where $\mathbf{r_{12}}$ is the vector connecting the two electron spins and g_1, g_2 are their g-values. The dipolar coupling tensor **D** can be expressed in its principal axes frame as:

$$\mathbf{D} = \frac{1}{4\pi}\frac{\mu_0}{r_{12}^3 h} g_1 g_2 \beta^2 \begin{bmatrix} -\nu_{dd} & & \\ & -\nu_{dd} & \\ & & 2\nu_{dd} \end{bmatrix} \qquad \text{Eq. (2.19)}$$

Since the dipolar frequency ν_{dd} is proportional to r_{12}^{-3}, the distance between the pair of electron spins can be extracted. The measurement of dipolar couplings is therefore a powerful tool to extract the information on distances between paramagnetic species in biomacromolecules, as discussed in Chapter 3.4.

2.2 Continuous wave EPR

The absorption of microwave irradiation resulting in an EPR signal requires the fulfillment of the resonance condition described by Eq. 2.4. In continuous wave (cw) EPR, this is realized by sweeping the magnitude B_0 of the external magnetic field $\vec{\mathbf{B}}_\mathbf{0}$ while the microwave frequency, ν_{mw}, is

kept constant. As follows from the resonance condition, EPR absorption can occur at different microwave frequencies as long as the corresponding static external magnetic field is adjusted to obtain the appropriate electron Zeeman splitting. The most widely used mw frequencies are X-band (9.4 GHz), Q-band (34 GHz) and W-band (94 GHz). To improve the signal-to-noise (S/N) ratio, the magnetic field is modulated with a frequency of typically 100 kHz, and only the modulated part of the detector output voltage is phase-sensitively detected. As a result, the 1st derivative shape of the cw EPR spectrum is recorded. In the simplest case of a single spin packet, i.e. spins experiencing the same local fields, the real part of the detected complex signal can be described by a Lorentzian shape absorption line. The width of the line is equal to $2/T_2$ (in angular frequency units), where T_2 is the transverse relaxation time due to spin-spin interactions. In most cases, however, the cw EPR spectrum of a powder-like sample consists of a superposition of spectra from many spin packets subject to slightly differing static magnetic fields since all orientations of the spin system with respect to the external magnetic field, $\vec{\mathbf{B}}_\mathbf{0}$, are present in the powder sample. The dependence of the spin system's Larmor frequencies on the orientation results in an inhomogeneously broadened EPR line, which often can be approximated by a Gaussian line shape. Additionally, if the hyperfine couplings with nearby nuclear spins are not resolved in the EPR spectrum, they also contribute to the EPR spectrum as inhomogeneous line broadening. As opposed to homogenous linewidth, the inhomogeneous linewidth is not related to the spin-spin relaxation time.

2.3 Pulsed EPR methods

In pulsed EPR, high-power and short (length in ns to μs range) mw and radiofrequency (rf) irradiation pulses are applied to drive spin transitions, as opposed to continuous irradiation used in cw EPR experiments. Although EPR theory is based on the quantum mechanical treatment, the basic aspects of mw pulse driven spin dynamics can be visualized in a simplified, classical representation through the motion of the macroscopic magnetization vector, $\vec{\mathbf{M}}$, that is the sum of individual magnetic moments associated with individual electron spins. In the presence of a static external magnetic field $\vec{\mathbf{B}}_\mathbf{0}$ (directed along z axis), the net magnetization, M_z, is observed along the direction of $\vec{\mathbf{B}}_\mathbf{0}$. The application of a mw pulse at frequency ν, which introduces a second magnetic field $\vec{\mathbf{B}}_\mathbf{1}$, perpendicular to $\vec{\mathbf{B}}_\mathbf{0}$, leads to a new resultant magnetic field component, about which the magnetization precesses with the Larmor frequency. In the simplest pulsed EPR experiment, a mw $\pi/2$ pulse is applied along the x axis, rotating the magnetization by 90° to the y axis. After the mw pulse is switched off, the magnetization vector precesses back to the equilibrium position along the *z* axis due to spin-lattice relaxation processes which are described by the T_1 relaxation time. The precession leads to oscillating M_x and M_y components of the magnetization vector, i.e. electron coherence in the xy-plane, which is monitored in the EPR experiment as free induction decay (FID).

In addition to spin-lattice relaxation processes, the transverse magnetization also dephases due to spin-spin relaxation, described by the T_2 relaxation time. Normally, this relaxation requires the pulse EPR experiments to be performed at low temperatures. This is opposed to cw EPR, where EPR spectra can be recorded at RT for a large number of spin systems, including nitroxide radicals. However, the main advantage of pulsed EPR over its continuous wave counterpart is the possibility to partially separate the magnetic interactions which are otherwise not resolved in the cw EPR spectrum

due to broad inhomogeneous lines. To measure, for example, electron-nuclear interactions, tailored pulse sequences are used as described in more detail below.

2.3.1 Echo-detected EPR spectrum

The FID signal usually starts to decay within the deadtime of the EPR spectrometer and the dephasing of the spins is caused by local field inhomogeneities or magnetic interactions which result from a distribution of Larmor frequencies of individual electron spins. To overcome this limitation, 2-pulse electron spin echo experiment can be performed, where the dephasing of the spin packets can be partially reversed. It is achieved by applying an additional π pulse after a time interval τ, refocusing the dephasing spin packet into an observable electron spin echo after a delay time of 2τ, see Fig. 2.4. This pulse sequence was first described in relation to nuclear spins by Hahn [6], hence its alternative name is Hahn echo sequence.

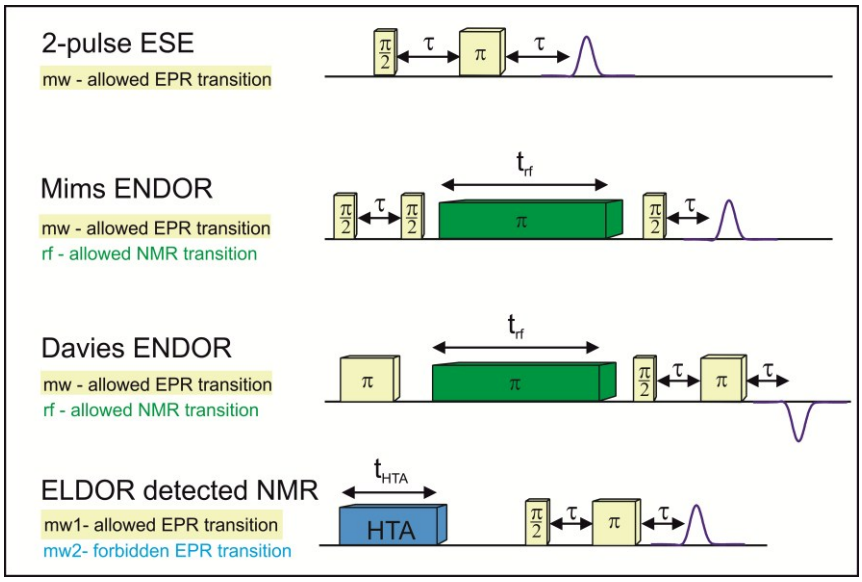

Figure 2.4 *Pulse sequences for the experiments employed in this work and described in the sections below. Spectra are generated by variation of the strength of the magnetic field* $\boldsymbol{B_0}$ *(field-swept echo-detected EPR), by incrementing the frequencies of the rf or mw pulses (ENDOR, EDNMR), or by combinations thereof (i.e. field-frequency ENDOR or EDNMR spectra).*

For a rectangular pulse of frequency ν, the excitation profile of a pulse corresponds to a sinc function, $|2 \cdot \sin(\pi v \cdot t_p/2)/\pi v|$, with the uniform excitation given in the range of $v \mp 1.2/t_p$, where t_p is the pulse length [3]. Hence, the length of the pulse determines the selectivity of the excitation. For a typically applied mw pulse length it is not possible to excite the full EPR spectrum with a single mw pulse. For example, the mw pulse length of 24 ns yields uniform excitation of 50 MHz around the carrier frequency, while the nitroxide radical EPR spectrum at W-band has a width of circa 450 MHz. Therefore, to record an EPR spectrum, the Hahn echo sequence is applied at multiple field positions B_0 over the magnetic field range. The integrated echo intensities at each magnetic field position yield the field-swept EPR absorption spectrum.

2.3.2 Hyperfine spectroscopy

ENDOR (electron-nuclear double resonance) and EDNMR (ELDOR-detected NMR) are *polarization-transfer* pulsed EPR methods that allow the detection of nuclear transition frequencies of paramagnetic systems. The nuclear frequencies are detected after the populations/polarizations of the electron-nuclear spin manifold are transiently changed with either a radiofrequency (rf) or a microwave (mw) pulse. In the following, the ENDOR and EDNMR experiments are described in more detail.

2.3.2.1 Mims and Davies ENDOR

ENDOR is an EPR technique that combines the advantages of EPR (high detection sensitivity) with those of NMR (high resolution capability) for the detection of the nuclear transition frequencies. Invented first as cw experiment [7], later ENDOR was extended to ESE-detected pulse versions by Mims [8] and Davies [9], see pulse sequences in Fig. 2.4.

The Mims ENDOR sequence is based on the stimulated echo sequence, i.e. three mw pulses separated by two constant time delays, π/2-τ-π/2-T-π/2. The first time delay, τ, typically lasts several hundreds of ns, while the second, during which a monochromatic rf π pulse is applied, is in the range of tens of μs. The first two mw pulses create electron polarization along the z-axis. Subsequently, an rf π pulse is applied, which induces spin flips of the nuclei by driving allowed NMR transitions ($\Delta M_S = 0$, $\Delta M_I = \pm 1$, see also Fig. 2.3) when the frequency of the nuclear transition is matched. This in turn leads to changes in the electron polarization observed as the amplitude of stimulated ESE at time τ after the last pulse. The change in echo intensity induced by the rf pulse is characterized by the ENDOR efficiency defined as:

$$F_{ENDOR} = \frac{1}{2}\sin^2(A\tau) \qquad \text{Eq. (2.20)}$$

where A is the hyperfine coupling constant expressed in angular frequency units, and τ is the time delay between the first and second mw pulses. The intrinsic sensitivity of Mims ENDOR experiment is high, as the ENDOR effect can reach 50% of the echo intensity. However, as follows from Eq. 2.20, for a given hyperfine coupling constant the sensitivity depends strongly on the interpulse delay τ. And for particular values of the hyperfine coupling, i.e. $A = n/\tau$, the ENDOR effect is completely suppressed ('blindspot'). For that reason, the Mims ENDOR sequence is better adapted for the detection of small hyperfine coupling constants, which are not distorted by the 'blind spot' phenomenon. For detection of larger couplings, in addition several spectra, recorded with different τ values, are necessary to ensure that all ENDOR signals are detected.

Alternatively, larger hyperfine coupling constants can be measured using the Davies ENDOR sequence. In this sequence, a selective mw π pulse is first applied, which inverts the spin population of the allowed EPR transition within a limited spin packet. This can be regarded as burning a hole into the EPR line. During the following mixing period, an rf π pulse is applied that drives the allowed NMR transitions. This results in a levelling of the population difference of the excited EPR transition, as shown schematically in Fig. 2.5. Subsequently, the changed electron polarization is converted to observable electron coherence using a Hahn echo detection sequence. Importantly, Davies ENDOR is insensitive to couplings within the linewidth of the created spectral hole. Therefore, for the detection of small hyperfine couplings, a highly selective inversion pulse would be required. Since the length of

the first preparation π pulse is in general longer than for pulses in the stimulated echo sequence used in Mims ENDOR, consequently a smaller fraction of spins takes part in the Davies ENDOR experiment. Hence, it is less sensitive compared to Mims ENDOR. For these reasons, Davies ENDOR is usually applied only for detecting larger hyperfine couplings.

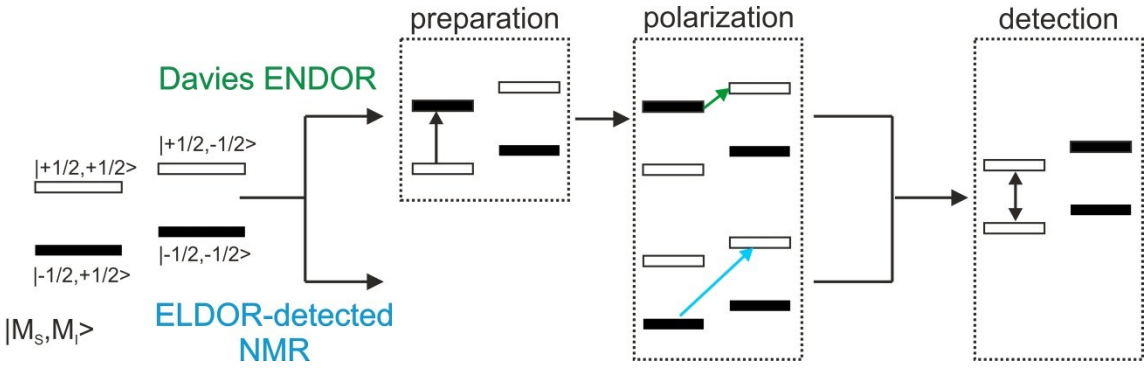

Figure 2.5 *Transition schemes for the spin state sublevels in Davies ENDOR and EDNMR experiments for a system with electron spin S = ½ and nuclear spin I = ½, analogous to the scheme shown in Fig. 2.3(a). On top, the spin state transitions in Davies ENDOR experiment are shown. First, the selective mw preparation pulse is used that inverts the populations of the electron spin states, then the mixing rf pulse drives a spin polarization transfer via the NMR transitions, as is shown by the green arrow. On the bottom, the HTA mw pulse at a second mw frequency that induces a spin polarization transfer by pumping allowed and forbidden transitions is shown by the blue arrow.*

For simple $S = 1/2$, $I = 1/2$ spin systems, a pair of lines corresponding to two nuclear transition frequencies, ν_α and ν_β, is detected in an ENDOR experiment. Depending on the relative magnitudes of the hyperfine coupling constant and the nuclear Larmor frequency, ENDOR spectra corresponding to the 'strong' or 'weak' coupling case are obtained, see Chapter 2.1.4 and Fig. 2.3(b). In reality, for disordered powder samples the lines are broader since numerous individual narrow lines from molecules with a set of differing orientations are summed up.

To extend a pulsed EPR spectrometer to a pulsed ENDOR spectrometer, an rf source, coils and a broadband high-power rf amplifier have to be added. Depending on the rf setup, the amplitude of the rf pulse, B_2, can exhibit variation over the frequency range, which is a drawback when larger rf sweeps are necessary, for example, to detect strongly coupled nuclei at high-field/high-frequency. Since the strength of the rf pulse is subject to technical limitations, the length of the rf pulses is usually on the order of tens of µs. This results in a small excitation bandwidth of the rf pulse. Hence the ENDOR spectrum is recorded by sweeping the rf frequency through the EPR spectrum. Due to the proximity of the rf coil to the sample, the conversion of the rf power to heat might result in baseline artefacts, particularly influencing broad ENDOR lines. For this reason, the ENDOR spectra are usually recorded by varying the rf stochastically instead of sweeping it linearly [10].

The effective flip angle of the rf pulse for a given nucleus depends on the nuclear g_n value. This is a considerable drawback for the investigation of low-γ nuclei, since longer rf pulses are needed to observe an ENDOR effect. For strongly coupled nuclei, this effect is partially compensated by the so-called hyperfine enhancement. It increases the ENDOR effect due to the presence of strong internal hyperfine fields in addition to the external rf field [11]. Since the optimal rf field strength is

dependent on the identity of the magnetic nuclei, transitions from multiple magnetic nuclei can seldom be simultaneously recorded within a single ENDOR experiment.

2.3.2.2 ELDOR-detected NMR (EDNMR)

ELDOR-detected NMR, similar to ENDOR, is a polarization-transfer method capable of probing nuclear transition frequencies. However, the two techniques differ in the way in which the population of the nuclear levels is changed. In the EDNMR experiment, the nuclear transitions of the spin manifold are probed indirectly by using a high-turning-angle (HTA) mw pulse at a second microwave frequency, mw2, see Fig. 2.4. This HTA pulse transfers the polarization across the forbidden electron transitions, i.e., transitions where both the electron and nuclear spin change their projection direction ($\Delta M_S = \pm 1$, $\Delta M_I = \pm 1, \pm 2$), see Fig. 2.5. This is followed by detection using a Hahn echo sequence in the first channel mw1 at the resonance frequency of the allowed EPR transitions.

The efficiency of polarization transfer across the forbidden transition, which is detected in the EDNMR, is determined by the optimum transition flip angle, β_f:

$$\beta_f = \beta_0 \cdot \sqrt{I_f} \qquad \text{Eq. (2.21)}$$

where β_0 is the nominal flip angle of the allowed EPR transition defined by $\beta_0 = t_{HTA} \cdot \omega_1$, and I_f is the probability of the forbidden transition. The EDNMR efficiency for the selected forbidden transition depends therefore on the HTA pulse length, t_{HTA} and the HTA pulse amplitude, ω_1^{HTA}, which are adjustable parameters. It also depends on the intensity of forbidden transitions, I_f, which is an inherent property of the spin system.

In detail, I_f depends both on the contribution of quadrupole (P) and anisotropic hyperfine (A) interaction parameters of the spin Hamiltonian, therefore it varies along the EPR spectrum in a predictable manner. In the g_{zz} spectral region of nitroxide radicals, the normalized intensity of the forbidden single-quantum EPR transition, without taking into account the quadrupole contribution, is given by:

$$I_f = \frac{\left| \nu_n^2 - \frac{1}{4}(\nu_\alpha - \nu_\beta)^2 \right|}{\nu_\alpha \cdot \nu_\beta} \qquad \text{Eq. (2.22)}$$

where ν_n is the nuclear Larmor frequency, ν_α and ν_β are the nuclear transition frequencies associated with the electron spin states $M_S = +1/2$ and $M_S = -1/2$, see Fig. 2.3.

The efficiency of and EDNMR experiment is defined as:

$$F_{EDNMR} = \frac{V_{echo}(\text{HTA off}) - V_{echo}(\text{HTA on})}{V_{echo}(\text{HTA off})} \qquad \text{Eq. (2.23)}$$

where V_{echo}(HTA off) and V_{echo}(HTA on) are the echo intensity when the HTA pulse is off and on resonance with the transition, respectively. The maximum efficiency of the EDNMR experiment is obtained when β_f results in a π flip angle.

Although already reported 20 years ago by Schosseler et al. [12] as an alternative for conventional ENDOR or electron-spin echo envelope modulation (ESEEM) techniques, EDNMR was

not widely applied until recently. This was due to the overlap of EDNMR lines of weakly coupled low-γ nuclei with the central 'blind spot', when EDNMR experiments were performed at low microwave frequencies (X-, Q-band). The development of high-field/high-frequency EPR, for instance at W-band, where the lines of such nuclei are shifted away from the central region due to increased nuclear Larmor frequencies, resulted in rather widespread applications of the EDNMR technique. Indeed, W-band EDNMR was recently shown to perform very well for characterizing weakly and strongly hyperfine-coupled nuclei [13-15]. It was also successfully applied to nitroxide radicals, to study the relative orientation between the g- and hyperfine tensors [16], and to obtain ^{14}N quadrupole couplings, P_{zz}, in frozen solutions [17].

Compared to ENDOR, high-field EDNMR presents several advantages for the investigation of low-γ nuclei coupled to the electron spin. EDNMR is more robust against fast electron spin-lattice relaxation, T_1, and spectral diffusion than pulsed ENDOR. This robustness is because no preparation of the electron spin system prior to the HTA pulse is required and short HTA pulses can be realized with the available microwave power. Moreover, the recorded EDNMR spectrum is not distorted by 'blindspots' around the nuclear Larmor frequencies, except for the central 'blind spot' at the mw detection frequency. EDNMR is also a more versatile method as it allows simultaneous detection of all magnetic nuclei present in the system.

2.4 High-field/high-frequency EPR

The only field-dependent terms of the spin Hamiltonian describing S=1/2, I=1 spin systems, e.g. nitroxide radicals, are the electron and nuclear Zeeman interactions. Hence, at sufficiently large values of the external magnetic field, the electron Zeeman interaction becomes the dominant term in the spin Hamiltonian, allowing to resolve the main g-matrix elements: g_{xx}, g_{yy} and g_{zz}. 'True' high-field experiments are, therefore, performed when the electron Zeeman interaction exceeds the inhomogeneous EPR linewidth due to unresolved hyperfine interactions. For nitroxide radicals, the term 'high-field EPR' is justified for mw frequencies of about 90 GHz or higher, corresponding to a static magnetic field of $B_0 > 3$ T. The increased spectral resolution offers the possibility to partially separate the overlapping EPR spectra of paramagnetic species with similar g-values, e.g. the EPR spectra of $P_{865}^{\bullet+}$ and $Q_A^{\bullet-}$ ionic states of native cofactors in the bacterial photosynthetic reaction center [18].

As discussed in section 2.1.1 of this chapter, molecules with different orientation with respect to the external magnetic field have distinct resonance field values, yielding a characteristic powder spectrum, see Fig. 2.6. Therefore, by applying a mw pulse at a certain spectral position in the EPR spectrum with resolved g-tensor anisotropy, a set of molecules with specific orientation relative to the external magnetic field is selected. This so-called 'orientation selection' enables one to extract the anisotropy of other interactions, e.g. the hyperfine interaction, and to determine the orientation of their main axes within the g-matrix axes system [19].

The increased field/frequency values are also of importance for the nuclear Zeeman interaction since it allows a better separation of the nuclear Larmor frequencies of different nuclei. The gain in ENDOR resolution of typical nuclei when going from X-band (9.5 GHz) to W-band (95 GHz) is shown in Fig. 2.7.

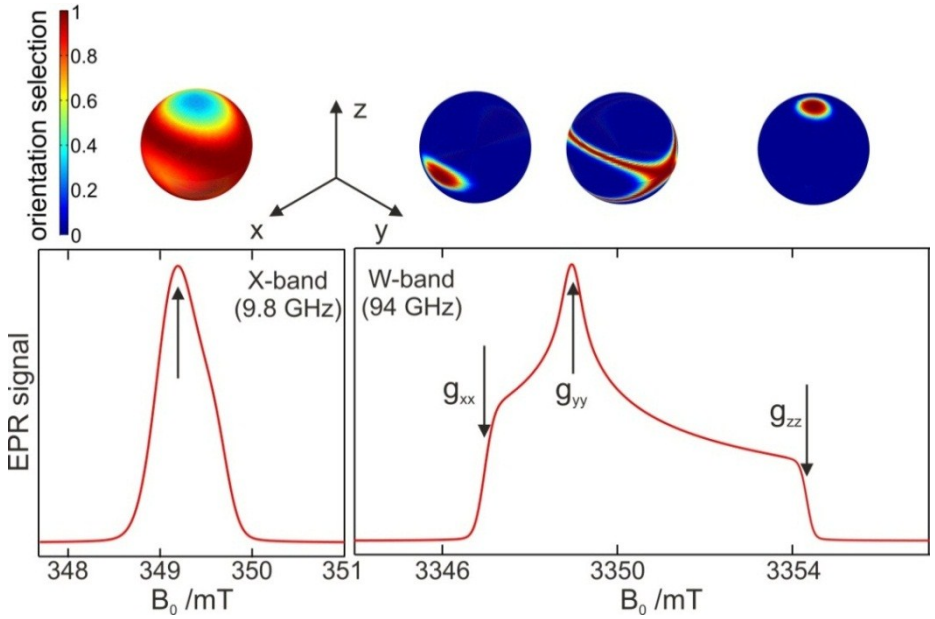

Figure 2.6 *Orientational selectivity for the radical anion state $Q_A^{\cdot-}$ of the primary quinone acceptor in the bacterial photosynthetic reaction center from Rhodobacter sphaeroides at X-band (left) and at W-band (right) using mw pulses with a 20 MHz excitation bandwidth profile (FWHM). Orientation selections on the unit sphere for the observer magnetic field positions corresponding to g_{xx}, g_{yy}, and g_{zz} are shown on top. The scale indicating which orientations are on resonance is shown in the upper left corner. Fig. adapted from [18].*

Moreover, when approaching the so-called high field condition, i.e. $|\nu_n| > |A|$, the nuclear spins are quantized along the external magnetic field and the pseudosecular contributions described in section 2.1.4 become negligible. This simplifies the interpretation of ENDOR spectra, since they become symmetric around the nuclear Larmor frequency. Additional advantages of high-field/high-frequency EPR are the enhanced detection sensitivity when limited-volume samples are studied and enhanced low-temperature electron-spin polarization. For a detailed description, see reviews [18;20;21].

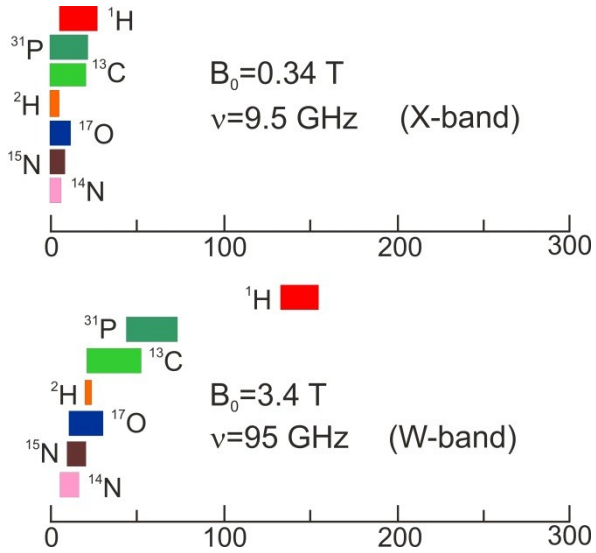

Figure 2.7 *Gain in ENDOR resolution for doublet-state systems (S=1/2, g=2) with increasing Zeeman field B_0 and microwave frequency ν from X-band to W-band. Figure adapted from [18].*

References

[1] A. Abragam, B. Bleaney *Electron paramagnetic resonance of transition metal ions*, Clarendon Press, Oxford, 1970.

[2] C. Rudowicz, S.K. Misra *Spin-Hamiltonian formalisms in electron magnetic resonance (EMR) and related spectroscopies*. Appl. Spectrosc. Rev. **2001,** 36*,* 11-63.

[3] A. Schweiger, G. Jeschke *Principles of pulse electron paramagnetic resonance*, Oxford University Press, Oxford, 2001.

[4] N.M. Atherton *Principles of electron spin resonance*, Ellis Horwood, New York, 1993.

[5] B.R. Mcgarvey *The isotropic hyperfine interaction*. J. Phys. Chem. **1967,** 71*,* 51-66.

[6] E.L. Hahn *Spin echoes*. Phys. Rev. **1950,** 80*,* 580-594.

[7] G. Feher *Observation of nuclear magnetic resonances via the electron spin resonance line*. Phys. Rev. **1956,** 103*,* 834-835.

[8] W.B. Mims *Pulsed ENDOR experiments*. Proc. R. Soc. Lond. A **1965,** 283*,* 452-457.

[9] E.R. Davies *A new pulse ENDOR technique*. Phys. Lett. A **1974,** 47*,* 1-2.

[10] B. Epel, D. Arieli, D. Baute, D. Goldfarb *Improving W-band pulsed ENDOR sensitivity: acquisition and pulsed special TRIPLE*. J. Magn. Reson. **2003,** 164*,* 78-83.

[11] A. Schweiger *Electron nuclear double resonance of transition metal complexes with organic ligands*, Springer, Berlin, 1982.

[12] P. Schosseler, Th. Wacker, A. Schweiger *Pulsed ELDOR detected NMR*. Chem. Phys. Lett. **1994,** 224*,* 319-324.

[13] I. Kaminker, H. Goldberg, R. Neumann, D. Goldfarb *High-field pulsed EPR spectroscopy for the speciation of the reduced* $[PV_2Mo_{10}O_{40}]^6$ *polyoxometalate catalyst used in electron-transfer oxidations*. Chem.-Eur. J. **2010,** 16*,* 10014-10020.

[14] L. Rapatskiy, N. Cox, A. Savitsky, W.M. Ames, J. Sander, M.M. Nowaczyk, M. Rögner, A. Boussac, F. Neese, J. Messinger, W. Lubitz *Detection of the water-binding sites of the oxygen-evolving complex of Photosystem II using W-Band* ^{17}O *electron-electron double resonance-detected NMR spectroscopy*. J. Am. Chem. Soc. **2012,** 134*,* 16619-16634.

[15] N. Cox, W. Lubitz, A. Savitsky *W-band ELDOR-detected NMR (EDNMR) spectroscopy as a versatile technique for the characterisation of transition metal-ligand interactions*. Mol. Phys. **2013,** 111*,* 2788-2808.

[16] G. Jeschke, H.W. Spiess *NMR-correlated high-field electron paramagnetic resonance spectroscopy*. Chem. Phys. Lett. **1998,** 293*,* 9-18.

[17] M. Florent, I. Kaminker, V. Nagarajan, D. Goldfarb *Determination of the* ^{14}N *quadrupole coupling constant of nitroxide spin probes by W-band ELDOR-detected NMR*. J. Magn. Reson. **2011,** 210*,* 192-199.

[18] K. Möbius, A. Savitsky *High-field EPR spectroscopy on proteins and their model systems*, RSC Publishing, Cambridge, 2009.

[19] G.H. Rist, J.S. Hyde *Ligand ENDOR of metal complexes in powders*. J. Chem. Phys. **1970,** 52*,* 4633-4643.

[20] M. Bennati, T.F. Prisner *New developments in high field electron paramagnetic resonance with applications in structural biology*. Rep. Prog. Phys. **2005,** 68*,* 411-448.

[21] K. Möbius, W. Lubitz, A. Savitsky *High-field EPR on membrane proteins - Crossing the gap to NMR*. Prog. Nucl. Magn. Reson. Spectrosc. **2013,** 75, 1-49.

Chapter 3

EPR spectroscopy on nitroxides

3.1 The principle of site-directed spin labeling

While most molecules contain magnetic nuclei and are thus amenable to NMR spectroscopy, the number of biological systems that comprise stable or transient paramagnetic states which are accessible to EPR spectroscopy is by far smaller. These include, for instance, enzyme cofactors with paramagnetic transition metals incorporated [1], radical enzymes [2] and radicals in photosynthetic proteins [3].

In case of biological systems that do not involve any native paramagnetic species, EPR spectroscopy can still be applied by resorting to artificial paramagnetic molecules that are introduced into the system. Nitroxides, stable free radicals with the structural unit $R_2NO\cdot$, are by far the most often applied class of these paramagnetic molecules since its development in the 1960s [4;5]. The chemical structure of nitroxide radicals of piperidine-, pyrroline- or pyrrolidine-type is shown in Fig. 3.1(a). The concept of site-directed spin labeling (SDSL) using nitroxide radicals has emerged from the pioneering work of Hubbell [6]. It involves attachment of the spin label to the sulfhydryl group of cysteine, which is either a native residue or is introduced through point-specific mutagenesis, see Fig. 3.1(b), but has since been tailored for application in proteins where functional cysteine residues are present [7]. The resulting modified protein side chain, referred to as R1 when MTS ((1-oxyl-2,2,5,5-tetramethylpyrroline-3-methyl)methanethiosulfonate) spin label (MTSSL) [8] is used, can then be investigated using EPR spectroscopy.

The important advantage of nitroxide labels, beside their stability, is the small molecular volume which they occupy, comparable to tryptophan or phenylalanine side chains. Therefore, relatively small or no perturbation in the structure or function of most proteins is introduced. However, in contrast to natural amino acid side chains, MTSSL is not rigidly connected to the protein backbone but linked by a rather flexible tether, see Fig 3.1(b).

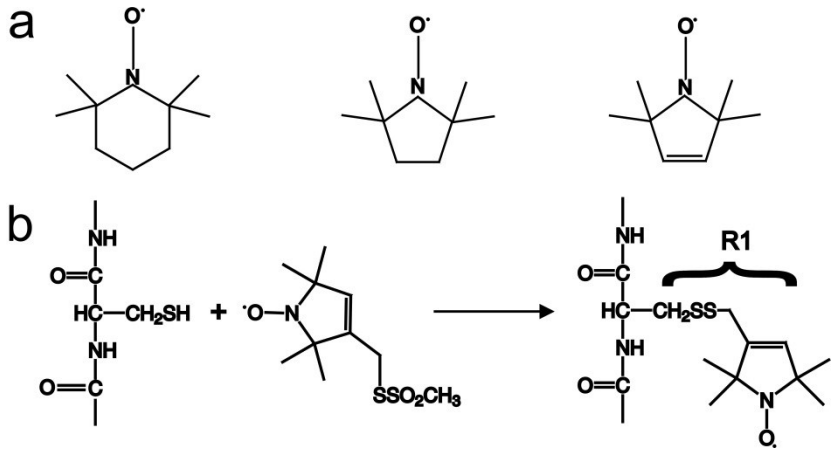

Figure 3.1 *(a) Chemical structure of, from left to right, piperidine-, pyrrolidine- and pyrroline-type nitroxides. (b) Scheme for the chemical modification of the cysteine residue with sulfhydryl-specific nitroxide spin label.*

The use of a nitroxide radical that anchors on the protein in two positions yields a more rigid spin label, but requires introduction of two mutated cysteines at proper spacing [9;10]. EPR spectroscopy on attached spin labels is used to investigate the dynamics of the protein, identify regions of regular secondary structure, determine the distance between protein fragments when pairs of spin labels are introduced in the protein and in studies of the immediate environment of the nitroxide radical, to name a few. Selected applications are described in more detail in the following parts.

In addition to spin labeling, i.e. covalent attachment of nitroxide to the macromolecule under study, stable free radicals can also be introduced as spin probes by admixing to the system of interest. Hence, spin probing usually requires less preparatory effort. Since spin probes are well-suited for characterization of the collective behavior of molecules [11], the problem at hand usually dictates which of the two approaches is more appropriate.

3.2 cw EPR spectra of nitroxide radicals

The molecular coordinate system of nitroxide radical is presented in Fig. 3.2(a). The z axis is usually defined as parallel to the $2p_z$ orbital of the nitrogen. The x axis is directed along the N-O bond and the y axis is directed perpendicular to the xz plane. Typical principal g values are g_{xx}=2.0090, g_{yy}=2.0060 and g_{xx}=2.0024, although the magnetic parameters differ slightly between different classes of nitroxides [12]. The deviation of the g value from g_e is due to spin orbit coupling in excited states which involves the lone pair orbitals on oxygen. The strongest g-shift is observed when the field is parallel to the N–O bond (the x axis of the molecular frame), is intermediate in the y–direction and almost negligible in the z-direction (along the lobes of the $2p_z$ orbital on the oxygen).

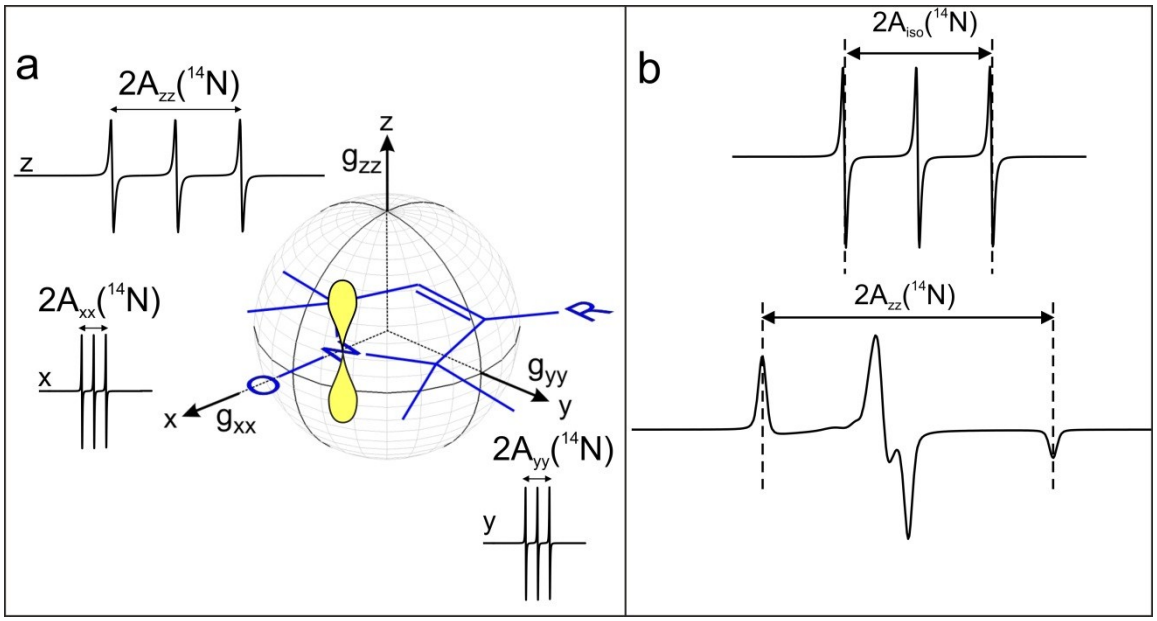

Figure 3.2 *(a) The structure of the nitroxide radical with its molecular axes is shown. The spectra showing the dependence of the ^{14}N hyperfine coupling on orientation of the magnetic field with respect to the molecular frame are presented. The $2p_z$ orbital of nitrogen atom is shown in yellow. (b) Typical X-band cw EPR liquid solution (top) and powder (bottom) spectra of nitroxide radicals.*

Typical hyperfine coupling values are $A_{xx} = A_{yy} = 12$ MHz, $A_{zz} = 96$ MHz, but again depend on the nitroxide structure. The ^{14}N hyperfine coupling contains a sizeable isotropic contribution due to Fermi contact interaction between the electron and $2s$ orbital on the nitrogen. An anisotropic

hyperfine contribution mainly arises from the spin density in the nitrogen $2p_z$ orbital. If the external magnetic field $\vec{\boldsymbol{B}}_{\mathbf{0}}$ is parallel to the $2p_z$ lobe, the hyperfine interaction and thus the splitting within the triplet is largest, if it is perpendicular to $2p_z$, the splitting is smaller, as shown in Fig. 3.2(b). Hence, the triplets of lines at different orientations of the molecule with respect to the field have different splittings and their centers are also shifted with respect to each other (g-shift). In planar nitroxides the **g**-matrix and hyperfine coupling tensor **A** can be assumed to be collinear, to a good approximation.

An example of typical liquid and powder cw EPR spectra for stable nitroxide radicals at X-band are shown in Fig. 3.2(b). In fluid media in the regime of fast motion, the anisotropic contributions average out and a simplified spectrum with only isotropic contributions is observed, see top spectrum in Fig. 3.2(b). The center line is at a field corresponding to the isotropic g value $\mathrm{g_{iso}} = (\mathrm{g_{xx}} + \mathrm{g_{yy}} + \mathrm{g_{zz}})/3$ and the splitting between the outer lines is equal to $2A_{iso}$, where $A_{iso} = (A_{xx} + A_{yy} + A_{zz})/3$.

The powder spectrum is given by superposition of the EPR spectra of randomly immobilized radicals, as described in Chapter 2.2. Since cw EPR spectra are recorded as first derivative of the EPR absorption, negative and positive contributions from neighboring orientations cancel. CW EPR powder spectra are thus dominated by contributions at the minimum and maximum resonance fields and by contributions at resonance fields that are common to many spins, see bottom spectrum in Fig. 3.2(b). At the magnetic field of 0.3 T (X-band), the shape of the powder spectrum is dominated by the hyperfine interaction of the electron spin with the nuclear spin of the internal ^{14}N.

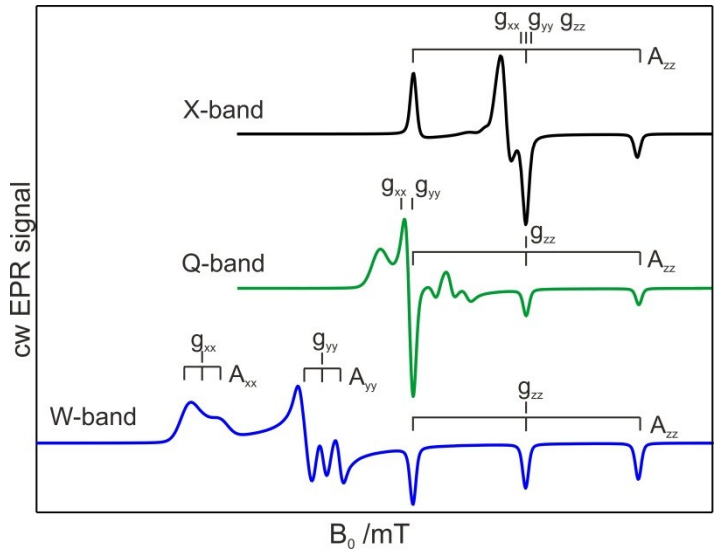

Figure 3.3 *Typical cw EPR powder spectra of nitroxide radicals at X-band (black trace), Q-band (green trace) and W-band (blue trace). The spectral positions that correspond to different principal g-tensor and A_{zz} values are indicated by dotted and dashed lines, respectively.*

The positive peak at the low-field edge corresponds to the edge of the line for $\mathrm{M_I} = +1$ ^{14}N magnetic quantum number and the negative peak at the high-field edge corresponds to the edge of the $\mathrm{M_I} = -1$ line. The detailed shape of the X-band powder spectrum can be simulated, but the interpretation is not always straightforward due to lack of spectral resolution and a similar magnitude of the hyperfine and g anisotropies. If one of these two interactions dominates, the spectra can be analyzed more easily. Hence, spectra are recorded at higher frequencies, e.g. at W-band, which allow for complete interpretation due to increased spectral resolution, see Fig. 3.3 and Chapter 2.4.

3.3 Local microenvironment characterization using nitroxides

The sensitivity of nitroxide radicals to polarity and proticity (defined as propensity for H-bond formation) of the surrounding medium has been recognized early [13-15]. It manifests as variation in magnetic parameters, providing information on the local environment characteristics. These magnetic parameters include:

- the g-tensor (reflecting the Zeeman and spin-orbit interactions of the unpaired electron spin), in particular its g_{xx} component
- the nitrogen hyperfine A-tensor (reflecting the interaction of the unpaired electron with a nuclear spin), in particular the A_{zz} component
- the nitrogen quadrupole P-tensor (reflecting the interaction of the nuclear quadrupole moment with the electric field gradient at this site), in particular the P_{yy} component

For nitroxide cw EPR spectra in the fast-motional regime, i.e. usually at room temp., the solvent effects are evaluated by measuring the isotropic magnetic parameter values, g_{iso} and A_{iso}.

The early EPR studies provided characterization of the directionality and magnitude of the observed spectral changes using nitroxide probes dissolved in various solvents. Such simple bimolecular systems of spin probe and solvent allowed for studying the influence exerted by a particular solvent parameter, e.g. the dielectric constant (ε) or dipole moment (μ), on the values of the magnetic parameters. In general it was reported, that increasing polarity (defined as an increased ε of the solvent) and proticity of the microenvironment result in a g_{iso} decrease while the A_{iso} value increases [13]. Nevertheless, considerable effort has been devoted to the determination of the solvent parameter that correlates best with A_{iso} values extracted from the analysis of X-band cw EPR spectra [16]. Importantly, it has been observed that in aprotic and protic solvents with comparable dielectric constants, the larger A_{iso} shifts are observed in the latter [13]. This lead to formulation of two main effects responsible for the shifts of nitroxide radical magnetic parameters:

i. non-specific interactions due to the bulk electric field, i.e. the polarity influence,
ii. specific interactions, mostly hydrogen bonds formed between a nitroxide radical, acting as H-bond acceptor, and a solvent molecule, that result in an additional local electric field and spin delocalization.

To justify the correlations and rationalize the observed shifts of magnetic parameters, several models were developed to describe the solvent effects on the nitroxide electronic structure [14;17]. These models, however, were mostly developed for particular cases, e.g. the electrostatic dipole-dipole approximation [17], which is applicable solely for the case of highly polar solvents. A most widely applied description, derived from Onsager's reaction field theory, predicts a linear variation of A_{iso} with $(\varepsilon-1)/(\varepsilon+1)$ [14]. While this was shown to be a valid correlation for aprotic solvents, it does not predict reasonable A_{iso} values neither for solvents with high dielectric constants nor for protic solvents. Since the slope of the linear g_{iso} vs A_{iso} plot in aprotic solvents is different from that in the protic ones, it was proposed to serve as an indication of the proticity of the local environment [13]. Indeed, the formation of H-bonded complexes between nitroxide radicals and various protic solvents was indicated based on the results of liquid-solution cw EPR [18-20], NMR [21;22] and calorimetric measurements [23]. However, the predicted higher sensitivity of g_{iso} than A_{iso} to H-bond formation does not exclude its influence on the A_{iso} values and, thus, does not validate the assumption that an

A_{iso} variation originates exclusively from polarity changes, this certainly would be an oversimplification.

The variation in A_{iso} and g_{iso} values as a response to microenvironment changes can be explained in terms of a π-electron spin density redistribution within the N-O• moiety's π system. In nitroxide radicals, the unpaired electron spin density is localized to a good approximation on the N-O• fragment:

$$\rho_N^{\pi} + \rho_O^{\pi} \simeq 1$$

where ρ_N and ρ_O are the electron spin densities on the oxygen and nitrogen atoms, respectively. When the microenvironment's perturbation, i.e. the electric field produced along the N-O• axis of the nitroxide, shifts the electron spin density toward the nitrogen it results in a ρ_N increase – which causes a proportional A_{iso} value increase. Within the valence-bond quantum chemistry formulation, this can be viewed as stabilization of the resonance form II in Fig. 3.4.

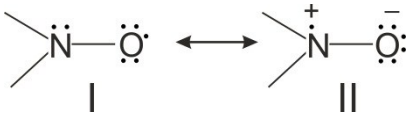

Figure 3.4 *Mesomeric structures of a nitroxide with the unpaired electron localized on the oxygen atom (I) and the nitrogen atom (II).*

A microenvironment influence on the electronic structure of the nitroxide radical can also be described within the framework of Hückel molecular orbital (MO) theory. In Fig. 3.5, the schematic representation of the orbitals for the N-O• group is presented. The two $2p_z$ orbitals of the nitrogen and oxygen are coupled to form a fully occupied bonding orbital π and a half-occupied nonbonding orbital π* that is closer in energy to the nitrogen $2p_z$ orbital.

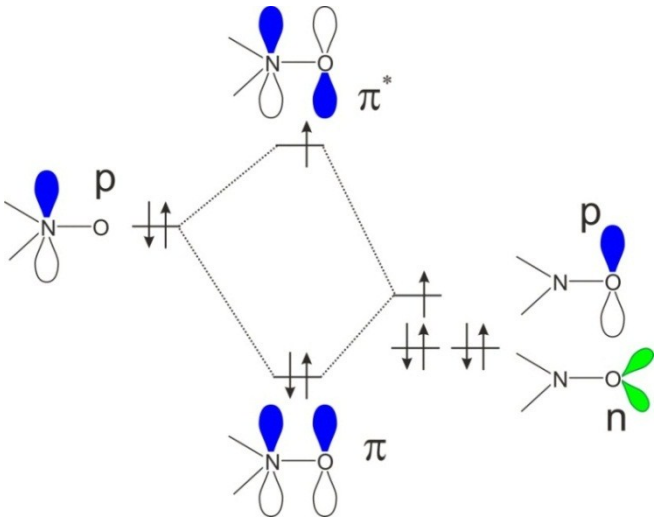

Figure 3.5 *Schematic representation of the energy levels and electronic configuration of the* N-O• *fragment of the nitroxide radical. Figure adapted from [24].*

When an electric field is present along the N-O bond direction, the energies of the parent $2p_z$ orbitals shift according to the difference in the electrostatic potentials at the two nuclei. A negative field along N-O• (electrostatic potential on the O atom larger than on N) destabilizes the nitrogen orbital relative to the oxygen orbital, leading to greater localization of the unpaired electron on the nitrogen. Since A_{iso} is proportional to ρ_N, it results in an A_{iso} increase. When a positive field is present

along N-O•, the opposite effect is observed, i.e. the A_{iso} value decreases. The specific interaction with the solvent, i.e. H-bond formation between nitroxide and the proton donor group, exerts an additional effect on the energies of the molecular orbitals. In detail, a redistribution of spin density between the n (non-bonding oxygen orbital) and π* energy levels takes place, and the increase in $\Delta E_{n\pi^*}$ (the energy of n – π* transition) causes a decrease in the g_{iso} value.

The nitroxide microenvironment can be also characterized on the basis of the anisotropic magnetic interaction parameters evaluated from nitroxide cw high-field/high-frequency EPR spectra which have been recorded below the glass-transition temperature of the solvent (i.e. in the rigid limit). High field/frequency EPR allows for resolving the nitroxide g-tensor principal components and to measure them precisely in addition to the nitrogen hyperfine tensor component A_{zz} (which can be obtained by standard X-band EPR in frozen samples, see Fig. 3.3. The g_{xx} component of the g-tensor was shown, both experimentally [12;15;25] and theoretically [26], to be the most sensitive principal component to probe the microenvironment. Since it is directed along the N-O bond (i.e. coplanar with the nonbonding n orbitals of the O atom), it is expected to be particularly influenced by H-bond formation. Similarly, the **A** tensor component, A_{zz}, directed along the nitrogen $2p_z$ orbital is the most sensitive indicator of polarity and proticity [25;27]. The direction of anisotropic parameters' shifts is the same as for the isotropic magnetic parameters, i.e. decrease of g_{xx} and increase of A_{zz} value is observed with increasing polarity and proticity of the microenvironment.

Nitroxide radicals were shown to be sensitive to the magnitude of electric fields that are typically found in proteins; this can even be used to measure such electric fields quantitatively [26;28;29]. Therefore, site-dependent variations of the nitroxide tensor components g_{xx} and A_{zz} could be used to establish and characterize the polarity and proticity profiles across phospholipid bilayers [30-32] and within protein regions [33-36]. However, with the advent of high-field/high-frequency EPR, it became apparent that in most cases not one, but two and up to three g_{xx} tensor components are observed in the g_{xx}-spectral region in cw EPR spectra recorded at W-band or higher frequencies (130 and 275 GHz) of nitroxide spin probes and in nitroxide spin-labeled systems [37-39]. The information on the various nitroxide radical populations is lost when measurements are performed at RT, since only isotropic values of magnetic parameters are accessible. This underlies the necessity to perform microenvironment characterization studies at high-field/high-frequency to resolve the overlapping contributions of different nitroxide populations. Only then the information on the magnetic interaction parameters can be translated adequately into the nitroxide microenvironment characteristics.

3.4 Local solvent accessibility studies using nitroxides

The number of experimental approaches that can measure site-specific water accessibility within the protein is limited, see [40-45]. The combination of EPR spectroscopy with SDSL using nitroxide radicals is a sensitive tool to probe the solvent accessibility in a site-specific manner. This is because the EPR signal originates exclusively from the spin label and, moreover, no upper limit on the protein molecular weight exists, as opposed to, for example, NMR spectroscopy.

As discussed in the previous section, the shifts of magnetic parameters of nitroxide radicals correlate with the polarity and proticity of the solvent and, hence, the relative water accessibility. However, additional factors like e.g. the presence of charged amino acid side groups in the nitroxide radical's vicinity, contribute to the overall characteristics of the microenvironment. Therefore, an interpretation of g_{xx} and A_{zz} values exclusively in terms of varying solvent accessibility is usually not

possible, except for less complex systems such as membranes and micelles. There, information on solvent penetration in the bilayer can be inferred from the low-temperature X- and W-band cw EPR spectra analysis [31;46].

Most often, the applied EPR method to characterize water accessibility is power saturation cw EPR [47]. Importantly, the measurements are performed at room temperature and hence the information on the solvent accessibility is obtained under physiological conditions. The method relies on the incorporation of paramagnetic quenchers into the system, which enhance the nitroxide relaxation rates via the Heisenberg exchange mechanism, see Chapter 2.1.5. From the saturation curve, i.e. the plot of the amplitude of the nitroxide central line as a function of the square root of the incident microwave power, the empirical $P_{1/2}$ value is obtained which is then used to calculate the more general accessibility parameter, Π. These parameters depend on the nitroxide relaxation rate, which in turn reflects the microenvironment of the spin label. Modification of the nitroxide local environment by admixture of paramagnetic quenchers allows, therefore, to infer whether the spin label is exposed to an aqueous environment. Low and high collision rates are expected depending on whether the residues are buried in the protein interior or located on the solvent-exposed surface. The variation of Π in the presence and absence of paramagnetic species reflects, therefore, the relative collision frequency and hence the 'relative accessibility' of the spin label toward the exchange reagent. These paramagnetic species can preferentially accumulate either in the polar (e.g. chromium oxalate) or in apolar (e.g. O_2) domains, facilitating the differentiation between protein sites that are buried in the protein from those that are embedded in the membrane. Since the protein secondary structure leads to a periodic variation of solvent accessibility, this method has been extensively used to determine the sequence-specific secondary structure by "scanning" the nitroxide attachment site through the protein sequence [48]. The possibility to measure the solvent accessibility under physiologically relevant conditions allowed, for example, to differentiate between the formation of unstructured loops in solution of visual arrestin, as opposed to reported helical structures formed in crystallographic tetramers [49] and to observe differences in site-specific accessibility for the protein integrin when embedded either in micelles or in liposomes [50].

An analogous technique that indirectly probes the solvent accessibility through the nitroxide relaxation properties is saturation-recovery EPR, as was demonstrated for spin-labeled T4-lysozyme [51]. It employs an intense, saturating microwave pulse that is applied at a frequency corresponding to the central EPR line and subsequently, the return of the spectral intensity is monitored using a weak cw observing microwave field. Changes in the spin-lattice relaxation T_1, induced by added paramagnetic agents, are measured at room temperature. Importantly, multiple protein conformations that are present in equilibrium in solution can be determined, as long as their individual solvent accessibilities differ. The clear disadvantage of the two above methods is that the accessibility toward the paramagnetic reagent, rather than water molecules, is obtained. Since the water soluble paramagnetic quenchers are in general larger than water molecules, the sampled protein surface/cavities might not correspond to the real water accessibility.

Electron spin echo envelope modulation (ESEEM) [52] is a pulsed EPR technique that can be used to gain insight into site-specific water accessibility. Since it relies on the measurement of the hyperfine interaction of the spin label with the nuclei of isotopically labeled water, water accessibility is probed directly. The hyperfine interaction with e.g. deuterium nuclei of D_2O results in modulation

of the electron spin echo decay, and the modulation depth depends on the local D_2O concentration. Comparison of ESEEM modulation depths for spin labels attached at different positions on the protein surface or along the lipid chain in the membrane gives site-specific information on water accessibility within the protein or on the water penetration profile across biological membranes [53-55]. In principle, the calibration of ESEEM amplitudes with respect to the deuterium water content in spin-labeled biological systems should allow for quantitative local water concentration measurement, this, however, is not trivial [56]. In general, the ESEEM spectrum at the deuterium nuclear Larmor frequency shows contributions of narrow and broad lines, see Fig. 3.6. The narrow line arises from interaction with distant D nuclei, while the broad line from interaction with a nearby deuterium that forms H-bonded complexes with the nitroxide radical.

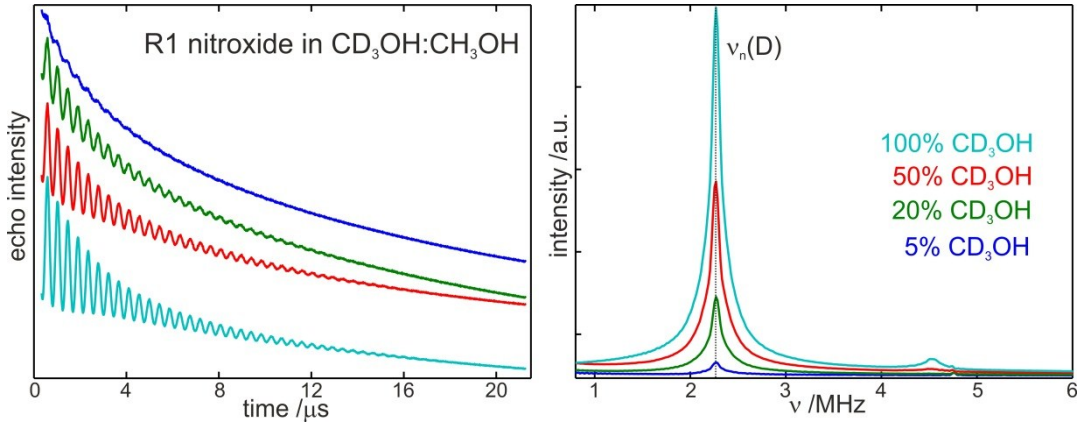

Figure 3.6 *(a) X-band deuterium ESEEM spectra recorded for R1 nitroxide dissolved in CD_3OH/CH_3OH mixture at 80 K. Spectra were recorded using the same experimental settings. (b) Fourier transformed experimental settings. The fraction of deuterated methanol was varied as indicated.*

This assignment is supported by DFT calculations [54]. Hence, using the ESEEM technique, information on directly coordinated as well as distant water molecules is obtained. The clear disadvantage of the method, however, is the necessity to perform the measurements at cryogenic temperatures.

Using the detergent-solubilized light-harvesting complex LHC II as a model protein system, water accessibility at specific protein site was characterized employing the EPR techniques discussed above with the aim to compare their results [57]. The ESEEM technique was shown to provide results that could be interpreted in the most straightforward and quantitative fashion.

Recently it was shown, that local solvent accessibility can also be measured using NMR enhanced via Overhauser dynamic nuclear polarization (DNP) [40;58;59]. In this way, the local hydration dynamics around nitroxides at room temperature could be probed and used, for example, to monitor protein aggregation [58]. The advantage of the technique is the direct measurement of the water accessibility under physiological conditions, however, a DNP-dedicated NMR setup is required.

3.5 Distance measurements by EPR using nitroxides

The dependence of the dipolar interaction on the distance between the electron spins, described in Chapter 2.1.5, can be utilized to extract the information on the separation of two electron spins. The established pulsed EPR methods allow to measure the distance constraints in the range of 1.8 nm to 6 nm and include both single-frequency [60-62] and double-frequency [63;64] EPR techniques. While

other specific spin labels have been developed for this purpose, distance determination employing nitroxide-nitroxide radical pairs is still most generally applied.

Despite apparent success of the methodology based on doubly-nitroxide labeled system, there exist limitations of this approach. For example, when measurements are performed at higher magnetic field, e.g. W-band, orientation selection occurs and translates into variable dipolar frequencies that cannot be directly converted into the distance information. Unless the specific information on the 3D geometry of the spin pair is sought [65;66], it is an unwanted effect. Additionally, spectroscopically undistinguishable spin labels do not allow to be separately addressed. Hence, the development of new spin labels, which would allow for orthogonal labeling, i.e. attachment of two non-identical spin labels, is highly desirable. For that purpose one can either use transition metal tags containing Cu^{2+} [67] or Gd^{3+} [68] ions or use the internal paramagnetic species, for example heme iron, in conjunction with nitroxide spin labels [69].

References

[1] S. Van Doorslaer, E. Vinck *The strength of EPR and ENDOR techniques in revealing structure-function relationships in metalloproteins*. Phys. Chem. Chem. Phys. **2007,** 9*,* 4620-4638.

[2] G. Jeschke *EPR techniques for studying radical enzymes*. Biochim. Biophys. Acta **2005,** 1707*,* 91-102.

[3] W. Lubitz, F. Lendzian, R. Bittl *Radicals, radical pairs and triplet states in photosynthesis*. Acc. Chem. Res. **2002,** 35*,* 313-320.

[4] A.K. Hoffmann, A.T. Henderson *A new stable free radical: di-t-butylnitroxide*. J. Am. Chem. Soc. **1961,** 83*,* 4671-4672.

[5] E.G. Rozantzev, M.B. Neiman *Organic radical reactions involving no free valence*. Tetrahedron **1964,** 20*,* 131-137.

[6] W.L. Hubbell, C. Altenbach *Site-directed spin labeling of membrane proteins.* in: S. H. White (Ed.), Membrane protein structure: Experimental approaches, Oxford University Press, London, 1994, pp. 224-248.

[7] M.R. Fleissner, E.M. Brustad, T. Kálai, C. Altenbach, D. Cascio, F.B. Peters, K. Hideg, S. Peuker, P.G. Schultz, W.L. Hubbell *Site-directed spin labeling of a genetically encoded unnatural amino acid*. Proc. Natl. Acad. Sci. USA **2009,** 106*,* 21637-21642.

[8] L.J. Berliner, J. Grunwald, H.O. Hankovszky, K. Hideg *A novel reversible thiol-specific spin label: papain active site labeling and inhibition*. Anal. Biochem. **1982,** 119*,* 450-455.

[9] T. Kálai, M. Balog, J. Jekö, K. Hideg *Synthesis and reactions of a symmetric paramagnetic pyrrolidine diene*. Synthesis **1999,** 973-980.

[10] A. Bowman, C.M. Hammond, A. Stirling, R. Ward, W. Shang, H. El-Mkami, D.A. Robinson, D.I. Svergun, D.G. Norman, T. Owen-Hughes *The histone chaperones Vps75 and Nap1 form ring-like, tetrameric structures in solution*. Nuc. Acids Res. **2014,** 42*,* 6038-6051.

[11] G. Jeschke *Site-specific information on macromolecular materials by combining CW and pulsed ESR on spin probes.* in: S. Schlick (Ed.), *Advanced ESR methods in polymer research*, John Wiley, New Yersey, 2006, pp. 165-196.

[12] Ya.S. Lebedev, O.Y. Grinberg, A.A. Dubinsky, O.G. Poluektov *Investigation of spin labels and probes by millimeter band EPR.* in: R. I. Zhdanov (Ed.), *Bioactive spin labels*, Springer-Verlag, Heidelberg, 1992, pp. 227-278.

[13] T. Kawamura, S. Matsunami, T. Yonezawa *Solvent effects on the g-value of di-t-butyl nitric oxide*. Bull. Chem. Soc. Jpn. **1967,** 40*,* 1111-1115.

[14] O.H. Griffith, P.J. Dehlinger, S.P. Van *Shape of hydrophobic barrier of phospholipid bilayers (evidence for water penetration in biological membranes)*. J. Membr. Biol. **1974,** 15*,* 159-192.

[15] M.A. Ondar, O.Y. Grinberg, A.A. Dubinskii, Y.S. Lebedev *Study of the effect of the environment on the magnetic-resonance parameters of nitroxide radicals by high-resolution electron-paramagnetic-resonance spectroscopy*. Khim. Fiz. **1984,** 3*,* 527-536.

[16] B.R. Knauer, J.J. Napier *The nitrogen hyperfine splitting constant of the nitroxide functional group as a solvent polarity parameter. The relative importance for a solvent polarity parameter of its being a cybotactic probe vs. its being a model process*. J. Am. Chem. Soc. **1976,** 98*,* 4395-4400.

[17] A.H. Reddoch, S. Konishi *The solvent effect on di-tert-butyl nitroxide. A dipole-dipole model for polar solutes in polar solvents*. J. Chem. Phys. **1979,** 70*,* 2121-2130.

[18] A.T. Bullock, C.B. Howard *Electron spin resonance study of the 1:1 hydrogen-bonded complex of di-t-butylnitroxide with methanol. An analysis of an acceptor: self-associated donor equilibrium*. J. Chem. Soc. Faraday Trans. **1977,** 73*,* 465-470.

[19] I.J. Brass, A.T. Bullock *1:1 Hydrogen bonded complexes of phenol and 4-fluorophenol with 2,2,6,6-tetramethylpiperidin-1-oxyl: an electron spin resonance study*. J. Chem. Soc. Faraday Trans. **1978,** 74*,* 1556-1561.

[20] W. Kolodziejski, Z. Kecki *ESR and PMR studies of alcohols hydrogen bonded with nitroxide radical*. Ber. Bunsenges. Phys. Chem. **1978,** 82*,* 1312-1314.

[21] Morishima.I, K. Endo, T. Yonezawa *Interaction between closed- and open-shell molecules. VI. ^{1}H and ^{13}C contact shifts and molecular orbital studies on the hydrogen bond of nitroxide radical*. J. Chem. Phys. **1973,** 58*,* 3146-3154.

[22] E. Dally, W. Müller-Warmuth *NMR investigations on solutions with nitroxide radical complexes. II. Hyperfine coupling constants, line widths, and relaxation of complexes with n-propanol, isopropanol and tert.-butanol*. Ber. Bunsenges. Phys. Chem. **1978,** 82*,* 792-798.

[23] Y.Y. Lim, R.S. Drago *Donor properties of a free-radical base*. J. Am. Chem. Soc. **1971,** 93*,* 891-894.

[24] M. Huber *Introduction to magnetic resonance methods in photosynthesis*. Photosynth. Res. **2009,** 102*,* 305-310.

[25] R. Owenius, M. Engström, M. Lindgren, M. Huber *Influence of solvent polarity and hydrogen bonding on the EPR parameters of a nitroxide spin label studied by 9-GHz and 95-GHz EPR spectroscopy and DFT calculations*. J. Phys. Chem. A **2001,** 105*,* 10967-10977.

[26] A.F. Gullá, D.E. Budil *Orientation dependence of electric field effects on the g factor of nitroxides measured by 220 GHz EPR*. J. Phys. Chem. B **2001,** 105*,* 8056-8063.

[27] M. Plato, H.-J. Steinhoff, C. Wegener, J.T. Törring, A. Savitsky, K. Möbius *Molecular orbital study of polarity and hydrogen bonding effects on the g and hyperfine tensors of site directed NO spin labelled bacteriorhodopsin*. Mol. Phys. **2002,** 100*,* 3711-3721.

[28] R.N. Schwartz, M. Peric, S.A. Smith, B.L. Bales *Simple test of the effect of an electric field on the ^{14}N-hyperfine coupling constant in nitroxide spin probes*. J. Phys. Chem. B **1997,** 101*,* 8735-8739.

[29] Z. Ding, A.F. Gullá, D.E. Budil *Ab initio calculations of electric field effects on the g-tensor of a nitroxide radical*. J. Chem. Phys. **2001,** 115*,* 10685-10693.

[30] K.A. Earle, J.K. Moscicki, M. Ge, D.E. Budil, J.H. Freed *250-GHz electron spin resonance studies of polarity gradients along the aliphatic chains in phospholipid membranes*. Biophys. J. **1994,** 66*,* 1213-1221.

[31] D. Kurad, G. Jeschke, D. Marsh *Lipid membrane polarity profiles by high-field EPR*. Biophys. J. **2003,** 85*,* 1025-1033.

[32] B. Dzikovski, D. Tipikin, J.H. Freed *Conformational distributions and hydrogen bonding in gel and frozen lipid bilayers: a high frequency spin-label ESR study*. J. Phys. Chem. B **2012,** 116*,* 6694-6706.

[33] H.-J. Steinhoff, A. Savitsky, C. Wegener, M. Pfeiffer, M. Plato, K. Möbius *High-field EPR studies of the structure and conformational changes of site-directed spin labeled bacteriorhodopsin*. Biochim. Biophys. Acta **2000,** 1457*,* 253-262.

[34] A. Savitsky, M. Kühn, D. Duché, K. Möbius, H.-J. Steinhoff *Spontaneous refolding of the pore-forming colicin A toxin upon membrane association as studied by X-band and W-band high-field electron paramagnetic resonance spectroscopy*. J. Phys. Chem. B **2004,** 108*,* 9541-9548.

[35] H. Brutlach, E. Bordignon, L. Urban, J.P. Klare, H.-J. Reyher, M. Engelhard, H.-J. Steinhoff *High-field EPR and site-directed spin labeling reveal a periodical polarity profile: The sequence 88 to 94 of the phototransducer NpHtrII in complex with sensory rhodopsin, NpSRII*. Appl. Magn. Reson. **2006,** 30*,* 359-372.

[36] T.I. Smirnova, T.G. Chadwick, M.A. Voinov, O. Poluektov, J. van Tol, A. Ozarowski, G. Schaaf, M.M. Ryan, V.A. Bankaitis *Local polarity and hydrogen bonding inside the Sec14p phospholipid-binding cavity: High-field multi-frequency electron paramagnetic resonance studies*. Biophys. J. **2007,** 92*,* 3686-3695.

[37] M.G. Finiguerra, H. Blok, M. Ubbink, M. Huber *High-field (275 GHz) spin-label EPR for high-resolution polarity determination in proteins*. J. Magn. Reson. **2006,** 180*,* 197-202.

[38] E. Bordignon, H. Brutlach, L. Urban, K. Hideg, A. Savitsky, A. Schnegg, P. Gast, M. Engelhard, E.J.J. Groenen, K. Möbius, H.-J. Steinhoff *Heterogeneity in the nitroxide micro-environment: polarity and proticity effects in spin-labeled proteins studied by multi-frequency EPR*. Appl. Magn. Reson. **2010,** 37*,* 391-403.

[39] P. Gast, R.T.L. Herbonnet, J. Klare, A. Nalepa, C. Rickert, D. Stellinga, L. Urban, K. Mobius, A. Savitsky, H.J. Steinhoff, E.J.J. Groenen *Hydrogen bonding of nitroxide spin labels in membrane proteins*. Phys. Chem. Chem. Phys. **2014,** 16*,* 15910-15916.

[40] B.D. Armstrong, S. Han *Overhauser dynamic nuclear polarization to study local water dynamics*. J. Am. Chem. Soc. **2009,** 131*,* 4641-4647.

[41] J.L. Kitevski-LeBlanc, F. Evanics, R.S. Prosser *Approaches for the measurement of solvent exposure in proteins by ^{19}F NMR*. J. Biomol. NMR **2009,** 45*,* 255-264.

[42] N.V. Nucci, M.S. Pometun, A.J. Wand *Site-resolved measurement of water-protein interactions by solution NMR*. Nat. Struct. Mol. Biol. **2011,** 18*,* 245-249.

[43] J.T. King, K.J. Kubarych *Site-specific coupling of hydration water and protein flexibility studied in solution with ultrafast 2D-IR spectroscopy*. J. Am. Chem. Soc. **2012,** 134*,* 18705-18712.

[44] J.K. Williams, M. Hong *Probing membrane protein structure using water polarization transfer solid-state NMR*. J. Magn. Reson. **2014,** 247*,* 118-127.

[45] M. Amaro, J. Brezovský, S. Kovácová, J. Sýkora, D. Bednár, V. Nemec, V. Lišková, N.P. Kurumbang, K. Beerens, R. Chaloupková, K. Paruch, M. Hof, J. Damborský *Site-specific analysis of protein hydration based on unnatural amino acid fluorescence*. J. Am. Chem. Soc. **2015,** 137*,* 4988-4992.

[46] D. Marsh *Spin-label EPR for determining polarity and proticity in biomolecular assemblies: Transmembrane profiles*. Appl. Magn. Reson. **2010,** 37*,* 435-454.

[47] C. Altenbach, T. Marti, H.G. Khorana, W.L. Hubbell *Transmembrane protein structure: spin labeling of bacteriorhodopsin mutants*. Science **1990,** 248*,* 1088-1092.

[48] C. Altenbach, D.A. Greenhalgh, H.G. Khorana, W.L. Hubbell *A collision gradient method to determine the immersion depth of nitroxides in lipid bilayers: Application to spin-labeled mutants of bacteriorhodopsin*. Proc. Natl. Acad. Sci. USA **1994,** 91*,* 1667-1671.

[49] D.J. Francis, W.L. Hubbell, C.S. Klug *Probing protein secondary structure using EPR: investigating a dynamic region of visual arrestin*. Appl. Magn. Reson. **2012,** 43*,* 405-419.

[50] L. Yu, W. Wang, S. Ling, S. Liu, L. Xiao, Y. Xin, C. Lai, Y. Xiong, L. Zhang, C. Tian *CW-EPR studies revealed different motional properties and oligomeric states of the integrin β_{1a} transmembrane domain in detergent micelles or liposomes*. Sci. Rep. **2015,** 5.

[51] J. Pyka, J. Ilnicki, C. Altenbach, W.L. Hubbell, W. Froncisz *Accessibility and dynamics of nitroxide side chains in T4 lysozyme measured by saturation recovery EPR*. Biophys. J. **2005,** 89*,* 2059-2068.

[52] W.B. Mims *Envelope modulation in spin-echo experiments*. Phys. Rev. B **1972,** 5*,* 2409-2419.

[53] R. Bartucci, R. Guzzi, D. Marsh, L. Sportelli *Intramembrane polarity by electron spin echo spectroscopy of labeled lipids*. Biophys. J. **2003,** 84*,* 1025-1030.

[54] D.A. Erilov, R. Bartucci, R. Guzzi, A.A. Shubin, A.G. Maryasov, D. Marsh, S.A. Dzuba, L. Sportelli *Water concentration profiles in membranes measured by ESEEM of spin-labeled lipids*. J. Phys. Chem. B **2005,** 109*,* 12003-12013.

[55] A. Volkov, C. Dockter, Y. Polyhach, H. Paulsen, G. Jeschke *Site-specific information on membrane protein folding by electron spin echo envelope modulation spectroscopy*. J. Phys. Chem. Lett. **2010,** 1*,* 663-667.

[56] A.D. Milov, R.I. Samoilova, A.A. Shubin, Yu.A. Grishin, S.A. Dzuba *ESEEM measurements of local water concentration in D_2O-containing spin-labeled systems*. Appl. Magn. Reson. **2008,** 35*,* 73-94.

[57] A. Volkov, C. Dockter, T. Bund, H. Paulsen, G. Jeschke *Pulsed EPR determination of water accessibility to spin-labeled amino acid residues in LHCIIb*. Biophys. J. **2009,** 96*,* 1124-1141.

[58] A. Pavlova, E.R. McCarney, D.W. Peterson, F.W. Dahlquist, J. Lew, S. Han *Site-specific dynamic nuclear polarization of hydration water as a generally applicable approach to monitor protein aggregation*. Phys. Chem. Chem. Phys. **2009,** 11*,* 6833-6839.

[59] A. Doll, E. Bordignon, B. Joseph, R. Tschaggelar, G. Jeschke *Liquid state DNP for water accessibility measurements on spin-labeled membrane proteins at physiological temperatures*. J. Magn. Reson. **2012,** 222, 34-43.

[60] S. Saxena, J.H. Freed *Double quantum two-dimensional Fourier transform electron spin resonance: Distance measurements*. Chem. Phys. Lett. **1996,** 251, 102-110.

[61] P.P. Borbat, J.H. Freed *Multiple-quantum ESR and distance measurements*. Chem. Phys. Lett. **1999,** 313, 145-154.

[62] S. Milikisyants, F. Scarpelli, M.G. Finiguerra, M. Ubbink, M. Huber *A pulsed EPR method to determine distances between paramagnetic centers with strong spectral anisotropy and radicals: The dead-time free RIDME sequence*. J. Magn. Reson. **2009,** 201, 48-56.

[63] A.D. Milov, A.B. Ponomarev, Yu.D. Tsvetkov *Electron-electron double resonance in electron spin echo: Model biradical systems and the sensitized photolysis of decalin*. Chem. Phys. Lett. **1984,** 110, 67-72.

[64] M. Pannier, S. Veit, A. Godt, G. Jeschke, H.W. Spiess *Dead-time free measurement of dipole-dipole interactions between electron spins*. J. Magn. Reson. **2000,** 142, 331-340.

[65] A. Savitsky, A.A. Dubinskii, M. Flores, W. Lubitz, K. Möbius *Orientation-resolving pulsed electron dipolar high-field EPR spectroscopy on disordered solids: I. Structure of spin-correlated radical pairs in bacterial photosynthetic reaction centers*. J. Phys. Chem. B **2007,** 111, 6245-6262.

[66] Y. Polyhach, A. Godt, C. Bauer, G. Jeschke *Spin pair geometry revealed by high-field DEER in the presence of conformational distributions*. J. Magn. Reson. **2007,** 185, 118-129.

[67] E. Narr, A. Godt, G. Jeschke *Selective measurements of a nitroxide-nitroxide separation of 5 nm and a nitroxide-copper separation of 2.5 nm in a terpyridine-based copper(II) complex by pulse EPR spectroscopy*. Angew. Chem. Int. Edit. **2002,** 41, 3907-3910.

[68] P. Lueders, G. Jeschke, M. Yulikov *Double electron-electron resonance measured between Gd^{3+} ions and nitroxide radicals*. J. Phys. Chem. Lett. **2011,** 2, 604-609.

[69] M. Ezhevskaya, E. Bordignon, Y. Polyhach, L. Moens, S. Dewilde, G. Jeschke, S. Van Doorslaer *Distance determination between low-spin ferric haem and nitroxide spin label using DEER: the neuroglobin case*. Mol. Phys. **2013,** 111, 2855-2864.

Chapter 4

High-field ELDOR-detected NMR study of nitroxide radicals in disordered solids: towards characterization of heterogeneity of microenvironments in spin-labeled systems

This chapter has been published as [20] and edited for consistency of notation:
A. Nalepa, K. Mobius, W. Lubitz, and A. Savitsky 'High-field ELDOR-detected NMR study of a nitroxide radical in disordered solids: Towards characterization of heterogeneity of microenvironments in spin-labeled systems' J. Magn. Reson. **2014,** 242, 203-213.

4.1 Introduction

Site-directed spin labeling (SDSL) of target proteins with nitroxide radicals in combination with electron paramagnetic resonance (EPR) spectroscopy is a powerful method for the elucidation of the protein structure and function-related conformational dynamics on the molecular level [1-3]. Specifically, information on the microenvironment properties at the site of spin-probe attachment like polarity (defined by the dielectric constant) and proticity (defined as propensity for hydrogen bond formation) can be inferred from the analysis of the magnetic interaction parameters of the nitroxide spin label. As pointed out in the Section 3.3, the characteristic of the microenvironment is best determined using high-field/high-frequency EPR below the glass transition temperature of the solvent. This allows one to resolve the g-tensor principal components of nitroxide-labeled systems and to measure precisely the g_{xx} component in addition to the nitrogen hyperfine-tensor component A_{zz} which can be obtained already by X-band EPR in frozen samples.

A meaningful interpretation of the experimentally obtained g_{xx} and A_{zz} values requires differentiation between the polarity and hydrogen-bonding situations of the environment. Generally it has been observed experimentally, that shifts in g_{xx} are much greater in hydrogen-bonding solvents than in aprotic solvents of comparable dielectric constant [4]. The separation of the influence of hydrogen-bonding from non-specific solute-solvent interactions on nitroxide magnetic interaction parameters is, however, not trivial. Both of these types of interaction affect the aforementioned parameters in the same way, i.e. both increasing solvent polarity or formation of H-bonds cause decrease in the g_{xx} and increase in the A_{zz} values. A semiempirical quantum chemical description of the g_{xx} versus A_{zz} relation for a nitroxide spin-label environment of different physical and chemical nature has been reported [5]. A linear plot of g_{xx} vs. A_{zz} was obtained that would indicate the presence or absence of H-bonds in the spin-label environment, i.e., its proticity. In this approach, it was assumed that the A_{zz} changes originate predominantly from variations of the polarity, which may be an oversimplification. DFT calculations for a nitroxide radical in protic solvents showed that treating the solvent only in the frame of the polarizable continuum model, i.e. excluding specific solute-solvent

interactions like H-bond formation, is not sufficient to provide A_{zz} values in satisfactory agreement with the experimental results [6].

Recent multi-frequency high-field cw EPR studies underline the complexity of the problem to treat the microenvironment of proteins adequately. Several distinctly different g_{xx} values were measured for different positions in labeled proteins [7-10] or lipid membranes [11]. This heterogeneity of the matrix was rationalized in terms of spin-label fractions that differ in the H-bonding characteristics of the nitroxide and its microenvironment, i.e. form 0, 1 or 2 H-bonds [8]. Distinctly different nitrogen hyperfine couplings A_{zz}, however, were not resolved for these fractions using cw EPR, owing to the large intrinsic EPR linewidth [11]. In order to obtain such information on slightly different A_{zz} values, the inhomogeneous EPR linewidth due to unresolved proton hyperfine couplings has to be reduced by complete deuteration of the system. Indeed, two distinct A_{zz} values were resolved in the X-band cw EPR spectrum of perdeuterated nitroxide (oxo-TEMPO) in ethanol-D_6 frozen solution [12]. In agreement with A_{zz} heterogeneity, for protonated nitroxides in frozen alcoholic solutions two distinct g_{xx} values were clearly detected by high-field cw EPR [9;11]. While distinct A_{zz} components are expected also for each respective g_{xx} value in nitroxide labeled protein sites, they can be resolved in cw EPR spectra only if the protein is perdeuterated, making it an expensive endeavor. Hence, an advanced pulsed EPR method is worth striving for by which one would get around the necessity for perdeuteration and would directly probe nuclear transitions in the frequency domain. Specifically, it should be capable to deliver precise nitrogen hyperfine and quadrupole coupling constants (A_{zz} and P_{zz}) for nitroxide spin labels in protonated systems.

There are several pulsed EPR techniques, presented in Chapter 2, which are particularly suitable for probing nuclear transition frequencies of paramagnetic compounds: ESEEM (electron spin echo envelope modulation), ENDOR (electron nuclear double resonance) and ELDOR (electron-electron double resonance) detected NMR [13]. However, at high fields / high frequencies the ESEEM technique fails due to limited microwave excitation bandwidth, which does not allow to probe the large nitrogen nuclear transition frequencies in the g_{zz} spectral region.

In this chapter, the question whether W-band EDNMR would be the method of choice for determining precise A_{zz} and P_{zz} principal components of ^{14}N hyperfine and quadrupole nitroxide tensors in SDSL proteins is examined. The results obtained using EDNMR technique are, therefore, compared to those of standard cw EPR and ENDOR experiments. As test systems for the limiting cases of pure aprotic and pure protic microenvironments, a pyrroline-type nitroxide radical dissolved in frozen solutions of aprotic *ortho*-terphenyl (OTP) and of protic 2-propanol are used. The choice of alcohol solution is justified by extensive existing studies on the formation of hydrogen bonds between the nitroxide moiety and alcohol hydroxyl proton using cw EPR, providing an excellent framework of reference [9;11;12;14]. The proper choice of the spin probe is important, as

(i) it has been shown that structural differences in the nitroxide probe result in different magnitudes of the hyperfine couplings derived [15]

(ii) hydrogen bond network around the nitroxides is expected to vary from probe to probe due to differences in steric hindrance of the nitroxide NO group [14;16].

The pyrroline-type nitroxide radical used in this work (R1 in Fig. 4.1) is the head group of the MTS spin label widely used in SDSL techniques of structural biology. The absolute A_{zz} and P_{zz} values obtained here can, thus, be translated to the MTS-probed environment in the labeled

biomacromolecule. Additionally, the optimization of EDNMR experimental settings, crucial for sensitivity and resolution of the method, is presented in the Materials and methods section of this chapter.

4.2 Materials and methods

Sample preparation

The molecular structure of the nitroxide spin probe R1 (3-hydroxymethyl-2,2,5,5-tetramethylpyrrolin-1-oxyl) is shown in Fig. 4.1. The R1 radicals in their protonated and perdeuterated (R1-D_{16}) form as well as in their ^{15}N substituted form (R1-^{15}N-D_{16}) were synthesized as described previously [17]. The perdeuterated TEMPOL-D_{17} was obtained from Isotec Stable Isotopes. The solvents, 2-propanol-H_8, 2-propanol-D_8 and benzene-D_6, were obtained from Fluka and Sigma-Aldrich in their purest commercially available form and used without further purification. *Ortho*-terphenyl-D_{14} (OTP-D_{14}) was supplied by Cambridge Isotope Laboratories and methanol-D_4 (99% D) was obtained from Deutero GmbH. Nitroxide radical was directly dissolved in 2-propanol, methanol or OTP/benzene (50%/50% v/v). The sample solution, containing 1 mM of nitroxide radical, was transferred into a quartz capillary (I.D. = 0.6 mm) for the W-band EPR measurements. A glass-type frozen solution was obtained by quick transferring of the sample into the precooled EPR cryostat.

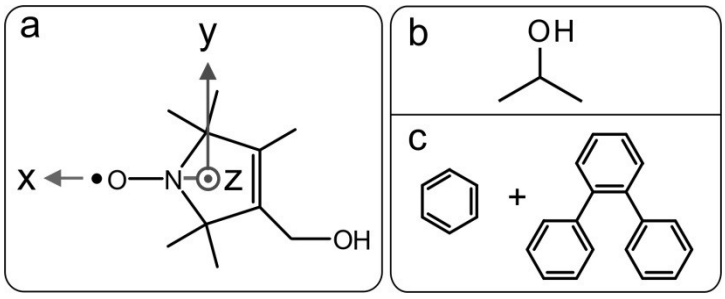

Figure 4.1. *Molecular structure of the nitroxide radical R1 (a), 2-propanol (b) and OTP/benzene (c) host for diluted nitroxide solutions. The conventional principal axes of the g-tensor of the nitroxide radical are indicated.*

W-band cw EPR experiments

All cw EPR experiments were performed at 90 K with a laboratory-built W-band spectrometer described previously [18;19], that operates at mw frequency of about 95 GHz. The sample temperature was controlled by a temperature-stabilized nitrogen gas-flow cryostat. The external B_0 field was modulated at 8 kHz with an amplitude of 30 μT. Low mw power (< 1 μW) incident on the critically coupled cavity (mw field amplitude $\omega_1 < 1.5 \cdot 10^5$ rad/s) was chosen to avoid saturation.

W-band pulsed EPR experiments

The pulsed EPR experiments were performed on a modified commercial W-band EPR spectrometer (Bruker Elexsys E680) operating at about 94 GHz [20]. The 2-pulse field-swept EPR spectra were acquired using the Hahn-echo pulse sequence (t_p)-τ-($2t_p$)-τ-*echo*. A π/2 pulse length of 56 ns was generally used to minimize distortions by nuclear ESEEM. The ENDOR experiments were performed using a Davies-type pulse sequence: t_{inv} - t_{RF} - T - t_p - τ - $2t_p$ - τ - echo with t_{inv} = 128 ns, t_p = 56 ns, T = 3 μs and τ = 372 ns. For RF excitation, an output power of 120 W from a broadband RF amplifier

(ZHL-120W-GAN+, Minicircuits, USA) was used. For recording the 2-dimensional ENDOR surfaces, the length of the RF pulse was set to $t_{RF} = 60$ µs. This pulse length is a compromise that allows detection of all ^{14}N and ^{15}N nuclear frequencies in the frequency range from 5 MHz to 70 MHz (to 90 MHz for the ^{15}N-substituted R1). For the ENDOR recordings in the A_{zz} spectral range, an RF pulse length of $t_{RF} = 90$ µs represents the optimal condition for measuring A_{zz} nitrogen transitions.
The EDNMR experiments were performed using the mw pulse sequence with Hahn-echo detection sequence, see Fig. 4.2. The HTA mw pulse was applied at frequency ν_2. The spectra were acquired by continuously sweeping the ν_2 frequency at fixed B_0 in steps of 30 kHz to 150 kHz, depending on the frequency range of interest. In general, the HTA pulse length was set to 1.6 µs at $\omega_2^{HTA}(\nu_2) = 2.6 \cdot 10^7$ rad/s mw field amplitude. The detection Hahn-echo pulse sequence at mw frequency ν_1, matched to the cavity resonance, was set 8 µs after the HTA pulse to ensure the decay of electron spin coherencies. A pulse length for the detection $\pi/2$ pulse, $t_p = 100$ ns, and a pulse separation, $\tau = 1$ µs, were generally used. The echo was integrated 1.4 µs around its maximum for optimal resolution. To ensure a proper magnetic field setting, EDNMR traces were recorded in the field range of 1.2 mT around the g_{zz}, $M_I = -1$ spectral field position. A pulse repetition rate of 500 Hz was used to allow the echo signal to restore between consecutive pulse trains.

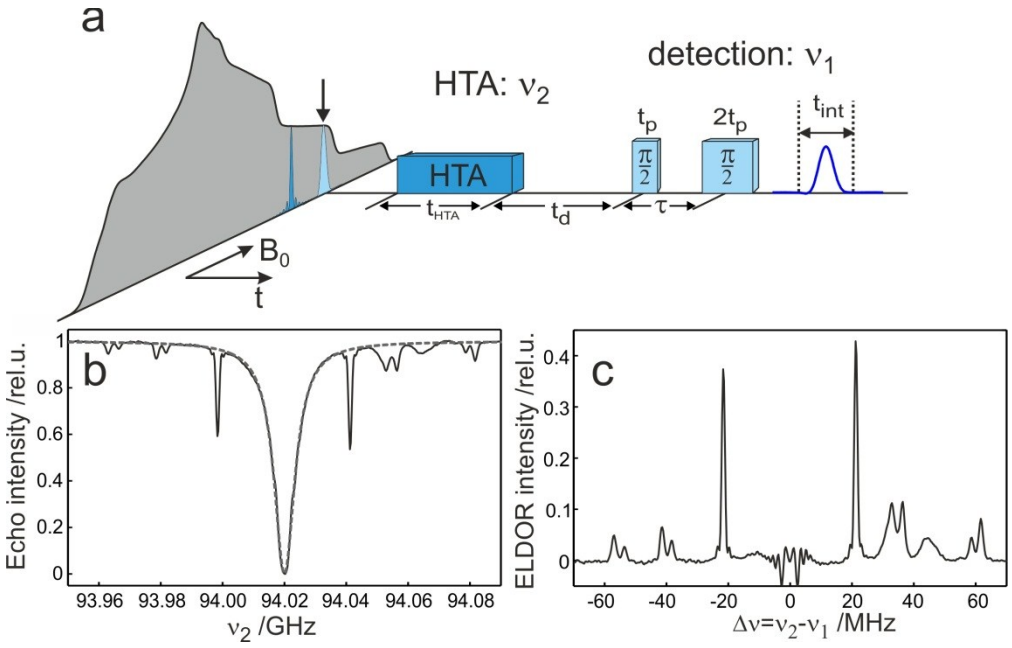

Figure 4.2 *(a) Microwave pulse sequence for the W-band EDNMR experiment based on Hahn-echo detection scheme with indicated experimental parameters that require optimization. (b) Representative example of an EDNMR recording of R1-D_{16} in 2-propanol-D_8 glass at 50 K, acquired at the spectral field position close to g_{zz}, $M_I = 0$. (c) EDNMR spectrum obtained after central blind spot correction (dashed trace in panel b).*

Figure 4.2(a) shows the representative example of an EDNMR recording of R1-D_{16} in 2-propanol-D_8 glass at 50 K, acquired at the field position close to g_{zz}, $M_I = 0$. For optimal resolution and sensitivity of the method, the HTA pulse settings and the integration window had to be adjusted for the forbidden transition of interest. Both EDNMR and ENDOR measurements were performed at 50 K, which is a trade-off between long electron phase-memory and short enough spin-lattice relaxation times.

Optimization of EDNMR experimental settings

The following experimental parameters, as marked in Fig. 4.2(a), have to be adjusted for optimal sensitivity and resolution of the EDNMR experiment:

(i) amplitude of the HTA mw pulse, ω_1^{HTA}

(ii) length of the HTA pulse, t_{HTA}

(iii) integration window of the echo response, t_{int}

(iv) interpulse distance in the detection pulse sequence, τ

(v) pulse length in the detection pulse sequence, t_p.

The influence of these experimental parameters on the shape and resolution of the EDNMR spectra is presented below [20]. The spectral feature dominating the unprocessed EDNMR spectrum is the central blindspot observed for ν_2 frequency close to the detection frequency ν_1, i.e. the frequency of the allowed EPR transitions. Figure 4.3 shows an example of central blind spot linewidth changes when varying the ELDOR mw power.

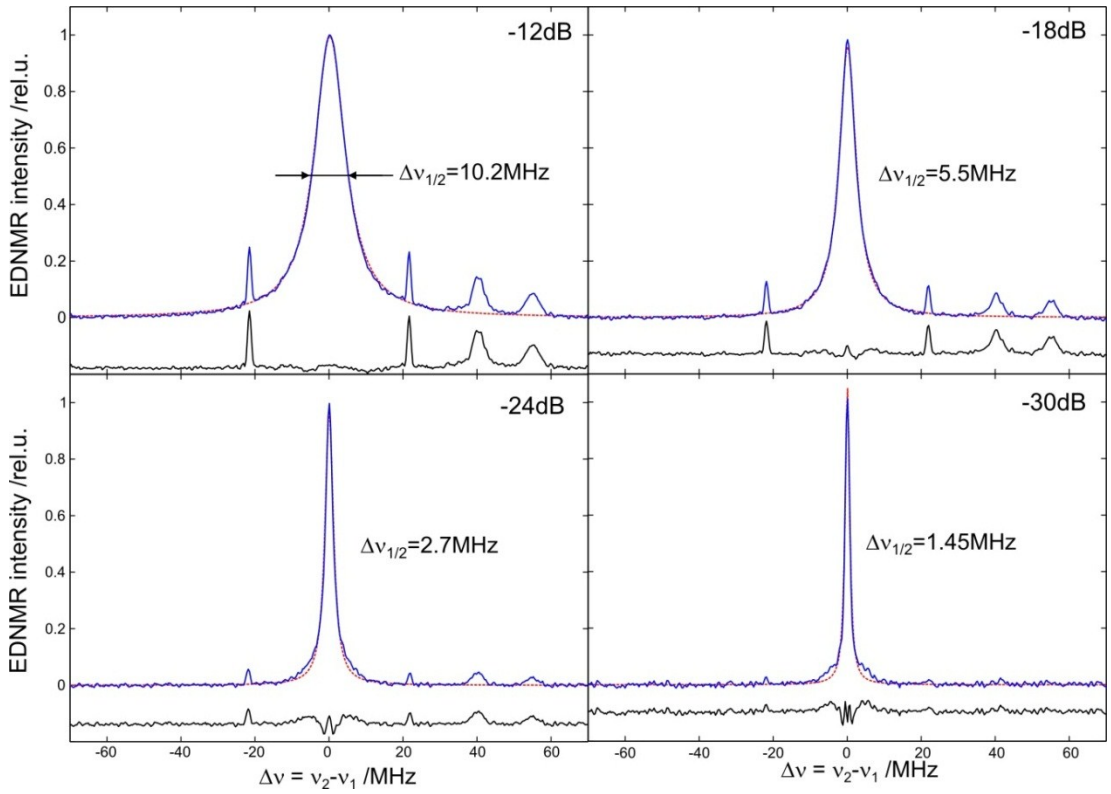

Figure 4.3 *EDNMR slices for R1-D_{16} in D_2O/trehalose glass at 50 K recorded close to the g_{zz}, $M_I = -1$ spectral position with the different settings of mw power of HTA pulse (6dB steps). The length of HTA pulse was set to 4 μs. The dashed red lines represents the best-fit results to the Lorentzian line centered at $\Delta\nu = 0$ with a FWHM given.*

For long HTA pulses, that is when $\omega_{eff} \cdot t_{HTA} >> 1$, the lineshape of the central blindspot can be described with a Lorentzian function:

$$C(\Delta\omega) = \left(\frac{\omega_1}{\omega_{eff}}\right)^2 = \frac{\omega_1^2}{\Delta\omega^2 + \omega_1^2} \qquad \text{Eq. (4.1)}$$

where $\omega_{eff}^2 = \Delta\omega^2 + \omega_1^2$, and $\Delta\omega = 2\pi\cdot(\nu_2-\nu_1)$ is the frequency difference between the ELDOR (ν_2) and detection (ν_1) mw frequencies. In the first step of the data processing, the simulated Lorentzian line was subtracted from the spectrum.

The FWHM (full width at half maximum) of the Lorentzian is equal to $2\cdot\omega_1$ ($\Delta\nu_{1/2} = \omega_1/\pi$ in linear frequency units). Hence, the width of the central blindspot is only determined by the mw field strength and as such independent of the HTA pulse length. The FWHM of the central blind spot can therefore be used to measure ω_1 at the mw frequency ν_1 of the detection pulse sequence. The HTA pulse amplitude was fixed at optimum in this case $\omega_1^{HTA}(\nu_2) = 2.6\cdot10^7$ rad·s^{-1} mw field amplitude, yielding the central blind spot line that does not overlap significantly with the spectral lines of interest. After the HTA pulse amplitude was fixed, the HTA pulse length was optimized to obtain the ELDOR π-pulse for the forbidden transition of interest. This optimization is performed by a nutation experiment, where at given mw power, the length of the HTA pulse is increased stepwise as shown schematically in Fig. 4.4(a).

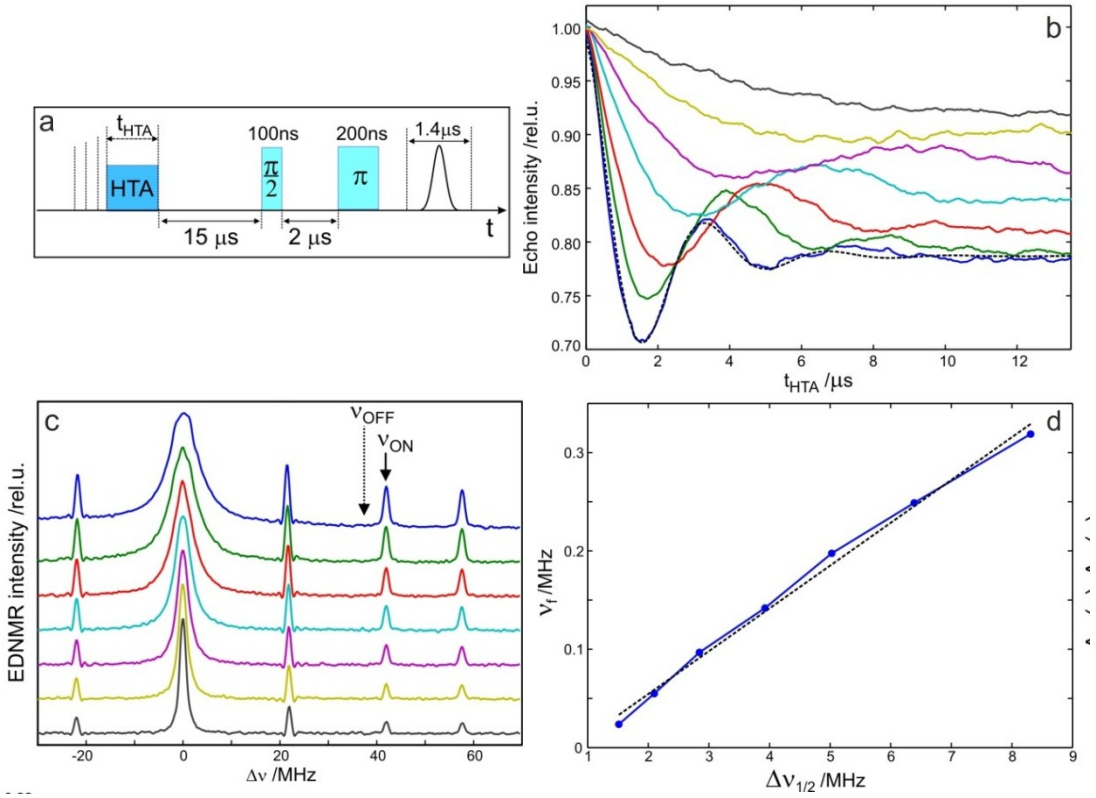

Figure 4.4 *(a) Microwave pulse sequence for EDNMR nutation experiment on R1-D_{16} in OTP/benzene frozen solution at 50 K. (b) Echo-decay traces recorded at different settings of mw power. They are calculated from the echo intensities, S(ν_{ON}) - S(ν_{OFF}), acquired at ON and OFF resonance frequencies, marked in (c). (c) EDNMR spectra recorded at t_{HTA} of the first minimum of the ec ɔ intensity in (b). The color code corresponds to that in (b). (d) ν_f in dependence on central blind spot width $\Delta1_{/2}$ which is obtained from EDNMR spectra in (b).*

Figure 4.4(b) presents the echo nutation traces t different mw power levels observed in such a nutation experiment, recorded at g_{zz}, $M_I = -1$ spectral position. The spectra are normalized relative to the nutation spectra recorded off resonance. The corresponding frequencies at which the ON and OFF

resonance nutation spectra where recorded indicated in Fig. 4.4(c). The time traces are satisfactorily described by the function [20]:

$$S_{nut} = A_0 \cdot \left[1 - \cos(2 \cdot \pi \cdot \nu_f \cdot t_{HTA}) \cdot e^{-t_{HTA}/\tau}\right] \qquad \text{Eq. (4.2)}$$

where the nutation frequency, ν_f, given by $\nu_f = \frac{\omega_1^{HTA} \cdot \sqrt{I_f}}{2\pi}$, with I_f being the intensity of the forbidden EPR transitions and A_0 is the initial amplitude of the envelope for the off-resonance nutation experiment as marked with an arrow in Fig. 4.4(c). An example of the simulation is shown by the dashed line in Fig. 4.4(b). As shown in Fig. 4.4(d), ν_f is linearly dependent on the central blind spot width $\Delta\nu_{1/2} = \omega_1^{HTA}/\pi$, which is evaluated from EDNMR recordings at corresponding mw power settings as shown in Fig. 4.4(c).

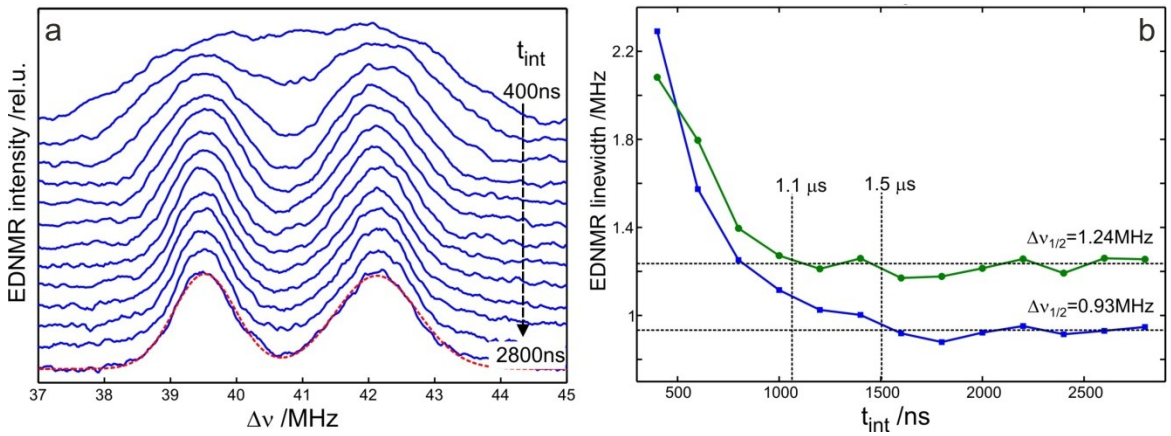

Figure 4.5 *(a) EDNMR spectra for Tempo-D_{17} in isopropanol-D_8 frozen solution at 50 K. The spectra were recorded at different settings of the echo integration window width t_{int} with all other experimental settings being fixed. (b) The FWHM Gaussian linewidth of (green) high-frequency and (blue) low-frequency EDNMR lines in (a) as evaluated from line analysis. An example of the analysis is shown by the red dashed line in (a).*

The last crucial experimental parameter to be adjusted is the width of the echo integration window. Fig. 4.5(a) presents the influence of varying the echo integration window (parameter t_{int} in Fig. 4.2(a)) on the linewidth of the EDNMR lines in the g_{zz}, M_I=−1 spectral region in the 37–45 MHz frequency range. As expected, increasing the integration window improves the spectral resolution. As the increase of the integration window requires a correspondingly larger interpulse separation in the detection pulse sequence, significant reduction of echo intensity in the case of short phase-memory time, T_m, of the spin system is expected. The following empirical relation for an estimation of the proper echo integration window width is obtained [20]:

$$t_{int} = 1.4/\nu_R \qquad \text{Eq. (4.3)}$$

where ν_R is the target resolution of the EDNMR experiment. Thus, to obtain a resolution of 1 MHz the integration window of 1.4 μs was chosen in the subsequent experiments.

Concerning the extraction of hyperfine coupling value A_{zz} from EDNMR recordings, Fig. 4.6 depicts the evaluation procedure of the EDNMR spectrum for R1-^{15}N-D_{16} nitroxide in OTP/benzene frozen

solution. The nuclear transition frequencies in the g_{zz} region, assuming the strong hyperfine-coupling regime, $A_{zz} > 2\nu_n$, are given to first-order by [21]:

$$\begin{aligned} v_2' - v_1 = \Delta v' &= \frac{A}{2} - v_n - \frac{3P}{2} \\ v_2'' - v_1 = \Delta v'' &= \frac{A}{2} + v_n + 3P/2 \end{aligned} \qquad \text{Eq. (4.4)}$$

Hence, a pair of lines centered about $A_{zz}/2$ and separated by $2\nu_n + 3P_{zz}$ is observed in the canonical g_{zz}, $M_I = -1$ position. To obtain the hyperfine and quadrupole parameters for each radical fraction, the EDNMR recordings at each magnetic field position are simulated using two Gaussian lines. For extracting the principal A_{zz} values, the line positions in the frequency dimension is interpolated to the corresponding g_{zz}, $M_I = -1$ spectral field position.

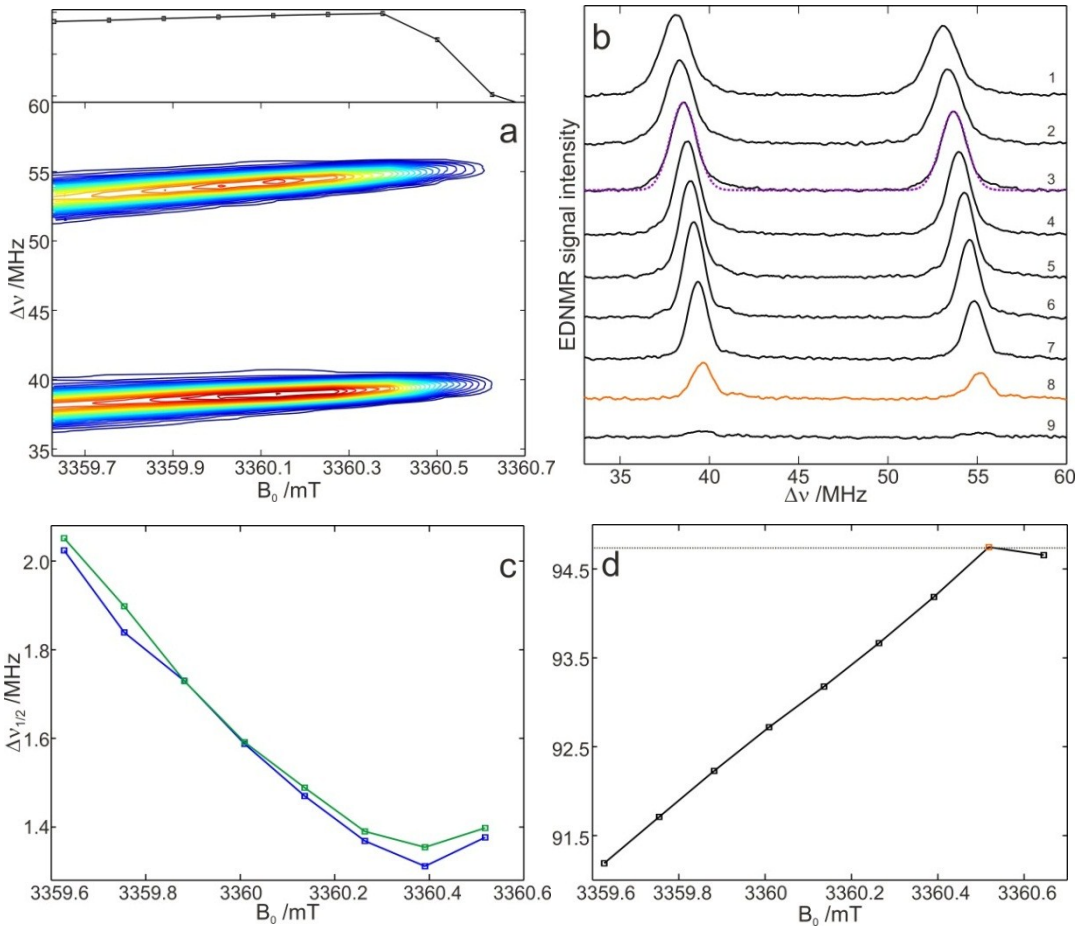

Figure 4.6 *Evaluation of the W-band EDNMR spectrum of R1-^{15}N-D$_{16}$ in OTP/benzene at 50 K. (a) Contour plot of field-frequency dependence of W-band EDNMR intensities around the g_{zz}, $M_I = -1$ spectral position. On top, the EPR intensity with indicated magnetic field positions of individual EDNMR recordings is shown. (b) Individual EDNMR recordings at magnetic field positions indicated in (a). The red line at position 6 shows the best-fit trace of the experimental trace to two Gaussian lines. (c) Magnetic field dependence of individual linewidths of (blue trace) low- and (green trace) high-frequency EDNMR lines. (d) Magnetic field dependence of (green trace) difference and (blue trace) sum of EDNMR line positions. The dashed lines indicate the frequencies at the g_{zz}, $M_I = -1$ spectral position.*

4.3 W-band cw EPR and EDNMR on nitroxide radical in 2-propanol

Continuous-wave EPR spectra

Figure 4.7(a) (top trace) shows the W-band cw EPR spectrum of the R1-H_{15} nitroxide radical in frozen solution of 2-propanol-H_8. The spectrum is clearly resolved into three separate spectral regions, which correspond to the principal values of the g-tensor, g_{xx}, g_{yy} and g_{zz}. The large inhomogeneous EPR linewidth of 15.5 MHz (given as FWHM), determined at the g_{zz}, $M_I = 0$ spectral position, is due to unresolved hyperfine interactions with neighbouring (internal and external) protons. This broadening does not allow for resolving the ^{14}N hyperfine splittings (A_{xx}, $A_{yy} \approx 12$ MHz) in the spectral regions of the g_{xx} and g_{yy} g-tensor components, but only the much larger A_{zz} component. However, an additional splitting of about 34 MHz can be recognized in the g_{xx} region, which is attributed to the contribution of a second radical fraction with a different g_{xx} value. An analogous situation was observed previously in the high-field cw EPR spectra of oxazolidine type nitroxide radicals in 2-propanol [9]. The width of the lines in the g_{zz}, $M_I = 0$ and $M_I = \pm 1$ spectral regions of 15.5 MHz and 18.0 MHz, respectively, does not allow one to extract the difference in A_{zz} values of the two radical fractions.

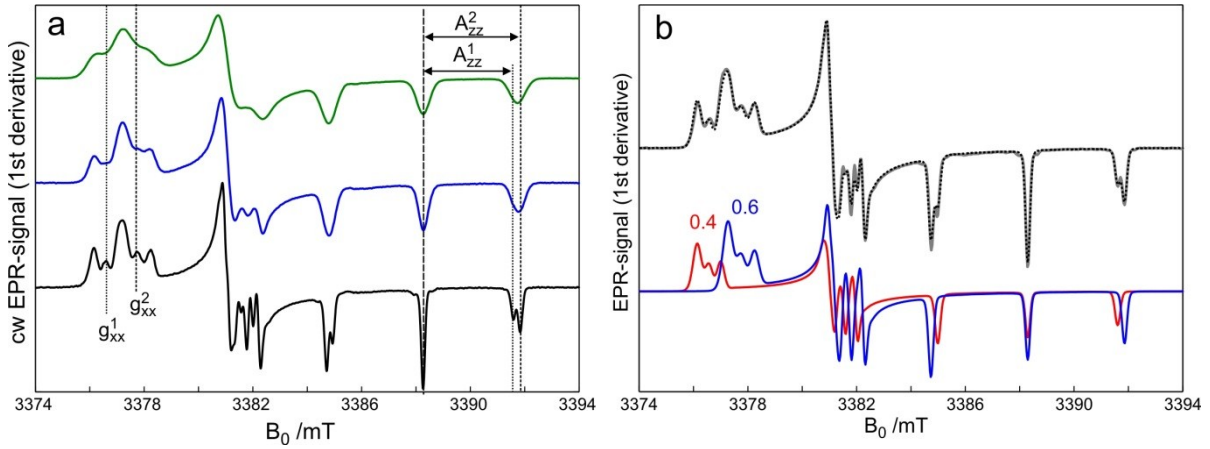

Figure 4.7 *(a) Experimental W-band cw EPR spectra of 1 mM R1 in frozen solution of 2-propanol recorded at 90 K for different deuteration situations: (top) R1-H_{15} in 2-propanol-H_8; (middle) R1-D_{16} in 2-propanol-H_8 and (bottom) R1-D_{16} in 2-propanol-D_8. The spectral positions that correspond to different principal g-tensor and A_{zz} values are indicated by dashed and dotted lines, respectively. (b) The best-fit calculated EPR spectrum obtained from a numerical solution of the spin Hamiltonian (top, dotted trace) overlayed with the experimental spectrum of R1-D_{16} in 2-propanol-D_8 (top, grey trace). Red and blue traces at the bottom depict the EPR spectra of two nitroxide fractions calculated using the respective best-fit parameter sets. The corresponding weight factors are indicated.*

Replacement of internal nitroxide protons by deuterons reduces the inhomogeneous EPR linewidth at g_{zz}, $M_I = 0$ to 12.3 MHz, and additional features are recognized in the EPR spectrum (Fig. 4.7(a), middle trace). The two components in the g_{xx} region become better distinguishable. Significantly different widths of the g_{zz}, $M_I = 0$ and g_{zz}, $M_I = \pm 1$ EPR lines of 12.3 MHz and 16.0 MHz are observed. This difference can be rationalized either in terms of a distribution of A_{zz} values or in terms of nitroxide radical fractions with discretely different A_{zz} values. The second explanation is supported by inspection of the EPR spectrum of the fully deuterated system (solvent and radical), see Fig. 4.7(a) (bottom trace). This perdeuteration causes a reduction of the EPR linewidth at g_{zz}, $M_I = 0$ to 5.0 MHz. Two lines are resolved at g_{zz}, $M_I = \pm 1$, which correspond to two nitroxide radical fractions with

different A_{zz} values. Additionally, the small inhomogenous linewidth allows one to resolve hyperfine structure in the g_{xx} and g_{yy} spectral regions. Figure 4.7(b) (top trace) shows the experimental spectrum of the fully deuterated system (grey trace) overlayed with the best-fit spectrum (dotted trace). The EPR spectrum was analyzed using the numerical solution of the spin Hamiltonian including the electron and nuclear Zeeman, the nitrogen hyperfine and nitrogen quadrupole terms, using two parameter sets for two nitroxide fractions as well as an orientation-dependent linewidth. The two traces in Fig. 4.7(b) (bottom) depict the EPR spectra of the two nitroxide fractions calculated using the best-fit parameter sets. The spectral intensities of the two contributions yield the weights of the nitroxide subensembles (1) and (2) of 0.40 ± 0.02 and 0.60 ± 0.02, respectively. The different weights of the two radical fractions allow one not only to determine the g_{xx} and corresponding A_{zz} values (g^1_{xx}= 2.00911 ±0.00005, g^2_{xx} = 2.00843 ±0.00005; A^1_{zz}= 93.2 ± 0.3 MHz, A^2_{zz}= 99.9 ±0.3 MHz), but also to find the respective parameters in the g_{yy} region. The full set of hyperfine and g-tensor components for the two nitroxide radical fractions, is summarized in Table 4.1. Additionally, different EPR linewidths in the g_{xx} (10.3 MHz) and g_{yy}, g_{zz} (5.0 MHz) canonical positions are obtained for both fractions. Significantly broader g_{xx} lines can be explained either by a distribution of g_{xx} values ("g-strain" [22]) within each nitroxide's subensemble or by orientation dependence of non-resolved hyperfine couplings of the internal nitroxide deuterons. The linewidth contribution due to g-strain can be extracted from a joined linewidth analysis of the completely protonated and deuterated systems. This broadening of about 9 MHz corresponds to the width (FWHM) $\Delta g_{1/2} \approx 2 \cdot 10^{-4}$ of a Gaussian-type g_{xx} distribution.

Table 4.1. *The magnetic interaction parameters of the R1-D_{16} nitroxide in frozen 2-propanol and OTP/benzene solutions obtained from the analysis of the W-band cw EPR spectra at 90 K.*

Solvent	$[A_{xx}; A_{yy}; A_{zz}]$ [a] /MHz	$[g_{xx}; g_{yy}; g_{zz}]$-2 [a] /10^{-5}	fraction
2-propanol (1)	12.0; 12.0; 93.2	911; 620; 219	0.40
2-propanol (2)	13.2; 13.4; 99.9	843; 606; 219	0.60
OTP/benzene [b]	12.0; 12.3; 93.8	905; 615; 220	1.0

[a] The absolute errors of the A-, g-values are ±0.3 MHz, $\pm 5 \times 10^{-5}$ respectively. The error for the g-value difference is $\pm 2 \times 10^{-5}$.

[b] The magnetic parameters for OTP/benzene are adopted from previous studies [17;23].

W-band ELDOR-detected NMR

The experimental W-band EDNMR spectrum of R1-D_{16} in 2-propanol-D_8 as a function of the external magnetic field is shown in Fig. 4.8(a). The spectrum is dominated by a single narrow line around 21.9 MHz appearing over the whole spectral region of nitroxide EPR absorption. This signal is assigned to the external and internal nitroxide deuterons. In the g_{zz} spectral region, ridges are formed which end up in well-resolved lines at the spectral positions corresponding to the principal A_{zz} values. The best-resolved lines are observed in the g_{zz}, M_I = -1 spectral region which appear at the positive frequencies, $\Delta\nu = \nu_2 - \nu_1 > 0$. These lines at frequencies of 38 MHz and 53 MHz originate from forbidden single-quantum transitions: $|M_S = -1/2, M_I = -1\rangle \rightarrow |1/2, 0\rangle$ and $|-1/2, 0\rangle \rightarrow |1/2, -1\rangle$, respectively. These forbidden transitions are indicated as ν_2' and ν_2'' in the energy level diagram for an S = 1/2, I = 1 spin system (Fig. 4.8(c)) and correspond to nuclear transition frequencies $\Delta\nu' = \nu_2' - \nu_1$

and $\Delta\nu''=\nu_2''-\nu_1$, respectively. The same nuclear transitions are observed in the g_{zz}, $M_I = 0$ spectral region at negative frequencies, as follows from the transition scheme in Fig. 4.8(c). A more detailed assignment of the observed EDNMR lines was performed in the work of Florent et al. [24].

In contrast to the g_{zz} spectral region, broad and non-structured EDNMR signals are observed in the g_{xx}-g_{yy} region at frequencies between -50 MHz and +50 MHz. These lines are assigned to the forbidden single- ($\Delta M_S = \pm 1$, $\Delta M_I = \pm 1$) and double-quantum ($\Delta M_S = \pm 1$, $\Delta M_I = \pm 2$) transitions. As pointed out in Materials and methods section, power and length of the HTA pulse were optimized for the detection of forbidden transitions in the g_{zz} spectral region, where their intensity is significantly lower than that of forbidden transitions in the g_{xx}-g_{yy} region.

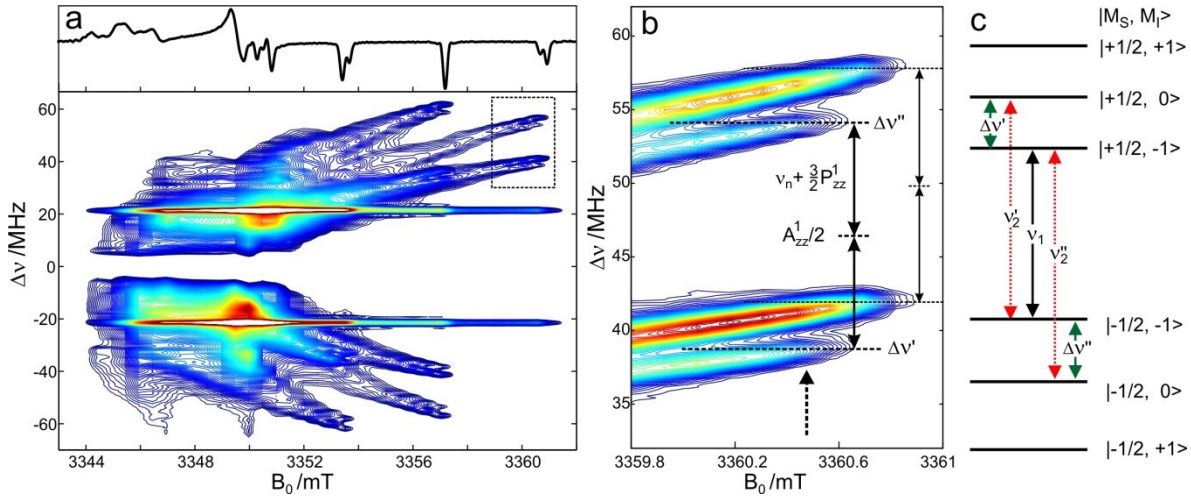

Figure 4.8 *(a) Contour plot of the field-frequency dependence of W-band EDNMR intensities of 1 mM R1-D_{16} in 2-propanol-D_8 glass at 50 K. The contour lines are shown as isohypses from 0.01 to 1 of the maximum ^{14}N EDNMR intensity. The overall measurement time was 30 minutes. On top, the 2-pulse echo-detected W-band EPR spectrum is shown in first derivative form. (b) The EDNMR spectrum recorded at 12 magnetic field values around the g_{zz}, $M_I = -1$ spectral position, as indicated in (a). The dashed arrow indicates the field position where the recordings presented in Fig. 4.9 were acquired. (c) Energy level diagram at g_{zz}, $M_I = -1$ spectral position for $g_n(^{14}N) > 0$, $A_{zz}(^{14}N) > 0$, $P_{zz}(^{14}N) < 0$.*

The intensity of the forbidden transitions depends on the contribution of quadrupole (P) and anisotropic hyperfine (A) interaction parameters of the spin Hamiltonian [21]. For the magnetic interaction parameters of R1 (see Table 4.1), the normalized intensity of forbidden transitions close ($\theta = 2°$) to the g_{zz}, $M_I = -1$ canonical position is calculated to $I_f = 0.5 \cdot 10^{-4}$ using Eq. 2.22. However, in the g_{xx}-g_{yy} spectral region it is significantly larger, reaching $I_f = 0.5$. Moreover, in the g_{xx}-g_{yy} region, the double-quantum forbidden transitions gain substantial intensities. Thus, the EDNMR settings optimized for the g_{zz} region are not ideal for the g_{xx} and g_{yy} regions. This leads to a broadening of the single-quantum EDNMR lines, which are overlayed with double-quantum EDNMR lines due to efficient pumping of these transitions.

Figure 4.8(b) shows a close-up view of the EDNMR spectrum in the g_{zz} spectral region. Well-resolved EDNMR spectra in this spectral region allow one to analyze the experimental recordings in great detail. Instead of the expected one pair of lines, two pairs of lines of different intensities and positions are observed. They are assigned to nitroxide fractions with different A_{zz} values, similar to what is observed in cw EPR. To obtain the hyperfine and quadrupole parameters for each radical

fraction, the EDNMR recordings at each magnetic field position were analyzed using four Gaussian lines analogously to simpler situation with single pair of lines discussed in Materials and methods section. For extracting the principal A_{zz} values, the line positions in the frequency dimension were interpolated to the corresponding g_{zz}, $M_I = -1$ spectral field positions. According to Eq. 4.4, the hyperfine couplings are equal to $A_{zz}^1 = 93.15 \pm 0.05$ MHz and $A_{zz}^2 = 99.74 \pm 0.05$ MHz. These values are in agreement with the respective values 93.2 ± 0.3 MHz and 99.9 ± 0.3 MHz from cw EPR. The width of the EDNMR lines is only about 1 MHz. This results in a higher precision of line position measurements and significantly smaller experimental errors as compared to cw EPR. Additionally, in high-field cw EPR the precision of the A_{zz} values is determined by the accuracy of the magnetic field calibration, which is necessary because of the non-linearity of the magnetic field sweep of superconducting magnets. The analysis of the high-field pulsed EDNMR spectra also yields the corresponding weight factors of the contributions of the nitroxide fractions. These weights are 0.40 ± 0.02 for the smaller A_{zz}^1 and 0.60 ± 0.02 for the largerA_{zz}^1, in agreement with the results of cw EPR. It can be concluded, that EDNMR on perdeuterated systems is capable of resolving slightly different A_{zz} values, but also of achieving this with higher precision as compared to cw EPR. Additionally, P_{zz} quadrupole parameters are obtained and are listed in Table 4.2.

4.4 W-band EDNMR spectral resolution in increasingly protonated systems

As was shown above, cw EPR fails to resolve different A_{zz} values for different nitroxide fractions even after only partial protonation of the system. To investigate the influence of inhomogenous EPR linewidth on the EDNMR resolution, an EDNMR experiment was performed on samples with gradually increased protonation. Figure 4.9(a) shows EDNMR recordings for R1 in 2-propanol with different deuteration degree of the system. They were recorded at the identical spectral position, as indicated in Fig. 4.8(b) by the dotted arrow. The deuterium EDNMR line intensity around 21.9 MHz decreases upon protonation and, naturally, is not observed at all for the fully protonated system. Figure 4.9(b) presents an expanded view of the 33 – 64 MHz frequency region, where two pairs of ^{14}N EDNMR lines are observed. The line positions and relative amplitudes are identical for the three recordings. The EDNMR spectra in the g_{zz}, $M_I = -1$ region were analysed in analogy to the fully deuterated system described above. The obtained parameters are summarized in Table 4.2.

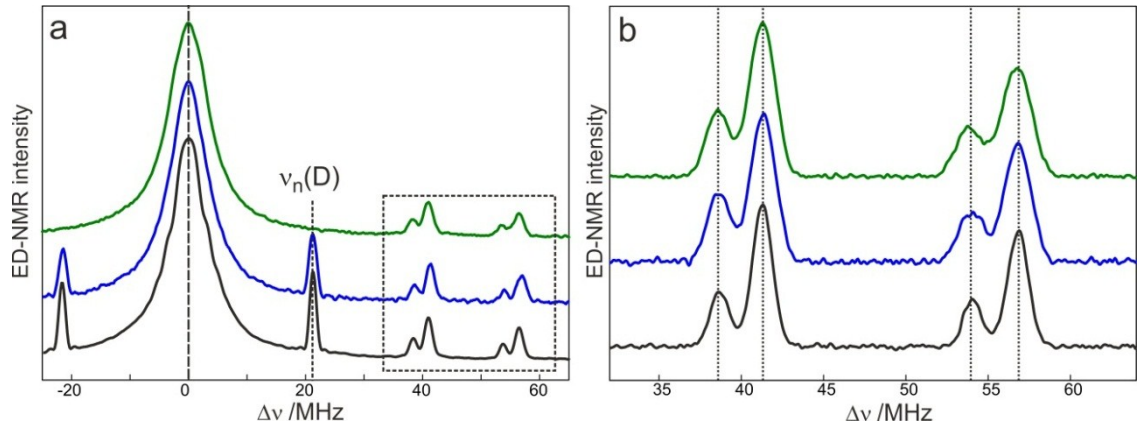

Figure 4.9 *Experimental W-band EDNMR spectra of R1 in frozen solution of 2-propanol taken under identical experimental settings at 50 K for different deuteration situations: (top) R1-H_{15} in 2-propanol-H_8; (middle) R1-D_{16} in 2-propanol-H_8 and (bottom) R1-D_{16} in 2-propanol-D_8. The field position of the EDNMR recordings is indicated by the dashed arrow in Fig. 4.8(b). (a) Recordings over the wide frequency range. The nuclear*

Larmor frequency of deuterium is marked as well as the nitrogen frequency range. (b) The EDNMR spectra in the ^{14}N frequency region after baseline correction.

The frequencies corresponding to the line positions are the same for all samples. Hence, the A_{zz} and P_{zz} values for the three systems agree within experimental error. Continuous increase of the EDNMR linewidth from 1.2 to 1.7 MHz is observed upon protonation, see Fig. 4.9(b) and Table 4.2. This broadening is caused by the increasing inhomogeneous EPR linewidth, which leads to an averaging of the EDNMR response across the magnetic field axis. However, taking into account that the frequency difference between the EDNMR lines of two different fractions is about 3 MHz, the EDNMR technique is still capable of providing precise A_{zz} and P_{zz} values and the relative weights of each nitroxide fraction even in the fully protonated system. The relative weights for both spectral components as determined from EDNMR are in good agreement for all three systems. This proves the reproducibility of the sample preparation and freezing conditions, which was mistakenly suggested previously to limit the precision of experimental A_{zz} values [4].

Table 4.2 *The magnetic parameters of the R1 nitroxide in 2-propanol solution for different isotope situations as obtained from the analysis of W-band EDNMR at 50 K.*

	R1-^{14}N-D_{16} 2-propanol-D_8	R1-^{14}N-D_{16} 2-propanol-H_8	R1-^{14}N-H_{15} 2-propanol-H_8	R1-^{15}N-D_{16} 2-propanol-D_8
$\Delta B_{1/2}$ /MHz [a)]	5.0	12.3	15.5	-
$\Delta\nu_{1/2}$ /MHz [b)]	1.2	1.6	1.7	1.7
$\lvert A^1_{zz}\rvert$ /MHz	93.15(5)	93.3(1)	93.3(1)	130.5(1)
$\lvert A^2_{zz}\rvert$ /MHz	99.74(5)	99.8(1)	99.7(1)	139.7(1)
P^1_{zz} /MHz	-1.77(3)	-1.79(5)	-1.79(5)	
P^2_{zz} /MHz	-1.62(3)	-1.64(5)	-1.67(5)	

[a)] The inhomogeneous (FWHM) linewidth (g_{zz}, $M_I = 0$ EPR line) due to unresolved internal and external ^{1}H and ^{2}H hyperfine couplings (Gaussian distribution) determined from the W-band cw EPR spectrum at 90 K. [b)] The linewidth of EDNMR line

Surprisingly, the recent EDNMR investigation of hydroxy-TEMPO (TEMPOL) in frozen solution of 2-propanol did not resolve two different A_{zz} contributions, and only a single value $A_{zz} = 98\pm2$ MHz was obtained [24]. An explanation could be that the authors conducted their EDNMR experiments with pulse sequence settings optimized for detection of double-quantum transitions. This resulted in a broadening of the single-quantum lines which probably prevented the resolution of two A_{zz} components. To check this reasoning, we performed W-band EDNMR experiments on TEMPOL-D_{15} in 2-propanol-D_8 frozen solution using identical experimental settings as used for the R1 radical in 2-propanol. The resulting EDNMR spectrum is depicted in Fig. 4.10. Parameters obtained from the analysis described above are summarized in Table 4.3. The analysis of the EDNMR spectra yields two A_{zz} values: A^1_{zz}=102.1±0.1 MHz and A^2_{zz}= 95.4±0.1 MHz. The mean value of 98.8 MHz is in agreement with that reported by Florent et al. [24]. The difference of $\Delta A_{zz} = 6.7$ MHz is, within experimental accuracy, equal to ΔA_{zz} for R1 in 2-propanol. The absolute A_{zz} values for R1 and TEMPOL nitroxides are, however, different because of the different structure of the nitroxide spin probe [15]. It is worth mentioning that the different structures of R1 and TEMPOL result in changed populations between the two nitroxide fractions. In R1, the larger fraction of weight 0.6 exhibits a

higher A_{zz} value. In TEMPOL, this fraction has only a weight factor of 0.5. Thus, the equilibrium between two different nitroxide subensembles depends on the radical structure (TEMPOL: non-planar 6-membered ring, R1: planar 5-membered ring) in agreement with previous observations [15].

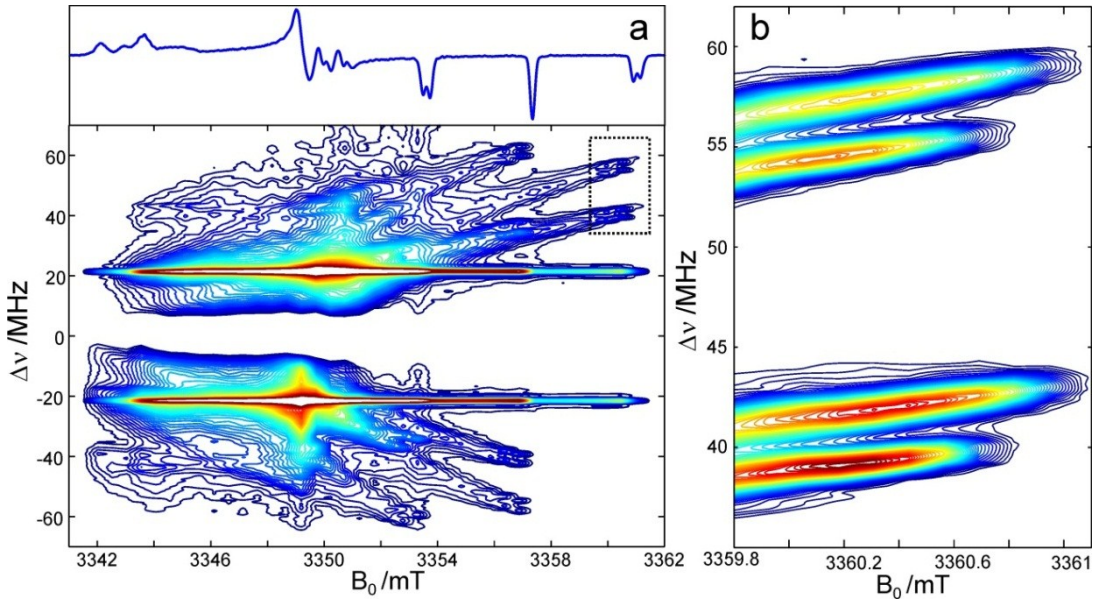

Figure 4.10 *(a) Contour plot of field-frequency dependence of W-band EDNMR intensities of 1 mM TEMPOL-D_{15} in 2-propanol-D_8 glass at 50 K. The contour lines are shown as isohypses from 0.01 to 1 of the maximum ^{14}N-EDNMR intensity. On top, the 2-pulse echo detected W-band EPR spectrum is shown in derivative form. (b) The EDNMR spectrum recorded at 12 field values around the g_{zz}, M_I= -1 spectral position as indicated in (a).*

Table 4.3 *The magnetic parameters of the TEMPOL-D_{15} in 2-propanol-D_8 solution obtained from the analysis of W-band EDNMR at 50 K.*

	(1)	(2)	from ref. [23]
Fraction	0.50±0.02	0.50±0.02	-
$\Delta B_{1/2}$ MHz (EDNMR)	1.2	0.9	-
$\|A_{zz}\|$ /MHz	102.1	95.4	98±2
P_{zz}	-1.53	-1.65	-1.77±0.10

4.5 Comparison of W-band EDNMR spectra in ^{14}N- and ^{15}N-labeled nitroxides

As pointed out in Chapter 2.7.5, the EDNMR technique is based on polarization transfer across forbidden EPR transitions. However, the intensity of forbidden transitions is approaching zero at the spectral positions close to g_{zz}, $M_I = -1$, see Eq. 2.22. Therefore, the principal values A_{zz} and P_{zz} obtained from experimental frequencies Δν' and Δν" have to be verified. This can be done using the ^{15}N-isotope substituted nitroxide radical R1-^{15}N. The missing quadrupole moment for ^{15}N nuclei (I = 1/2), allows one to evaluate the experimentally obtained nuclear transition frequencies solely in terms of the hyperfine coupling and nuclear Larmor frequency, see Eq. (4.4). Figure 4.11(a) presents the EDNMR spectrum of R1-^{15}N-D_{16} in a 2-propanol-D_8 matrix. The spectrum is dominated by a narrow deuterium line around 21.9 MHz in the whole spectral range, analogous to the EDNMR spectrum depicted in Fig. 4.8(a). In the g_{xx} - g_{yy} region, the EDNMR spectrum of R1-^{15}N is significantly simplified as compared to the R1-^{14}N spectrum. This is due to the absence of double-quantum transitions ($\Delta M_I = \pm 2$) for I = 1/2 nuclei. In the g_{zz}, $M_I = +1/2$ region, two well-resolved pairs

of lines are observed, see Fig. 4.11(b), which were analysed as described above. From the EDNMR line positions at g_{zz}, $M_I = +1/2$, a splitting between corresponding lines of $\Delta\Delta\nu = \Delta\nu'' - \Delta\nu' = 28.8 \pm 0.1$ MHz was obtained for both nitroxide fractions. This value is lower than the expected one, twice the nuclear Larmor frequency, $2 \cdot \nu_N(^{15}N) = 29.00$ MHz at a magnetic field of 3360 mT. However, the experimental $\Delta\Delta\nu$ value was determined using Eq. (4.4), which includes only first-order terms. Hence, the experimental value of 28.8 ± 0.1 MHz has to be compared with $\Delta\Delta\nu = 28.90$ MHz calculated using the second-order approximation which, for S = 1/2, I = 1/2, is given by [25]:

$$\Delta\Delta\nu = \left| \frac{2 \cdot g_n \cdot \beta_n \cdot B_0}{h} + \frac{h \cdot A_{zz}^2}{2 \cdot g \cdot \beta \cdot B_0} \right| \qquad \text{Eq. (4.5)}$$

where β_n is the nuclear magneton, β the Bohr magneton, h the Planck constant, g_n and g are the nuclear and electronic g factors, respectively. The good agreement of both $\Delta\Delta\nu$ values reveals that the quadrupole-tensor component P_{zz} can be obtained from EDNMR spectra with high precision after considering second-order effects.

Principal ^{15}N hyperfine coupling values of $A_{zz} = 130.5 \pm 0.1$ MHz and 139.7 ± 0.1 MHz for the two nitroxide fractions are obtained for R1-^{15}N. These A_{zz} values, when scaled down by the ratio of the ^{15}N and ^{14}N g_n-values, result in 93.00 ± 0.07 MHz and 99.60 ± 0.07 MHz. These values are slightly lower than values measured for the ^{14}N radical, 93.15 ± 0.05 MHz and 99.74 ± 0.05 MHz. This is because the sum of the nuclear transition frequencies, $\Delta\nu'+\Delta\nu''$, for I = 1/2 nuclei does not contain second-order shifts, whereas for I = 1 it does [25]:

$$\Delta\nu' + \Delta\nu'' = \left| A_{zz} - \frac{h \cdot A_{zz}^2}{2 \cdot g \cdot \beta \cdot B_0} \right| \qquad \text{Eq. (4.6)}$$

Therefore, for ^{14}N the second-order correction of about 30 kHz has to be included if high-precision A_{zz} values are required.

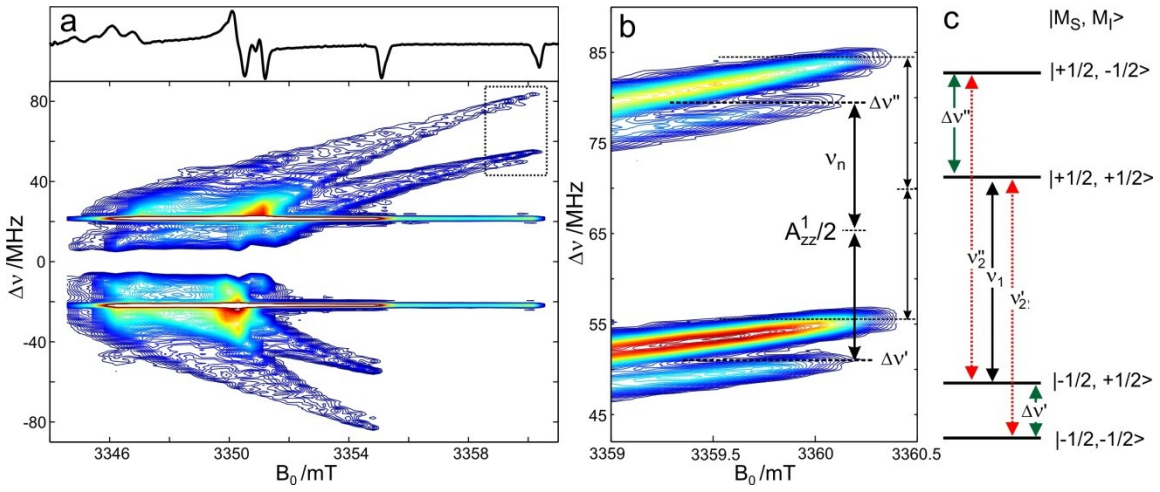

Figure 4.11 *(a) Contour plot of the field-frequency dependence of W-band EDNMR intensities of R1-^{15}N-D_{16} in 2-propanol-D_8 glass at 50 K. The contour lines are shown as isohypses from 0.01 to 1 of the maximum ^{15}N EDNMR intensity. On top, the 2-pulse echo detected W-band EPR spectrum is shown in first-derivative form. (b) The EDNMR spectrum recorded at 12 magnetic field values around the g_{zz}, $M_I = +1/2$ spectral position, as indicated by the dotted line area in (a). (c) Energy level diagram at the g_{zz}, $M_I = +1/2$ spectral position for $g_n(^{15}N) < 0$, $A_{zz}(^{15}N) < 0$.*

Interestingly, the comparison of the EDNMR spectra depicted in Figs. 4.8(b) and 4.10(b) does not reveal any gain in resolution for the R1-^{15}N nitroxide as compared to R1-^{14}N. Such gain would be expected because of the larger ^{15}N hyperfine couplings, which would result in a larger difference in EDNMR line positions for both nitroxide radical fractions. The expected resolution enhancement is, however, compensated by the larger EDNMR linewidth for R1-^{15}N (1.7 MHz) than for R1-^{14}N (1.2 MHz). The linewidth of R1-^{15}N is scaled up by the same factor as the nitrogen hyperfine coupling, i.e., by the ratio of $g_n(^{15}N) / g_n(^{14}N)$.

The above analysis of R1-^{14}N and R1-^{15}N EDNMR spectra verified the accuracy of A_{zz} and P_{zz} values obtained from the EDNMR spectra, yielding A_{zz} values in agreement with those obtained from W-band cw EPR. To assess the sensitivity and resolution of the EDNMR method, it has to be compared with the ENDOR method, which directly probes allowed nuclear transitions.

4.6 Comparison of W-band EDNMR and ENDOR sensitivity

In Figs. 4.12(a) and 4.12(b) the experimental 2D-ENDOR spectra for R1-D_{16} and R1-^{15}N-D_{16} radicals in frozen OTP/benzene solution are shown. This nonpolar and aprotic matrix was chosen to obtain a well-defined nitroxide radical fraction which is described by only a single set of magnetic interaction parameters, as seen in EDNMR spectra in Fig. 4.6. The signal-to-noise (S/N) ratio is very low despite the long acquisition time of 6 hours. The deuterium ENDOR line from both internal and external nuclei is visible throughout the spectrum, analogous to what is observed in the EDNMR spectra. All spectral features in the g_{xx}-g_{yy} spectral region can be recognized and are in agreement with ESEEM spectra of the same system reported previously [17]. In the g_{zz} spectral region, ridges are formed, which end up at the canonical magnetic field positions. The intensity, however, is stronger for the high-frequency ENDOR lines. The low-frequency ENDOR lines expected around 38 MHz for R1-D_{16} and 48 MHz for R1-^{15}N-D_{16} are strongly suppressed. This is due to the "hyperfine enhancement" effect [21] and the superimposed frequency dependence of the RF amplitude, B_2.

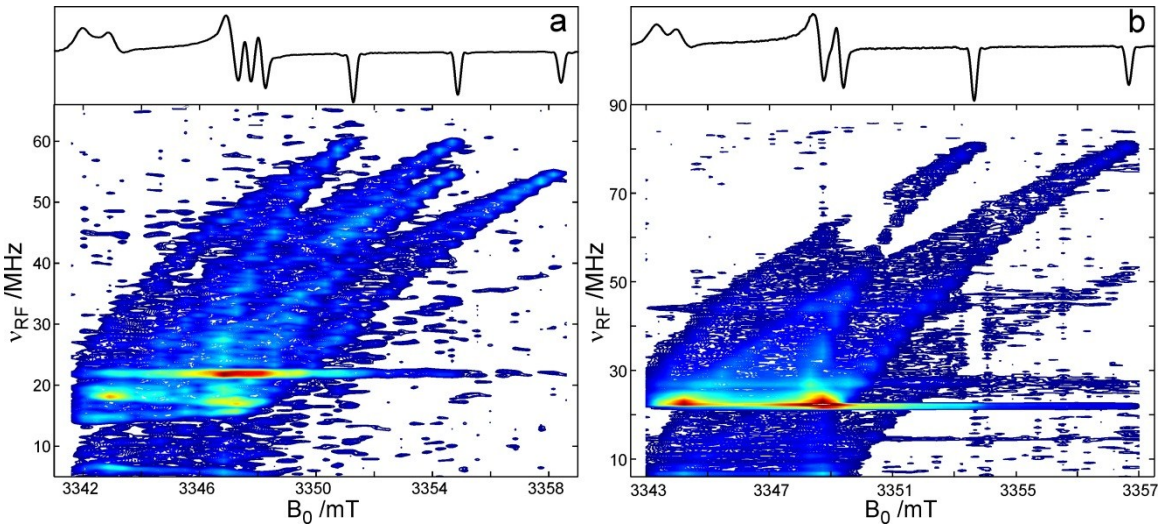

Figure 4.12 *(a) Contour plot of the field-frequency dependence of W-band ENDOR intensities of (a) R1-D_{16} and (b) R1-^{15}N-D_{16} in OTP-D_{14}/benzene-D_6 frozen solution at 50 K. Contour lines are shown as isohypses from 0.02 to 1 of the maximum ENDOR intensity. The spectra were acquired at 40 field positions averaging 500 recordings while varying the RF frequency in 512 steps. The overall measurement time per data surface was 6 hours. On the top, the corresponding 2-pulse echo-detected W-band EPR spectra are shown in first-derivative form.*

For strict comparison of sensitivity and resolution of both techniques, EDNMR and ENDOR spectra were recorded consecutively at the same magnetic field position. Figure 4.13(a) presents EDNMR and ENDOR recordings for R1 at field position close to g_{zz}, M_I =-1, at the same frequency (ν_2; ν_{RF}) sweep range and pulse repetition rate, but using a different number of averages per point (100 for EDNMR, 500 for ENDOR). The line positions of the ENDOR and EDNMR recordings exactly coincide. First, the sensitivity of both techniques was compared by the S/N ratio for the recordings in Fig. 4.13(a). Taking into account that for the determination of A_{zz} and P_{zz} values, the frequency positions of both low- and high-frequency lines are required, the S/N ratio was calculated for the line with lowest NMR response intensity. For ENDOR, an S/N ratio of 0.2 per shot was obtained. In contrast, for EDNMR the respective number is S/N = 6. Hence, the sensitivity of EDNMR is superior to ENDOR by a factor of 30. This means that the same information can be obtained in a 900 × shorter measurement time. Next, the spectral resolution was compared.

Figures 4.13(b) and 4.13(c) show the recordings of the high-frequency NMR response in the same frequency range for the R1-D_{16} and R1-^{15}N-D_{16} radicals. The line positions in the ENDOR and EDNMR spectra coincide for a given nitrogen isotope. EDNMR as well as ENDOR spectra can be simulated with Gaussian lines. For ^{14}N nuclei, EDNMR exhibits a slightly broader linewidth of 1.2 MHz compared to 1.1 MHz in the case of ENDOR. This small difference, however, can be eliminated by increasing the integration window at the expense of the S/N ratio. For the ^{15}N substituted nitroxide, linewidths of 1.7 MHz and 1.6 MHz are obtained from EDNMR and ENDOR, respectively. Thus, both linewidths of R1-^{15}N are scaled up compared to R1 by the ratio of $g_n(^{15}N)/g_n(^{14}N)$, similar to the nitroxide/2-propanol system. The origin of the EDNMR and ENDOR line broadening can be assigned to a distribution of A_{zz} values, i.e., to A-strain, analogous to the observed g-strain of g_{xx} values.

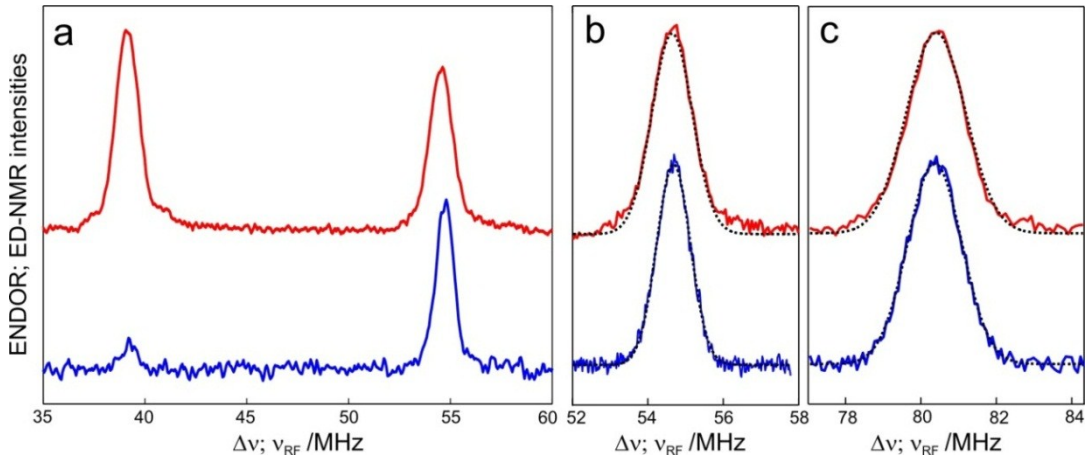

Figure 4.13 *Comparison of the sensitivity and resolution of the W-band EDNMR and ENDOR methods. (a) EDNMR (top) and Davies-ENDOR (bottom) spectra of R1-D_{16} in frozen OTP-D_{14}/benzene-D_6 solution recorded at the same B_0 close to the g_{zz}, M_I = -1 spectral position at 50 K using 100 and 500 averages per point, respectively. Spectra were recorded with pulse repetition rate of 380 Hz and 512 spectral points resulting in acquisition time of 10 min and 2 min for ENDOR and EDNMR traces, respectively. (b) and (c) EDNMR (top) and ENDOR (bottom) lines of the high-frequency transition of R1-^{14}N-D_{16} (b) and R1-^{15}N-D_{16} (c) in frozen OTP-D_{14}/benzene-D_6 solution recorded at the same field position close to g_{zz}, (^{14}N: M_I = -1; ^{15}N: M_I = +1/2) at 50 K. The best-fit Gaussian lines are shown by dotted lines overlayed with the corresponding experimental recordings.*

Table 4.3 *The magnetic parameters of the R1 and R1-^{15}N nitroxides in OTP-D_{14}/benzene-D_6 solution as obtained from the analysis of the W-band EDNMR and Davies-ENDOR spectra at 50 K*

	R1-^{14}N-D_{16}	R1-^{15}N-D_{16}
$\Delta\nu_{1/2}$ (EDNMR) /MHz	1.2	1.7
$\Delta\nu_{1/2}$ (ENDOR) /MHz	1.1	1.6
$\lvert A_{zz}\rvert$ /MHz	94.70(5)	132.5(1) / 94.5 [a)]
P_{zz} / MHz	-1.74(3)	-

[a)] The ^{15}N hyperfine value scaled by the ratio of magnetic moments of the ^{14}N and ^{15}N nuclei.

4.7 Discussion and conclusions

For the R1 nitroxide radical in frozen solution of polar, protic 2-propanol, a pronounced heterogeneity was observed both in W-band cw EPR and EDNMR spectra. Two nitroxide radical subensembles could be resolved which are described with two sets of magnetic interaction parameters, g^1_{xx}= 2.00911, A^1_{zz} = 93.2 MHz, P^1_{zz}= -1.77 MHz and g^2_{xx}= 2.00843, A^2_{zz}= 99.8 MHz, P^2_{zz}= -1.62 MHz. In contrast, only one parameter set, g_{xx} = 2.00905, A_{zz} = 94.7 MHz, P_{zz}= -1.74 MHz, is sufficient to describe the EPR spectra of R1 dissolved in the nonpolar, aprotic OTP/benzene matrix.

Apart from the observed shift of magnetic parameters depending on the solvent type, the presence of two different g_{xx} spectral components of nitroxide radicals in frozen solutions of some protic solvents has been reported previously [4;9;11;15]. However, the absolute g_{xx} values reported in the previous high-field EPR literature are difficult to compare. This is because of possible differences of the magnetic field calibration as well as because of structural differences of the nitroxide radicals used. From the extensive work by Lebedev et al., see [15] for a review, it is known that the structure of the nitroxide radical affects not only the absolute g_{xx} value, but also the number of g_{xx} spectral components and their relative intensity ratio. For the interpretation of the g_{xx} heterogeneity, however, the comparison of the difference values Δg_{xx} for several g_{xx} spectral components can be useful because the difference of g_{xx} values is less dependent on the nitroxide type and magnetic field calibration procedures. Two g_{xx} values with $\Delta g_{xx} = 6.6\cdot10^{-4}$ were resolved in 130 GHz echo-detected EPR and 220 GHz cw EPR spectra of 5-doxyl-SA, 2-(3-carboxypropyl)-4,4-dimethyl-2-tridecyl-3-oxazolidinyloxy, nitroxide dissolved in 2-propanol [9]. The difference between both g_{xx} values is close to that reported here, $\Delta g_{xx} = 6.8\cdot10^{-4}$, suggesting a similar nature of the observed spectral components despite the different structure of the nitroxide probe. The g_{xx} values for both components were found to be the same for simple alcohols like methanol, ethanol, 2-propanol and butanol within experimental accuracy. However, the relative spectral contribution of the high g_{xx}-value fraction increases with increasing size of the alcohol molecules [9]. An analogous situation was observed for the MTSSL-β-mercaptoethanol radical (MTSSL with a β-mercaptoethanol covalently bound to it [4]). The analysis of the W-band cw EPR spectra in frozen 1-octanol, 1-hexanol, 1-butanol, ethanol and methanol revealed two g_{xx} spectral contributions with relative weights depending on the type of alcohol solvent. A difference between both g_{xx} values of $\Delta g_{xx} = (4 - 8)\cdot10^{-4}$ was found. For a number of nitroxides dissolved in ethanol, the presence of two g_{xx} components was observed also in the 240 GHz cw EPR spectra, and a $\Delta g_{xx} = (5.8 - 7.2)\cdot10^{-4}$ was reported [11].

All EPR studies performed so far on different protonated radical/solvent systems do not consider the possibility of A_{zz} heterogeneity owing to the limited cw EPR resolution. Such heterogeneity is, however, observed in the present study. In deuterated ethanol frozen solution, the presence of two

nitroxide fractions with different A_{zz} values was previously demonstrated for perdeuterated oxo-TEMPO nitroxide [12]. Two different A_{zz} values of A_{zz}^1=100.5 MHz and A_{zz}^2= 94.2 MHz were obtained from the X-band cw EPR spectrum.

The nature of the nitroxide subensembles in frozen alcohols with different g_{xx} and A_{zz} parameters is still under discussion. The magnetic parameters of the two nitroxide fractions in a homogeneous, polar and protic 2-propanol matrix show two distinctly different local environments. These differ only in the hydrogen-bond situation of the nitroxide radical with respect to the solvent molecules. Such an assignment is supported by the agreement ofg_{xx}^1, A_{zz}^1, P_{zz}^1 parameters with those obtained in the nonpolar, aprotic OTP/benzene matrix. Thus, the magnetic parameters should predominantly be sensitive to the hydrogen-bond characteristics of the nitroxide. The effect of solvent polarity is probably only of minor importance. This hypothesis ought to be validated by additional experiments on nitroxides in different matrices. Both interaction parameters, g_{xx} and A_{zz}, can be used to evaluate the microenvironmental situation of the nitroxide probe. For a precise characterization of the microenvironment, independent information about both magnetic parameters is required. This needs two types of EPR experiments: g_{xx} is best determined by cw EPR, while A_{zz} is best determined by EDNMR.

As pointed out above, the cw EPR linewidth in the g_{xx} spectral region and the EDNMR linewidth in the A_{zz} spectral region are influenced by possible distributions of the g_{xx} and A_{zz} values, i.e., by g- and A-strains. Such distributions are most probably due to specific internal properties of the nitroxide molecules, for instance small structural changes or out-of-plane motion of the oxygen atom [23], because the same strains are observed in the three different microenvironments. The width (FWHM) of both distributions, $\Delta g_{1/2} \approx 2 \cdot 10^{-4}$ and $\Delta A_{1/2} \approx 1$ MHz (for ^{14}N nitroxide), was evaluated. The effect of the g-strain depends on the external magnetic field B_0, whereas the A-strain acts field-independently.

Hence, the optimal magnetic field/microwave frequency for an EPR experiment to precisely determine g_{xx} values can be estimated. For perdeuterated nitroxides in a protonated environment the W-band EPR line shape in the g_{xx} region is governed by the A_{xx} hyperfine splitting, see Fig. 4.3(a). With increasing magnetic fields the linewidth contribution will increase and eventually outweigh the hyperfine contribution of $2A_{zz} \approx 28$ MHz at a B_0 field of about 10 T. Above this magnetic field, which corresponds to about 280 GHz EPR frequency, no further improvement of resolution in the g_{xx} spectral region will be achieved. The resolution capability of cw EPR above 280 GHz and EDNMR at W-band can be compared using the differences $\Delta g_{xx} = 6.8 \cdot 10^{-4}$ and $\Delta A_{zz} = 6.7$ MHz of the two R1 nitroxide subensembles in 2-propanol. The frequency difference of two EDNMR lines belonging to different fractions is determined by $\Delta A_{zz}/2 = 3.35$ MHz (neglecting the quadrupole contribution). Thus, the g_{xx} resolution of cw EPR and the A_{zz} resolution of EDNMR become equal because of $\Delta g_{xx}/\Delta g_{1/2} \approx 1/2 \cdot \Delta A_{zz}/\Delta A_{1/2} \approx 3.4$. In order to obtain precise g_{xx} values very high-field EPR is required, for instance at about 10 T/275 GHz [7;26] or even 14 T/360 GHz [27;28], whereas precise A_{zz} values can be obtained already at moderately high magnetic fields, for instance at 3.4 T/95 GHz (W-band EPR).

References

[1] G.E. Fanucci and D.S. Cafiso *Recent advances and applications of site-directed spin labeling* Curr. Opin. Struct. Biol. **2006,** 16, 644-653.

[2] W.L. Hubbell and C. Altenbach *Investigation of structure and dynamics in membrane proteins using site-directed spin labeling* Curr. Opin. Struct. Biol. **1994,** 4, 566-573.

[3] W.L. Hubbell, H.S. Mchaourab, C. Altenbach, and M.A. Lietzow *Watching proteins move using site-directed spin labeling* Structure **1996,** 4, 779-783.

[4] R. Owenius, M. Engström, M. Lindgren, and M. Huber *Influence of solvent polarity and hydrogen bonding on the EPR parameters of a nitroxide spin label studied by 9-GHz and 95-GHz EPR spectroscopy and DFT calculations* J. Phys. Chem. A **2001,** 105, 10967-10977.

[5] M. Plato, H.-J. Steinhoff, C. Wegener, J.T. Törring, A. Savitsky, and K. Möbius *Molecular orbital study of polarity and hydrogen bonding effects on the g and hyperfine tensors of site directed NO spin labelled bacteriorhodopsin* Mol. Phys. **2002,** 100, 3711-3721.

[6] P. Cimino, M. Pavone, and V. Barone *Structural, thermodynamic, and magnetic properties of adducts between TEMPO radical and alcohols in solution: New insights from DFT and discrete-continuum solvent models* Chem. Phys. Lett. **2006,** 419, 106-110.

[7] M.G. Finiguerra, H. Blok, M. Ubbink, and M. Huber *High-field (275 GHz) spin-label EPR for high-resolution polarity determination in proteins* J. Magn. Reson., **2006,** 180, 197-202.

[8] E. Bordignon, H. Brutlach, L. Urban, K. Hideg, A. Savitsky, A. Schnegg, P. Gast, M. Engelhard, E.J.J. Groenen, K. Möbius, and H.-J. Steinhoff *Heterogeneity in the nitroxide micro-environment: polarity and proticity effects in spin-labeled proteins studied by multi-frequency EPR* Appl. Magn. Reson. **2010,** 37, 391-403.

[9] T.I. Smirnova, T.G. Chadwick, M.A. Voinov, O. Poluektov, J. van Tol, A. Ozarowski, G. Schaaf, M.M. Ryan, and V.A. Bankaitis *Local polarity and hydrogen bonding inside the Sec14p phospholipid-binding cavity: High-field multi-frequency electron paramagnetic resonance studies* Biophys. J. **2007,** 92, 3686-3695.

[10] L. Urban and H.-J. Steinhoff *Hydrogen bonding to the nitroxide of protein bound spin labels* Mol. Phys. **2013,** 111, 2873-2881.

[11] B. Dzikovski, D. Tipikin, and J.H. Freed *Conformational distributions and hydrogen bonding in gel and frozen lipid bilayers: a high frequency spin-label ESR study* J. Phys. Chem. B **2012,** 116, 6694-6706.

[12] J.S. Hwang, R.P. Mason, L.-P. Hwang, and J.H. Freed *Electron spin resonance studies of anisotropic rotational reorientation and slow tumbling in liquid and frozen media. III. Perdeuterated 2,2,6,6-tetramethyl-4-piperidone N-oxide and an analysis of fluctuating torques* J. Phys. Chem. **1975,** 79, 489-511.

[13] P. Schosseler, Th. Wacker, and A. Schweiger *Pulsed ELDOR detected NMR* Chem. Phys. Lett. **1994,** 224, 319-324.

[14] M. Pavone, A. Sillanpaa, P. Cimino, O. Crescenzi, and V. Barone *Evidence of variable H-bond network for nitroxide radicals in protic solvents* J. Phys. Chem. B **2006,** 110, 16189-16192.

[15] Ya.S. Lebedev, O.Y. Grinberg, A.A. Dubinsky, and O.G. Poluektov, Investigation of spin labels and probes by millimeter band EPR, in *Bioactive spin labels,* R.I. Zhdanov (Ed.), Springer-Verlag, Heidelberg, **1992,** pp. 227-278.

[16] C. Houriez, N. Ferré, D. Siri, and M. Masella *Further insights into the environmental effects on the computed hyperfine coupling constants of nitroxides in aqueous solution* J. Phys. Chem. B **2009,** 113, 15047-15056.

[17] A. Savitsky, A.A. Dubinskii, M. Plato, Y.A. Grishin, H. Zimmermann, and K. Möbius *High-field EPR and ESEEM investigation of the nitrogen quadrupole interaction of nitroxide spin labels in disordered solids: Toward differentiation between polarity and proticity matrix effects on protein function* J. Phys. Chem. B **2008,** 112, 9079-9090.

[18] K. Möbius, A. Savitsky, A. Schnegg, M. Plato, and M. Fuchs *High-field EPR spectroscopy applied to biological systems: characterization of molecular switches for electron and ion transfer* Phys. Chem. Chem. Phys. **2005,** 7, 19-42.

[19] K. Möbius and A. Savitsky, *High-field EPR spectroscopy on proteins and their model systems*, RSC Publishing, Cambridge, **2009**.

[20] A. Nalepa, K. Mobius, W. Lubitz, and A. Savitsky *High-field ELDOR-detected NMR study of a nitroxide radical in disordered solids: Towards characterization of heterogeneity of microenvironments in spin-labeled systems* J. Magn. Reson. **2014,** 242, 203-213.

[21] A. Schweiger and G. Jeschke, *Principles of pulse electron paramagnetic resonance*, Oxford University Press, Oxford, **2001**.

[22] J.R. Pilbrow, *Transition ion electron paramagnetic resonance*, Oxford University Press, Oxford, **1990**.

[23] A. Savitsky, M. Plato, and K. Möbius *The temperature dependence of nitroxide spin-label interaction parameters: a high-field EPR study of intramolecular motional contributions* Appl. Magn. Reson. **2010,** 37, 415-434.

[24] M. Florent, I. Kaminker, V. Nagarajan, and D. Goldfarb *Determination of the ^{14}N quadrupole coupling constant of nitroxide spin probes by W-band ELDOR-detected NMR* J. Magn. Reson. **2011,** 210, 192-199.

[25] N.M. Atherton, *Principles of electron spin resonance*, Ellis Horwood, New York, **1993**.

[26] H. Blok, J.A.J.M. Disselhorst, S.B. Orlinskii, and J. Schmidt *A continuous-wave and pulsed electron spin resonance spectrometer operating at 275 GHz* J. Magn. Reson. **2004,** 166, 92-99.

[27] K. Möbius, A. Savitsky, C. Wegener, M. Plato, M. Fuchs, A. Schnegg, A.A. Dubinskii, Y.A. Grishin, I.A. Grigor'ev, M. Kühn, D. Duché, H. Zimmermann, and H.-J. Steinhoff *Combining high-field EPR with site-directed spin labeling reveals unique information on proteins in action* Magn. Reson. Chem. **2005,** 43, S4-S19.

[28] M.R. Fuchs, T.F. Prisner, and K. Möbius *A high-field/high-frequency heterodyne induction-mode electron paramagnetic resonance spectrometer operating at 360 GHz* Rev. Sci. Instrum. **1999,** 70, 3681-3683.

Chapter 5

Investigation of nitroxide spin labels H-bonded to different solvent molecules using 244 GHz cw EPR and W-band ENDOR and EDNMR

5.1 Introduction

The heterogeneity of the environment in the vicinity of nitroxide radicals translates into a continuous broad distribution of their magnetic parameters. However, when distinctly different microenvironments are present, discrete numbers of nitroxide radical populations, described by different sets of magnetic parameters, are expected. Indeed, the presence of several distinct g_{xx} values in low-temperature high-field/high-frequency cw EPR spectra was reported for spin probes dissolved in protic solvents [1;2] and in spin-labeled proteins [3-6]. This g_{xx} heterogeneity was postulated to originate from specific interactions between the nitroxide radical and the H-bond donor group of the solvent or protein [4], although the cw EPR spectra presented no clue in terms of the nature of the H-bond donor. The possibility of specific interactions of nitroxide radicals with various protic solvents was extensively investigated in the past, using both liquid-state NMR [7-17] and EPR [18-21]. Most of these studies were performed on non-cyclic nitroxides, e.g. di-methyl-nitroxide (DMNO), di-*tert*-butyl nitroxide (DTBN) or 6-membered ring nitroxides that do not have planar structures, as opposed to the most often used spin label MTS ((1-oxyl-2,2,5,5-tetramethylpyrroline-3-methyl)methanethiosulfonate). This deviation from planarity influences the absolute value of the ^{14}N hyperfine coupling constant [22], but also changes the ratio of different spin probe populations, as was demonstrated in Chapter 4 using 4-hydroxy-TEMPO and R1 (3-hydroxymethyl-2,2,5,5-tetramethylpyrrolin-1-oxyl) nitroxide radicals, both dissolved in 2-propanol. Nevertheless, NMR studies corroborated the possibility of H-bond formation between nitroxide and protic solvents. Such conclusions were based on the paramagnetic contact shifts of ^{1}H and ^{13}C nuclei in the proton donor molecule.

In general, four main types of geometrical arrangements for the intermolecular nitroxide:solvent H-bond were proposed, as depicted for the nitroxide:methanol bimolecular system in Fig. 5.1. In σ H-bond geometry, the H-bonded proton lies in plane with the $NO^{\cdot}$ group, forming an angle θ between the $NO^{\cdot}$ bond and the axis of the OH bond, interacting with the lone pair of the nitroxide oxygen. In the π H-bond, the hydroxyl proton is located directly above the $2p_z$ orbital of oxygen (π(O) type) or nitrogen atom (π(N) type) with the OH bond axis perpendicular to the nitroxide plane. Nevertheless, based on NMR results, no consensus in terms of geometry of the formed H-bond was achieved, with contradictory interpretations of the results presented [8;11].

The formation of H-bonds between nitroxides and protic solvents has been implicated in many liquid-state cw EPR studies based on the comparison of isotropic g_{iso} and A_{iso} magnetic parameters in

protic and aprotic solvents of similar polarity [23;24]. However, up-to-date only a single study attempted a direct characterization of spin populations resolved in high-field/high-frequency cw EPR spectra, by measuring the anisotropic hyperfine interaction between the electron spin with the nuclear spin of the H-bond donor molecule. This was shown for 5-doxyl stearic acid (5-DSA), a typical spin probe used in EPR studies of phospholipid bilayers, that was dissolved in a series of aliphatic alcohols [25]. This is opposed to another system where H-bonds are formed between open- and closed-shell molecules, i.e. quinone anion radicals dissolved in organic ligands. This is a well-studied system, both experimentally [26] and theoretically [27;28].

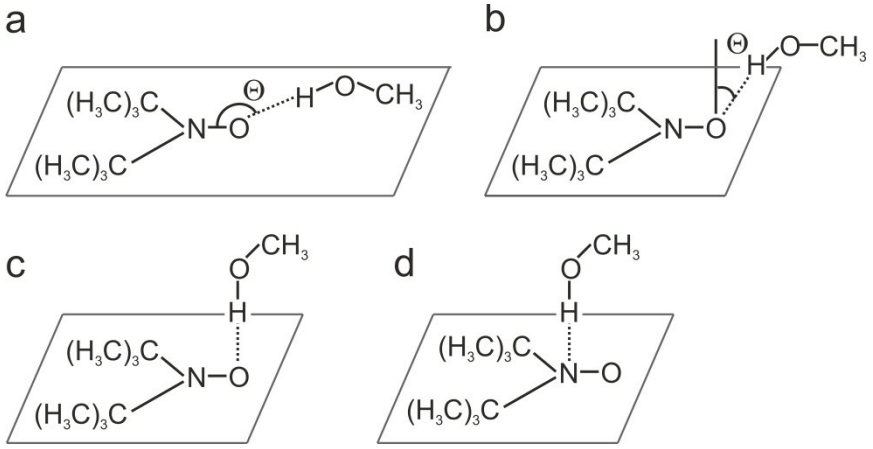

Figure 5.1 *Models of the hydrogen-bonded DMNO/methanol bimolecular system with various configurations: a) σ(θ) type, b) π(θ) type, c) π(O) type and d) π(N) type.*

In the previous chapter it was shown, that for nitroxide radicals dissolved in protic 2-propanol, heterogeneity of g_{xx}, A_{zz} is present that can be resolved using the W-band EDNMR technique. The distinct A_{zz} values describe nitroxide radical populations that sense different local environments. As a continuation of that work, several protic solvents were chosen that represent the most abundant H-bond donor groups of amino acid side chains in proteins, e.g. the OH group attached to an aliphatic chain or aromatic ring. The number and fractions of different nitroxide radical populations in each solvent studied was characterized. Using both W-band EDNMR and 244 GHz cw EPR allowed for extracting $A^{(i)}_{zz}$ and $g^{(i)}_{xx}$ parameters values. In this chapter, the nature of the observed spin probe populations is also clarified, especially whether they originate from specific interactions between nitroxides and protic solvents. The assignment of fractions corresponding to the H-bonded nitroxide is verified using the ENDOR technique. The assignment is based on the observation of the hyperfine interaction between the electron spin with the nuclei of proton donor molecule. Since the investigated spin probe corresponds to the head group of the widely used MTS spin label, the information on its H-bonding capabilities is relevant also for spin-labeled sites in proteins.

At W-band (95 GHz) the nitroxide g-tensor anisotropy is resolved. W-band ENDOR can be used not only to confirm the presence of a specific interaction but also to determine the geometry of the formed H-bonds. A similar approach was applied in orientation-selective ENDOR studies of quinone radicals [26;28]. An experimental determination of precise magnetic parameters that characterize H-bonded and non-H-bonded nitroxides, is crucial for a critical evaluation of interaction parameters derived from *ab initio* or DFT calculations.

5.2 Materials and methods

Sample preparation

The molecular structure of nitroxide spin probe used, termed R1 (3-hydroxymethyl-2,2,5,5-tetramethylpyrrolin-1-oxyl), is shown in Fig. 4.1 in Chapter 4. The R1 radical in its perdeuterated form (R1-D_{16}) was used for 244 GHz cw EPR and W-band EDNMR measurements. The solvents glycerol-D_8, aniline-D_5, aniline-D_6 and phenol-D_6 were obtained from Sigma Aldrich and used without further purification. Benzene-D_6 was obtained from Deutero GmbH. *Ortho*-terphenyl-D_{14} (OTP-D_{14}) was supplied by Cambridge Isotope Laboratories. Methanol-D_4 was obtained from Euriso-Top GmbH. Table 5.1 presents an overview of the dielectric constants and dipole moments of the solvents studied. Spin probe R1-D_{16} was directly dissolved in glycerol-D_8 or in OTP-D_{14}/benzene-D_6 (50%/50% v/v) to a final concentration of about 1 mM. For studies in aniline and phenol solvents, the solution of about 1 mM nitroxide in OTP-D_{14}/benzene-D_6 was doped with 10% w/w of these solvents to maintain the glass forming properties of the solvent while negligibly diluting the spin probe. The sample solution was transferred into a Teflon sample holder for 244 GHz cw EPR measurements. For W-band measurements, the sample solution was transferred into a quartz capillary (I.D. = 0.6 mm). A glass-type frozen solution was obtained by transferring the sample into the precooled EPR cryostat at 90 K.

Table 5.1 *Physicochemical properties of the solvents studied (data based on http://www.engineeringtoolbox.com/liquid-dielectric-constants-d_1263.html).*

solvent	dielectric constant (ε) (temp. in °C)	dipole moment /D
OTP/benzene	2.3 (benzene) (20)	-
methanol	33.1 (20)	2.87 (20°C)
2-propanol	17.9 (-)	1.66 (30°C)
phenol	4.3 (10)	
aniline	7.3 (20)	1.55
H_2O	80.4 (20)	1.87 (20°C)
glycerol	42.5 (25)	2.6

W-band cw EPR

W-band cw EPR experiments were performed with the laboratory-built W-band spectrometer described previously [29;30], that operates at a mw frequency of about 95 GHz. For measurements at 90 K, the sample temperature was controlled by a temperature-stabilized nitrogen gas-flow cryostat. The external B_0 field was modulated at 8 kHz with an amplitude of 30 µT. Low mw power (< 1µW) incident on the critically coupled cavity (mw field amplitude $\omega_1 < 1.5 \cdot 10^5$ rad/s) was chosen to avoid saturation.

244 GHz cw EPR

244 GHz cw EPR spectra were recorded using the home-built HF-EPR spectrometer operating at 122 GHz or 244 GHz and equipped with a 12 T magnet [31]. A sample volume of 30-50 µl was used. The spectra were measured at 70 K or 90 K, as indicated, with a mw frequency of 243.767 GHz. All spectra were recorded over the same magnetic field range (field sweep 90 mT) at the same scan rate

(80 μT/s) with 4000 data points. The spectra were recorded at a mw power of 0.5 mW and modulation amplitude of 0.5 mT. The modulation frequency was set to 5 kHz. To calibrate the magnetic field sensed by the EPR sample, LiF:Li was used as a g-value marker, since its g-value is known to a high accuracy [32]. The magnetic field sweep linearity, was ensured by measuring the EPR lines of Mn^{2+} in a MgO powder sample (about 0.15% Mn^{2+}). Subsequently, the spectrum of nitroxide probe dissolved in aniline together with Mn^{2+}:MgO was recorded.

244 GHz cw EPR data analysis

The processing of the four-channel cw EPR signal (in-phase and out-of-phase modulation signals from two lock-in amplifiers) is necessary for each spectrum. It was done using the plugin available in the Kazan Viewer program. The two channels of each lock-in amplifier were combined in order to correct the field modulation phase. The resulting two traces were then combined to correct the microwave phase. Subsequently, field linearization was performed by polynomial fitting of the field axis produced by the Hall sensor, using a home-written routine in Matlab. The LiF:Li spectral line was fitted to a Lorentzian lineshape, yielding the resonance field B_0, see Fig. 5.1(a) (top).

Based on the known high-accuracy g-value of LiF:Li [32], $g_{LiF:Li} = 2.002293 \pm 0.000002$, and the microwave frequency, the magnetic field axis was shifted to match the theoretical resonance position of LiF:Li. Simultaneous recording of LiF:Li and Mn^{2+}:MgO samples, see Fig. 5.1, allowed for proper magnetic field sweep linearization in addition to the field axis shift. The expected Mn^{2+} line positions were calculated using the following equation (corrected for 2nd order hyperfine shift) [33]:

$$B_{m_I} = B_0 - a_{iso} \cdot m_I - \left(\frac{{a_{iso}}^2}{2} \cdot B_0\right) \cdot [I \cdot (I+1) - m_I^2] + (\alpha^2/B_0) \cdot \varepsilon \qquad \text{Eq. (5.24)}$$

where $a_{iso} = -8.706$ mT and $\alpha = 2$ are the isotropic hyperfine coupling constant and the cubic field parameters for Mn^{2+} in MgO, respectively. Resonance field position B_0 was calculated using $g = 2.00101 \pm 0.00005$ [33]. The Mn^{2+}:MgO experimental spectrum was compared with the calculated spectrum and the field axis was subsequently corrected to match the expected line separation due to hyperfine splitting. The obtained field axis was used for the spectrum of nitroxide spin probe R1-D_{16} dissolved in OTP/benzene with 10% (w/w) of aniline-D_5 and Mn^{2+}:MgO standard, see Fig. 5.1(b). The g_{zz}, $M_I = 0$ spectral line in the spin probe spectrum was fitted to a Gaussian lineshape. The calculated $g_{zz} = 2.002246 \pm 0.000002$ served as a reference point for all subsequently analyzed nitroxide spin probe spectra, providing reference for a linear field shift if necessary. After linearization, the magnetic field axis was used for all nitroxide cw EPR spectra since the same frequency, field sweep and B_0 were used in all measurements.

Since the 244 GHz cw EPR spectra might contain a minor contribution of dispersion signal, the simulation of the entire cw EPR spectrum was not undertaken, but only the g_{xx} spectral region was analyzed to extract the corresponding g_{xx} values. In detail, the g_{xx} spectral region was fitted with one to three Gaussian lines (in first-derivative form), depending on the number of observed spectral components. In most cases the shoulder of an additional Gaussian line was included in the fit to compensate for the residual contribution of the g_{yy} peak. All parameters, namely line positions, line widths and intensities were left unrestricted. The fitting was performed using home-written Matlab routines. The peak positions of Gaussian lines were then used to calculate the g_{xx} values of each spin

probe population and the area under each fitted curve as a measure of the fraction of each population. Additionally, the 'g-strain' was calculated based on Eq. 5.2 [34]:

$$B_{1/2}\,(strain) = \sqrt{\Delta B_{xx}^2 - \Delta B_{zz}^2} \qquad \text{Eq. (5.25)}$$

where ΔB_{xx} and ΔB_{zz} are the linewidths (FWHM) in the g_{xx} and g_{zz}, $M_I = 0$ spectral regions, respectively.

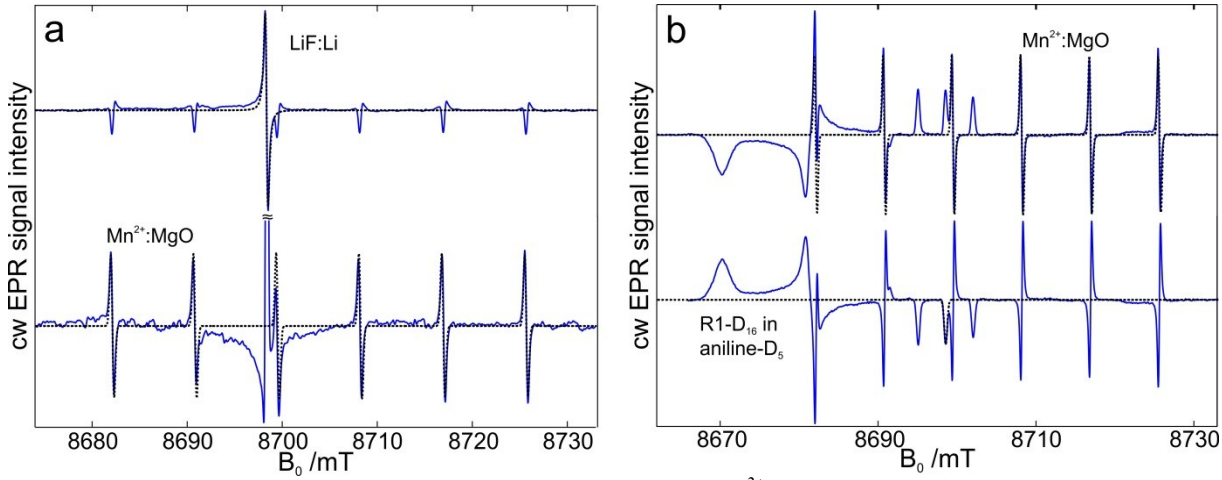

Figure 5.1 *(a) (top) 244 GHz cw EPR spectrum of LiF:Li and Mn^{2+}:MgO (blue trace) recorded at 70K. The spectrum is overlayed with a Lorentzian line fit to the LiF:Li spectral line (black dotted line). (bottom) 244 GHz cw EPR spectrum of LiF:Li and Mn^{2+}:MgO (blue trace) recorded at 70 K. The spectrum is overlayed with a Gaussian line fit to the Mn^{2+} spectrum (black dotted line). (b) (top) Simultaneous 244 GHz cw EPR spectrum of Mn^{2+}:MgO and of nitroxide R1-D_{16} (blue trace) dissolved in aniline-D_5, recorded at 70 K. The spectrum is overlayed with a Gaussian line fit to Mn^{2+} spectral lines (black dotted line). (bottom) Simultaneous 244 GHz cw EPR spectrum of Mn^{2+}:MgO and of nitroxide R1-D_{16} dissolved in aniline-D_5 (blue trace) recorded at 70 K. Spectrum is overlayed with a Gaussian line fit to the g_{zz}, $M_I = 0$ field region of the nitroxide EPR spectrum (black dotted line).*

W-band EDNMR and ENDOR

The pulsed EPR, EDNMR and ENDOR experiments were performed on a modified commercial W-band EPR spectrometer (Bruker Elexsys E680) operating at about 94 GHz [35]. The 2-pulse field-swept EPR spectra were acquired using the Hahn-echo pulse sequence (t_p)-τ-$(2t_p)$-τ-*echo*. A π/2 pulse length of 56 ns was generally used.

The EDNMR experiments were performed as described in Chapter 2.7.5. In general, the HTA pulse length was set to 1.6 µs at $2.6 \cdot 10^7$ rad/s mw field amplitude. A pulse length for the detection π/2 pulse, t_p = 100 ns, and a pulse separation, τ = 1 µs, were generally used. The echo was integrated over 1.4 µs around its maximum for optimal resolution.

The proton ENDOR experiments were performed using a Davies-type pulse sequence with selective π pulse length of 128 ns. The deuterium ENDOR experiments were performed using a Mims-type pulse sequence with π/2 pulse length of 24 ns and rf pulse length of t_{RF} = 30 µs. For recording the 2-dimensional ENDOR surfaces, the ENDOR spectra were usually taken at 40 field positions.

5.3 244 GHz cw EPR on nitroxide dissolved in various solvents

Figure 5.2(a) presents W-band cw EPR spectra of the R1-D_{16} nitroxide radical measured at 90 K in frozen OTP-D_{14}, methanol-D_4 and phenol-D_6 solutions. The spectra exhibit the typical powder

pattern lineshape expected for a dilute distribution of nitroxides. They are clearly resolved into three separate regions corresponding to the principal values of the g-tensor, g_{xx}, g_{yy} and g_{zz}. By reducing the inhomogeneous linewidth through perdeuteration of the nitroxide radical, the nitrogen hyperfine splitting in all g-regions of the nitroxide cw EPR spectrum in the OTP-D_{14} host matrix can be observed. The R1-D_{16} spectrum in frozen solution of OTP-D_{14} can be simulated with a single set of magnetic parameters, i.e., *g*-tensor, nitrogen hyperfine tensor, homogeneous EPR linewidth as well as orientation dependent EPR inhomogeneous linewidths, which were previously reported [35;36]. Similarly, for R1-D_{16} dissolved in methanol-D_4, a single set of magnetic parameters is sufficient to simulate the W-band EPR spectrum satisfactorily. Hence, only a single nitroxide radical population is present. A different situation is observed for R1-D_{16} dissolved in phenol-D_6. In the g_{zz}, $M_I = \pm 1$ spectral regions, two, partially resolved nitrogen hyperfine lines of various widths can be recognized. The linewidth of 5.3 MHz (FWHM) for the line corresponding to the smaller A_{zz} value is significantly smaller than for the line corresponding to the larger A_{zz} value with a width of 12.3 MHz, both determined at the g_{zz}, $M_I = -1$ spectral position. These two hyperfine coupling components indicate the presence of two spin probe populations, each described with a different set of magnetic parameters. Indeed, in the g_{xx}-region the presence of nitroxide fractions with different g_{xx} values can be inferred. However, due to the poor spectral resolution the accuracy of the extracted $g_{xx}^{(i)}$ values is limited.

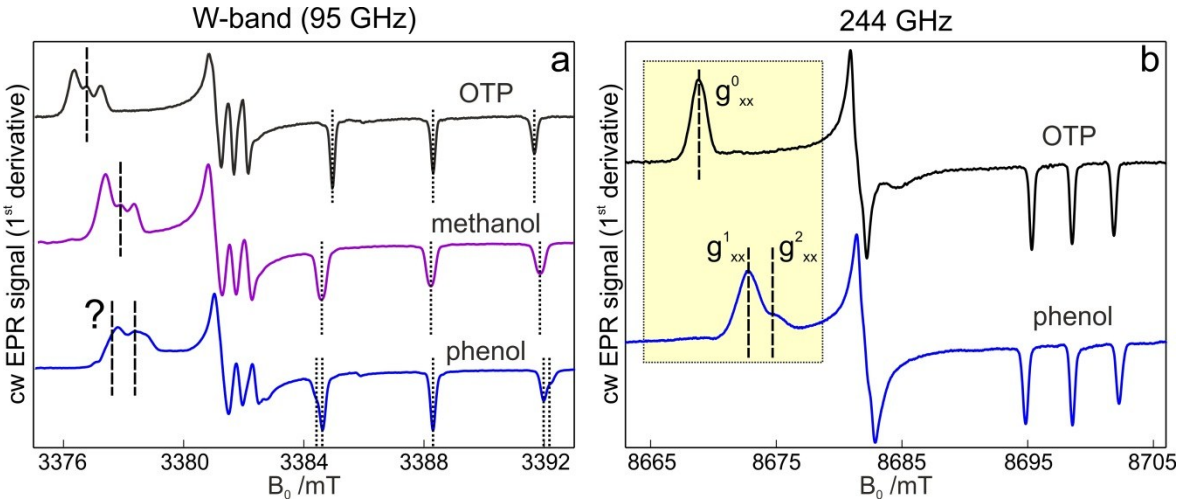

Figure 5.2 *Comparison of the experimental (a) W-band (95 GHz) and (b) 244 GHz cw EPR spectra of nitroxide radical R1-D_{16} in frozen solutions of OTP-D_{14} (black trace), methanol-D_3 (purple trace) and phenol-D_6 (blue trace) taken at 90 K (except for methanol-D_3 that was measured at 70 K). The spectral positions that correspond to different principal g-tensor and A_{zz} values are indicated by dashed and dotted lines, respectively.*

To yield unambiguous information on the presence of different nitroxide sub-ensembles in various protic solvents it is necessary to record cw EPR spectra at higher field/frequency to increase the spectral resolution of the g-axis. Therefore, 244 GHz cw EPR spectra were recorded for R1-D_{16} dissolved in a series of protic solvents and additionally, as a reference system, in OTP-D_{14} that is apolar and aprotic. Figure 5.2(b) shows examples of 244 GHz cw EPR spectra of R1-D_{16} measured at 70 K in frozen solutions of OTP-D_{14} and phenol-D_6. For R1-D_{16} dissolved in OTP-D_{14} matrix, the information content of the 244 GHz cw EPR spectrum is not increased as compared to the W-band cw

EPR spectrum. On the contrary, the nitrogen hyperfine splittings in the g_{xx} and g_{yy} regions are no longer resolved due to an increased contribution of 'g-strain' to the linewidth at higher Zeeman field. A single Gaussian line satisfactorily fits the spectrum in the g_{xx} spectral region, corroborating the presence of a single nitroxide radical population. A different situation is observed for nitroxide dissolved in phenol-D_6, where in the g_{xx} region higher g-axis resolution allows to partially resolve two spectral contributions that do not derive from nitrogen hyperfine or quadrupole splittings. The corresponding $g_{xx}^{(i)}$ values can be extracted with higher accuracy, as compared to the analysis of W-band cw EPR spectrum, see Table 5.2. However, the increased linewidth due to 'g-strain' masks the splitting of EPR lines in the g_{zz}, $M_I=\pm1$ spectral region that derives from two distinct A_{zz} values describing distinct spin probe populations.

Figure 5.3 shows a detailed view of the g_{xx} spectral region for nitroxide radical dissolved in all the solvents studied, together with fitted Gaussian lines. As clearly visible, the number and position of lines in the g_{xx} spectral region varies, depending on the host matrix used. The improved g-axis resolution not only confirms the presence of various nitroxide sub-ensembles, but importantly allows to extract precise $g_{xx}^{(i)}$ values and their distribution based on a linewidth analysis. The results in terms of evaluated $g_{xx}^{(i)}$ values and fractions of distinct spin probe populations are summarized in Table 5.2.

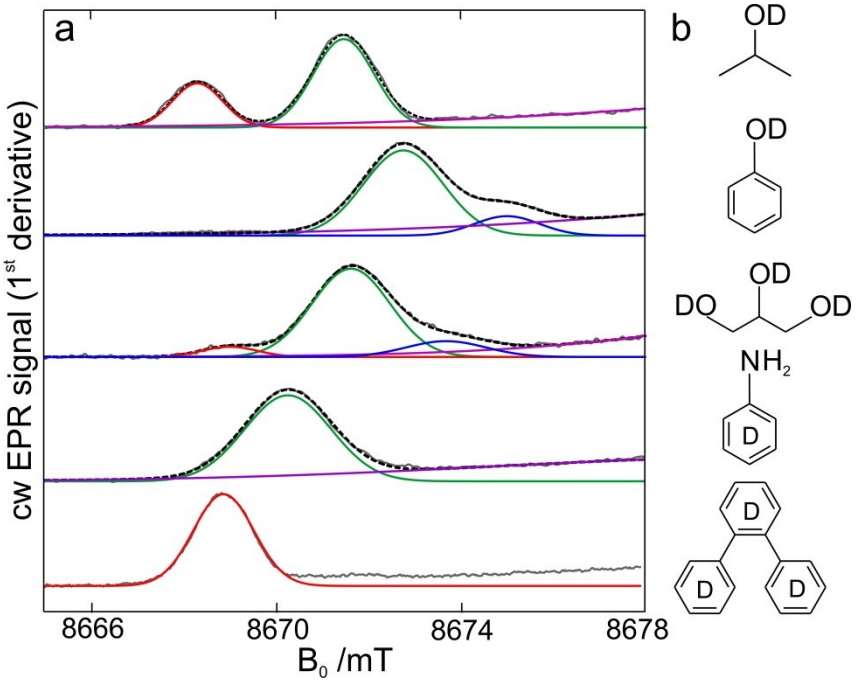

Figure 5.3 *(a) Comparison of the g_{xx} region of 244 GHz cw EPR spectra of nitroxide radical R1-D_{16} in frozen solutions of (from top to bottom) 2-propanol-D_8, phenol-D_6, glycerol-D_8, aniline-D_5 and OTP-D_{14}. The spectra were recorded at 70 K. The spectral range presented is indicated by the shaded area in Fig. 5.2(b). (b) Molecular structure of solvents used as hosts for diluted nitroxide solutions.*

For the OTP-D_{14} matrix, which is apolar and non-protic, only a single nitroxide spin population is present and, consequently, only a single Gaussian line is necessary to satisfactorily reproduce the g_{xx}-region of the 244 GHz cw EPR spectrum. Similarly, for the aniline-D_5 matrix only a single g_{xx} component is observed. However, it is shifted to lower g_{xx} values and, additionally, is broader as compared to OTP-D_{14} with the linewidths (FWHM) of 61.6 MHz and 43 MHz, respectively. The shift

is expected to originate from specific interactions between the nitroxide N-O• group and protons of the $–NH_2$ group in aniline, i.e. from H-bond formation, although a minor contribution to the line shift can originate from the slight polarity difference between both solvents. Indeed, the formation of H-bonded complexes of nitroxide and aniline molecules was previously implicated based on contact shift data and proton relaxation rates measured using NMR [16]. In glycerol-D_8 solvent, three nitroxide populations have to be included in the fit to the g_{xx}-region of the 244 GHz EPR spectrum. One predominant fraction is present that comprises about 80% of the total signal intensity in this spectral region. This main component can be tentatively assigned to a nitroxide population that forms a single H-bond with the OH group of glycerol. It is described with a $g_{xx}^{(1)}$ value of 2.008456±0.00005, i.e. shifted to lower g_{xx} as compared to aniline. Additionally, a small nitroxide radical fraction with lower $g_{xx}^{(2)}$ is present, most likely originating from nitroxides that form two H-bonds with either glycerol molecules or with trace amounts of water admixed to the glycerol. The latter explanation is more likely, since molecular dynamics simulations predict water to be the only solvent that can form two H-bonds with nitroxide, owing to the smallest steric hindrance imposed. In addition to those two fractions, a third small contribution is seen in the g_{xx} spectral region of the 244 GHz spectrum. This third population is described with the largest $g_{xx}^{(0)}$ that is close to the value obtained in the OTP-D_{14} solvent, indicating no H-bond (see Table 5.2).

Table 5.2 *Summary of spectral parameters extracted from analysis of low-temperature 244 GHz EPR spectra of R1-D_{16} dissolved in various solvents. The values of $g_{xx}^{(i)}$ and of $fr^{(i)}$ (i = 0,1,2) are obtained from the Gaussian fit of the g_{xx}-region of the 244 GHz spectra. The g-values are presented as deviations from g = 2 in units of 10^{-5}. The absolute error of g-values is ±5 × 10^{-5} and the error for the g-value difference is ±2 × 10^{-5}.*

solvent	$g_{xx}^{(1)}$	$g_{xx}^{(2)}$	$fr^{(1)}$	$fr^{(2)}$	$\Delta B_{1/2}$ /MHz [b]	g-strain of 1 [c]	g-strain of 2 [c]
OTP-D_{14}	910.5	-	1	-	11.5	3.43	-
glycerol-D_8	845.6	798.7 907.0 [d]	0.79	0.06 0.15	13.8	4.44	-
2-propanol-D_8	923.1	854.5	0.29	0.71	8.6	2.65	3.28
aniline-D_5	877.3	-	1	-	13.5	4.71	-
phenol-D_6	819.9	767.9	0.84	0.16	13.6	4.69	3.82

a) value after subtraction from -2/10^{-5}
b) the inhomogeneous (FWHM) linewidth obtained at the g_{zz}, $M_I = 0$ spectral position from the 244 GHz EPR spectrum at 70 K or 90 K.
c) divided by/10^{-4}
d) this additional fraction is assumed to originate from formation of two H-bonds

In fact, it has been reported that the ratio between two nitroxide radical fractions in alcohol solvents varies depending on the length of the alcohol aliphatic chain, possibly due to increasing steric

hindrance [1;2]. Hence it most likely corresponds to nitroxide radicals lacking specific interactions with the solvent. In 2-propanol-D_8, two Gaussian lines described by two different g_{xx} values are resolved in the g_{xx} spectral region of the 244 GHz EPR spectrum, in agreement with W-band cw EPR spectra shown in Chapter 4. The difference of about $670 \cdot 10^{-6}$ between both g_{xx} values is similar to the case of glycerol, suggesting a similar nature of both components in these two solvents. These can be tentatively assigned to a nitroxide forming a single H-bond (smaller $g_{xx}^{(1)}$) and lacking specific interactions with the solvent (larger g_{xx}^{0} value). The nitroxide population described by $g_{xx}^{(1)}$ in 2-propanol-D_8 comprises 70% of the total nitroxide population, as opposed to the situation in methanol-D_4 where all nitroxide radicals could be described with a single g_{xx} of similar value. In phenol-D_6, two Gaussian lines are necessary to reproduce the g_{xx} spectral region with a nitroxide radical population of larger g_{xx}^{1} value, it comprises ca. 84% of the spectral intensity in the g_{xx}-region. The two spin probe populations show slightly different linewidths. The population of the smaller $g_{xx}^{(2)}$ value shows a larger distribution of the g_{xx} values, being broader by $\Delta B_{½}$=3.7 MHz. While previously nitroxides were postulated to form H-bonds with phenol molecules based on RT cw EPR spectra [19;21], a detailed assignment of the two spin probe populations is not obvious. At this point it can only be speculated that the fraction described by $g_{xx}^{(2)}$ possibly originates from nitroxides forming a single H-bond with the OH group of phenol. It is unlikely that $g_{xx}^{(2)}$ describes nitroxides forming simultaneously two H-bonds with two phenol molecules due to steric hindrance. The nature of nitroxide-phenol interactions for both spin probe populations is discussed in more detail below.

5.4 W-band EDNMR on nitroxide radical dissolved in various protic solvents

To characterize the heterogeneity of the nitroxide local environment by means of A_{zz} values, W-band EDNMR spectra were recorded for R1-D_{16} dissolved in protic solvents described above. Fig. 5.4(b) shows an example of experimental W-band EDNMR recordings for R1-D_{16} dissolved in phenol-D_6 as a function of the external magnetic field.

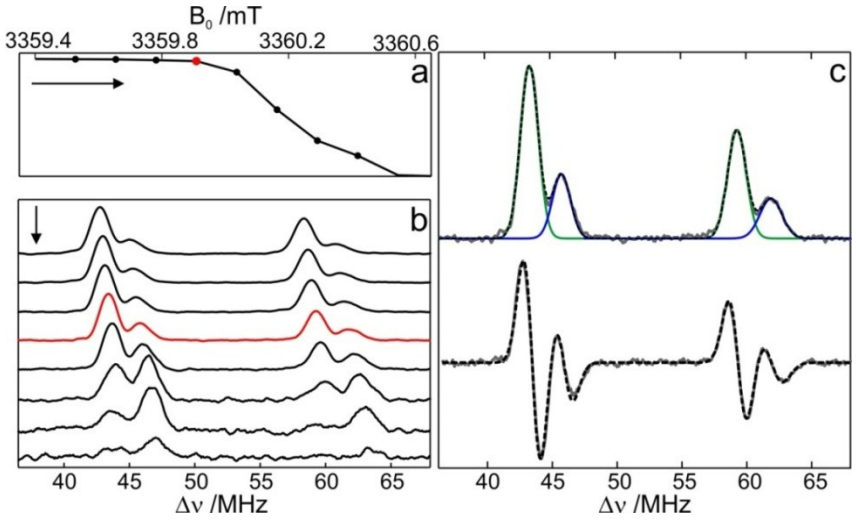

Figure 5.4 *W-band EDNMR spectrum of R1-D_{16} in phenol-D_6 at 50 K. (a) The EPR intensity around the g_{zz}, M_I = -1 spectral position with indicated magnetic field positions of individual EDNMR recordings. (b) Individual EDNMR recordings at magnetic field positions indicated in (a). (c) (top) Example of best-fit Gaussian line (black dotted trace) to the experimental EDNMR spectrum (grey trace) marked in red (b). The two fitted components are marked in blue and green. (bottom) Experimental spectrum, as marked in red in (b), overlayed with the best-fit performed in the first derivative mode (black dotted trace).*

The spectra were recorded in the g_{zz}, $M_I = -1$ spectral region where ^{14}N EDNMR lines appear in the 35-70 MHz frequency range. To obtain the hyperfine and quadrupole parameters for the nitroxide radical dissolved in each of the solvents, EDNMR recordings at each magnetic field position were analysed using either one or two pairs of Gaussian lines depending on the number of distinct spin probe populations present. Figure 5.4(c) shows an example of the best fit to the experimental W-band EDNMR trace for R1-D_{16} dissolved in phenol-D_6 in the first-derivative (bottom) and absorption (top) mode. For extracting the principal A_{zz} values, the line positions in the frequency dimension were interpolated to the corresponding g_{zz}, $M_I = -1$ canonical field positions as described in Chapter 4. Fig. 5.5 presents the W-band EDNMR spectra recorded close to the respective canonical positions in the g_{zz}, $M_I = -1$ spectral region for R1-D_{16} dissolved in the studied solvents. The spectra are overlayed with their best-fit using Gaussian lines. The fitting results in terms of $A^{(i)}_{zz}$ values and respective fractions ($fr^{(i)}$) of distinct spin probe populations are collected in Table 5.3. Overall, the number of nitroxide spin probe fractions characterized by different A_{zz} values as resolved in W-band EDNMR spectra, is in agreement with 244 GHz EPR results.

In detail, in OTP-D_{14}, aniline-D_5 and methanol-D_4 only a single pair of lines is observed in the EDNMR recordings, i.e. only a single nitroxide radical population is present. The lines are centered around different A_{zz} values which increase in the order A_{zz}(OTP-D_{14})<A_{zz}(aniline-D_5)<A_{zz}(methanol-D_4). Based on the dielectric constants and dipole moments of these solvents, this trend is expected, see Table 5.1. Moreover, similar to the cw EPR results, the EDNMR linewidth for R_1-D_{16} dissolved in aniline-D_5 is broadened as compared to OTP-D_{14} and methanol-D_4, see Table 5.3.

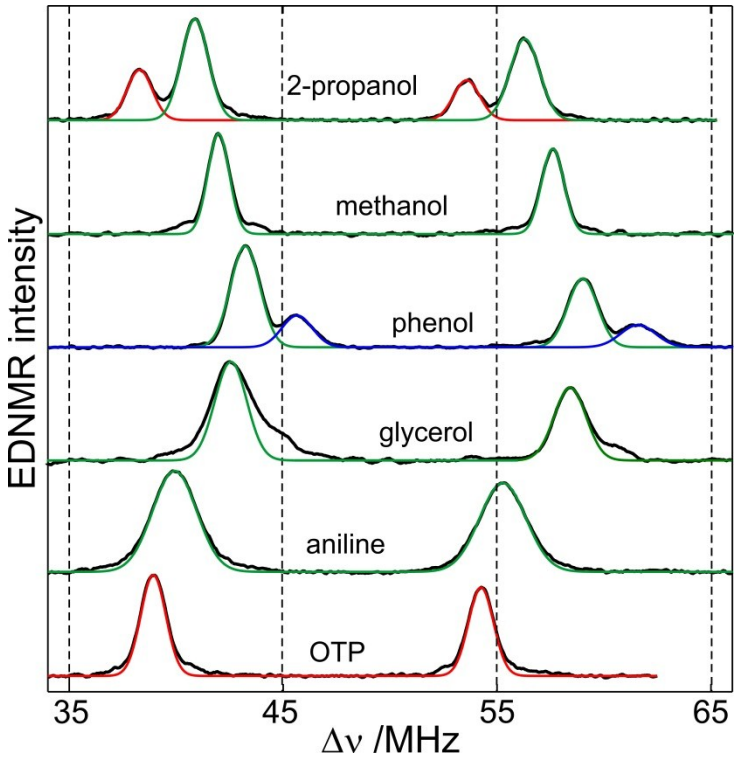

Figure 5.5 *Comparison of W-band EDNMR spectra of nitroxide radical R1-D_{16} in frozen solutions of (from top to bottom) 2-propanol-D_8, methanol-D_4, phenol-D_6, glycerol-D_8, aniline-D_5 and OTP-D_{14}. The spectra were recorded close to the g_{zz}, $M_I = -1$ spectral position at 50 K. The experimental spectra (black traces) are overlayed with best-fit Gaussian lines that are tentatively assigned to nitroxide radicals forming either zero (red trace), one (green trace) or two (blue trace) H-bonds with the solvent molecules. The fits were performed in the first derivative mode of the experimental traces.*

Since the nitroxide radical was implicated to form H-bonds with aniline [16], such a significant distribution of A_{zz} values is presumably due to the presence of other nitroxide:aniline H-bond geometries that have similar energy. In case of R_1-D_{16} dissolved in 2-propanol, two pairs of lines are present in W-band EDNMR recordings, as was shown in Chapter 4. The comparison with spectra recorded in apolar, aprotic OTP-D_{14} and protic, polar methanol-D_4, supports the tentative assignment of two nitroxide fractions present in the 2-propanol-D_8 solvent. Indeed, $A_{zz}^{(0)}$ in 2-propanol is close to the $A_{zz}^{(0)}$ value obtained for R_1-D_{16} dissolved in OTP-D_{14}, while $A_{zz}^{(1)}$ is essentially the same as the hyperfine constant in methanol-D_4, see Table 5.3. The nitroxide population described by $A_{zz}^{(1)}$ in 2-propanol most likely forms H-bonds with solvent molecules while the population described by $A_{zz}^{(0)}$ lacks specific interactions with the solvent. The presence of a single nitroxide population in methanol is in agreement with theoretical predictions [37], according to which all nitroxide molecules are preferentially H-bonded with methanol molecules. The decrease in the ratio of H-bonded nitroxides in 2-propanol is explained by steric hindrance: the bulky CH_3 groups of the alcohol reduce the space available to the nitroxide molecules for accessing the hydroxyl proton. In glycerol-D_8, a predominant nitroxide population with $A_{zz} = 101.9$ MHz is present. Shoulders around both low- and high-frequency EDNMR lines suggest the presence of residual nitroxide fractions, in agreement with cw EPR results, but these shoulders could not be reliably analyzed in the EDNMR recordings.

Table 5.3 *Summary of data for R1-D_{16} nitroxide radicals dissolved in the listed solvent. The values of $A^{(i)}{}_{zz}$ and $fr^{(i)}$ (i = 0,1,2) are extracted from the Gaussian fits of ^{14}N lines in the g_{zz} M_I = -1 spectral region of the W-band EDNMR spectra. The errors of the A -values are ±0.1 MHz.*

	OTP-D_{14}	aniline-D_5	methanol-D_4	2-propanol-D_8	phenol-D_6	glycerol-D_8
$\Delta\nu_{1/2}{}^{(0)}$ /MHz	1.20	–	–	1.39	–	–
$\Delta\nu_{1/2}{}^{(1)}$ /MHz	–	2.55	1.25	1.45	1.64	1.75
$\Delta\nu_{1/2}{}^{(2)}$ /MHz	–	–	–	–	1.94	–
$A_{zz}^{(0)}$ /MHz	94.70	–	–	93.13	–	–
$A_{zz}^{(1)}$ /MHz	–	98.3	100.87	99.43	103.84	101.9
$A_{zz}^{(2)}$ /MHz	–	–	–	–	109.82	–
$P^{(0)}{}_{zz}$	-1.74	–	–	-1.75	–	–
$P^{(1)}{}_{zz}$	–	-1.64	-1.60	-1.63	-1.57	-1.59
$P^{(2)}{}_{zz}$	–	–	–	–	-1.46	–

In the last solvent studied, phenol-D_6, two nitroxide populations, that is two pairs of lines, are resolved in the W-band EDNMR spectra. The pair of lines centered about the smaller A_{zz} value is expected to originate from a nitroxide radical fraction that forms a single H-bond with the hydroxyl group of phenol. The observed shift to even higher A_{zz} values, as compared to methanol and 2-propanol, is most likely due to additional electron spin density originating from phenol as a conjugated π-system. The pair of lines centered about the larger A_{zz} value, can in this case be explained only by simultaneous formation of two H-bonds, but most likely not with two different

phenol molecules, as was discussed above. Similar to cw EPR spectra, the two EDNMR spectral components exhibit different linewidths, i.e. the larger distribution in $A_{zz}^{(2)}$ values suggests a larger distribution of H-bond geometries for this nitroxide population.

In addition to ^{14}N hyperfine coupling constants, precise $P_{zz}^{(i)}$ values could be obtained, each describing a resolved spin probe populations in the studied solvents, see Table 5.3. The quadrupole coupling constant, P_{yy}, was shown to have the same microenvironment probing properties as g_{xx} and A_{zz} and, additionally, to be exclusively sensitive to the electric field gradient in the vicinity of the nitrogen [36]. In contrast to the hyperfine coupling constant A_{zz}, the P_{zz} values for the nitroxide probe are rather insensitive to specific interactions with the solvent: The nitroxide dissolved in OTP-D_{14} and fraction (1) in 2-propanol have very similar P_{zz} values of ca. -1.75 MHz. Analogously, for nitroxide presumably forming a single H-bond with the solvent molecule, P_{zz} values are grouped around - 1.62 MHz, see Table 5.3.

The possibility to access, for the first time, experimentally the A_{zz} heterogeneity in a series of protic solvents, allows for a re-examination of reported g_{xx} vs. A_{zz} dependences. Fig. 5.6 presents the plot of $g_{xx}^{(i)}$ vs $A_{zz}^{(i)}$ for the protic solvents studied. Clearly three groups of points can be distinguished that correspond to resolved magnetic parameters of distinct spectral components: (i) nitroxide spin populations lacking specific interactions with the solvent (marked in red), (ii) nitroxide radicals presumably forming a single H-bond with the solvent and (iii) nitroxide spectral components described by $A_{zz}^{(2)}$ and $P_{zz}^{(2)}$ in phenol, likely to form two H-bonds with the solvent. To support the assignment of the nitroxide sub-ensembles, supplementary ENDOR measurements were performed, that allow to directly probe the hyperfine interaction of the electron spin with a proton of the solvent molecule that participates in the H-bond formation with the N-O· group. A similar correlation is observed for the $A_{zz}^{(i)}$ and $P_{zz}^{(i)}$ magnetic parameters.

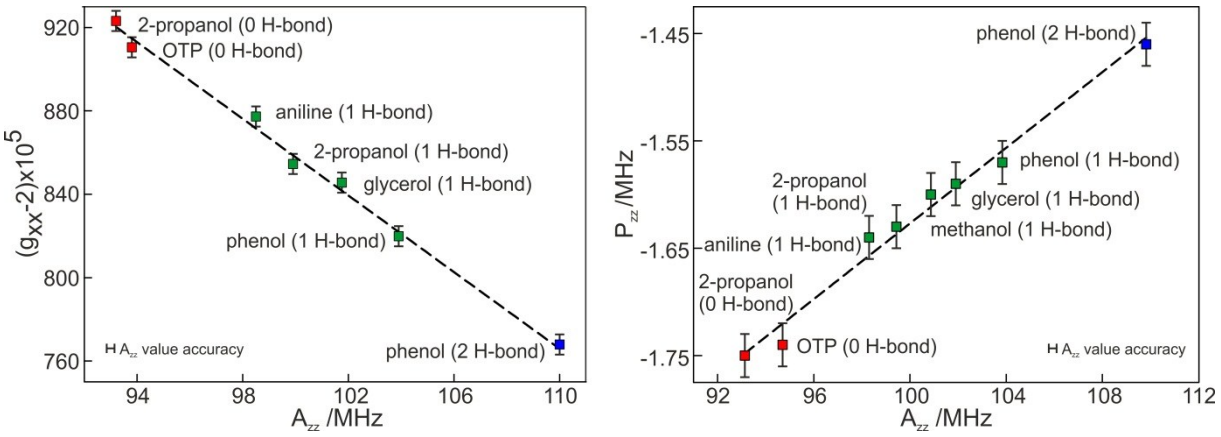

Figure 5.6 *The g_{xx} vs A_{zz} plot for the studied solvents using g_{xx} values extracted from the 244 GHz cw EPR spectra analysis and A_{zz} values obtained from W-band EDNMR recordings.*

5.5 W-band ENDOR on nitroxide spin probes dissolved in various protic solvents

The solvation of nitroxide radicals by solvent molecules is accompanied by a delocalization of the unpaired electron into the solvent molecule, resulting in the appearance of hyperfine interaction with the solvent nuclei. At 95 GHz high-field/high-frequency ENDOR the nuclear Larmor frequencies of ^{1}H (≈141 MHz) and ^{2}H (≈22 MHz) are well separated from each other, so that the

ENDOR spectra of weakly coupled protons and deuterons do not overlap. Therefore, to selectively probe the specific interaction of the nitroxide with a protic solvent, selective isotope labeling of the H-bond donor group was employed. For example, for R_1-D_{16} dissolved in methanol-D_3 (CD_3OH), only OH protons of methanol contribute to the proton ENDOR spectrum. Conversely, for R1-H_{15} dissolved in methanol-D_1 (CH_3OD), only deuterium in the OD group is probed in a deuterium ENDOR experiment, yielding additional information on the deuterium quadrupole coupling constant. For a weakly coupled proton, the ENDOR lines are centered around the ^{1}H Larmor frequency and are split by the hyperfine coupling constant, A, as described in Chapter 2.1.4. The field-frequency ENDOR spectra are shown in a contour plot representation with the ^{1}H Larmor frequency subtracted from the nuclear frequency axis.

The ENDOR spectra were first recorded for R1-D_{16} dissolved in methanol-D_3, since in this bimolecular system only a single spectral component is present both in the 244 GHz cw EPR and W-band EDNMR spectra. Figure 5.7(a) shows the W-band proton Davies ENDOR spectrum of R1-D_{16} dissolved in methanol-D_3. At each spectral position, the ENDOR spectrum is a superposition of the signal originating from solvent protons beyond the first coordination sphere to the NO· group, i.e. the ENDOR spectrum reveals 'matrix' protons [38] that appear around the proton Larmor frequency, and symmetrically displaced signals that originates from coupled ‘inner’ protons. The presence of a coupled ‘inner’ proton is a direct proof of the H-bond formation between the nitroxide radical and the hydroxyl group of methanol: it originates from the delocalization of electron spin density from the NO· group to the proton of the diamagnetic solvent molecule through H-bond formation. From the field-frequency dependence of the proton ENDOR signal it becomes apparent that the hyperfine coupling constant is mostly anisotropic, i.e. the observed hyperfine coupling constant varies with the spectral position within the nitroxide EPR spectrum.

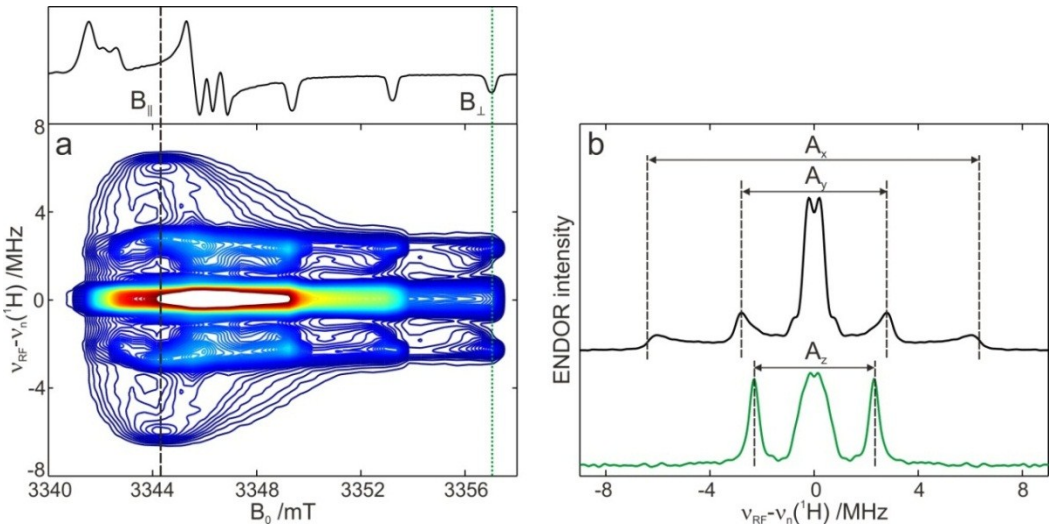

Figure 5.7 *(a) Field-frequency dependence of the experimental W-band proton Davies ENDOR of 1 mM R1-D_{16} in methanol-D_3(OH) glass at 60 K. The contour lines are shown as isohypses from 0.05 to 0.9 of the maximum ENDOR intensity. The trace on the top shows the 2-pulse echo-detected W-band EPR spectra in the absorption and first-derivative form. The pulse settings of Davies type ENDOR experiment are t_π(pump)=200 ns, t_{RF}=20 µs, $t_{\pi/2}$ = 32 ns, averages per point =160, pulse repetition rate=500 Hz, number of field points 40. (b) Experimental W-band proton Davies ENDOR of 1 mM R1-D_{16} in methanol-D_3(OH) glass at 60 K recorded at two spectral positions, $B_\parallel$ and $B_\perp$ indicated in (a).*

The anisotropic part of the hyperfine coupling tensor, which arises from the dipolar interaction between the unpaired electron and the proton within the framework of the point-dipole approximation is given by [39]:

$$T_i = \frac{g\beta g_n \beta_n}{hr^3}\rho(3cos^2\theta - 1) = \frac{79.2}{r^3}\rho(3cos^2\theta - 1) \qquad \text{Eq. (5.3)}$$

where g and g_n are the electron and nuclear g-values, θ is the angle between the applied field and the direction of the H-bond, ρ = 0.40 ± 0.2 is the unpaired electron spin density on the oxygen atom, and r is the length of the H-bond (measured in Å). The traceless dipolar hyperfine coupling tensor resulting from this approximation is axially symmetric with parallel $v(\theta=0)=v_{\parallel}=2T$ and perpendicular $v(\theta=90°)=v_{\perp}=-T$ components.

The orientation selection in solid-state EPR experiments is given by:

$$g(\theta_A, \varphi_A)^2 = \left(g_{xx}^2 \cdot \cos^2\varphi_A + g_{yy}^2 \cdot \sin^2\varphi_A\right) \cdot \sin^2\theta_A + g_{zz}^2 \cdot \cos^2\theta_A \qquad \text{Eq. (5.4)}$$

The angles θ_A and φ_A that describe the orientation of the external magnetic field with respect to the molecular coordinate system of the nitroxide radical are shown in Fig. 5.8. Therefore, by performing the measurement at the g_{xx}, g_{yy} or g_{zz} spectral positions, subsets of nitroxide molecules are selected for which the external magnetic field is directed along the x, y or z axes of the nitroxide molecular coordinate system, respectively.

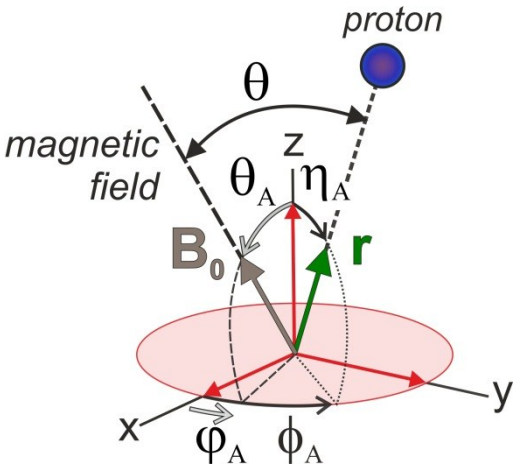

Figure 5.8 *Definition of angles describing the orientation of the external magnetic field* $\vec{B}_0$ *(grey arrow) with respect to the molecular axes frame of the nitroxide radical and the orientation of the electron-nuclear dipolar vector (green arrow) with respect to* $\vec{B}_0$.

Since the perpendicular hyperfine component (θ=90°) in the field-frequency deuterium ENDOR for R1-D_{16} in methanol-D_3 appears in the g_{zz} spectral region where the external magnetic field is directed along the z axis (i.e. θ_A=90°, η_A=0°), it can be immediately concluded that the proton of the methanol hydroxyl group lies in the xy-plane of the nitroxide ring. Hence, the nitroxide:methanol H-bonded complex has σ-type geometry.

The parallel dipolar coupling frequency, on the other hand, appears at a magnetic field value $B_{\parallel}$ that is shifted with respect to the canonical g_{xx} spectral position towards the g_{yy} spectral region. At this parallel field, those orientations of the nitroxide molecules are selected for which the field director is tilted by the azimuth angle φ from the x-axis in the xy plane of the nitroxide ring. The parallel hyperfine response appears at the unique parallel EPR resonance field position:

$$B_{\parallel} = \frac{h \cdot v}{g(\theta = 0°, \varphi) \cdot \beta} \qquad \text{Eq. (5.5)}$$

where the electron-nuclear dipolar vector coincides with the direction of the external magnetic field (θ=0°). Since the hydrogen-bonded proton lies in the xy plane of the g-tensor frame, Eq. 5.3 simplifies to:

$$g_{xx}^2 \cdot cos^2\varphi + g_{yy}^2 \cdot sin^2\varphi = (\frac{\beta \cdot B_{\parallel}}{h \cdot v})^2 \qquad \text{Eq. (5.6)}$$

The EPR resonance conditions for g_{xx} and g_{yy} principal components are given by: $h \cdot v = g_{xx(yy)} \cdot \beta \cdot B_{xx(yy)}$. Taking that into account, the azimuth angle φ that describes the tilting of the O…H-O bond from the x-axis (directed along the NO· group) can be calculated from the ratio of the resonance field differences:

$$sin^2\varphi = \frac{B_{\parallel} - B_{xx}}{B_{yy} - B_{xx}} \qquad \text{Eq. (5.7)}$$

From the evaluation of the B_{xx}, B_{yy} and $B_{\parallel}$ spectral field positions in the EPR spectrum, the φ angle can be determined. This is possible even without knowing the absolute magnetic field values – as long as the linearity of the magnetic field sweep is ensured. In the case of R1-D_{16} dissolved in methanol-D_3, the parallel hyperfine response occurs at $B_{\parallel}$ located between the B_{xx} and B_{yy} field positions; it is shifted by $B_{\parallel} - B_{xx}$=2.2 ± 0.2 mT from the g_{xx} resonance field position. The difference between the g_{xx} and g_{yy} resonance fields, $B_{yy} - B_{xx}$=4.2 ± 0.2 mT, was determined from the echo-detected EPR spectrum. Based on Eq. 5.7, $sin^2\varphi = 0.47 \pm 0.05$ providing the azimuth angle $\varphi = 45 \pm 3°$. The three principal hyperfine coupling components that are read out from the ENDOR spectra recorded at $B_{\parallel}$ and $B_{\perp}$ field positions are marked in Fig. 5.7(b) and listed in Table 5.4.

Table 5.4 *Magnetic parameters of H-bonded proton and deuterium obtained from analysis of W-band ENDOR spectra for R1-D_{16} nitroxide radicals dissolved in methanol. The accuracy of hyperfine coupling values is ±0.05 MHz.*

	CD_3OH	CH_3OD
$\|A_x\|$	4.6	0.709
$\|A_y\|$	5.58	0.878
$\|A_z\|$	12.79	1.973
P_x	-	0.051
Euler angles between A and g ^{1}H-bond	Θ=0, φ=45.7°	
Euler angles between A and g ^{2}H-bond	Θ=0, φ=46°	
P_y	-	0.050
P_z	-	0.101

When nitroxide R1-H_{15} is dissolved in methanol-D_1(OD), only the deuterons from D-bonds to the nitroxide NO· group are measured in the deuterium ENDOR experiment. The deuteron quadrupolar interaction, causes a splitting of the deuteron ENDOR lines by 3P, where P is the deuteron quadrupole constant, see Fig. 5.10. Due to this splitting of ENDOR lines, the hyperfine coupling constants could be evaluated at the $B_{\parallel}$ and $B_{\perp}$ field positions with higher accuracy, as compared to proton ENDOR. Table 5.4 summarizes the magnetic parameters evaluated for the

hydroxyl deuteron of methanol complexed to the nitroxide radical.To corroborate the assumption that the nitroxide population in 2-propanol, which is characterized by $g_{xx}^{(1)}$, A_{zz}^{1} and $P_{zz}^{(1)}$, originates from a nitroxide radical forming an H-bond with the hydroxyl group of the alcohol, ENDOR measurements were performed. In Fig. 5.11, the deuterium Mims ENDOR spectrum is shown for R1-H_{15} dissolved in 2-propanol-D_1(OD).

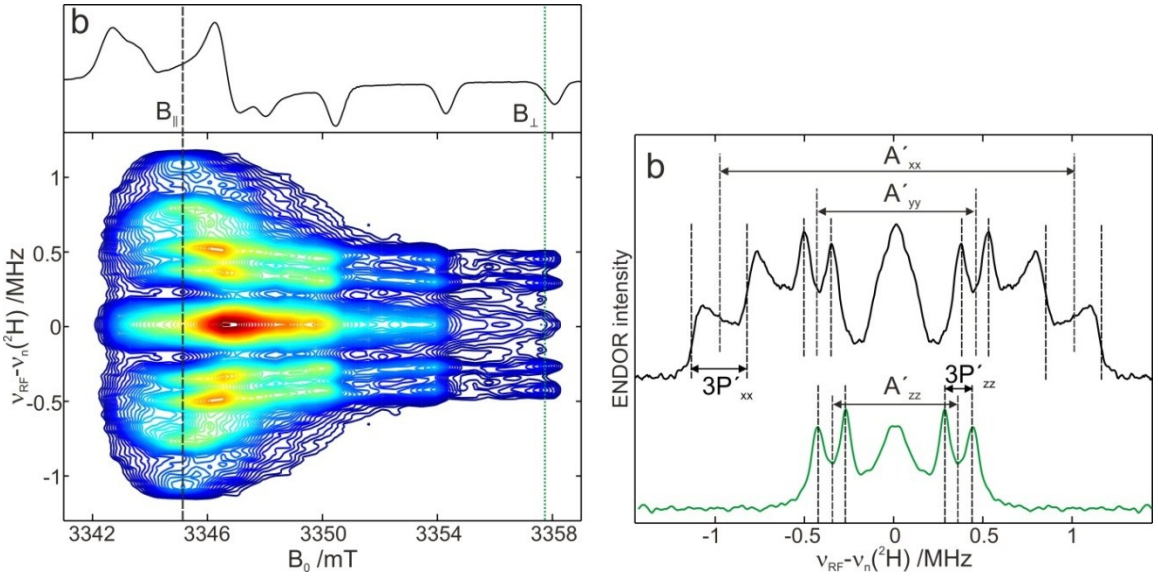

Figure 5.10 *(a) Frequency-field dependence of the experimental W-band deuterium Mims ENDOR of 1 mM R1-H_{16} in methanol-D_1(OD) glass at 60 K. The contour lines are shown as isohypses from 0.05 to 1 of the maximum ENDOR intensity. The trace on the top shows the 2-pulse echo-detected W-band EPR spectra in the first-derivative form. The pulse settings of the Mims type ENDOR experiment are t_π(pump)=200 ns, t_{RF}=20 µs, $t_{\pi/2}$ = 32 ns, averages per point =160, pulse repetition rate=500 Hz, number of field points 40. (b) Experimental W-band deuterium Mims ENDOR of 1 mM R1-H_{15} in methanol-D_1(OD) glass at 60 K recorded at two spectral positions, $B_\parallel$ and $B_\perp$ indicated in (a)*

The shape of the field-frequency ENDOR contour plot is exactly the same as the signal observed for R1-H_{15} dissolved in methanol-D_1, see Figs. 5.10 and 5.11. The appearance of the characteristic doublet lines in the ENDOR spectrum, that originate from a dipolar coupled proton, indeed correlates with the position of the $g_{xx}^{(1)}$ component in the echo-detected field swept EPR spectrum, see Fig. 5.11(a). The ENDOR lineshape and the measured hyperfine coupling constants are identical to those determined in methanol, see Table 5.4. This indicates that the geometry and strength of the formed H-bond is the same for the two aliphatic alcohols studied. The influence of increasing bulkiness of the aliphatic alcohol manifests itself only as a decreased fraction of the nitroxide population that forms an H-bond with the hydroxyl proton, but does not influence the geometry of the H-bond.In the next example, the H-bond formation between the nitroxide radical and phenol molecules was investigated. 244 GHz EPR and W-band EDNMR experiments as due to formation of a single H-bond or of two H-bonds with two different phenol molecules.

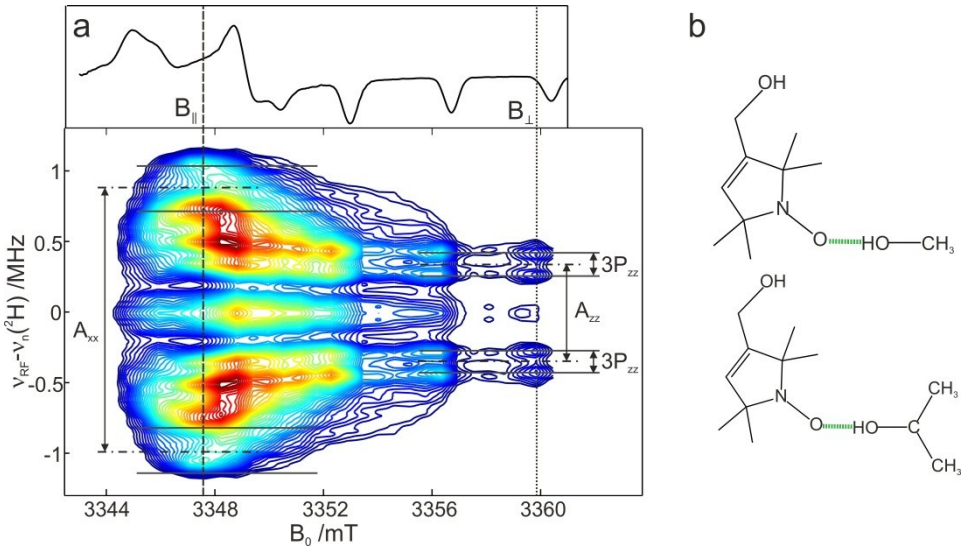

Figure 5.11 *(a) Field-frequency dependence of the experimental W-band deuterium Mims ENDOR of 1 mM R1-H_{16} in 2-propanol-D_1(OD) glass at 60 K. The contour lines are shown as isohypses from 0.05 to 1 of the maximum ENDOR intensity. The trace on the top shows the 2-pulse echo-detected W-band EPR spectra in the first-derivative form. The pulse settings of the Mims-type ENDOR experiment are t_π(pump)=200 ns, t_{RF}=20 µs, $t_{\pi/2}$ = 32 ns, averages per point =160, pulse repetition rate=500 Hz, number of field points 40. (b) The proposed geometry of the H-bond formed between the nitroxide radical and the solvent molecules of methanol (top) and 2-propanol (bottom).*

Figure 5.12(a) presents the proton Davies-type ENDOR spectrum recorded for R1-D_{16} dissolved in phenol-D_5(OH). Again, the signal from the dipolar coupled proton is present at all spectral positions, corroborating the assumption of H-bond formation between the nitroxide radical and the hydroxyl group of phenol. From the field-frequency dependence of the proton ENDOR signal it is clear that the hyperfine coupling constant is anisotropic, i.e. it varies depending on the field position within the nitroxide EPR spectrum. Analogous to the previously discussed solvents, the perpendicular hyperfine component appears in the g_{zz} spectral region. The H-bond is planar with the OH group located in the xy-plane of the nitroxide radical. In the g_{xx}-g_{yy} spectral region a single parallel hyperfine coupling constant can be distinguished, see Fig. 5.12(a). This excludes the interpretation of two spectral components in both. It is plausible, however, that in addition to the single H-bond formed by nitroxide with a phenol molecule, which is probed in the deuterium ENDOR experiment, a fraction of nitroxides can form a non-optimal H-bond with simultaneous interaction with the hydroxyl group and with the proton in the aromatic ring, see Fig. 5.12(c). This would result in an intermediate situation between a single and two H-bonds formed, influencing the magnetic parameters of the nitroxide in the fashion observed. The coupling with the proton in the phenol ring is not visible in this experiment because isotopically labeled phenol with D nuclei in the aromatic ring is used.

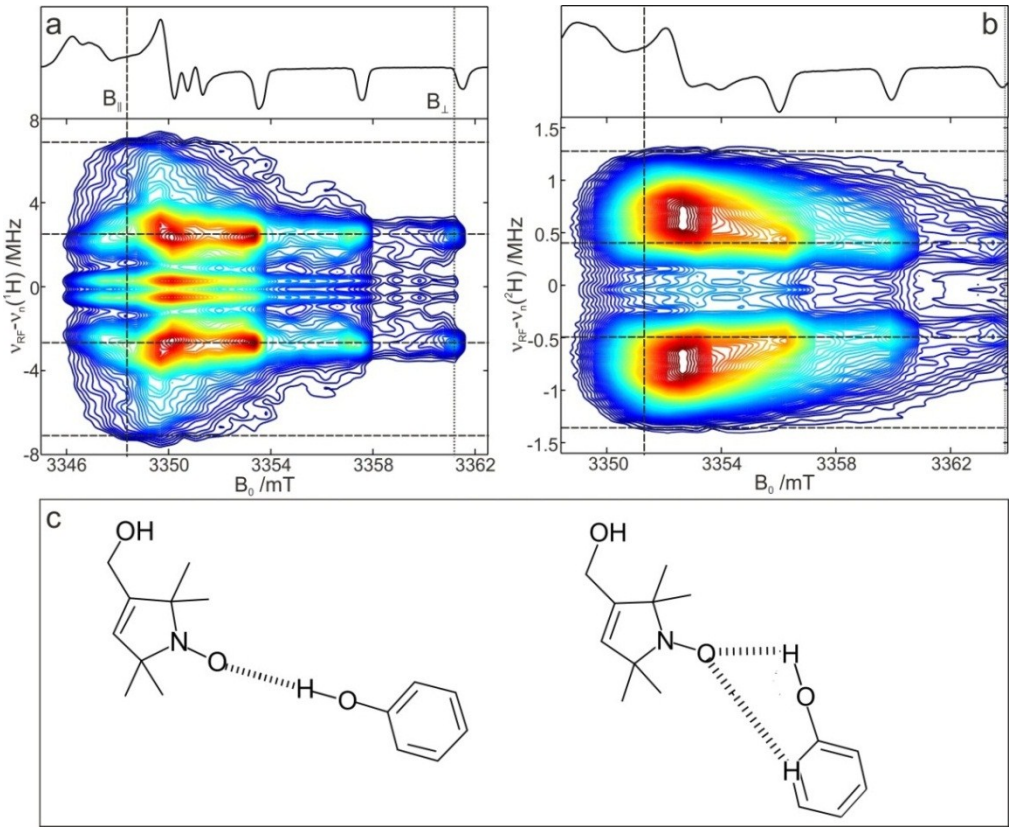

Figure 5.12 *(a) Frequency-field dependence of the experimental W-band proton Davies ENDOR of 1 mM R1-D_{16} in phenol-D_5 glass at 50 K. The contour lines are shown as isohypses from 0.05 to 1 of the maximum ENDOR intensity. The trace on the top shows the 2-pulse echo-detected W-band EPR spectra in the absorption and first-derivative form. The pulse settings of Davies-type ENDOR experiment are t_π(pump)=200 ns, t_{RF}=20 µs, $t_{\pi/2}$ = 32 ns, averages per point =160, pulse repetition rate=500 Hz, number of field points 40. (b) Frequency-field dependence of the experimental W-band D Mims ENDOR of 1 mM R1-H_{16} in phenol-OD glass at 50 K. The contour lines are shown as isohypses from 0.05 to 1 of the maximum ENDOR intensity. The trace on the top shows the 2-pulse echo-detected W-band EPR spectra in the absorption and first-derivative form. The pulse settings of Davies-type ENDOR experiment are t_π(pump)=200 ns, t_{RF}=20 µs, $t_{\pi/2}$ = 32 ns, averages per point =160, pulse repetition rate=500 Hz, number of field points 40. (c) The determined geometry of the H-bond formed between the nitroxide radical and the solvent molecules of phenol.*

In the last step, the possible H-bond formation between the nitroxide radical and aniline molecules was investigated. Figure 5.13(a) presents the proton Davies-type ENDOR spectrum of R1-D_{16} in aniline-D_5(NH_2). In addition to the 'matrix' proton line, the symmetric doublet lines originating from a coupled proton are visible throughout the spectrum. This allows to conclude, that the single component resolved in W-band EDNMR and 244 GHz EPR originates from nitroxide H-bonded with an aniline molecule. From the field-frequency dependence of the proton ENDOR signal it is clear that the hyperfine coupling is anisotropic, i.e. it varies depending on the field position within the nitroxide EPR spectrum. Similar to the situation observed in methanol and 2-propanol, the perpendicular hyperfine component appears in the g_{zz} spectral region. This proves that also in the case of aniline, the H-bond is planar with the NH_2 group located in the xy-plane of the nitroxide radical. However, in the g_{xx}-g_{yy} spectral region up to four different parallel hyperfine coupling constants can be discerned, see Fig. 5.13(a). The presence of one large, two intermediate and one small parallel hyperfine coupling constant suggests different geometries of the H-bonds formed that are simultaneously present in the

frozen solution of nitroxide in aniline. The magnitudes of the observed hyperfine couplings can be explained by the following two geometries: (i) One proton of the NH_2 group forms a H-bond with an angle that is φ>45°, resulting in the largest hyperfine coupling determined, while the second proton exhibits the smallest hyperfine coupling, see Fig. 5.13(c), (ii) Both protons of the NH_2 group simultaneously form H-bonds with the NO· group, which results in the two intermediate couplings measured. To support this assumption, ^{15}N Mims-type ENDOR spectra were recorded for R1-H_{16} dissolved in aniline-$^{15}NH_2$. The field frequency dependence of the ^{15}N ENDOR signal is shown in Fig. 5.13 (b). The observed signal is largely isotropic, i.e. the coupling does not vary much at different spectral positions. Two different hyperfine coupling constants are resolved in the ENDOR spectrum, $A^{(1)}_{iso}$=0.48 MHz and $A^{(2)}_{iso}$=2.0 MHz, that support the conclusions from proton ENDOR experiments. Nevertheless, it is worth reiterating that despite two main geometries of the H-bonds formed, the nitroxide:aniline complex is planar and no π H-bond geometry is present even for the more bulky H-bond donor group.

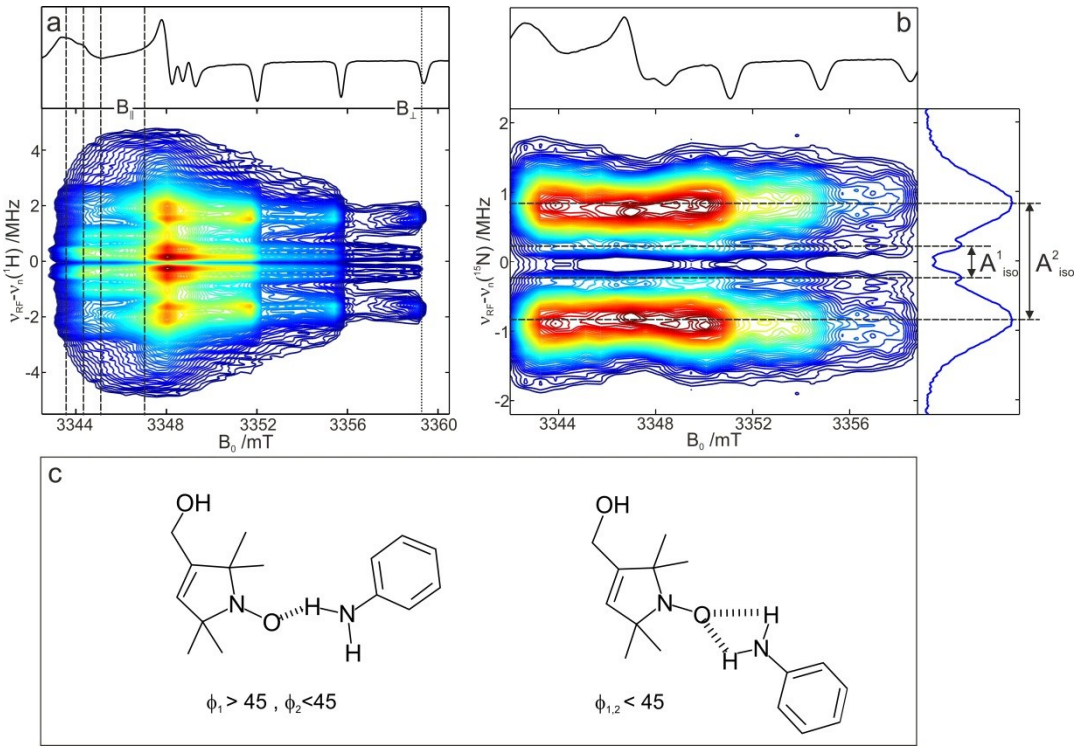

Figure 5.13 *(a) Frequency-field dependence of the experimental W-band proton Davies ENDOR of 1 mM R1-D_{16} in aniline-$D_5(NH_2)$ glass at 50 K. The contour lines are shown as isohypses from 0.05 to 1 of the maximum ENDOR intensity. The trace on the top shows the 2-pulse echo-detected W-band EPR spectra in the first-derivative form. The pulse settings of the Davies-type ENDOR experiment are t_π(pump)=200 ns, t_{RF}=20 μs, $t_{\pi/2}$ = 32 ns, averages per point =160, pulse repetition rate=500 Hz, number of field points 40. (b) Frequency-field dependence of the experimental W-band ^{15}N Mims ENDOR of 1 mM R1-H_{16} in aniline-$^{15}NH_2$ glass at 50 K. The contour lines are shown as isohypses from 0.05 to 1 of the maximum ENDOR intensity. The trace on the top shows the 2-pulse echo-detected W-band EPR spectra in the absorption and first-derivative form. The pulse settings of the Davies-type ENDOR experiment are t_π(pump)=200 ns, t_{RF}=20 μs, $t_{\pi/2}$ = 32 ns, averages per point =160, pulse repetition rate=500 Hz, number of field points 40. (c) The proposed geometry of the H-bond formed between the nitroxide radical and the solvent molecules of aniline.*

5.6 Discussion

Using two complementary approaches, i.e. 244 GHz cw EPR and W-band EDNMR, the characterization of nitroxide radical sub-ensembles present in various protic solvents was performed. Use of high-field/high-frequency EPR is crucial to ensure sufficient g-axis spectral resolution to resolve multiple components in the g_{xx} spectral region. The number of distinct nitroxide radical populations characterized by different A_{zz} values was also determined based on W-band EDNMR recordings in the g_{zz}, $M_I = -1$ spectral region. The results obtained using both techniques are in agreement, supporting the applicability of W-band EDNMR to characterize the heterogeneity of the microenvironment by means of nitroxide radical populations characterized by distinct A_{zz} values. The presence of multiple R1 nitroxide radical fractions strongly depends on the characteristics of the solvent. In methanol and aniline, a single microenvironment is sensed by the spin probe that results in a single set of magnetic parameters describing the nitroxide. The absolute values of both g_{xx} and A_{zz} parameters differ between the various solvents due to the different bulk polarity sensed by the nitroxide. However, in general three types of nitroxide radical sub-ensembles could be distinguished, similar to what has been observed in spin-labeled proteins [4;6]:

(i) a nitroxide radical population described by $g_{xx}^{(0)}$ and $A_{zz}^{(0)}$ that shows no specific interactions with the solvent, e.g. nitroxide dissolved in OTP and fraction (1) in 2-propanol,

(ii) a nitroxide fraction described by $g_{xx}^{(1)}$ and $A_{zz}^{(1)}$ that forms a single H-bond with the solvent molecule, e.g. nitroxide dissolved in methanol and fraction (2) in 2-propanol,

(iii) a nitroxide fraction presumably forming two H-bonds with the solvent molecule, i.e. fraction (2) for nitroxides dissolved in phenol.

The g_{xx} difference, $\Delta g_{xx} = g_{xx}^{(1)} - g_{xx}^{(0)}$, between two nitroxide radical populations in the studied solvents is in the range of $470\text{-}690 \cdot 10^{-6}$. This difference is comparable with Δg_{xx} reported for protic solvents and for spin-labeled proteins [1;4;6]. It is slightly larger than the theoretically predicted shift of $\Delta g_{xx} = 440 \cdot 10^{-6}$ upon H-bond formation with the $NO^{\cdot}$ group of a nitroxide radical [22]. Similarly, as in the case of Δg_{xx}, the difference between the $A_{zz}^{(i)}$ values characterizing nitroxide sub-ensembles in a single solvent varies depending on the solvent used, but in general is in the order of 6 MHz. Different Δg_{xx} and ΔA_{zz} shifts of magnetic parameters in various solvents possibly reflect subtle differences in the geometries of H-bonds formed between the nitroxide and the proton donor group. Although for the same class of solvents, i.e. aliphatic alcohols in this study, the geometry of the H-bond formed is essentially the same, a similar observation has been reported for the 5-ring spin probe in alcohol solutions [25].

It has been suggested previously that g_{xx} parameters of a nitroxide radical in frozen model membranes [2] and in spin-labeled proteins [6], reflects to a large extent the distribution between hydrogen-bonded and non-hydrogen-bonded forms of the nitroxide, rather than polarity. The results of the present study prove that in addition to g_{xx}, A_{zz} of ^{14}N in nitroxides is also to a large extent sensitive to the formation of hydrogen bonds – and thus can be used to probe the hydrogen-bond network in biomacromolecules. This observation is opposed to the generally accepted view that hydrogen-bond formation between the nitroxide moiety and the proton donor group has a major effect on g_{xx} but provides only a minor contribution to the A_{zz} value [1;23;40]. W-band EDNMR can be therefore used as an alternative to 240 GHz and 360 GHz cw EPR studies to probe the availability of H-bond donor groups in the vicinity of nitroxides.

While both 244 GHz cw EPR and W-band EDNMR yield information on the different extent of H-bond formation, the H-bond donor group cannot be identified. The differentiation between solvent protons and exchangeable protons from non-exchangeable protein protons can be accessed by means of Has was recently shown ^{2}H-ESEEM [5]. In the present work on protic solvents, the H-bond formation could be directly measured using W-band ENDOR and specific isotope labeling of the solvent. Our studies not only confirm the nature of the components observed in cw EPR and EDNMR studies, but also provide new insight in terms of the geometry of the H-bond network between nitroxide and solvent molecules. While there were several attempts to characterize H-bond formation between solvent molecules and nitroxide radicals, these were mostly performed on non-planar nitroxides. The systematic studies presented above allow to investigate in detail the preferred geometry of H-bond formation between planar structure nitroxide radicals and proton donor groups. The data presented here show H-bond formation with primary amines, e.g. aniline, and aromatic alcohols. These data are not in agreement with previous NMR data reported for non-planar nitroxides. The ^{1}H upfield and ^{13}C downfield contact shifts of methanol nuclei in a methanol/di-*tert*-butyl nitroxide bimolecular system were interpreted in terms of the spin polarization mechanism of electron spin transfer from the nitroxide to the methanol molecule. The observed negative spin density on the proton in the H-bond was reproduced by theoretical unrestricted Hartree-Fock MO calculations (INDO method) only for the π(O) H-bond geometry [8]. However, to reproduce the measured spin density it was necessary to include significant contributions from the nitroxide radical that forms the σ H-bond. Interestingly, the MO calculation for the DMNO/methanol bimolecular system showed that the σ H-bond model is energetically comparable or even more favorable than the π model [11]. Hence, it is likely that upon freezing of the nitroxide solution, only the energetically more favorable σ geometry is stabilized, as is shown here by low-temperature W-band ENDOR for the R1 spin probe. The difference between NMR and EPR structure results might originate in different nitroxide structures – and in different molecular dynamics which affects the nitroxide structure at low and room temperatures.

Ideally, it should be possible to differentiate between different H-bond donors to nitroxide spin labels attached to proteins. This would require systematic studies on the dependence of H-bond parameters for different H-bond donor groups. A detailed characterization of specific interactions between the nitroxide probe molecule and the matrix might facilitate the precise location of the spin label at its protein binding site.

References

[1] R. Owenius, M. Engström, M. Lindgren, M. Huber *Influence of solvent polarity and hydrogen bonding on the EPR parameters of a nitroxide spin label studied by 9-GHz and 95-GHz EPR spectroscopy and DFT calculations*. J. Phys. Chem. A **2001,** 105*,* 10967-10977.

[2] B. Dzikovski, D. Tipikin, J.H. Freed *Conformational distributions and hydrogen bonding in gel and frozen lipid bilayers: a high frequency spin-label ESR study*. J. Phys. Chem. B **2012,** 116*,* 6694-6706.

[3] M.G. Finiguerra, H. Blok, M. Ubbink, M. Huber *High-field (275 GHz) spin-label EPR for high-resolution polarity determination in proteins*. J. Magn. Reson. **2006,** 180*,* 197-202.

[4] E. Bordignon, H. Brutlach, L. Urban, K. Hideg, A. Savitsky, A. Schnegg, P. Gast, M. Engelhard, E.J.J. Groenen, K. Möbius, H.-J. Steinhoff *Heterogeneity in the nitroxide micro-environment: polarity and proticity effects in spin-labeled proteins studied by multi-frequency EPR*. Appl. Magn. Reson. **2010,** 37*,* 391-403.

[5] L. Urban, H.-J. Steinhoff *Hydrogen bonding to the nitroxide of protein bound spin labels*. Mol. Phys. **2013,** 111*,* 2873-2881.

[6] P. Gast, R.T.L. Herbonnet, J. Klare, A. Nalepa, C. Rickert, D. Stellinga, L. Urban, K. Möbius, A. Savitsky, H.-J. Steinhoff, E.J.J. Groenen *Hydrogen bonding of nitroxide spin labels in membrane proteins*. Phys. Chem. Chem. Phys. **2014,** 16*,* 15910-15916.

[7] N.A. Sysoeva, A.U. Stepanyants, A.L. Buchachenko *Paramagnetic shift of solvent protons in the presence of organic radicals*. Zh. Strukt. Khim. **1968,** 9*,* 311-312.

[8] I. Morishima, K. Endo, T. Yonezawa *Studies on nuclear magnetic resonance contact shifts induced by hydrogen bonding with organic radicals. I. ^{1}H and ^{13}C contact shifts of protic molecules in the presence of nitroxide radical*. J. Am. Chem. Soc. **1971,** 93*,* 2048-2050.

[9] L. Morishima, K. Endo, T. Yonezawa *Molecular orbital studies of hydrogen bond and NMR contact shifts in nitroxide radical/methanol system*. Chem. Phys. Lett. **1971,** 9*,* 143-146.

[10] Morishima.I, K. Endo, T. Yonezawa *Interaction between closed- and open-shell molecules. VI. ^{1}H and ^{13}C contact shifts and molecular orbital studies on the hydrogen bond of nitroxide radical*. J. Chem. Phys. **1973,** 58*,* 3146-3154.

[11] A.S. Kabankin, G.M. Zhidomirov, A.L. Buchachenko *Structure of complexes of radicals with organic ligands*. J. Magn. Reson. **1973,** 9*,* 199-204.

[12] I. Morishima, K. Ishihara, K. Tomishima, T. Inubushi, T. Yonezawa *Nitroxide radical induced Nuclear Magnetic Resonance contact shift studies. Potential utility of specific downfield ^{1}H contact shifts induced by hydrogen bonding with di-tert-butyl nitroxide radical*. J. Am. Chem. Soc. **1975,** 97*,* 2749-2756.

[13] E. Dally, W. Müller-Warmuth *High-resolution NMR in solutions with nitroxide radical complexes*. Ber. Bunsenges. Phys. Chem. **1977,** 81*,* 1133-1137.

[14] K. Endo, I. Morishima, T. Yonezawa *Use of a stable free radical as a NMR spin probe for studying intermolecular interactions.XIV. A proton relaxation study of the hydrogen bond involving a stable free radical*. J. Chem. Phys. **1977,** 67*,* 4760-4767.

[15] E. Dally, W. Müller-Warmuth *NMR investigations on solutions with nitroxide radical complexes. II. Hyperfine coupling constants, line widths, and relaxation of complexes with n-propanol, isopropanol and tert.-butanol*. Ber. Bunsenges. Phys. Chem. **1978,** 82*,* 792-798.

[16] U. Stark, W. Müller-Warmuth *Hydrogen bond formation and molecular motion in solutions of aniline with nitroxide free radicals*. Ber. Bunsenges. Phys. Chem. **1990,** 94*,* 168-172.

[17] I.G. Shenderovich, Z. Kecki, I. Wawer, G.S. Denisov *NMR and EPR study of the nitroxide radical TEMPO interaction with phenols*. Spectrosc. Lett. **1997,** 30*,* 1515-1523.

[18] A.T. Bullock, C.B. Howard *Electron spin resonance study of the 1:1 hydrogen-bonded complex of di-t-butylnitroxide with methanol. An analysis of an acceptor: self-associated donor equilibrium*. J. Chem. Soc. Faraday Trans. **1977,** 73*,* 465-470.

[19] I.J. Brass, A.T. Bullock *1:1 hydrogen bonded complexes of phenol and 4-fluorophenol with 2,2,6,6-tetramethylpiperidin-1-oxyl: an Electron Spin Resonance study*. J. Chem. Soc. Faraday Trans. **1978,** 74*,* 1556-1561.

[20] W. Kolodziejski, Z. Kecki *ESR and PMR studies of alcohols hydrogen bonded with nitroxide radical*. Ber. Bunsenges. Phys. Chem. **1978,** 82*,* 1312-1314.

[21] A.T. Bullock, C.B. Howard *Hydrogen-bonding studies of nitroxides with phenols. Effect of donor acidity*. J. Chem. Soc. Faraday Trans. **1981,** 77*,* 137-140.

[22] M. Plato, H.-J. Steinhoff, C. Wegener, J.T. Törring, A. Savitsky, K. Möbius *Molecular orbital study of polarity and hydrogen bonding effects on the g and hyperfine tensors of site directed NO spin labelled bacteriorhodopsin*. Mol. Phys. **2002,** 100*,* 3711-3721.

[23] T. Kawamura, S. Matsunami, T. Yonezawa *Solvent effects on the g-value of di-tert-butyl nitric oxide*. Bull. Chem. Soc. Jpn. **1967,** 40*,* 1111-1115.

[24] O.H. Griffith, P.J. Dehlinger, S.P. Van *Shape of hydrophobic barrier of phospholipid bilayers (evidence for water penetration in biological membranes)*. J. Membr. Biol. **1974,** 15*,* 159-192.

[25] T.I. Smirnova, A.I. Smirnov, S.V. Paschenko, O.G. Poluektov *Geometry of hydrogen bonds formed by lipid bilayer nitroxide probes: A high-frequency pulsed ENDOR/EPR study*. J. Am. Chem. Soc. **2007,** 129*,* 3476-3477.

[26] M. Flores, R.A. Isaacson, R. Calvo, G. Feher, W. Lubitz *Probing hydrogen bonding to quinone anion radicals by ^{1}H and ^{2}H ENDOR spectroscopy at 35 GHz*. Chem. Phys. **2003,** 294*,* 401-413.

[27] M. Kaupp, C. Remenyi, J. Vaara, O.L. Malkina, V.G. Malkin *Density functional calculations of electronic g-tensors for semiquinone radical anions. The role of hydrogen bonding and substituent effects*. J. Am. Chem. Soc. **2002,** 124*,* 2709-2722.

[28] S. Sinnecker, E. Reijerse, F. Neese, W. Lubitz *Hydrogen bond geometries from electron paramagnetic resonance and electron-nuclear double resonance parameters: Density functional study of quinone radical anion-solvent interactions*. J. Am. Chem. Soc. **2004,** 126*,* 3280-3290.

[29] K. Möbius, A. Savitsky, A. Schnegg, M. Plato, M. Fuchs *High-field EPR spectroscopy applied to biological systems: characterization of molecular switches for electron and ion transfer*. Phys. Chem. Chem. Phys. **2005,** 7*,* 19-42.

[30] K. Möbius, A. Savitsky High-field EPR spectroscopy on proteins and their model systems, RSC Publishing, Cambridge, 2009.

[31] E. Reijerse, P.P. Schmidt, G. Klihm, W. Lubitz *A CW and pulse EPR spectrometer operating at 122 and 244 GHz using a quasi-optical bridge and a cryogen-free 12 T superconducting magnet*. Appl. Magn. Reson. **2007,** 31*,* 611-626.

[32] A. Stesmans, G. Van Gorp *Improved measurement of the g factor of conduction electrons in Li particles embedded in LiF:Li*. Phys. Lett. A **1989,** 139*,* 95-98.

[33] O. Burghaus, M. Rohrer, T. Götzinger, M. Plato, K. Möbius *A novel high-field/high-frequency EPR and ENDOR spectrometer operating at 3 mm wavelength*. Meas. Sci. Technol. **1992,** 3*,* 765-774.

[34] J.R. Pilbrow Transition ion electron paramagnetic resonance, Oxford University Press, Oxford, 1990.

[35] A. Nalepa, K. Möbius, W. Lubitz, A. Savitsky *High-field ELDOR-detected NMR study of a nitroxide radical in disordered solids: Towards characterization of heterogeneity of microenvironments in spin-labeled systems*. J. Magn. Reson. **2014,** 242*,* 203-213.

[36] A. Savitsky, A.A. Dubinskii, M. Plato, Y.A. Grishin, H. Zimmermann, K. Möbius *High-field EPR and ESEEM investigation of the nitrogen quadrupole interaction of nitroxide spin labels in disordered solids: Toward differentiation between polarity and proticity matrix effects on protein function*. J. Phys. Chem. B **2008,** 112*,* 9079-9090.

[37] M. Pavone, A. Sillanpää, P. Cimino, O. Crescenzi, V. Barone *Evidence of variable H-bond network for nitroxide radicals in protic solvents*. J. Phys. Chem. B **2006,** 110*,* 16189-16192.

[38] A.V. Astashkin, A. Kawamori *Matrix line in pulsed electron-nuclear double resonance spectra*. J. Magn. Reson. **1998,** 135*,* 406-417.

[39] N.M. Atherton Principles of electron spin resonance, Ellis Horwood, New York, 1993.

[40] M. Engström, R. Owenius, O. Vahtras *Ab initio g-tensor calculations of hydrogen bond effects on a nitroxide spin label*. Chem. Phys. Lett. **2001,** 338*,* 407-413.

Chapter 6

Annealing induced nitroxide H-bond network rearrangement studied using W-band cw EPR and EDNMR

This chapter has been partially published as [22] and edited for consistency of notation:
E. Bordignon, A.I. Nalepa, A. Savitsky, L. Braun, G. Jeschke *Changes in the microenvironment of nitroxide radicals around the glass transition temperature*. J. Phys. Chem. B **2015,** 119, 13797-13806.

6.1 Introduction

The combination of pulsed dipolar (PD) EPR techniques [1-3] and site-directed spin-labeling (SDSL) employing nitroxide radicals [4;5], has turned out to be a powerful methodology in probing the structure and function-associated structural changes of proteins [6-9]. With the development of pulsed-electron double resonance (PELDOR), the range of distances between 20 to 80 Å has become accessible and postulated to exceed 100 Å when the protein is perdeuterated [10]. Importantly, using pulsed EPR techniques not only the average distance can be elucidated, but also the distance distribution that reports on the distribution of biomacromolecule's conformational states [11]. Indeed, proteins show complicated energy landscapes with anharmonic motion present, which has been postulated to correlate with the function and results in a conformational distribution at physiological temperatures [12;13]. While only few recent studies report on pulsed EPR distance measurements at physiological temperatures [14-16], they require immobilization of the biomacromolecule and are, therefore, not generally applicable. The established PD EPR methods, i.e. 4-pulse PELDOR [2] in conjunction with nitroxide spin labeling, still require cryogenic temperatures:

(i) to prevent the rotational diffusion, which averages the dipolar interaction,
(ii) to achieve sufficiently long spin-spin relaxation time of the electron spins and hence, increase the upper limit of experimentally accessible distances.

Ideally, fast freezing of the sample should ensure that the ensemble of trapped structures corresponds to dynamic states observed at RT, yielding a relevant distance distribution. In reality, the measured conformational ensemble corresponds to equilibrium at the glass transition temperature, T_g [17], which is around 175 K for the water molecules in the first hydration layer of proteins [18].

Additionally, the distance constraints obtained using PELDOR can be interpreted in terms of protein structure only if conformations of the spin label itself are taken into account [19]. The attachment of the most widely used spin label MTS to cysteine residue results in >7 Å separation between the unpaired electron in the $NO^{\bullet}$ group and the C_α atom of the amino acid. The presence of five torsion angles in MTS attached to protein leads to a large number of possible conformations of the spin label and subsequently different positioning of the spin center. One of the approaches to narrow the

conformational space probed by the nitroxide spin probe is the refinement of a 'tether-in-a-cone' model using rotamer libraries of the free label that are derived from molecular dynamics (MD) simulations. This is the so called rotamer library approach (RLA). This approach has been implemented into MMM (Multiscale modeling of macromolecular systems) [20] and MtsslWizard [21] open-source programs. In the case of MtsslWizard, the complete conformational space of the label is sampled and only MTSSL rotamers that clash with the surrounding protein are excluded. In the MMM program, on the other hand, assumptions are made about the rotamer probabilities at RT or at 175 K, i.e. the estimated T_g of water in the first hydration layer of protein, and scoring based on interaction energies is performed. Recently, the possibility to extract experimentally the local glass transition temperature in spin-labeled proteins was demonstrated using X-band power saturation cw EPR [22]. This EPR technique was previously successfully applied to extract the T_g values for nitroxide spin probes and spin labels in polymers [23;24]. Since nitroxide motion around the bonding tether and the internal motions of the nitroxide ring are active in a particular temperature range, refinement of the T_g value should result in more precise selection of rotamers for a specific spin label attachment site in the protein. However, at present the main obstacle in reliable prediction of conformational ensemble of the spin label side group is the lack of proper treatment for the intermolecular interactions, especially the hydrogen bond formation, which are not explicitly taken into account so far. While in most cases, RLA results in plausible distance predictions [25], it has been shown that some nitroxide dihedral angles observed in crystal structures of spin-labeled proteins are not predicted from the rotamer libraries [26]. It seems plausible that certain rotamers, which are energetically unfavorable for the free spin probe, are promoted by the specific interaction with the local protein environment. This influence of the protein environment is expected to be more pronounced at tight labeling sites. Such a case has been demonstrated recently for the high-resolution crystal structure of spin-labeled azurin [27]. Indeed, the specific interactions of nitroxide radicals with solvent or with protein side chains that contain H-bond donor groups have been shown experimentally, either indirectly [28-30] or directly [31] (see also Chapter 5.3). Weighting of the rotamers, based on an energy scoring function that explicitly takes into account the influence of the protein environment, especially the H-bonding, would reflect the situation more realistically.

The importance of the buffer composition is another point worth reiterating, when reliable distance information is to be obtained. The presence of osmolytes is known to influence the conformation equilibria of the protein [32]. Recently, it has been demonstrated that not only the concentration of the cryoprotectant, but also the freezing rate plays a role in selection of spin label rotamers as was shown for doubly spin-labeled T4 lysozyme mutants [33].

The aim of this study is, therefore, to probe possible changes in the local environment of the nitroxide radical around the local glass transition temperature, T_g, by characterizing the spin label populations. To extract this information, sample annealing is performed by increasing the temperature above T_g of the solvent and subsequent cooling down. To characterize the nitroxide H-bond network, W-band cw EPR and EDNMR methods were used. Since the dynamic behavior of the protein was shown to be correlated with a glass transition in the surrounding solvent [34;35], the situation in biologically relevant solvent, i.e. water, is studied. 244 GHz and W-band cw EPR and EDNMR measurements are performed using the deuterated nitroxide spin probe R1-D_{16} (3-hydroxymethyl-2,2,5,5-tetramethylpyrrolin-1-oxyl), see Fig. 4.1, dissolved in D_2O with different glycerol-D_8 content

(5, 10, 50%) and in anhydrous glycerol-D_8. In the first part, the nitroxide probe R1-D_{16} dissolved in D_2O/glycerol-D_8 mixtures is studied. This can be considered as a limiting case in relation to the solvent exposed spin-label sites in proteins. The highest concentration of the typical cryoprotectant (glycerol) was also included, since such concentrations are used, for example in [36], to increase the electron spin echo intensity due to longer T_M time and hence offering a possibility to decrease the sample concentration. To investigate the influence of annealing on the reorganization of the nitroxide:water H-bond network, a comparison of cw EPR and EDNMR spectra of R1 dissolved in water/glycerol mixtures and in pure glycerol was done at 80 K, both before and after sample annealing. Additionally, as an example of a protein system, single spin-labeled T4-lysozyme was also investigated to confirm whether the situation observed for spin probes can be extrapolated to spin-labeled proteins.

6.2 Materials and methods

Sample preparation

The perdeuterated nitroxide spin probe R1-D_{16} (3-hydroxymethyl-2,2,5,5-tetramethylpyrrolin-1-oxyl) used in this study was synthesized as described previously [37]. The solvents D_2O and glycerol-D_8 were obtained from Deutero GmbH and Sigma Aldrich, respectively. R1-D_{16} was directly dissolved in D_2O and subsequently the nitroxide stock solution was mixed with anhydrous glycerol-D_8 to obtain a predefined cryoprotectant concentration (% v/v) with about 1 mM final nitroxide concentration. MTS spin-labeled T4-lysozyme was prepared in 25 mM MOPS buffer, 10% glycerol-H_8 (v/v) at pH=7, and subsequently mixed with additional 20% (v/v) of glycerol-D_8. The protein was a kind gift from Prof. E. Bordignon (FU Berlin). The sample solution was transferred into a quartz capillary (I.D. 0.6 mm) for W-band EPR measurements. A glass-type frozen solution was obtained by transferring the sample, either equilibrated at RT or shock-frozen in liquid nitrogen, into the pre-cooled EPR cryostat at about 85 K. For both types of freezing protocol the same results were obtained. For all samples, W-band cw EPR and EDNMR spectra were recorded with the same thermal history:

- insertion of the sample equilibrated at RT into EPR cavity precooled at 85 K,
- acquisition of cw EPR and EDNMR spectra at 80 K,
- subsequent annealing of the sample at 200 K (for D_2O/glycerol-D_8 mixtures and spin-labeled T4-lysozyme) or at 230 K (for R1 dissolved in pure glycerol-D_8) for 1 hour,
- cooling down of the sample and acquisition of cw EPR and EDNMR spectra at 80 K with identical experimental settings as before annealing.

The exact temperature of the sample was controlled using an external thermocouple. The reproducibility of the results was ensured by repeating some of the experiments.

W-band EPR and EDNMR

The W-band cw EPR and EDNMR experiments were performed on a modified Bruker Elexsys E680 spectrometer operating at about 94 GHz. For cw EPR experiments the magnetic field was modulated at 100 kHz with an amplitude of 0.1 mT. The EDNMR experiments made use of two-pulse Hahn-echo detection at a microwave frequency ν_1, matched to the cavity resonance. The HTA microwave pulse was applied at the microwave frequency ν_2. The spectra were acquired by continuously

sweeping ν_2 at a fixed magnetic field, in steps of 70 kHz. The length and amplitude of the HTA pulse were adjusted to obtain an ELDOR π -pulse on the forbidden transition of interest at the g_{zz}, $M_I = -1$ field position. The HTA pulse length was set to 2.5 μs at mw field amplitude of $6.4 \cdot 10^7$ rad/s (for nitroxide spin probe) or 1.8 μs at $4.5 \cdot 10^7$ rad/s (for MTS spin-labeled T4-lysozyme). The detection sequence was set 7.5 μs after the HTA pulse to ensure the decay of electron-spin coherency. The length of the $\pi/2$ pulse in the Hahn-echo detection sequence was set to 100 ns, and the pulse separation to 1 μs. The echo was integrated over 1.4 μs (for nitroxide spin probe) or 1.2 μs (for MTS spin-labeled T4-lysozyme) around its maximum for optimal EDNMR resolution. For 2D-EDNMR spectra, EDNMR traces were recorded in the field range of 1.2 mT around the g_{zz}, $M_I = -1$ spectral field position. The measurement repetition rate of 330 Hz was used to allow the echo signal to restore between consecutive pulse trains. The EDNMR data analysis was performed according to the procedure described in Chapter 4.2.

244 GHz cw EPR

244 GHz cw EPR spectra were recorded using the home-built high-field EPR spectrometer operating at 122 or 244 GHz and equipped with 12 T magnet [38]. A sample volume of 30-50 μl was used. The measurements were performed at 70 K with the mw frequency set to 243.767 GHz. For each spectrum the field sweep was recorded over the magnetic field range of 90 mT at the scan rate 80 μT/s and with 4000 data points. A mw power of 0.5 mW and a modulation amplitude of 0.5 mT at the modulation frequency of 5 kHz were used. The calibration of the magnetic field sensed by the EPR sample was performed using LiF:Li as a *g*-value marker, as described in detail in Chapter 5.2. The magnetic field sweep nonlinearity was corrected by measuring the EPR spectrum of Mn^{2+} in MgO (about 0.15% Mn^{2+}) as standard with subsequent correction of the field axis. The g_{xx} spectral region was fitted to two Gaussian lines in first-derivative representation. An additional Gaussian line was fitted to compensate for the residual contribution of the g_{yy} peak. All parameters, namely line positions, line widths and intensities were left unrestricted. The fitting was performed using home-written Matlab routines. The maxima of Gaussian lines were used in the next step to calculate the g_{xx} values for different spin probe populations; the area under the fitted curves was used as a measure of the spin probe population.

6.3 Influence of annealing on the H-bond network of nitroxide spin probes dissolved in glycerol and D_2O/glycerol mixtures

W-band and 244 GHz cw EPR

Figure 6.1(a) (bottom) shows the W-band cw EPR spectrum of the nitroxide radical R1-D_{16} in frozen solution of D_2O/glycerol-D_8 (5% v/v). The EPR spectrum is clearly resolved into three separate spectral regions, which correspond to the principal values of the g-tensor, g_{xx}, g_{yy} and g_{zz}. In the g_{zz} region, three nitrogen hyperfine lines split by the hyperfine coupling tensor component $A_{zz,}$ are visible. The inhomogeneous EPR linewidth of 7.1 MHz (FWHM), determined at the g_{zz}, $M_I = 0$ spectral position, allows for partial resolving of the ^{14}N hyperfine splitting ($A_{yy} \sim 12$ MHz) in the g_{yy} spectral region, in addition to the fully resolved large A_{zz} component. In the g_{xx} spectral region, the presence of two nitroxide spin probe fractions with different g_{xx} values can be inferred. However, the

strong overlap of their EPR lines limits the accuracy of determining the corresponding $g^{(i)}_{xx}$ values. The two spectral contributions in the g_{xx} region become partially resolved in the cw EPR spectrum recorded at 244 GHz, see Fig. 6.1(a) (top). The overall shape of the g_{xx} spectral region at 244 GHz is different from that at W-band where the nitrogen hyperfine/quadrupole structure is still only partially resolved.

The g_{xx} spectral region in the 244 GHz cw EPR spectrum could be satisfactorily fitted to two Gaussian lines in first-derivative form. From the peak positions, the corresponding g_{xx} values of two spin probe populations were obtained: $g^{(1)}_{xx} = 2.00842 \pm 0.00004$ and $g^{(2)}_{xx} = 2.00800 \pm 0.00004$. These g^{i}_{xx} values were used in the numerical calculation of the W-band cw EPR spectrum of R1-D_{16}. The simulation was obtained by numerical solution of the spin Hamiltonian including the electron Zeeman, nuclear Zeeman, nitrogen-hyperfine and nitrogen-quadrupole interactions. The overlay of the experimental and calculated W-band cw EPR spectra is shown in Fig. 6.1(b) (top). The calculated spectra of the individual populations are presented in Fig. 6.1(b) (bottom). The two spectral contributions are ascribed to two nitroxide radical fractions, which form either one (population 1) or two (population 2) hydrogen bonds with water molecules. The difference of $420 \cdot 10^{-6}$ in their g_{xx} values is virtually identical to the difference observed for different spin label populations in SDSL proteins, which were assigned to singly and doubly hydrogen-bonded nitroxide radicals [28]. It also agrees well with the theoretically predicted g_{xx} change upon formation of the second hydrogen bond to a nitroxide radical [39], thereby supporting the assignment.

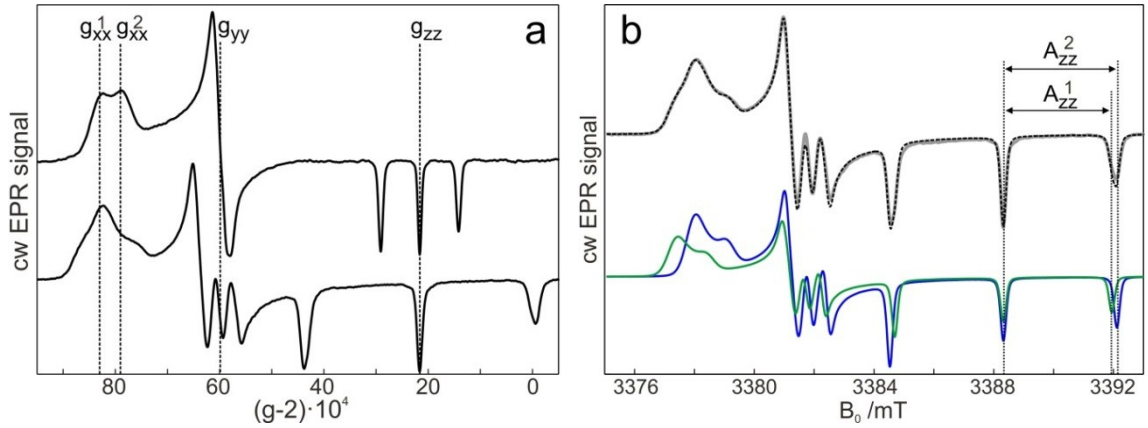

Figure 6.1 *(a) cw EPR spectra of 1 mM R1-D_{16} in frozen solution of D_2O/glycerol-D_8 (5% v/v) at 244 GHz and 40 K (top) and at 94 GHz and 80 K (bottom). (b) (top) Experimental W-band cw EPR spectrum of 1 mM R1-D_{16} in frozen solution of D_2O with 5% glycerol-D_8 (v/v) recorded at 80 K (gray line) overlaid with the calculated spectrum (dashed line), obtained by numerical solution of the spin Hamiltonian making use of the experimentally determined EPR parameters and fractional weights of the two spin probe populations. (bottom) The calculated spectra of the individual nitroxide spin probe populations.*

Concomitantly with the observation of two different g_{xx} values, one would expect distinctly different A_{zz} values, similarly to situation observed for R1-D_{16} dissolved in 2-propanol (see Chapter 4.3). However, no additional splitting is visible at g_{zz}, $M_I = \pm 1$ spectral positions that would indicate the presence of a second hyperfine coupling constant. The linewidth of about 11.5 MHz (FWHM) in these spectral regions, as compared to 7.1 MHz at the g_{zz}, $M_I = 0$, possibly masks the presence of two distinct A_{zz} values. Additionally, a possible distribution of A_{zz} values within both spin label populations would contribute to the linewidth at the g_{zz}, $M_I = \pm 1$ spectral positions.

To ensure that water:nitroxide as opposed to glycerol:nitroxide specific interactions are preferentially probed, W-band cw EPR spectra of R1-D_{16} in D_2O, containing 5, 10 or 50% (v/v) of glycerol-D_8, were recorded, see Fig. 6.2. The cw EPR spectra for samples with different glycerol-D_8 admixture are identical. This observation supports the initial assumption that the nitroxide radical preferentially interacts with water molecules instead of glycerol molecules. However, with increasing glycerol-D_8 content the linewidths at g_{zz}, $M_I = 0$ and g_{zz}, $M_I = -1$ spectral field positions decrease. At g_{zz}, $M_I = 0$, a narrowing from 7.1 MHz to 5.9 MHz is seen when the glycerol-D_8 content is increased from 5 to 50%. The most likely explanation is a decrease in the number of deuterium atoms in the vicinity of the nitroxide group when increasing the glycerol concentration. Therefore, a smaller number of unresolved deuterium couplings contributes to the nitroxide linewidth. However, even at the highest glycerol-D_8 content used (50% v/v), two spectral components with different A_{zz} values are still not resolved in the g_{zz}, $M_I = \pm 1$ spectral regions of the W-band cw EPR spectrum.

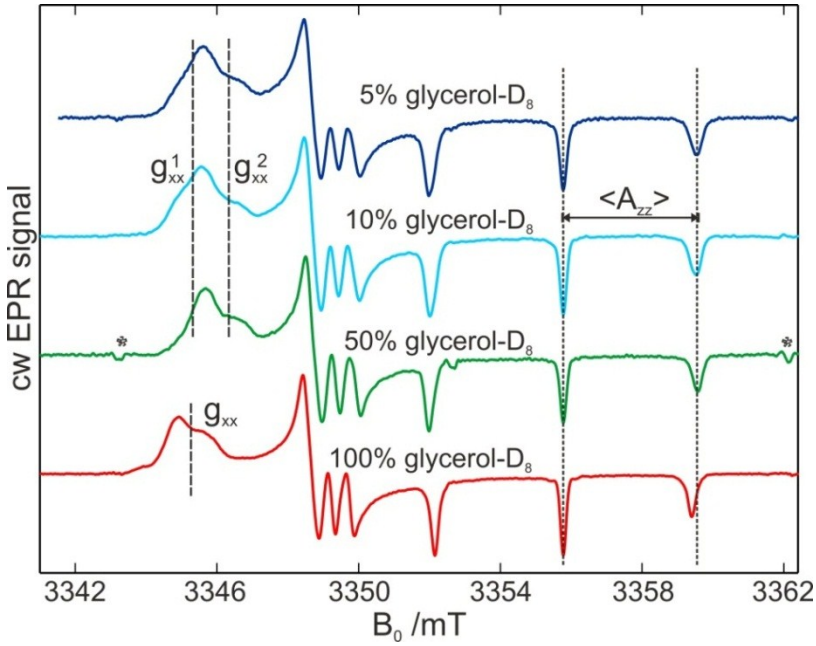

Figure 6.2 *Experimental W-band cw EPR spectra of 1 mM R1-D_{16} in frozen solution of D_2O/glycerol-D_8 mixtures recorded at 80 K for rapidly frozen samples. The amounts of added glycerol-D_8 are indicated. The spectral positions that correspond to different principal g_{xx}-tensor and average A_{zz} values are indicated by dashed and dotted lines. The (*) indicate the location of two Mn^{2+} lines.*

The W-band cw EPR spectrum of nitroxide spin probe dissolved in anhydrous glycerol-D_8 is shown in Fig. 6.2 (bottom). As opposed to water/glycerol mixtures, the spectrum can be simulated satisfactorily with a single set of magnetic parameters. The single g_{xx} value of $g^{(1)}_{xx} = 2.00846 \pm 0.00004$, extracted from the analysis of the 244 GHz cw EPR spectrum, describes the nitroxide spin population that comprises ~80% of total spectral intensity. The average A_{zz} value is equal to 101.7± 0.5 MHz and is smaller than the value of $\langle A_{zz} \rangle = 106.1 \pm 0.5$ MHz obtained for R1-D_{16} dissolved in D_2O/glycerol-D_8 mixtures, see Fig. 6.2.

The W-band cw EPR spectra for R1-D_{16} in frozen solution of D_2O/glycerol-D_8 (50/50 v/v%) that was shock frozen by plunging into the liquid nitrogen and subsequently annealed for 1 h at 200 K are presented in Fig. 6.3(a). Sample annealing for 1 h at the temperature above T_g of the solvent, results in the spectral changes in the g_{xx} region of W-band cw EPR spectrum. These changes can be explained

through change in the ratio of nitroxide radical populations with different H-bonding situation. The spectrum after annealing could, therefore, be simulated with the same set of magnetic parameters as before annealing except for changing ratio between two nitroxide radical populations. For the shock-frozen sample, the ratio between two fractions is about 2:1 in favour of the nitroxide radical population forming two H-bonds with water molecules, see Table 6.1. After annealing, the ratio changes to 1:1. This observation is somewhat surprising, since the formation of a second H-bond between a nitroxide radical and water molecule has been shown theoretically to be energetically favourable (~-0.5 kcal/mol) [40].

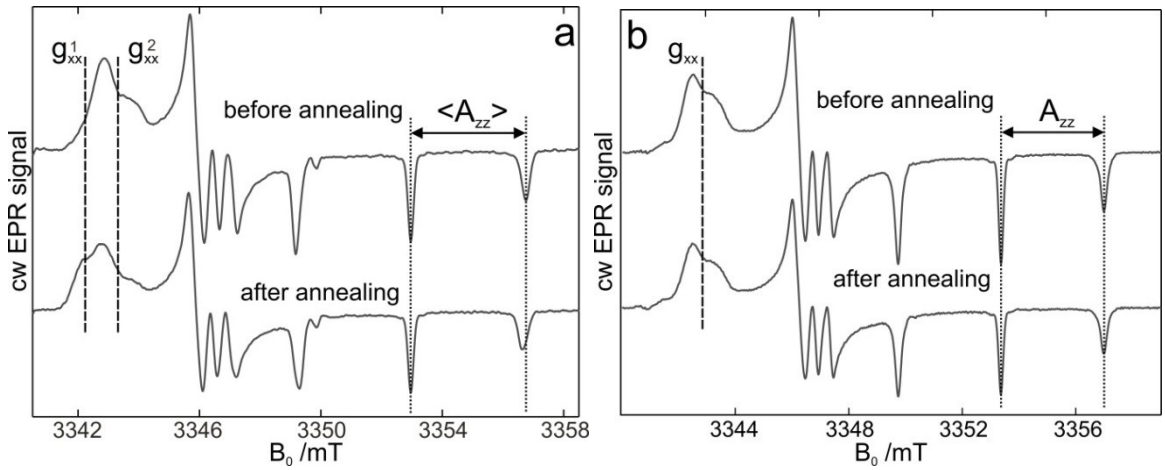

Figure 6.3 *(a) Experimental W-band cw EPR spectra of 1 mM R1-D_{16} in frozen solution of D_2O/glycerol-D_8 (50/50 v/v) recorded at 80 K before (upper trace) and after (lower trace) annealing the sample for 1 h at 200 K. (b) Experimental W-band cw EPR spectra of 1 mM R1-D_{16} in frozen solution of anhydrous glycerol-D_8 recorded at 80 K before (upper trace) and after (lower trace) annealing the sample for 1 h at 230 K. The spectral positions that correspond to principal g_{xx}-tensor and average A_{zz} values are indicated by dashed and dotted lines.*

The annealing does not influence the inhomogeneous EPR linewidth at g_{zz}, $M_I = 0$, and in the g_{zz}, $M_I = \pm 1$ spectral regions, within experimental accuracy. However, the average A_{zz} value, which can be read out from the spectra, decreases by about ΔA_{zz}=2.5 MHz. This shift can be rationalized in terms of changing the ratio between nitroxide radical populations described by different A_{zz} values that are not resolved in the W-band cw EPR spectrum. For R1-D_{16} dissolved in D_2O with 5, 10 or 50% of glycerol-D_8 (v/v), identical W-band cw EPR spectra are obtained after annealing. It can be concluded, that the observed changes are due to reorganization of the H-bond network with water molecules around the nitroxide radical and are probed exclusively in the EPR experiment as opposed to the interaction with glycerol molecules. Interestingly, similar effect has been reported for nitroxide spin probe dissolved in ethanol and for spin-labeled lipids in biological membranes [41]. Similarly, the shape of the g_{xx} spectral region in 240 GHz cw EPR spectra was varying depending on whether slow or shock freezing of the samples was performed.

In contrast to D_2O/glycerol-D_8 mixture, no changes in the g_{xx} spectral region are observed after annealing if anhydrous glycerol-D_8 is used as a solvent, see Fig. 6.3(b). The W-band cw EPR spectrum can be described satisfactorily with the same set of magnetic interaction parameters as those before the annealing.

W-band EDNMR

Concomitantly with W-band cw EPR spectra, EDNMR recordings for R1-D_{16} dissolved in D_2O/glycerol-D_8 mixtures and in anhydrous glycerol-D_8 were acquired at 80 K. Fig. 6.4(a) shows representative experimental EDNMR recordings at the g_{zz}, $M_I = -1$ spectral region for a frozen solution of R1-D_{16} in D_2O/glycerol-D_8 (50/50 v/v) acquired before annealing. Contributions from two, partially resolved pairs of lines centered around two different nitrogen hyperfine tensor components, A^i_{zz}, are visible in the W-band EDNMR spectra. Similarly, two pairs of EDNMR lines were observed for nitroxide radicals dissolved in 2-propanol (see Chapter 4.3). EDNMR recordings at each magnetic field position were fitted to four Gaussian lines as outlined in Chapter 4.2. Due to inherently broader lines than in 2-propanol, the spectra were fitted in the first-derivative representation.

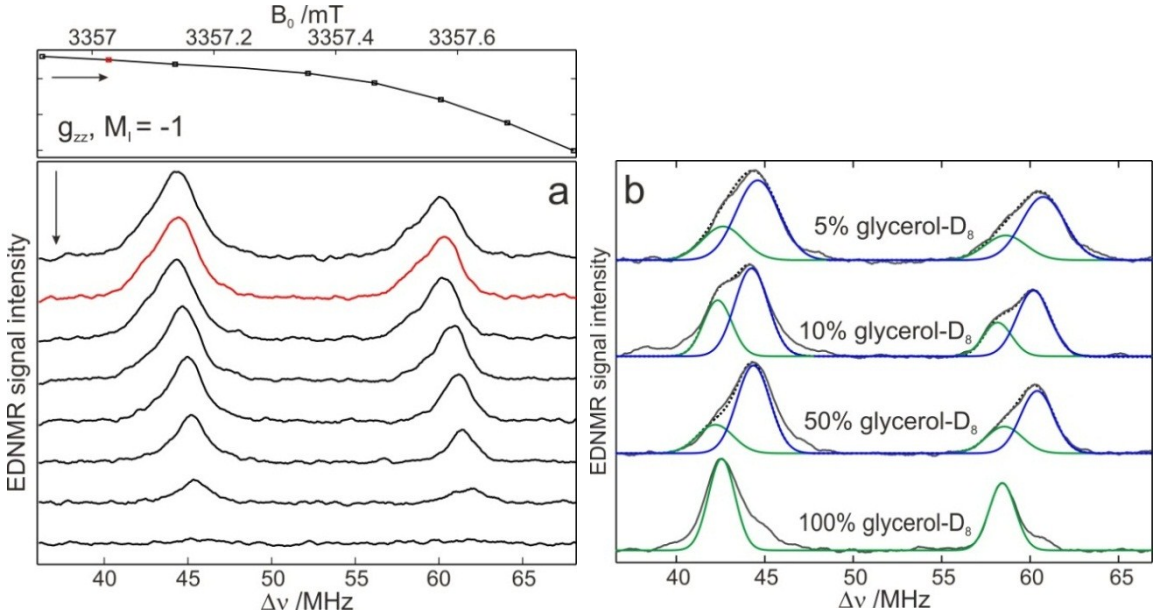

Figure 6.4 *(a) Individual experimental EDNMR recordings at magnetic field positions indicated at the top acquired for 1 mM R1-D_{16} in frozen solution of D_2O/glycerol-D_8 (50/50 v/v). They are recorded at 80 K before annealing the sample for 1 h at 200 K. The red line shows the trace chosen for simulation. (b) Experimental W-band EDNMR spectra of R1-D_{16} in frozen solution of D_2O/glycerol-D_8 mixtures recorded under identical experimental settings at 80 K before annealing the sample for 1 h at 200 K (230 K). The volume of added glycerol-D_8 is indicated. The simulated spectral contributions corresponding to single and double hydrogen bonded fractions of nitroxides are shown by green and blue traces, respectively. The black dashed lines give the resulting simulated EDNMR spectra.*

Figure 6.5(b) shows the example of the best fit to the experimental EDNMR recording for R1-D_{16} in frozen solution of D_2O/glycerol-D_8 (50/50 v/v), as indicated in Fig. 6.4(a), and of analogous spectra for other D_2O/glycerol-D_8 mixtures. In agreement with W-band cw EPR, EDNMR recordings for different D_2O/glycerol-D_8 compositions are the same, i.e. the positions of ^{14}N EDNMR lines coincide. Only a small variation in the ratio of the spectral components is observed. Table 6.1 contains the summary of evaluated A_{zz} values together with the calculated weights of two nitroxide spin probe fractions. This again confirms the preferential interaction of the nitroxide radical with D_2O molecules over glycerol-D_8. The obtained A_{zz} values for nitroxide dissolved in water are equal to $A^{(1)}_{zz} = 101.6 \pm 0.2$ MHz and $A^{(2)}_{zz} = 106.1 \pm 0.2$.

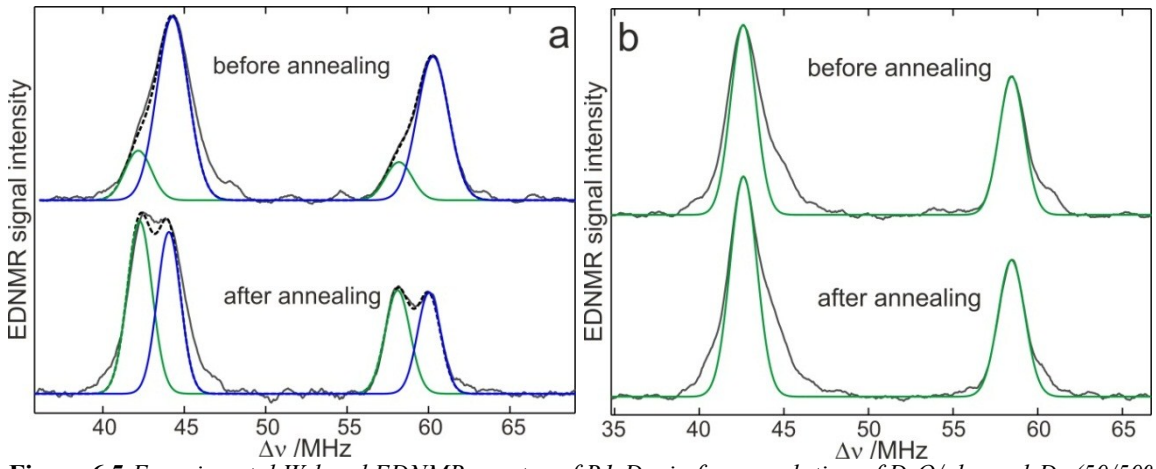

Figure 6.5 *Experimental W-band EDNMR spectra of R1-D_{16} in frozen solution of D_2O/glycerol-D_8 (50/50% v/v) (a) or in anhydrous glycerol-D_8 (b) taken under identical experimental settings at 80 K before (upper grey trace) and after (lower grey trace) annealing the sample for 1 h at 200/230 K. The simulated spectral contributions corresponding to single and double hydrogen bounded fractions of nitroxides are shown by green and blue traces, respectively. The black dashed lines give the resulting simulated EDNMR spectra.*

Table 6.1 *The magnetic parameters of the R1 in frozen solution of D_2O/glycerol-D_8 mixtures obtained from the analysis of W-band EDNMR at 80 K.*

annealing		**5% glycerol-D_8**	**10% glycerol-D_8**	**50% glycerol-D_8**	**100% glycerol-D_8**
before	**$A^{(1)}_{zz}$ /MHz**	101.7 ± 0.2	101.6 ± 0.2	101.6 ± 0.2	101.9 ± 0.1
	$fr^{(1)}$	0.28 ± 0.03	0.33 ± 0.03	0.22 ± 0.04	~ 0.80 ± 0.05
	$\Delta B_{½}{}^{(1)}$ /MHz	2.7 ± 0.1	1.9 ± 0.1	2.4 ± 0.1	1.75 ± 0.1
	$A^{(2)}_{zz}$ /MHz	106.4 ± 0.2	106.2 ± 0.2	106.1 ± 0.2	—
	$fr^{(2)}$	0.72 ± 0.03	0.67 ± 0.03	0.78 ± 0.04	—
	$\Delta B_{½}{}^{(2)}$ /MHz	2.9 ± 0.1	2.2 ± 0.1	2.2 ± 0.1	—
after	**$A^{(1)}_{zz}$ /MHz**	101.8 ± 0.2	101.7 ± 0.2	101.3± 0.2	101.8 ± 0.1
	$fr^{(1)}$	0.47 ± 0.04	0.48 ± 0.04	0.47 ± 0.03	~ 0.80 ± 0.05
	$\Delta B_{½}{}^{(1)}$ /MHz	2.2 ± 0.1	1.95 ± 0.1	1.7 ± 0.1	1.9 ± 0.1
	$A^{(2)}_{zz}$ /MHz	106.2 ± 0.2	106.3 ± 0.2	106.0 ± 0.2	—
	$fr^{(2)}$	0.53 ± 0.04	0.52 ± 0.04	0.53 ± 0.03	—
	$\Delta B_{½}{}^{(2)}$ /MHz	2.2 ± 0.1	1.95 ± 0.1	1.9 ± 0.1	—

They characterize nitroxide spin probe populations that form single H-bond and two H-bonds with water molecules, respectively. Detailed analysis of W-band EDNMR spectra recorded before and after annealing gives insight into the possible influence exerted by the annealing procedure on the average A_{zz} hyperfine coupling value, as determined in W-band cw EPR experiment. Fig. 6.5(a) presents the EDNMR recordings at corresponding spectral positions when measured before and after the annealing. Interestingly, the annealing does not shift the position of EDNMR lines, but influences the ratio of the two spectral components in favor of the pair that is centered around the smaller A_{zz} hyperfine coupling constant, see Table 6.1. Therefore it can be concluded, that annealing promotes a change in the equilibrium between two nitroxide spin probe populations in favour of single H-bonded

nitroxide. This is opposed to the situation encountered in shock-frozen samples, where double H-bonded nitroxides dominate. In addition, upon annealing the EDNMR linewidth slightly decreases for both spectral components. The annealing results in more homogenous and better defined spin probe environment.

To ascertain the assignment of nitroxide spin probe fractions, the magnetic parameters, i.e. g_{xx} and A_{zz} values obtained from 244 GHz cw EPR and W-band EDNMR experiments, were included in the g_{xx} vs. A_{zz} plot presented in Chapter 5.

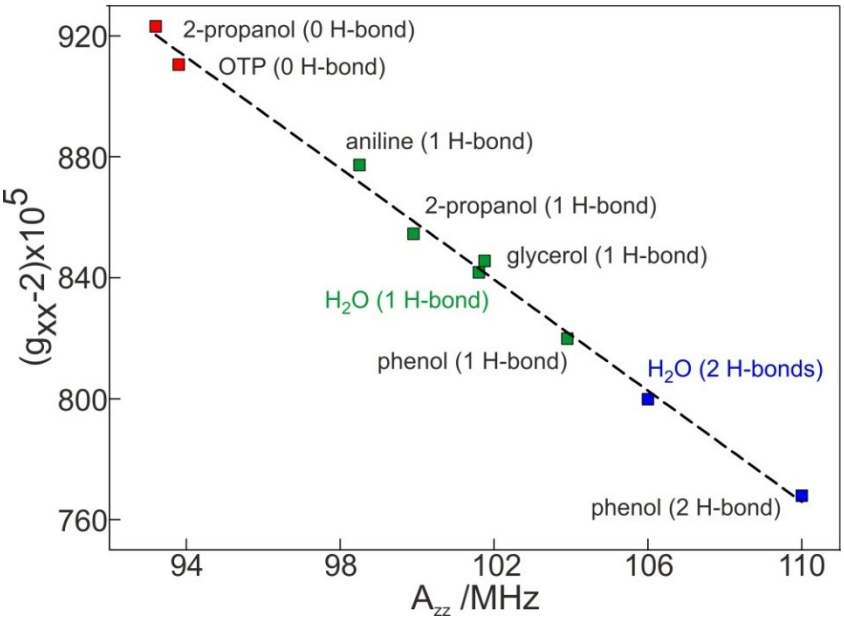

Figure 6.6 *Plot of g_{xx} vs A_{zz} for spin probe R1-D_{16} dissolved in various solvents. The values measured for nitroxide dissolved in D_2O/glycerol-D_8 mixture are marked in red.*

Indeed, the values extracted for nitroxide dissolved in water/glycerol mixtures align perfectly on the line calculated for certain protic solvents. This supports the assignment of nitroxide forming one and two H-bonds with water molecules. Moreover, the points can be divided in certain groups: nitroxide forming 0 H-bonds, 1 H-bond or 2 H-bonds.

The obtained g_{xx} vs A_{zz} slope is -2.57±0.05 T^{-1}. It is smaller than theoretically calculated value of -6.5 T^{-1}, but comparable to previously obtained experimental value of Wegener et al.

6.4 Annealing induced rearrangement of the H-bond network around the nitroxide spin label in spin-labeled T4-lysozyme

A single mutant of spin-labeled T4-lysozyme was used as a test example to investigate whether the rearrangement of the H-bond network observed for spin probes dissolved in water/glycerol mixtures is seen to the same extent in spin-labeled proteins. Fig. 6.7 presents the structure of the chosen T4-lysozyme mutant together with pre-computed nitroxide rotamers for the spin-labeled position 96, using the RLA approach implemented in the MMM program. Irrespective of whether rotamers pre-calculated at RT or at 175 K are chosen, a similar set of rotamers is obtained (25 and 27 rotamers at 175 K or RT, respectively).

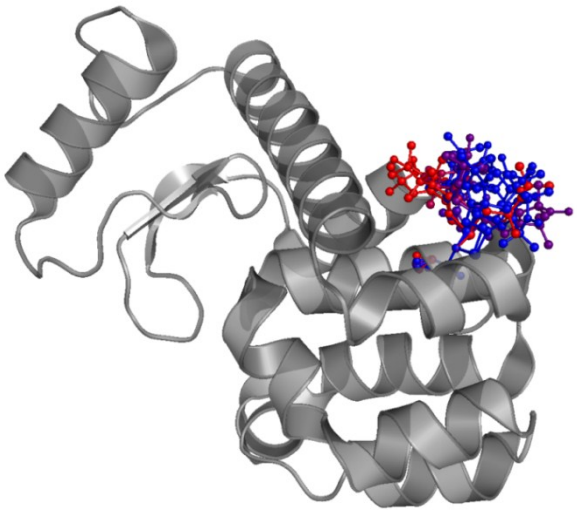

Figure 6.7 *A cartoon representation of the T4 lysozyme crystal structure, (PDB ID: 2Q9D), spin-labeled at position 96. The R1 rotamers calculated with MMM at cryogenic temperature (175 K) are shown in the 'ball and stick' representation with the color coded occupancy (blue for the smallest occupancy and red for the largest).*

The W-band EDNMR spectra recorded before and after annealing are shown in Fig. 6.8. In the chosen T4-lysozyme mutant, the spin label is solvent exposed, hence a behavior similar to spin probe in water/glycerol matrix would be expected. Interestingly, the change in the fractions of spin-label populations is minimal − the fraction of single H-bonded nitroxide radical changes from 35% to 39%, see Table 6.2.

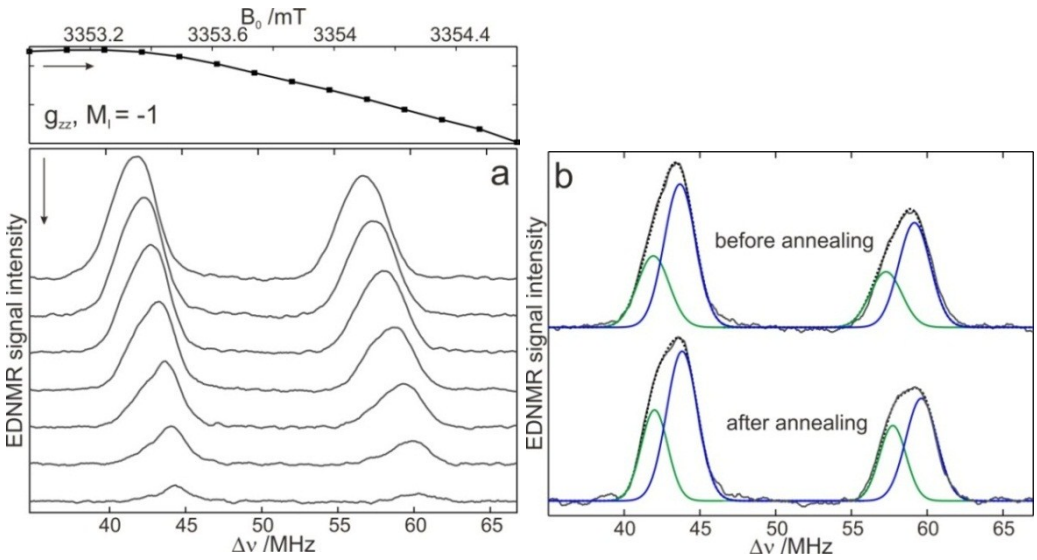

Figure 6.8 (a) *Individual experimental EDNMR recordings at magnetic field positions indicated at the top acquired at 60 K for 270 μM MTS spin-labeled T4-lysozyme in frozen solution of 25 mM MOPS buffer, pH = 7.6 with 20% glycerol-D_8 (v/v) before (a) and after (b) annealing the sample for 1 h at 200 K. (b) Experimental W-band EDNMR spectra of 270 μM MTS spin-labeled T4-lysozyme in 25 mM MOPS buffer, pH = 7.6, recorded under identical experimental settings at 60 K before (upper grey trace) and after (lower grey trace) annealing the sample for 1 h at 200 K. The simulated spectral contributions corresponding to single and double hydrogen bounded fractions of nitroxides are shown by green and blue traces, respectively. The black dashed lines give the resulting simulated EDNMR spectra.*

This might suggest that for the chosen spin label position, shock freezing of the sample promotes a nitroxide microenvironment where a single H-bond to the nitroxide moiety is formed. It cannot be excluded, however, that the local glycerol concentration is enhanced as compared to free radical in solution, thereby decreasing the fraction of nitroxide population forming two H-bonds in the shock frozen sample. Therefore, during the process of shock-freezing the intermolecular H-bonds which are energetically more demanding are already disrupted.

Table 6.2 *The magnetic parameters of MTS spin-labeled T4-lysozyme obtained from the analysis of W-band EDNMR spectra at 60 K.*

annealing	$A_{zz}^{(1)}$ /MHz	$fr^{(1)}$	$A_{zz}^{(2)}$ /MHz	$fr^{(2)}$
before	100.6 ± 0.2	0.35 ± 0.06	104.6 ± 0.2	0.65 ± 0.05
after	100.5 ± 0.2	0.39 ± 0.04	104.3 ± 0.2	0.61 ± 0.04

6.5 Conclusions and outlook

The thermal history of frozen samples of nitroxides in water solutions causes variation in the microenvironment of the nitroxide spin probes. In detail, the water H-bond network around the nitroxide reorganizes upon sample annealing, i.e. heating above 180 K. This rearrangement occurs at temperature close to T_g, as was shown recently for nitroxide spin probes dissolved in water/glycerol mixtures using X-band power saturation cw EPR study [22] and for small protein using various NMR relaxations [42]. As a result, H-bond network trapped by freezing the solution is modified towards a nitroxide population with prevalent single H-bond. This poses important consequences for the analysis of the polarity/proticity in the vicinity of nitroxide spin probe/radical since similar annealing can be achieved simply by storing the sample in a -80°C freezer. Therefore, reproducible sample preparation methodology would be necessary to obtain reliable polarity/proticity profiles in biomacromolecules. However, since in the studied SDSL protein example no pronounced changes were observed, further studies including larger number of spin-labeled proteins are necessary to determine whether different protein sites, depending on the degree of solvent accessibility, would correspond differently to the thermal history of the sample. Interestingly, it was observed for different spin-labeled T4-lysozyme, that the cooling rate played an important role in determining the ensemble of trapped spin label rotamers, influencing the measured distance distribution − but not the average nitroxide-nitroxide distance extracted from 4-pulse PELDOR measurements [33].

References

[1] A.D. Milov, A.B. Ponomarev, Yu.D. Tsvetkov *Electron-electron double resonance in electron spin echo: Model biradical systems and the sensitized photolysis of decalin*. Chem. Phys. Lett. **1984,** 110*,* 67-72.

[2] M. Pannier, S. Veit, A. Godt, G. Jeschke, H.W. Spiess *Dead-time free measurement of dipole-dipole interactions between electron spins*. J. Magn. Reson. **2000,** 142*,* 331-340.

[3] G. Jeschke *DEER distance measurements on proteins*. Annu. Rev. Phys. Chem. **2012,** 63*,* 419-446.

[4] W.L. Hubbell, C. Altenbach *Investigation of structure and dynamics in membrane proteins using site-directed spin labeling*. Curr. Opin. Struct. Biol. **1994,** 4*,* 566-573.

[5] W.L. Hubbell, C.J. López, C. Altenbach, Z. Yang *Technological advances in site-directed spin labeling of proteins*. Curr. Opin. Struct. Biol. **2013,** 23*,* 725-733.

[6] J.P. Klare, H.-J. Steinhoff Structural information from spin-labelled membrane-bound proteins. in: C. R. Timmel and J. R. Harmer (Eds.), Structural information from spin-labels and intrinsic paramagnetic centers in the biosciences, Springer-Verlag, Heidelberg, 2014, pp. 206-249.

[7] S. Bleicken, G. Jeschke, C. Stegmueller, R. Salvador-Gallego, A.J. García-Sáez, E. Bordignon *Structural model of active Bax at the membrane*. Mol. Cell **2014,** 56*,* 496-505.

[8] I. Hänelt, D. Wunnicke, E. Bordignon, H.-J. Steinhoff, D.J. Slotboom *Conformational heterogeneity of the aspartate transporter* Glt_{Ph}. Nature Struct. Mol. Biol. **2013,** 20*,* 210-214.

[9] L. Hoffman, R.A. Stein, R.J. Colbran, H.S. Mchaourab *Conformational changes underlying calcium/calmodulin-dependent protein kinase II activation*. EMBO J. **2011,** 30*,* 1251-1262.

[10] R. Ward, A. Bowman, E. Sozudogru, H. El-Mkami, T. Owen-Hughes, D.G. Norman *EPR distance measurements in deuterated proteins*. J. Magn. Reson. **2010,** 207*,* 164-167.

[11] G. Jeschke, A. Koch, U. Jonas, A. Godt *Direct conversion of EPR dipolar time evolution data to distance distributions*. J. Magn. Reson. **2002,** 155*,* 72-82.

[12] H. Frauenfelder, S.G. Sligar, P.G. Wolynes *The energy landscapes and motions of proteins*. Science **1991,** 254*,* 1598-1603.

[13] F.G. Parak *Physical aspects of protein dynamics*. Rep. Prog. Phys. **2003,** 66*,* 103-129.

[14] Z. Yang, Y. Liu, P. Borbat, J.L. Zweier, J.H. Freed, W.L. Hubbell *Pulsed ESR dipolar spectroscopy for distance measurements in immobilized spin labeled proteins in liquid solution*. J. Am. Chem. Soc. **2012,** 134*,* 9950-9952.

[15] Z. Yang, G. Jiménez-Osés, C.J. López, M.D. Bridges, K.N. Houk, W.L. Hubbell *Long-range distance measurements in proteins at physiological temperatures using saturation recovery EPR spectroscopy*. J. Am. Chem. Soc. **2014,** 136*,* 15356-15365.

[16] G.Yu. Shevelev, O.A. Krumkacheva, A.A. Lomzov, A.A. Kuzhelev, O.Yu. Rogozhnikova, D.V. Trukhin, T.I. Troitskaya, V.M. Tormyshev, M.V. Fedin, D.V. Pyshnyi, E.G. Bagryanskaya *Physiological-temperature distance measurement in nucleic acid using triarylmethyl-based spin labels and pulsed dipolar EPR spectroscopy*. J. Am. Chem. Soc. **2014,** 136*,* 9874-9877.

[17] G. Jeschke, M. Sajid, M. Schulte, N. Ramezanian, A. Volkov, H. Zimmermann, A. Godt *Flexibility of shape-persistent molecular building blocks composed of p-phenylene and ethynylene units*. J. Am. Chem. Soc. **2010,** 132*,* 10107-10117.

[18] W. Doster, S. Busch, A.M. Gaspar, M.-S. Appavou, J. Wuttke, H. Scheer *Dynamical transition of protein-hydration water*. Phys. Rev. Lett. **2010,** 104*,* 098101-1-098101-4.

[19] G. Jeschke *Conformational dynamics and distribution of nitroxide spin labels*. Prog. Nucl. Magn. Reson. Spectr. **2013,** 72*,* 42-60.

[20] Y. Polyhach, E. Bordignon, G. Jeschke *Rotamer libraries of spin labelled cysteines for protein studies*. Phys. Chem. Chem. Phys. **2011,** 13*,* 2356-2366.

[21] G. Hagelueken, R. Ward, J.H. Naismith, O. Schiemann *MtsslWizard: In silico spin-labeling and generation of distance distributions in PyMOL*. Appl. Magn. Reson. **2012,** 42*,* 377-391.

[22] E. Bordignon, A.I. Nalepa, A. Savitsky, L. Braun, G. Jeschke *Changes in the microenvironment of nitroxide radicals around the glass transition temperature*. J. Phys. Chem. B **2015,** 119, 13797-13806.

[23] Y. Miwa, K. Yamamoto *Simple and highly sensitive measurement method for detection of glass transition temperatures of polymers: Application of ESR power saturation phenomenon with conventional spin-probe technique*. J. Phys. Chem. B **2012,** 116*,* 9277-9284.

[24] Y. Miwa, O. Urakawa, A. Doi, K. Yamamoto, S. Nobukawa *Glass transition temperature and β relaxation temperature around chain end of polystyrene determined by site specific spin labeling*. J. Phys. Chem. B **2012,** 116*,* 1282-1288.

[25] D. Klose, J.P. Klare, D. Grohmann, C.W.M. Kay, F. Werner, H.-J. Steinhoff *Simulation vs. reality: A comparison of in silico distance predictions with DEER and FRET measurements*. PLoS One **2012,** 7*,* e39492.

[26] Y. Polyhach, G. Jeschke *Prediction of favourable sites for spin labelling of proteins*. Spectrosc.- Int. J. **2010,** 24*,* 651-659.

[27] N. Florin, O. Schiemann, G. Hagelueken *High-resolution crystal structure of spin labelled (T21R1) azurin from Pseudomonas aeruginosa: a challenging structural benchmark for in silico spin labelling algorithms*. BMC Struct. Biol. **2014,** 14.

[28] E. Bordignon, H. Brutlach, L. Urban, K. Hideg, A. Savitsky, A. Schnegg, P. Gast, M. Engelhard, E.J.J. Groenen, K. Möbius, H.-J. Steinhoff *Heterogeneity in the nitroxide micro-environment: polarity and proticity effects in spin-labeled proteins studied by multi-frequency EPR*. Appl. Magn. Reson. **2010,** 37*,* 391-403.

[29] P. Gast, R.T.L. Herbonnet, J. Klare, A. Nalepa, C. Rickert, D. Stellinga, L. Urban, K. Möbius, A. Savitsky, H.-J. Steinhoff, E.J.J. Groenen *Hydrogen bonding of nitroxide spin labels in membrane proteins*. Phys. Chem. Chem. Phys. **2014,** 16*,* 15910-15916.

[30] A. Nalepa, K. Möbius, W. Lubitz, A. Savitsky *High-field ELDOR-detected NMR study of a nitroxide radical in disordered solids: Towards characterization of heterogeneity of microenvironments in spin-labeled systems*. J. Magn. Reson. **2014,** 242*,* 203-213.

[31] L. Urban, H.-J. Steinhoff *Hydrogen bonding to the nitroxide of protein bound spin labels*. Mol. Phys. **2013,** 111*,* 2873-2881.

[32] C.J. López, M.R. Fleissner, Z. Guo, A.K. Kusnetzow, W.L. Hubbell *Osmolyte perturbation reveals conformational equilibria in spin-labeled proteins*. Protein Sci. **2009,** 18*,* 1637-1652.

[33] E.R. Georgieva, A.S. Roy, V.M. Grigoryants, P.P. Borbat, K.A. Earle, C.P. Scholes, J.H. Freed *Effect of freezing conditions on distances and their distributions derived from Double Electron Electron Resonance (DEER): A study of doubly-spin-labeled T4 lysozyme*. J. Magn. Reson. **2012,** 216*,* 69-77.

[34] I.E.T. Iben, D. Braunstein, W. Doster, H. Frauenfelder, M.K. Hong, J.B. Johnson, S. Luck, P. Ormos, A. Schulte, P.J. Steinbach, A.H. Xie, R.D. Young *Glassy behavior of a protein*. Phys. Rev. Lett. **1989,** 62*,* 1916-1919.

[35] V. Réat, R. Dunn, M. Ferrand, J.L. Finney, R.M. Daniel, J.C. Smith *Solvent dependence of dynamic transitions in protein solutions*. Proc. Natl. Acad. Sci. USA **2000,** 97*,* 9961-9966.

[36] R. Ward, D.J. Keeble, H. El-Mkami, D.G. Norman *Distance determination in heterogeneous DNA model systems by pulsed EPR*. ChemBioChem **2007,** 8*,* 1957-1964.

[37] A. Savitsky, A.A. Dubinskii, M. Plato, Y.A. Grishin, H. Zimmermann, K. Möbius *High-field EPR and ESEEM investigation of the nitrogen quadrupole interaction of nitroxide spin labels in disordered solids: Toward differentiation between polarity and proticity matrix effects on protein function*. J. Phys. Chem. B **2008,** 112*,* 9079-9090.

[38] E. Reijerse, P.P. Schmidt, G. Klihm, W. Lubitz *A CW and pulse EPR spectrometer operating at 122 and 244 GHz using a quasi-optical bridge and a cryogen-free 12 T superconducting magnet*. Appl. Magn. Reson. **2007,** 31*,* 611-626.

[39] M. Plato, H.-J. Steinhoff, C. Wegener, J.T. Törring, A. Savitsky, K. Möbius *Molecular orbital study of polarity and hydrogen bonding effects on the g and hyperfine tensors of site directed NO spin labelled bacteriorhodopsin*. Mol. Phys. **2002,** 100*,* 3711-3721.

[40] M. Pavone, A. Sillanpää, P. Cimino, O. Crescenzi, V. Barone *Evidence of variable H-bond network for nitroxide radicals in protic solvents*. J. Phys. Chem. B **2006,** 110*,* 16189-16192.

[41] B. Dzikovski, D. Tipikin, J.H. Freed *Conformational distributions and hydrogen bonding in gel and frozen lipid bilayers: a high frequency spin-label ESR study*. J. Phys. Chem. B **2012,** 116*,* 6694-6706.

[42] J.R. Lewandowski, M.E. Halse, M. Blackledge, L. Emsley *Direct observation of hierarchical protein dynamics*. Science **2015,** 348*,* 578-581.

Chapter 7

Investigation of local water exchange processes in photosynthetic reaction centers (bRCs) of *Rhodobacter sphaeroides* R26 embedded in trehalose matrices

7.1 Introduction

Water molecules play an important role in the process of protein folding [1], modulate the protein dynamics [2] and can be directly involved in the protein function, e.g. by facilitating the proton transfer [3]. To understand the extent of influence exerted by H_2O on the structure and function of a particular protein, it is of importance to obtain information on site-specific water accessibility. As reviewed in chapter 3.4, EPR spectroscopy at X-band in conjunction with nitroxide spin labeling offers an attractive methodology to obtain this information both in the case of soluble and membrane proteins. The local water accessibility can be measured directly by probing the hyperfine interaction of the unpaired electron spin with D or ^{17}O nuclei of isotopic labeled water by pulsed EPR. The often-used ESEEM technique fails when moving to higher magnetic fields, e.g. W-band (94 GHz/3.4 T), due to limited mw power and pulse excitation bandwidth [4]. Performing the solvent accessibility studies by EPR at higher magnetic fields, however, offers the advantage of very small sample volume required: only ≈ 5 µl at W-band as compared to ≈ 100 µl typically required at X-band, significantly reducing the sample preparation costs. In previous chapters the sensitivity of W-band EDNMR method to probing the local environment using the hyperfine coupling constant associated with internal ^{14}N of nitroxide radical could be demonstrated. This chapter evaluates the applicability of W-band EDNMR technique for characterization of site-specific water accessibility in proteins, it therefore requires sensitive detection of weakly coupled, external nuclei. As a model protein system, the bacterial photosynthetic reaction center (bRC) from *Rhodobacter sphaeroides* R26 was chosen, see Fig. 7.1. This protein catalyzes the initial photochemical processes in the conversion of light into chemical free energy. A number of reviews provide detailed descriptions of the mechanism of light-driven electron transfer in this bacterial reaction centres, see [5-7]. The first crystal structure of bRC from *Rb. sphaeroides* was obtained already in the 1980s [8;9] and recently, the structure with the highest up-to-date resolution of 1.87 Å was reported [10]. Bacterial RC is formed by three polypeptide subunits (termed L, M and H), with subunits L and M spanning across the membrane and the subunit H protruding towards the cytoplasm. The protein contains five cysteine residues which are buried within the protein interior, except for cysteine 156 in subunit H. It can therefore be selectively labeled with the MTS spin label [11;12], making it amenable to EPR studies. Additionally, the protein

itself contains 9 cofactors, some becoming transiently paramagnetic during subsequent electron transfer steps. Fig. 7.1(a) shows the structural arrangement of the native cofactors within the bRC from *Rb. sphaeroides* R26. These include four molecules of bacteriochlorophyll *a* (BChl *a*), two molecules of bacteriopheophytin *a* (BPhe *a*), two molecules of ubiquinone (primary quinone Q_A and secondary quinone Q_B) and a non-heme iron, Fe^{2+}. Two BChl molecules, P_A and P_B, which form a special pair P_{865}, are located between the L and M subunits, close to the periplasmic side of the membrane. The first tetrapyrrole rings of both molecules overlap and the small distance between the two macrocycle planes (ca. 3.4 Å) results in electronic overlap, albeit with asymmetric electronic distribution [13]. The remaining cofactors form two electron transfer branches, A and B, that lead from the BChl P_{865} dimer to the secondary quinone, Q_B, on the cytoplasmic side of the membrane, see Fig. 7.1(a).

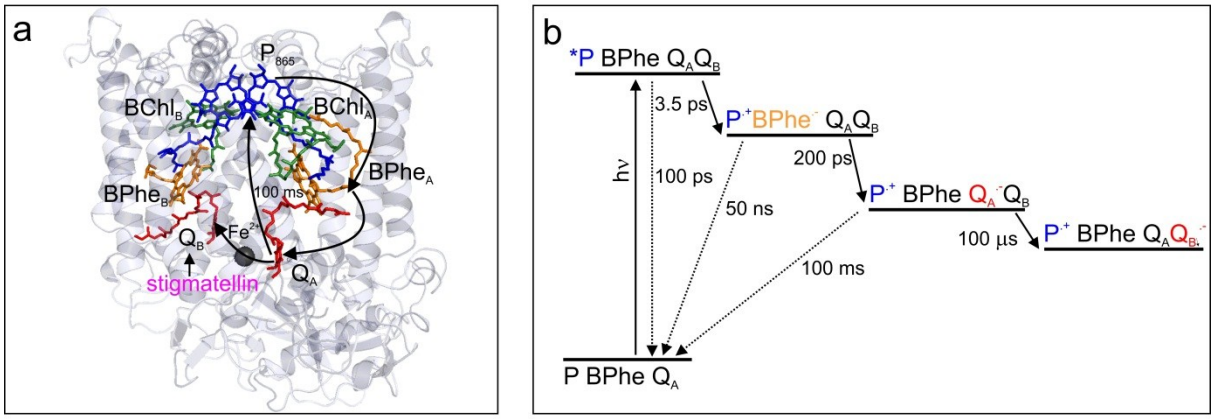

Figure 7.1 *(a) Structure of bRC from Rb. sphaeroides R26 based on the X-ray structural model, (pdb id: 1AIJ), with the protein subunits marked in light grey and the cofactors P_{865}, BChl, BPhe, Q, Fe in a stick representation. (b) The cascade of transmembrane charge-separation steps with the electron transfer time constants at room temperature in liquid solution.*

Despite the apparent twofold local symmetry of the cofactor arrangement, the electron transfer (ET) pathway is one-sided and takes place along the A branch. Light excitation of the bRC photo-oxidizes the primary donor, P_{865}, and the electron transfer takes place through a series of electron acceptors: bacteriochlorophyll, bacteriopheophytin and two ubiquinone molecules Q_A and Q_B as schematically shown in Fig. 7.1(b). Upon double reduction, Q_B binds two protons forming the dihydroquinone, Q_BH_2, and dissociates from the bRC. The resultant proton gradient generated across the membrane drives the ATP synthesis. When the electron transfer to Q_B is prevented by quinone deprivation or binding of inhibitor at the Q_B site, the primary charge separated state $P_{865}^{+\cdot}Q_A^{-\cdot}$ recombines to $P_{865}Q_A$, see scheme in Fig. 7.1(b). The two native cofactors of interest for this study are the ionic states of P_{865} and Q_A that form charge-separated state $P_{865}^{+\cdot}Q_A^{-\cdot}$ when weakly bound Q_B is replaced from its protein pocket by stigmatellin.

Bacterial RC is therefore exceptionally suited as model system for solvent accessibility studies, providing three paramagnetic centers with very different spectral characteristics and location within the protein: spin label attached to protein surface and two native cofactors that can be prepared conveniently in the paramagnetic state, see Figs. 7.2(a) and (b). The amino acid environment in the vicinity of these paramagnetic centers is well-known, based on the available X-ray structures [10;17;18]. Understandably the water molecules and protonable residues in the vicinity of Q_B have been characterized in most detail in order to identify possible pathways for proton transfer into the

bRC [18;19], eventually leading to identification of a chain of strongly bound water molecules in the vicinity of Q_B that connect the Q_B binding pocket to the surface of protein [18;20;21]. However, a cluster consisting of 10 strongly-bound water molecules has also been identified in the vicinity of the primary quinone, Q_A, separated from it by 5-12 Å [21].

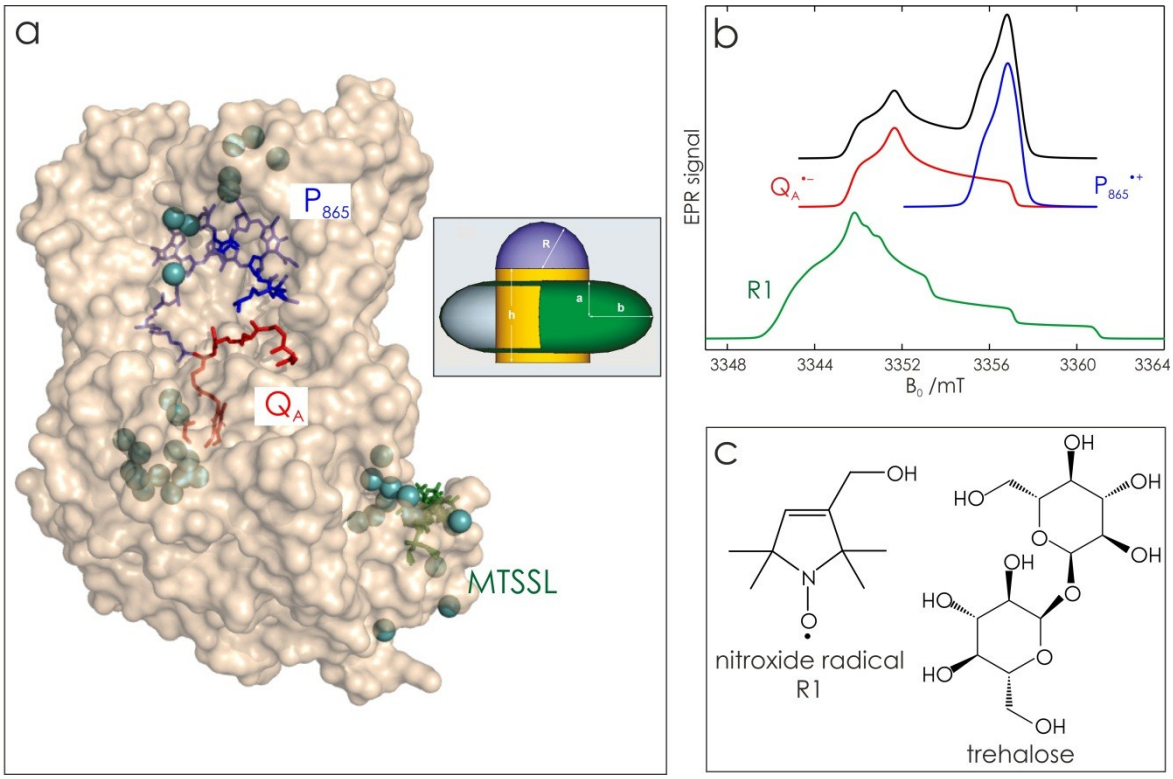

Figure 7.2 *(a) The molecular surface representation of RC from Rhodobacter sphaeroides with indicated primary donor P_{865} (in blue), primary acceptor Q_A (in red) cofactors and nitroxide radical attached to Cys156 in H-subunit (in black). Strongly bound water molecules within 10 Å radius of each paramagnetic center are shown as cyan spheres, based on X-ray structure (pdb: 1AIJ). The inset shows the geometric model of detergent belt around L and M subunits of bRC, adapted from [29]. (b) On top the simulated rigid limit W-band EPR absorption spectra of $P_{865}^{\bullet+}$ (blue trace) and $Q_A^{\bullet-}$ (red trace) ionic states of primary donor and acceptor are shown. For the simulation previously reported magnetic parameters values were used [14;15]. On bottom the simulated rigid limit W-band EPR absorption spectrum of MTS spin label (green trace) is shown. The used magnetic parameters values were previously reported for a nitroxide dissolved in water/glycerol mixture [16]. (c) Chemical structures of pyrroline type nitroxide radical R1 and trehalose.*

It is worthwhile to mention that bRC has been extensively used as a model system to investigate the structure-function-dynamics relationship in membrane proteins, owing to the fact that the electron transfer steps strongly depend on the protein's conformational dynamics [22]. The pivotal work of Kleinfeld et al. [22], subsequently extended by McMahon [23], showed that following a short (ns) photoexcitation, at room tempeature the bRC relaxes from a 'dark-adapted' to a 'light-adapted' conformation, which stabilizes the primary charge separated state $P_{865}^{+}Q_A^{-}$. The crystal structures of bRC in these two conformations could be obtained [20], allowing to analyze the structural differences in detail. The two conformations can be trapped by freezing the bRCs at cryogenic temperatures in dark or under illumination. At low temperature, the kinetics of $P_{865}^{+}Q_A^{-}$ recombination in 'dark-

adapted' bRCs becomes largely distributed in rate. This indicates that the bRCs are trapped over a large ensemble of conformational substates that differ in the stability of the charge separated state. Similar inhibition of the protein dynamics, as judged by lifetime of the charge separated $P_{865}^{+}Q_A^{-}$ state, could be achieved at room temperature in the presence of a dehydrated sugar glassy matrix embedding the bRCs due to coupling between sugar matrix and protein that blocks the transition between conformational sub-states [24-27]. Importantly, increasingly dehydrated sugar becomes a rigid matrix which stabilizes the protein structure despite extensive dehydration, preventing it from unfolding [28]. Therefore, in this work the bRC was similarly embedded in trehalose matrix allowing for hydration level variation while preserving the protein fold. The aim was to test the influence of dehydration/rehydration on local water accessibility at the sites of three paramagnetic centers using W-band EDNMR. The two hydration levels investigated in this work correspond to two very different regimes of protein dynamics: at lower hydration level, the recombination kinetic of the $P_{865}^{+}Q_A^{-}$ state after a laser pulse becomes strongly accelerated and distributed in rate, mimicking at room temperature the effects observed at cryogenic temperatures [29], while at higher hydration level the charge recombination kinetics indicates that protein dynamics in sugar is close to that in solution. The EPR measurements, however, are done at low temperature as required by the relaxation properties of paramagnetic centers. For practical reasons two bRC variants were investigated in this work: (i) native bRC with Fe^{2+} replaced by diamagnetic Zn^{2+} and (ii) nitroxide spin-labeled bRC. This is necessary due to partial overlap of the respective EPR spectra of ionic states of native cofactors with nitroxide radical, see Fig. 7.2(b).

7.2 Material and methods

Chemicals

LDAO (N,N-dimethyldodecylamine N-oxide) solution (~30% in H_2O) was purchased from Fluka. Trehalose (α-D-glucopyranosil α-D-glucopyranoside), stigmatellin, lithium chloride, potassium carbonate and sodium chloride salts were obtained from Sigma-Aldrich. The nitroxide spin probe 3-hydroxymethyl-2,2,5,5-tetramethylpyrrolin-1-oxyl, whose structure is shown in Fig. 7.1 (c), was used in protonated form and is referred to as R1 throughout the text. The nitroxide radical used for spin labeling of RC was MTS ((1-oxyl-2,2,5,5-tetramethylpyrroline-3-methyl)methanethiosulfonate). The nitroxide radicals were synthesized as described previously [30] and kindly provided by Herbert Zimmermann (MPI for Medical Research, Heidelberg).

Sample preparation

The reaction centers (RCs) from *Rhodobacter sphaeroides* R26 were purified according to previously published protocol using LDAO as a detergent [31]. Two protein variants were investigated: (i) nitroxide-labeled variant, further referred to as SL-RC, obtained by labeling the native cysteine H156 with MTS spin label [11] (ii) protein variant with the non-heme Fe^{2+} replaced by diamagnetic Zn^{2+} [32], referred to as Zn^{2+}-RC throughout the text. The protein was kindly provided by Dr. Marco Malferrari and Prof. Giovanni Venturoli (Dipartimento di Farmacia e Biotecnologie, University of Bologna).

Both Fe^{2+}- and Zn^{2+}-containing RCs preparations were concentrated to 335 μM and supplemented with stigmatellin, potent inhibitor of the $Q_A^{\bullet-}$-to-Q_B electron transfer [33]. The replacement of Q_B with

stigmatellin and removal of the iron in Zn^{2+}-RC variant allows to avoid fast spin relaxation of $Q_A^{\bullet-}$ radical anion by high spin Fe^{2+} (S = 2) and also the formation of semiquinone biradical $Q_A^{\bullet-}$ $Q_B^{\bullet-}$ in the next electron transfer step. Hence, exclusively charge-separated primary donor-acceptor radical pair, $P_{865}^{\bullet+}$-$Q_A^{\bullet-}$, is formed in Zn^{2+}-RC variant upon illumination.

The RCs/trehalose glassy samples for EPR measurements were prepared as described previously [27]. In short, 25 μL of the concentrated (335 μM) RC solution was mixed with 25 μL of 1.67 M trehalose dissolved in 10 mM Tris/HCl buffer containing 0.025% LDAO, resulting in the sugar/RC molar ratio of $5 \cdot 10^3$. The RC/trehalose solution was layered on an optical glass and dried in a desiccator under N_2 flow at room temperature. The glassy sample was obtained after about 4 h of flux. Subsequently, samples were transferred into sealed container where further dehydration occured via exposition to an atmosphere of low relative humidity (RH) of 11%. This isopiestic method has been already employed in both IR [29;34] and EPR studies on RC/trehalose films [35]. The dehydrated RC/trehalose glasses were then crumbled into small flakes and inserted into the cylindrical quartz capillaries (i.d. 0.6 mm) for further equilibration with either D_2O or $H_2{}^{17}O$ vapor to desired RH using saturated solution of adequate salt [36] prepared in isotope labeled water. In the present study the three hydration levels of RC/trehalose glasses were obtained at room temperature using LiCl (RH=11%), K_2CO_3 (RH=43%) or NaCl (RH=74%) saturated solutions. Placing of the layer of saturated salt solution inside EPR capillary resulted in change of RH, which translates into overall change of sugar glass hydration level. Throughout the text, the type of water vapor used in the equilibration is indicated in the brackets following the value of RH, e.g. 11% (D_2O) corresponds to equilibration at RH=11% using saturated LiCl solution prepared in D_2O.

The R1 nitroxide spin probe/trehalose glasses were prepared in an analogous way, except for higher nitroxide concentration (~1 mM) and lack of detergent in the starting trehalose solution.

EPR measurements

The pulsed EPR experiments were performed on a modified Bruker Elexsys E680 spectrometer operating at about 94 GHz (W-band) [37]. For optical sample irradiation, the light was guided to the cavity through a quartz fiber. The electron transfer was initiated by singlet excitation of the primary donor P_{865} at wavelength of 695 nm using cw diode laser. The RC/trehalose glasses were frozen in the dark and transferred into the precooled EPR cryostat. The EPR measurements were performed at either 60 K (for SL-RC and R1) or 130 K (for Zn^{2+}-RC).

The ESE measurements were performed using two-pulse Hahn-echo sequence for primary spin-echo generation: t_p-τ-$2t_p$-τ-echo. The pulse length t_p of the π/2 mw pulse was generally set to 56 ns for nitroxide radical and to 24 ns for $P_{865}^{+\cdot}$ and $Q_A^{-\cdot}$ ionic states of cofactors. The EPR signals originating from nitroxide radicals and charge-separated primary donor-acceptor radical pair $P_{865}^{\cdot+}Q_A^{\cdot-}$ partially overlap at W-band frequency, see Fig. 7.2(b). Hence, two protein variants were prepared, allowing selective detection of EPR signal originating from nitroxide radical (SL-RC) or ionic states of primary donor and acceptor (Zn^{2+}-RC). In the dark-adapted state of Zn^{2+}-RC variant, the residual echo-detected EPR signal from $Q_A^{\cdot-}$ is present. The $P_{865}^{\cdot+}Q_A^{\cdot-}$ charge separated state was generated in Zn^{2+}-RCs by continuous light illumination at 865 nm, resulting in the steady-state EPR signal. When the laser is switched off, the EPR signal of $P_{865}^{\cdot+}Q_A^{\cdot-}$ charge separated state decays and virtually no

accumulated P_{865}^{+} signal is observed. Hence, there is no irreversible damage to RCs during continuous sample illumination.

The EDNMR experiments made use of two-pulse Hahn-echo detection at microwave frequency ν_1, matched to the cavity resonance. The high-turning angle (HTA) microwave pulse was applied at the microwave frequency ν_2. The spectra were acquired by continuously sweeping ν_2 at a fixed magnetic field, usually in steps of 70 kHz. The ν_2 sweep range was adjusted depending on the signal of interest. The width of the central blind spot that occurs when ν_2 matches ν_1 was used to measure the mw field amplitude, ω_1, at the mw frequency ν_1 of the detection pulse sequence as described in [37]. The HTA pulse length and mw field amplitude were optimized for the nuclei of interest. For detection of D nuclei in R1/trehalose and SL-RC/trehalose the HTA pulse length was set to 14 μs at $\omega_1^{HTA}(\nu_1)$= 2.2-2.4×10^7 rad/s mw field amplitude. The echo integration window was set to 1.1 or 1.2 μs. For detection of D nuclei in Zn^{2+}-RC, due to overlap with ^{14}N signal, the mw field amplitude was decreased to 1.7·10^7 rad/s and the HTA pulse length was increased to 16 μs. The echo integration window was set to 600 ns. For detection of ^{14}N nuclei in R1/trehalose the HTA pulse length was set to 1.1 μs at $\omega_1^{HTA}(\nu_1)$= 2.6·10^7 rad/s mw field amplitude. The echo integration window was set to 1.0 μs. For detection of ^{17}O nuclei in SL-RC/trehalose the HTA pulse length was set to 20 μs at $\omega_1^{HTA}(\nu_1)$= 1.67×10^7 rad/s mw field amplitude. The echo integration window was set to 800 ns.

The length of the π/2 pulse in detection sequence was always set to 100 ns, the inter-pulse separation was adjusted depending on the chosen integration window. The detection sequence was usually set 4 μs after the HTA pulse to ensure the decay of electron-spin coherency. EDNMR spectra were processed as described previously [37;38]. In short, the spectra were inverted and normalized with respect to the central blind spot depth. The blind spot was subsequently fitted using either Lorentzian line shape or cubic spline and subtracted. The resulting EDNMR signals have intensities between 0 and 1. Since the information content for weakly coupled D and ^{17}O signals is equivalent for left ($\nu_2<\nu_1$) and right ($\nu_2<\nu_1$) hand sides of the EDNMR spectra, only $\Delta\nu=\nu_2-\nu_1>0$ is shown.

ENDOR spectra were recorded using Mims ENDOR sequence for deuterium or Davies ENDOR for ^{17}O nuclei. The τ value of 320 ns was chosen for Mims ENDOR. The length of selective π pulse in Davies ENDOR was set to 300 ns. For RF excitation, an output power of 120 W from a broadband RF amplifier (ZHL-120W-GAN+, Minicircuits, USA) was used. The radiofrequency pulse length was set to 35 μs for D and to 23 μs for ^{17}O.

7.3 Results and discussion

7.3.1 Kinetics of water diffusion within R1/trehalose glass

To use trehalose as a matrix for controlled water exchange around and possibly within the protein embedded in it, first the kinetics of its rehydration alone was determined. The nitroxide/trehalose matrix was first prepared in dehydrated state, using LiCl saturated solution to close the EPR capillary that contained on the opposite end the nitroxide/trehalose powder, thus creating in between the gas phase layer with low relative humidity (RH=11%) set by saturated LiCl solution. Subsequently, the saturated salt solution was exchanged for NaCl salt prepared in isotopic labeled water, resulting in much higher RH of 74% that introduces the isotopic labeled water into the sugar. The D_2O content within the trehalose matrix was monitored via embedded nitroxide spin probe

R1, using EDNMR technique at W-band. Fig. 7.3(b) shows EDNMR spectra recorded at g_{zz}, M_I=0 spectral position within nitroxide EPR spectrum for a series of R1/trehalose glasses incubated in the presence of NaCl (D_2O) saturated solution for indicated period of time. The spectra were baseline corrected and normalized as described in Materials and methods section. The feature of interest is the EDNMR line centered at deuterium Larmor frequency, ν_n(D), ca. 21.8 MHz at 94 GHz. The signal is absent in the control sample prepared using LiCl (H_2O) but appears in all trehalose samples where solution of NaCl in D_2O was used, including shortest tested equilibration time of 3 hours. In addition to deuterium line, much broader signals in 30-55 MHz frequency range are always present that originate from strongly coupled, internal nitrogen ^{14}N of nitroxide radical [37;39]. Due to strong overlap of ^{14}N signals with line centered at ν_n(D) for spectral positions in g_{xx}-g_{yy} region of nitroxide EPR spectrum, see Fig. 4.8, the g_{zz}, M_I=0 was chosen as optimal position for detecting weakly-coupled deuterium in nitroxide spin-labeled systems using EDNMR technique at W-band. The characteristic position of ^{14}N lines can, however, be used to an advantage to ensure that EDNMR recordings are taken at the same spectral position.

The intensity of deuterium line in EDNMR recordings taken after different equilibration times was used as a measure of deuterium content in the sugar, reporting on the progress of rehydration. During the investigated equilibration period of 9 days, the intensity of deuterium line strongly increases during the first 24 hours, see Fig. 7.3(c). It then reaches a plateau after about 3 days with final signal intensity of 0.2, see Table 7.1, indicating that the rehydration process is to a large extent completed.

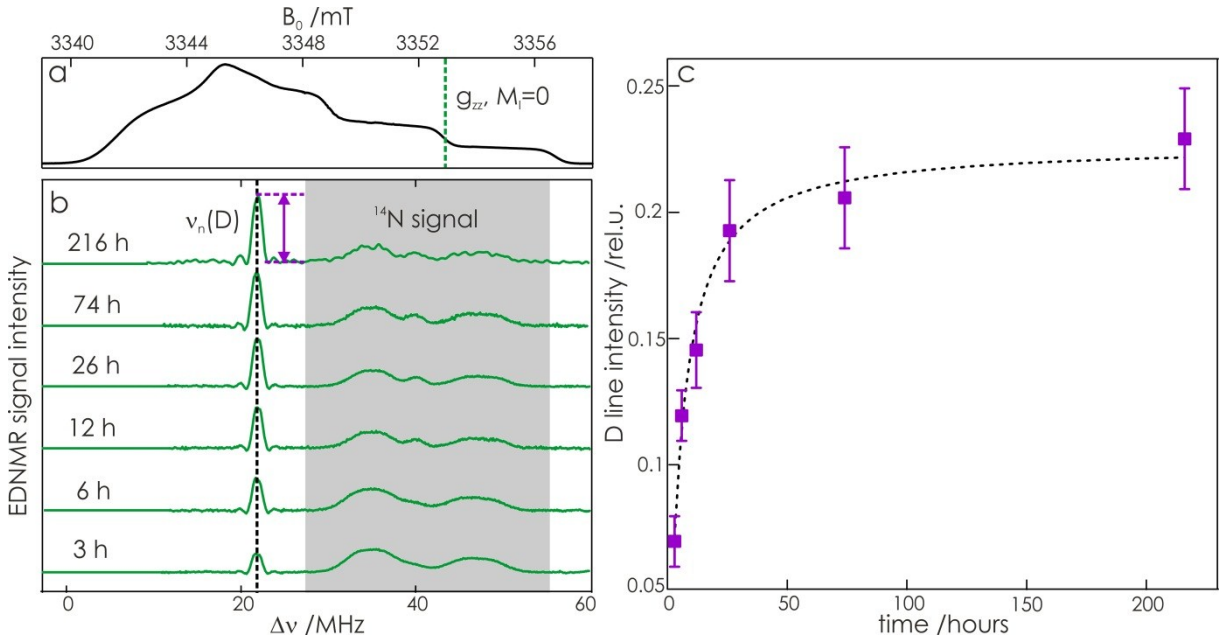

Figure 7.3 *(a) Echo-detected field-swept EPR spectrum of nitroxide radical R1 embedded in trehalose glass. The g_{zz}, M_I=0 spectral position is marked. (b) EDNMR spectra recorded for R1 /trehalose glassess equilibrated for indicated amount of time with saturated NaCl solution prepared in D_2O. The spectra were recorded at field position shown in (a). (c) Plot of the intensity of deuterium line read out from EDNMR recordings presented in (b) as a function of equilibration time.*

It has been proposed that nitroxide radicals can form up to two H-bonds with nearby H-bond donor groups [37;40;41]. Hence, the D signal observed in EDNMR recordings is expected to originate from

both the isotopic water directly coordinated to nitroxide and from D_2O molecules beyond the 1st hydration shell. Since the hyperfine interaction, A, of directly coordinated D nuclei is smaller the $2\cdot|\nu_n(D)|$, it results in a signal centered at $\nu_n(D)$ and split by the hyperfine interaction. It therefore coincides with signal from more distant D_2O molecules that contribute a Gaussian line centered at $\nu_n(D)$, so called 'matrix line'. However, in all EDNMR spectra the signal at $\nu_n(D)$ could be satisfactorily fitted to a Gaussian line shape with a FWHM of ca. 1.1 MHz at all equilibration times. It does not show any additional structure. This is due to a limited resolution of EDNMR method with respect to narrow signals, like deuterium in this case. As a result, the information on the relative contributions of coordinated and distant water molecules is not available.

Table 7.1 *The intensity of D line for spin-labeled bRC embedded in trehalose glass equilibrated with NaCl (D_2O) water vapour for indicated period of time. The intensity is obtained as the average of D line intensity for $\Delta\nu>0$ and $\Delta\nu<0$ in W-band EDNMR spectra.*

time	3 h	6 h	12 h	26 h	74 h	216 h
intensity	0.064±0.005	0.112±0.007	0.139±0.007	0.17±0.02	0.187±0.020	0.214±0.008

To gain insight into the organization of coordinated and distant water molecules around nitroxide probe, W-band Mims ENDOR technique was employed. Fig. 7.4 shows Mims ENDOR spectra recorded at different times during rehydration of R1/trehalose glasses at RH=74% (D_2O), analogous to above EDNMR recordings. Even at the shortest tested equilibration time of 3 hours, both matrix D line and directly coordinated (coupled) water are present in ENDOR spectrum, see bottom trace in Fig. 7.4(a). The largest observed hyperfine coupling at this spectral position is equal ca. 1.89±0.02 MHz (dashed lines in Fig. 7.4(a)) and becomes better resolved after about 24 hours of equilibration. In the course of rehydration, the magnitude of deuterium hyperfine coupling resolved in ENDOR spectra at g_{zz}, $M_I=0$ spectral position does not change, but additional sharp features placed symmetrically around the matrix line appear in ENDOR spectra after about 12 h of incubation. This additional splitting is due to resolved quadrupole interaction (D nuclei has spin I=1), with a quadrupole coupling constant of Q_2 = 60 kHz. The shape of coupled D signal in ENDOR spectra does not show significant changes after about 12 h of incubation, suggesting that largest sugar matrix reorganization occurs within that time period. As a result of increased trehalose glass plasticity due to higher hydration level, the formation of better-defined nitroxide-water H-bond network is possible, as is reflected by narrower ENDOR lines of coupled D. However, the width and relative intensity of matrix line in ENDOR still increases in time, as is expected based on increasing D line intensity in EDNMR recordings. Owing to sufficient g-tensor resolution at W-band, the deuterium nuclear transition frequencies can be selectively recorded across nitroxide EPR spectrum and can, in principle, be related to the nitroxide molecular frame (given by the principal g-tensor values) yielding the orientation of H-bonded water molecule. The recorded field-frequency ENDOR spectra for R1/trehalose glass after 72 h of equilibration are shown in Fig. 7.4(b).

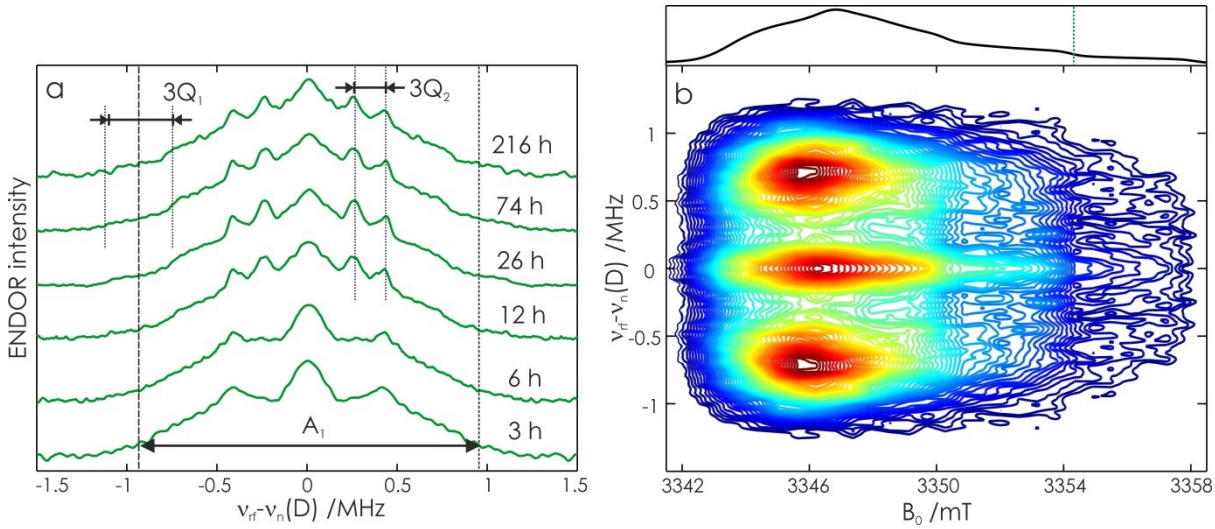

Figure 7.4 *(a) W-band Mims ENDOR spectra recorded for R1/trehalose glasses equilibrated for different amount of time at RH=74% (D_2O). The spectra were recorded at g_{zz}, M_I=0 spectral field position. (b) W-band D Mims ENDOR recordings taken at field positions across the R1 spectrum shown on top for R1/trehalose glass equilibrated at RH=74%. The separation between the first two π/2 pulses in the pulse sequence was set to τ=250ns and t_{rf}=35 μs. The contour lines are shown as isohypses from 0.05 to 1 of the maximum ENDOR intensity. The spectra were recorded at 60 K.*

The orientation-resolved ENDOR spectrum indeed demonstrates the dipolar hyperfine interaction pattern with the broad ridge corresponding to largest hyperfine coupling of 1.99 MHz seen in g_{xx}-g_{yy} spectral positions range. However, the pattern cannot be easily analyzed with respect to H-bond orientation due to broad distribution of hyperfine coupling values across the nitroxide EPR spectrum. Nevertheless, it proves the presence of H-bonded water molecules in the vicinity of nitroxide radical. Plausible explanations for non-resolved dipolar pattern are (i) large geometry distribution of the hydrogen bonded nitroxide/water complexes that results in distribution of hyperfine tensor orientations with respect to the g-tensor frame of nitroxide, (ii) possibility to form simultaneously two H-bonds with water molecules that yield two hyperfine tensors with different orientations that overlap in ENDOR spectrum.

In addition to monitoring the hyperfine interaction of nitroxide radical with nuclei of incorporated isotopic water, one can also revert to using the internal ^{14}N lines to learn about H-bonding state of nitroxide. It has been shown in chapters 4 and 5, that depending on H-bond donor, different number of ^{14}N lines can be seen in EDNMR recordings of nitroxide radical, directly reporting on the nitroxide H-bonding situation [16;37]. Figs. 7.5 shows ^{14}N lines in EDNMR spectra recorded close to g_{zz}, M_I=-1 spectral position during rehydration process. At the three equilibration times shown, the ^{14}N lines can be simulated as a superposition of two Gaussian lines of varying amplitude and linewidth, see Fig. 7.5(d). The Gaussian line at lower frequency contributes largely to ^{14}N EDNMR spectrum at shortest rehydration time and decreases in intensity with time. For high frequency Gaussian line reversed trend is observed in the course of rehydration. From comparison of extracted ^{14}N A_{zz} hyperfine coupling values with values reported for nitroxide dissolved in water/glycerol mixtures [16], it can be assumed that Gaussian line at lower frequency corresponds to nitroxide radical forming single H-bond, see Table 7.2. The line at higher frequency reflects nitroxide fraction forming two H-bonds. In line with W-band ENDOR spectra, the nitroxide H-bonding

equilibrium is established after about 12 h of rehydration with predominant fraction of nitroxides forming two H-bonds with solvent.

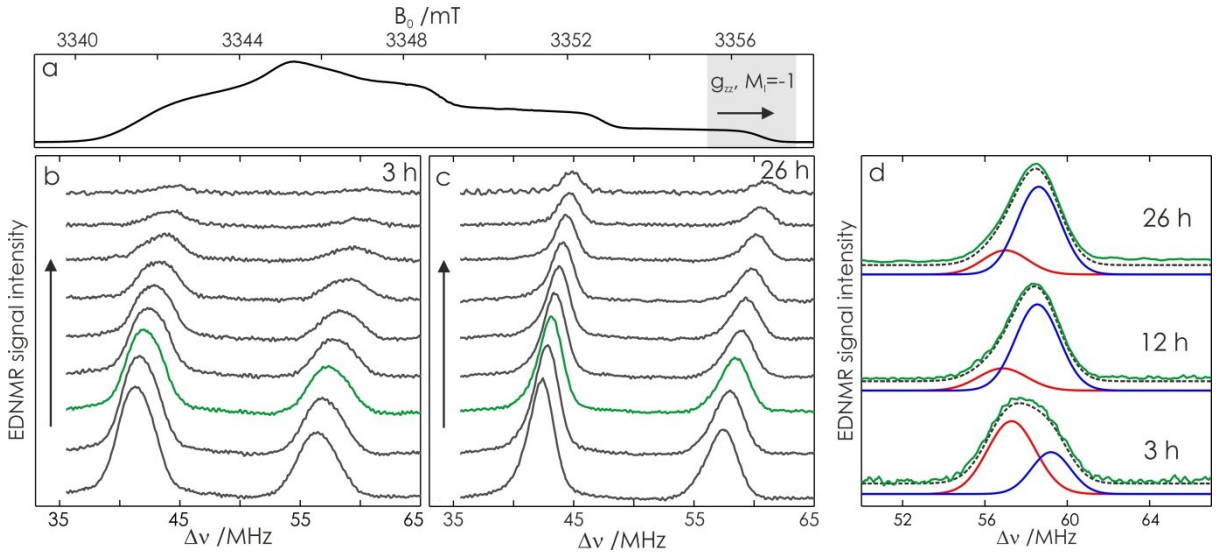

Figure 7.5 *W-band EDNMR spectra in g_{zz}, M_I=-1 spectral region for R1/trehalose glasses rehydrated for 3h (b) and 26 hours (c). (d) W-band EDNMR spectra recorded close to g_{zz}, M_I=-1 spectral field position in the frequency range corresponding to high frequency ^{14}N EDNMR line. The R1/trehalose glasses were rehydrated for 3, 12 or 36 hours. The two Gaussian lines contributing to ^{14}N signal are shown in red and blue.*

Table 7.2 *The magnetic parameters of the R1 in trehalose glasses equilibrated at RH=74% for indicated period of time obtained from the analysis of W-band EDNMR recordings in g_{zz}, M_I=-1 spectral region.*

	R1/trehalose glass after 3 hours	R1/trehalose glass after 26 hours
$\Delta\nu^1_{1/2}$ /MHz	2.7±0.2	2.6±0.2
$\lvert A^1_{zz}\rvert$ /MHz	100.8±0.3	101.1±0.3
fraction of 1	0.68±0.05	0.22±0.05
$\Delta\nu^2_{1/2}$ /MHz	2.2±0.2	2.5±0.2
$\lvert A^2_{zz}\rvert$ /MHz	105.6±0.3	105.6±0.3
fraction of 2	0.32±0.05	0.78±0.05

7.3.2 Water accessibility of R1/trehalose glasses at different RH

In the next step we compared whether differences between R1/trehalose glasses equilibrated at different relative humidity values can be seen in EDNMR spectra. Based on observed rehydration kinetics, R1/trehalose glasses were equilibrated for 3 days in the presence of appropriate saturated salt solutions prepared in D_2O, see Materials and methods. Fig. 7.6(a) shows W-band EDNMR spectra recorded at g_{zz}, M_I=0 spectral position within nitroxide EPR spectrum for R1/trehalose at RH=11% (D_2O), 43% (D_2O) and 74% (D_2O). The spectral content of all EDNMR spectra is the same except for varying intensity of deuterium line, see Table 7.3, and could be fitted using a Gaussian line shape.

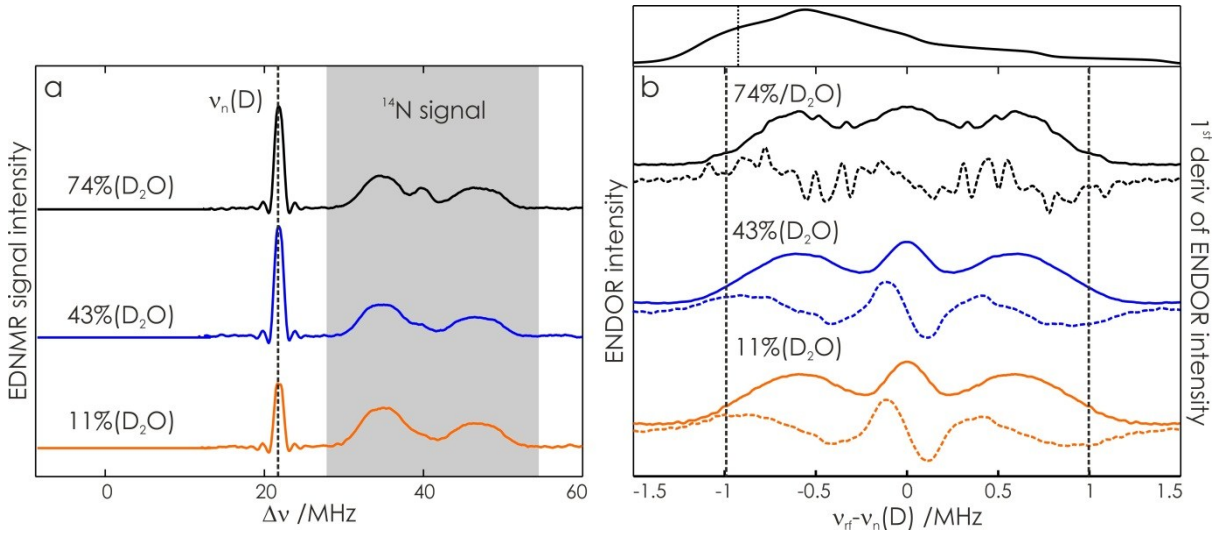

Figure 7.6 *(a) The W-band EDNMR spectra recorded at g_{zz}, M_I=0 spectral position for R1 /trehalose glasses equilibrated for 3 days with saturated NaCl (black trace), K_2CO_3 (blue trace) and LiCl (orange trace) solutions prepared in D_2O. (b) Analogous W-band Mims ENDOR recordings for R1/trehalose glasses equilibrated at indicated RH. The same color code as in (a) is used. The ENDOR spectra were recorded in g_{xx}–g_{yy} spectral region as indicated in echo-detected EPR spectrum above.*

As expected, at lowest studied hydration level the D signal has lowest intensity. It is worthwhile to emphasize that for trehalose glass at RH=11% (D_2O) the hydration level of sample is not changed since the sugar was already pre-equilibrated at RH=11% (H_2O). The isotope labeled water is introduced in the trehalose glass only due to exchange of water molecules between the gaseous phase and the residual water retained in the sugar matrix at RH=11% (which is about 0.5 water molecule per trehalose molecule [35]).

Table 7.3 *The intensity of D peak for R1 spin probe embedded in trehalose glass and equilibrated at specified relative humidity level. The reported line intensity is the average of D line intensity at left and right hand side of the spectrum. The D intensity in different samples is reported compared to central blindspot intensity that is set as 1.*

	RH=11%	RH=43%	RH=74%
intensity	0.123±0.014	0.204±0.016	0.189±0.014
FWHM /MHz	1.2±0.02	1.1±0.02	1.1±0.02

Surprisingly, the intensity of D line in glasses equilibrated at RH=43% and RH=74% is the same within experimental accuracy. The overall water content in trehalose matrices at these three hydration levels was previously estimated using FTIR and it was shown to vary by a factor of about 3 between RH=43% (0.7 water molecules per sugar molecule) and 74% (2.4 water molecules per sugar molecule) [35]. The different scaling of D EDNMR line intensity at these two hydration levels can be explained by the fact that in EPR only local water changes in the radius of about 5-6 Å around spin probe are detected, as opposed to e.g. IR measurements where the overall water content is determined. It has been shown that EDNMR signal increases linearly with increasing D_2O content [42], the reason for these peculiar results must therefore lie in the structural organization of the sugar matrix. Indeed,

the trehalose glass has been shown to become heterogeneous at the microscopic level upon rehydration [35] and during that process the nitroxide probe diffuses into water-rich domain. It therefore reports on different local water content and simply reflects different structural organization of the matrix.To confirm this assumption, the structure of coupled water at these two hydration levels was compared using Mims ENDOR technique. Based on field-frequency spectra in Fig. 7.4(b), the spectra were recorded in the g_{xx}-g_{yy} spectral region where the largest hyperfine coupling from main H-bonded deuterium is resolved, as predicted based on rehydration experiments. For all three investigated hydration levels of nitroxide/trehalose glasses the ENDOR spectra have contributions from both coupled and distant deuterium, see Fig. 7.6(b). For R1/trehalose glass kept at RH = 74%, the ENDOR lineshape is virtually the same as after trehalose rehydration process at longer equilibration times. The shape of ENDOR spectrum for R1 in trehalose equilibrated at RH = 43% suggests H-bonding situation similar to those at RH=11%: the ENDOR lines are broad and only indication of quadrupole splitting is seen, see dotted lines in Fig. 7.6 (b). Despite differences in ENDOR lineshape, the largest hyperfine coupling in all three systems is about the same and equal to 1.99±0.02 MHz as determined for RH=74%.

7.3.3 Water accessibility of SL-RC/trehalose glass at different RH

The manipulation of sugar matrix hydration, as shown in previous paragraph, might translate into changes of thickness of the 1st solvation shell of protein. However, one has to keep in mind the unusual efficacy of trehalose in stabilizing the protein structure, for example see [43]. One of the hypotheses aiming to explain these properties states that the layer of water between protein surface and trehalose is strongly immobilized [44;45]. Since the nitroxide spin label is facing towards the protein surface, see Fig. 7.2, it directly reports on changes in the protein solvation shell upon changing sugar matrix hydration. Figure 7.7(a) shows the comparison of W-band EDNMR traces recorded for SL-RC/trehalose glasses equilibrated at two RH levels, 11% (D_2O) and 74% (D_2O) for 3 days. The line centered at ν_n(D) is present at both hydration levels. For SL-RC/trehalose equilibrated at RH=11% (D_2O) the deuterium signal originates exclusively from the exchange of water retained in the protein solvation shell with the isotopic labeled water in surrounding sugar matrix, since no change in sugar hydration level takes place. For RH=74%, increase in sugar matrix hydration results also in additional water appearing in the hydration shell of protein embedded in the sugar. The intensity of D signal at RH=11% (D_2O) is lower as compared to RH=74% (D_2O), but surprisingly only by about a factor of two, see Table 7.4. The hydration level of protein/trehalose films at two indicated hydration levels was estimated previously using FTIR. Based on their results, the H_2O/RC molar ratios of $1.1x10^3$ (RH=11%) and $8.2x10^3$ (RH=74%) in RC/trehalose glasses were determined [24]. Therefore, the overall water content of protein/trehalose glasses equilibrated at RH=74% and 11% is expected to differ by a factor of about 7.5. This ratio, however, reflects rather the overall difference in water content, while in this study site-specific difference in water content is probed, similarly to the case of sugar matrix alone discussed above. At this point it can only be concluded that even though the conformational dynamics of the protein is significantly retarded at low hydration level, the efficient exchange between the water within the sugar matrix and water in the protein hydration shells occurs. Based on W-band ENDOR measurements, both water directly coordinated to nitroxide label and more distant water are present at both hydration levels, see Fig. 7.6(b).

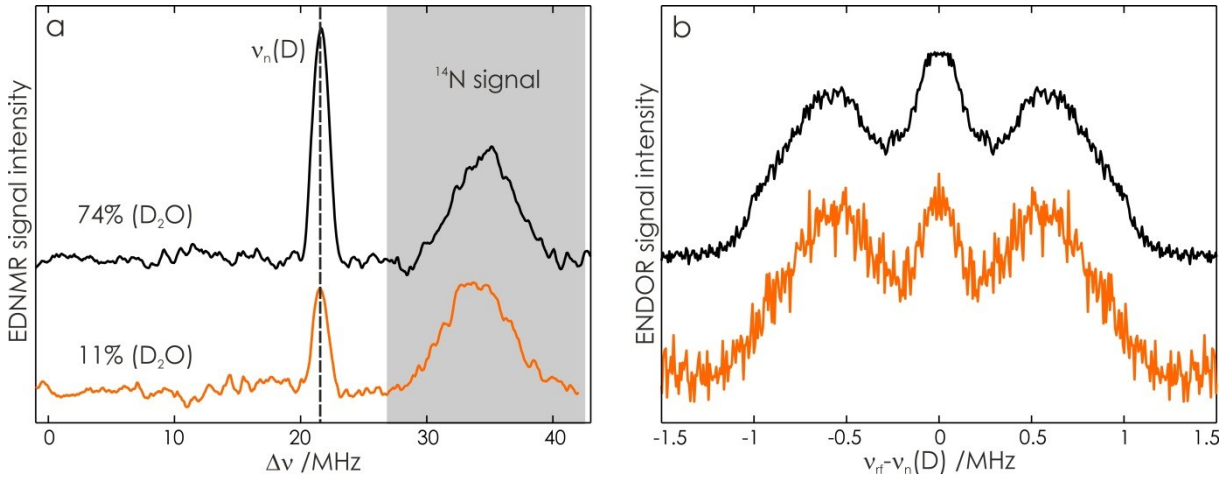

Figure 7.6 *(a) W-band EDNMR spectra for SL-RC /trehalose glasses equilibrated at two 11% (D_2O) and 74% (D_2O) RH (orange and black traces, respectively). (b) W-band Mims ENDOR spectra for SL-RC /trehalose glasses equilibrated at two 11% (D_2O) and 74% (D_2O) RH, same color code as in a. All spectra were recorded at g_{zz}, M_I=0 spectral field position at 60K.*

Table 7.3 *The intensity of D peak for SL-RC and Zn^{2+}-RC embedded in trehalose glass at specified relative humidity level or in frozen solution using D_2O, obtained as the average of the D peak intensity for Δν>0 and Δν<0 in W-band EDNMR spectra. The D intensity is reported relative to the intensity of the central blindspot which is taken as equal 1.*

D signal intensity	RH=11% (D_2O)	RH=74% (D_2O)	D_2O buffer
SL-bRC	0.0985±0.0015	0.212±0.008	-
$Q_A^{\cdot-}$ in Zn^{2+}-RC	0.004±0.001	0.046±0.005	0.048±0.005

7.3.4 Local water accessibility in the vicinity of native cofactors in RCs embedded in trehalose

In analogy to protein surface-exposed nitroxide label, the solvent accessibility of two native paramagnetic probes, $P_{865}^{\cdot+}$ and $Q_A^{\cdot-}$, was studied for protein embedded in trehalose matrix at two hydration levels. The increased g-tensor resolution at high-field/high-frequency allows for partial spectral separation in the EPR spectrum of donor-acceptor radical pair, see Fig. 7.7(a). Fig. 7.7(b) shows W-band EDNMR spectra recorded at g_{yy}, i.e. the maximum of the spectral intensity of $Q_A^{\cdot-}$ for Zn^{2+}-RC dissolved in buffer prepared in D_2O and for Zn^{2+}-RC/trehalose glasses equilibrated at RH=74% (D_2O) and RH=11% (D_2O). The spectral content in EDNMR spectra for Zn^{2+}-bRC in solution and embedded in trehalose glasses is the same, except for different line intensities. Starting from the lowest frequency, the first spectral feature is broad line centered at 10.4 MHz (^{14}N Larmor frequency) that originates form weakly coupled nitrogen. This signal originates most likely from the peptide nitrogen NH of Ala M260 and/or the imidazole nitrogen $N^{\delta(1)}$-H group of His M219, that are within H-bonding distance to two carbonyl oxygens of Q_A (distance of 2.8 Å and 3.2 Å respectively). The ^{14}N couplings and nuclear quadrupole paramaters of these nitrogens have been characterized previously using X-band ESEEM showing that the effective ^{14}N hfc is close to 2 MHz [46;47]. In current study only broad, featureless ^{14}N lines are observed since the EDNMR pulse settings are

optimized for detection of deuterium nuclei. The hyperfine coupled nitrogen contributes additional signal observed in EDNMR spectrum, i.e. pair of lines centered at $2\cdot \nu_n(^{14}N)$ and split by twice the hyperfine coupling value. These lines originate from pumping of double quantum nitrogen transitions which due to their lower probability result in significantly weaker signals.

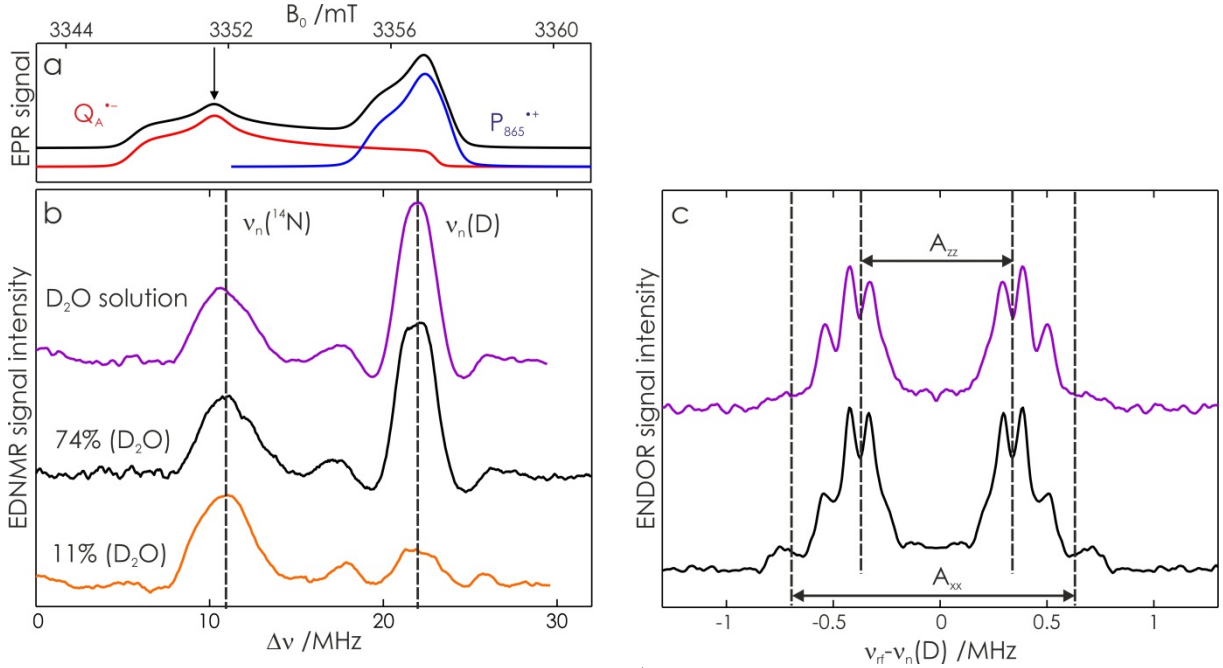

Figure 7.7 *(a) The sum of EPR absorption spectra of $P_{865}^{\bullet+}$ and $Q_A^{\bullet-}$ ionic states of cofactors (black trace). The simulated spectra corresponding to $Q_A^{\bullet-}$ only (red trace) or $P_{865}^{\bullet+}$ only (blue trace) are also shown. (b) W-band EDNMR spectra recorded at maximum intensity of $Q_A^{\bullet-}$ EPR spectrum (see arrow in (a)) for Zn^{2+}-RCs dissolved in Tris/HCl buffer prepared in D_2O and for Zn^{2+}-RC/trehalose glasses equilibrated at RH=74% (D_2O) and RH=11% (D_2O). (c) W-band ENDOR spectra for Zn^{2+}-RC dissolved in Tris/HCl buffer prepared in D_2O and for Zn^{2+}-RC/trehalose glasses equilibrated at RH=74% (D_2O).*

The line centered at D Larmor frequency is evident in EDNMR spectra of Zn^{2+}-RC either dissolved in D_2O buffer or equilibrated at RH=74% (D_2O). Interestingly, the intensities of deuterium line in trehalose glass at RH=74% and in D_2O solution are the same to within experimental accuracy, see Table 7.3. It clearly shows that the diffusion of water within the protein embedded in trehalose glass when equilibrated at high RH is not hampered as compared to protein in solution. Interestingly, in the case of dehydrated protein/trehalose glasses (RH=11% (D_2O)), D signal is also observed, although its intensity is only about 1/10 of that in the fully hydrated system. This is interesting finding, showing that retarded conformational flexibility of protein still allows for the exchange of water molecules deeply within the protein.

The semiquinone $Q_A^{\bullet-}$ is stabilized in the protein pocket by two hydrogen bonds between the carbonyl oxygens of quinone and amino acids side chains, the deuterium signal is therefore expected to originate rather from nearbly water molecule, either belonging to a water cluster identified in the vicinity of the primary quinone in X-ray structure [21] or possibly not resolved in the crystal. The EDNMR linewidth of 2.4±0.1 MHz (FWHM) does not allow to conclude on the nature of D signal, therefore, ENDOR spectra were recorded at the g_{yy} field position in $Q_A^{\bullet-}$ EPR spectrum. Fig. 7.7 (c) shows the comparison of D ENDOR spectra for Zn^{2+}-RC equilibrated at RH=74% (D_2O) and dissolved in D_2O. Surprisingly, at both hydration levels, exclusively the signal from hydrogen-bonded

deuterium is present, with narrow ENDOR lines ($\Delta\nu_{½} < 0.1$ MHz determined at g_{zz} spectral position) suggesting very well defined geometry. This allows analyzing the pattern in more detail as compared to ENDOR spectra of nitroxide radical. At this spectral position the powder spectrum is expected to consist of sharp features corresponding approximately to the parallel and the perpendicular components of an axially symmetric hfc tensor, see chapter 5 for detailed description. It can be immediately recognized that the hyperfine and quadrupole couplings for $Q_A^{\bullet-}$ in Zn^{2+}-RC/trehalose glasses equilibrated at RH=74% (D_2O) are the same as in the frozen D_2O solution, i.e. they originate from the same coupled deuterium. The signal must therefore originate from one of exchangeable protons of amino acids that are coordinating the quinone in its binding pocket. The possibility to selectively deuterate one of the H-bonds to Q_A has been shown previously by incubating RCs in D_2O [48;49]. Extensive EPR studies using ^{17}O-labeled [50] and ^{13}C-labeled [51] ubiquinone, performed in the past clearly demonstrated that hydrogen bonds to the oxygen of quinone carbonyls are inequivalent. Two different proton-deuterium exchange rates were associated with those two distinct hydrogen bonded protons belonging to alanine (M260) and histidine (M219) [48], see also Fig. 7.8(c). Similar conclusions were also drawn from analogous FTIR experiments [52;53]. To precisely determine the magnetic parameters for the hydrogen bonded deuterium, field-frequency Mims ENDOR recordings across $P_{865}^{\bullet+}$-$Q_A^{\bullet-}$ EPR spectrum were acquired for Zn^{2+}-RC dissolved in D_2O, see Fig. 7.8(a). Indeed, well-defined dipolar patter is seen, suggesting well-defined geometry of the quinone/H-bond donor complex.

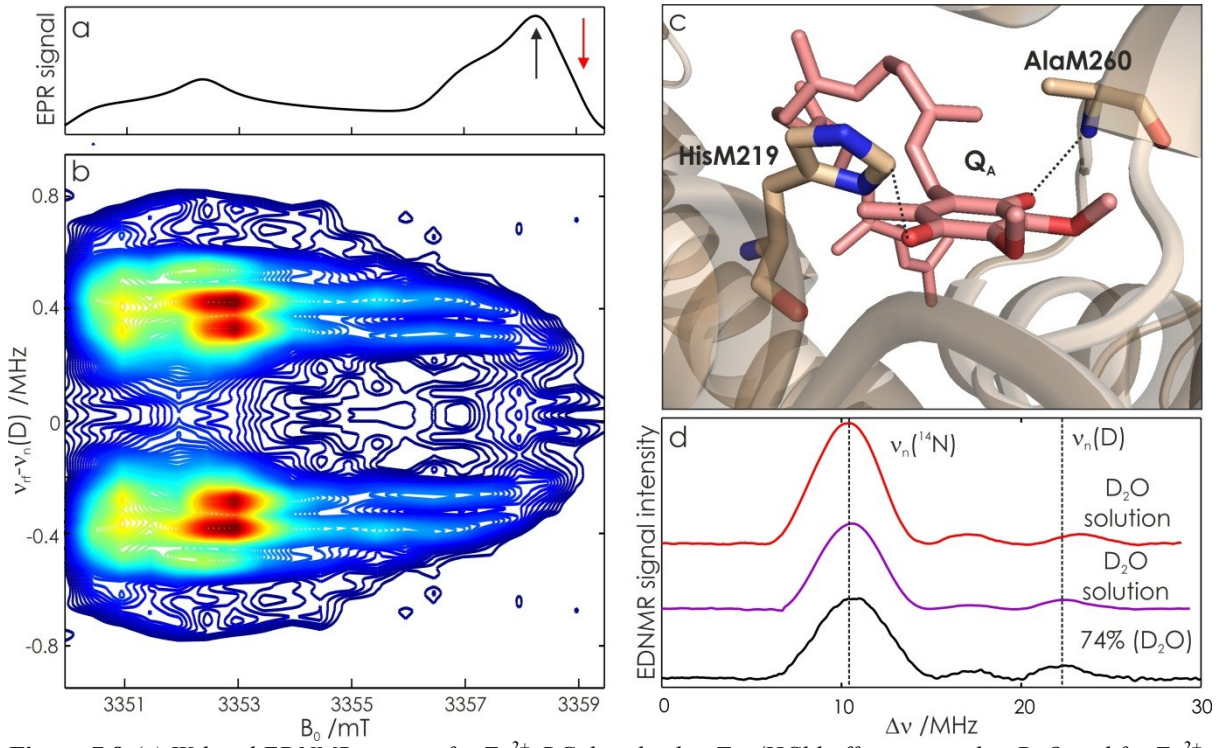

Figure 7.8 *(a) W-band EDNMR spectra for Zn^{2+}-RC dissolved in Tris/HCl buffer prepared in D_2O and for Zn^{2+}-RC/trehalose glasses equilibrated at RH=74% (D_2O). (b) W-band Mims ENDOR recordings taken at field positions across the $P_{865}^{\bullet+}Q_A^{\bullet-}$ spectrum shown on top. The separation between the first two π/2 pulses in the pulse sequence was set to τ=360 ns and t_{rf}= 35 µs. The spectra were recorded at 130 K.(c) The two amino acids stabilizing QA in its binding pocket. (d) W-band EDNMR spectra recorded at maximum intensity of $P_{865}^{\bullet+}$EPR spectrum or on the shoulder (see arrow in (a)) for Zn^{2+}-RCs dissolved in Tris/HCl buffer prepared in D_2O and for Zn^{2+}-RC/trehalose glasses equilibrated at RH=74% (D_2O).*

The comparison of extracted hyperfine and quadrupole coupling values with the work of Flores et al. [49], allows to conclude that ENDOR and EDNMR spectra are essentially due to deuterons on O_1 hydrogen-bonded to alanine (M260), see Table 7.4. The fact the identical spectral parameters are obtained for protein in solution and protein embedded into sugar is supported by previous time-resolved EPR measurements where it was shown that the protein hydrogen bonding to Q_A does not change upon the RC/trehalose glass dehydration [27].

Table 7.4 *Comparison of magnetic parameters obtained from analysis of deuterium ENDOR spectra of Zn^{2+}-RC embedded in trehalose at RH=74% (D_2O) with previously reported parameters obtained for Zn^{2+}-RC dissolved in D_2O [49].*

	A_x' /MHz	**A_y' /MHz**	**A_z' /MHz**
N-D·····O_4 (His M219)*	-0.98±0.01	-1.00±0.01	+1.36±0.02
N-D·····O_1 (Ala M260)*	-0.70±0.01	-0.76±0.01	+1.37±0.03
this work	-0.69±0.1	-0.72±0.1	+1.35±0.1
	P_x'' /MHz	**P_y'' /MHz**	**P_z'' /MHz**
N-D·····O_1 (Ala M260)*	-70±6	-31±8	+101±10
this work	-44±0.01	-30±0.01	+72±10

*Data adapted from reference [49].

W-band EDNMR spectra recorded at max P_{865}^{+} spectral intensity for Zn^{2+}-RC dissolved in D_2O or equilibrated at RH=74% (D_2O) are shown in Fig. 7.8(d). Similarly as for $Q_A^{\bullet-}$, ^{14}N lines originating from single and double quantum nitrogen transitions are seen in EDNMR spectra at both hydration levels. For $P_{865}^{+\cdot}$ these originate from ^{14}N nuclei in the bacteriochlorophyll rings and possibly from more distant amino acids located in the vicinity of the special pair, for example Tyr M210 (near pyrrole ring I of B_A) or Gly M280 (near ring V of B_A). Similarly as for $Q_A^{\bullet-}$, the double quantum ^{14}N lines partially overlap with deuterium line centered at ν(D), that is present in RC dissolved in D_2O and embedded in trehalose glass at RH=74% (D_2O). In the case of P_{865}^{+} comparison of D line intensities is not direct due to varying contribution of Q_A^{-} signal at the maximum of P_{865}^{+} spectral intensity in the W-band echo-detected EPR spectrum for frozen solution and trehalose glass (e.g. due to different positioning of light fiber in the cavity). Due to this spectral overlap with signal from primary acceptor, EDNMR spectrum was recorded at the field position corresponding to the high-field edge of P_{865}^{+} spectrum where no contribution from Q_A^{-} is present. Surprisingly, no signal centered at ν_n(D) is present and only double quantum ^{14}N lines contribute to the EDNMR spectrum in that frequency range. This finding is somewhat surprising, since based on the X-ray structure of RC [17] a number of strongly bound water molecules in the vicinity of P_{865} has been identified: 5 of them are embedded within 8-10 Å and 5 within 10-15 Å. The polarization of these water molecules and protein hydrogens in the vicinity of the special pair, was suggested to stabilize the excited P_{865}* before the primary electron transfer step [54]. In particular a single water molecule located between P_{865} and the first electron acceptor, BPhe, was shown to have strong effects on the rate of charge separation [55]. Seven additional, bridging water molecules, that form H-bonds with both RC and cyt c_2 have been determined in the RC:cyt c_2 co-crystal structure, that should provide the pathway for exchange of

water molecules between the $P_{865}^{\cdot-}$ protein pocket and the solvent [56]. At this point it cannot be assumed that this strongly bound water is not present in vicinity of primary donor. The fact that it is not seen also for Zn^{2+}-RC in solution can be either due to it being non-exchangeable but more likely due to large delocalization of electron spin density over $P_{865}^{\cdot+}$ as quantum calculations have shown [57]. Therefore, the small electron spin density at any given position within the bacteriochlorophyll ring results in negligible hyperfine coupling and lack of signal in EDNMR and ENDOR.

7.3.5 W-band EDNMR and Davies ENDOR on RC/trehalose equilibrated with $H_2{}^{17}O$

While use of D_2O water in solvent accessibility studies provides necessary contrast to internal protons within protein, the H/D exchange cannot be avoided, making quantitative data interpretation not possible. Using of ^{17}O labelled water is of advantage, solving the problem of background from exchangeable protons. Despite high cost of ^{17}O labelled water, the setup used in this study requires only several microliters of saturated salt solution prepared in $H_2{}^{17}O$, making the studies feasible. Since no distant water molecules were observed in the vicinity of native cofactors, studies employing ^{17}O detection were done using SL-RC variant, where matrix water signal could be detected around nitroxide label at both hydration levels. Fig. 7.9 (s) shows W-band EDNMR spectra for SL-RC at two hydration levels and for protein/trehalose sample back-equilibrated using LiCl (H_2O) solution. At higher hydration level, the ^{17}O signal has shape that deviates from simple Gaussian line as was the case for D EDNMR line. The signal shape originates from two contributions, that of the ^{17}O of directly coordinated water ligands, giving rise to coupled signal, and that of second shell water ligands, which manifest as Gaussian line centred at the Larmor frequency of ^{17}O. Due to larger ^{17}O hyperfine coupling these two contributions are partially resolved. At lower hydration level the signal can be fitted to a Gaussian line and due to lower signal-to-noise ratio it is difficult to judge on the relative intensities of coupled/matrix ^{17}O. Nevertheless, based on the intensity of ^{17}O EDNMR line, the six-fold change in ^{17}O amount is seen, which is closer to the value reported by FTIR [24].

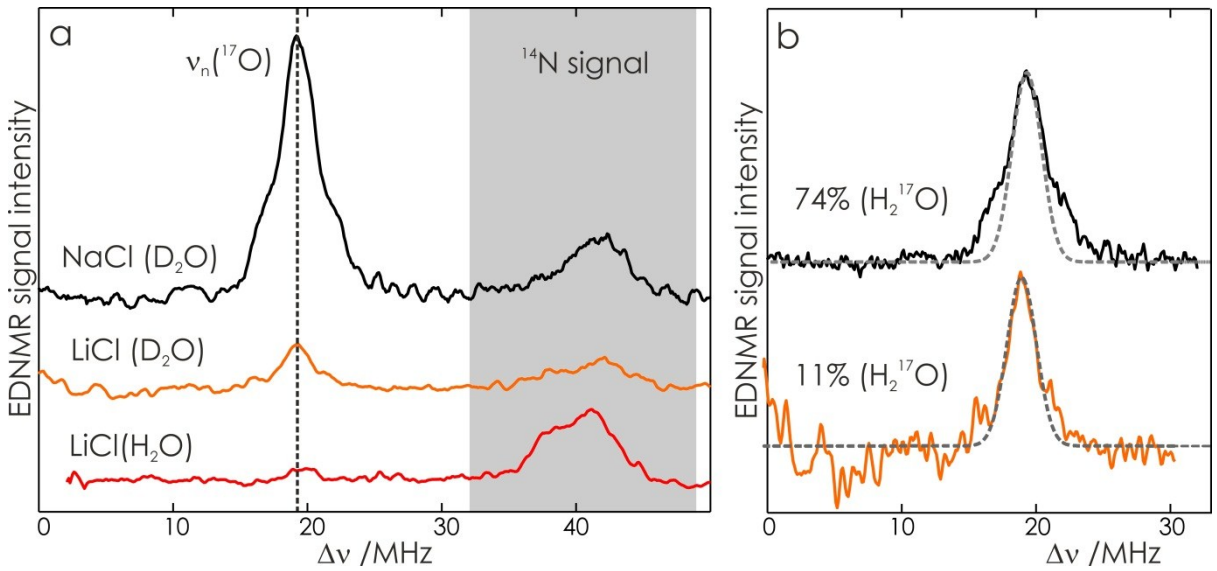

Figure 7.9 *(a) ^{17}O EDNMR recordings for SL-RC/trehalose glasses equilibrated for 3 days with saturated NaCl (black trace) and LiCl (orange trace) solutions prepared in $H_2{}^{17}O$. Additionally the sample back-equilibrated using LiCl (H_2O) solution is shown (red trace). The EDNMR spectra were recorded close to g_{zz}, M_I=0 canonical*

position. b) Simulation of ^{17}O EDNMR line with Gaussian line shape of FWHM of 2.6 MHz for SL-RC/trehalose glasses equilibrated with saturated NaCl (black trace) and LiCl (orange trace) solutions prepared in $H_2{}^{17}O$.

Table 7.5 *The intensity of ^{17}O line for SL-RC embedded in trehalose glass and equilibrated at specified RH. The value was read out for normalized EDNMR spectra after central blind spot subtraction. The reported value is the average of ^{17}O line intensity in left and right hand side of EDNMR spectra and the error is half of the difference between two intensities.*

	SL-RC/trehalose at RH=11% ($H_2{}^{17}O$)	SL-RC/trehalose at RH=11% (H_2O)	SL-RC/trehalose at RH=74% ($H_2{}^{17}O$)
^{17}O line intensity	0.017±0.002	0.006±0.002	0.108±0.01

To judge on the reliability of obtained spectral shape, the EDNMR signal was compared to ^{17}O Davies ENDOR. Despite higher linewidth resolution in the ENDOR experiment, essentially the same coupling is resolved in both experiments, see Fig. 7.10(b). This is possible due to a large quadrupole and hyperfine coupling of ^{17}O nuclei as compared to D nuclei, resulting in intrinsically broader lines. It has been shown that by testing the power dependence of EDNMR line, the number of different chemical environments of a nucleus of interest can be revealed [38]. In this particular case, by varying the mw field amplitude one can suppress the signal from distant ^{17}O. This is possible since the former nuclei exhibit significantly larger hyperfine/quadrupole interactions with the unpaired electron spin of nitroxide radical and therefore have intrinsically larger transition intensities, i.e. can be driven by a lower amplitude HTA pulse. The latter, instead have a much smaller interaction with the unpaired electron spin and as such require a higher amplitude HTA pulse to drive these spin transitions [38]. Fig. 7.10 (a) shows EDNMR spectra recorded for SL-RC/trehalose at RH=74% ($H_2{}^{17}O$) using HTA pulse at a series of mw field amplitudes. At highest used mw field amplitude, the ^{17}O NMR line reached up to 10% of echo intensity, demonstrating high sensitivity of the method. In the opposite case of shorter HTA pulse length and lower mw amplitude, EDNMR spectrum resembling Davies ENDOR spectrum is obtained. For ^{17}O detection the EDNMR experiment poses advantage over standard ENDOR experiment, since the weakly coupled 2nd shell waters at the ^{17}O Larmor frequency can be enhanced by using higher amplitude HTA pulses, while in Davies ENDOR experiment they are suppressed due to blind spotting at the nuclear Larmor frequency.

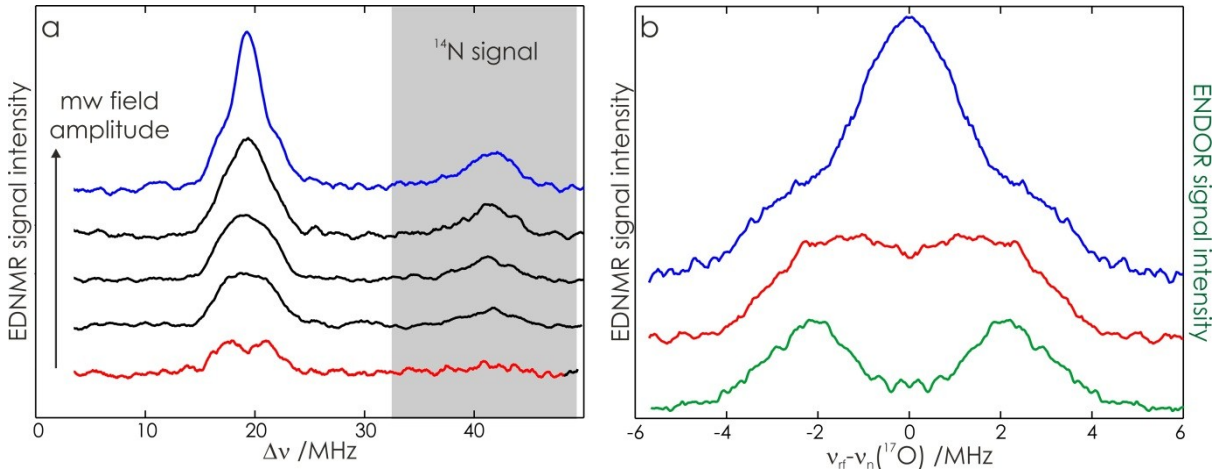

Figure 7.10 *MW field amplitude dependence of ^{17}O EDNMR spectra recorded for SL-RC/trehalose glasses equilibrated for 3 days with saturated NaCl solution prepared in $H_2{}^{17}O$. Only the left hand side of EDNMR spectra is shown with absolute values of frequency axis for easier comparison. The following mw field amplitudes were used (from top to bottom trace): 1.67×10^7 rad/s (18dB, 20μs), 1.2×10^7 rad/s (21dB, 20μs), 1.0×10^7 rad/s (24dB, 20μs), 0.9×10^7 rad/s (27dB, 20μs), 0.8×10^7 rad/s (27dB, 7μs). (b) ^{17}O EDNMR (blue and red traces as in (a)) and ENDOR (green trace) recordings for SL-RC/trehalose glass at 74% relative humidity in presence of ^{17}O vapor. The ENDOR and EDNMR spectra were recorded at the same spectral position close to g_{zz}, M_I=0 canonical position.*

7.4 Conclusions

In this work the applicability of W-band EDNMR technique to determine local solvent accessibility in proteins was tested. The bacterial photosynthetic reaction center from *Rb. sphaeroides* that possesses internal paramagnetic centers and additionally surface-exposed native cysteine residue which could be labeled with nitroxide radical is an ideal test system for such study: spin probes are very differently localized within the protein and have different spectroscopic characteristics. Before the solvent accessibility at investigated sites within the protein could be compared, the sugar matrix embedding the protein was characterized. The rehydration timescale of amorphous trehalose matrix from initial dehydrated state RH=11% to RH=74% could be determined. The EDNMR method proved to be exceptionally sensitive in detecting hyperfine-coupled deuterium originating from D_2O introduced into sugar matrix. However, due to resolution limitation of the method the details of H-bond network in the vicinity of nitroxide spin probe could be characterized only using Mims ENDOR technique. Upon influx of water vapour into sugar matrix, the nitroxide was seen to form not only more but also better geometrically defined hydrogen bonds as compared to strongly dehydrated matrix. Since the sugar is doped with nitroxide, the reorganization of the matrix during rehydration forces non-uniform spin probe dispersion due to loss of matrix homogeneity as has been previously observed [35]. Hence, the intensity of D signal in EDNMR recordings of nitroxide/sugar matrices prepared at different RH does not scale proportionally to overall water content of matrices (previously determined using FTIR) (ref) but rather reflects local solvent accessibility within structural domain that nitroxide is redistributed to. Interestingly, the isotopic labeled water is also efficiently introduced into the matrix in the place of residual H_2O retained within the sugar at constant RH=11%. Despite matrix rigidity in dehydrated state, the residual water is exchangeable, i.e. weakly bound.

Previously, it has been demonstrated that the dehydration of trehalose matrix gradually blocks the dynamics of bRC and formulated under 'anchorage model' [26]. Another interesting aspect of embedding the protein into sugar matrix is the extent to which water from the protein hydration shell and strongly bound internal water molecules are depleted during sugar matrix hydration level manipulations. The two existing hypotheses aiming at the explanation of trehalose efficacy in bioprotection predict opposite changes in the 1st solvation shell of protein upon dehydration. The 'water replacement theory' states that upon drying, the interaction of polar groups with water on protein surface is replaced by hydrogen bonds to the sugar, by which interaction the protein structure is stabilized [58]. The 'water entrapment theory' on the other hand states that water molecules become entrapped at the interface between amorphous sugar matrix and protein surface [44;45]. To differentiate between these two a sensitive method capable of direct water detection in a site-specific manner is needed. W-band EDNMR is shown to be very promising methodology for addressing this issue in detail in the future. It however requires use of $H_2{}^{17}O$ water, since in D_2O experiments even at low hydration level the exchangeable protons in the vicinity of spin label result in several fold increase in D line intensity as compared to analogous ^{17}O experiments. This discrepancy in signal intensities points towards 'water replacement' theory being more relevant for protein stabilization, as scaling of ^{17}O intensity is closer to overall water content changes reported in FTIR studies and does not suggest significant layer of water entrapped on the protein surface. However, clear distinction between two discussed mechanisms requires investigation of larger number of sites on the protein surface.

Unfortunately, no distant water molecules could be probed in the vicinity of two native cofactors in solution and at two investigated hydration levels. For P_{865}, it is a result of spectroscopic characteristics of the paramagnetic probe, i.e. large electron spin distribution, which makes it inefficient in sensing localized water molecule. The exchange of proton hydrogen-bonded to oxygen in quinone, Q_A, even at the low hydration level is a surprising finding. Clearly, while progressive dehydration effectively blocks larger-scale protein motions, the residual protein mobility still allows for exchange of stronger-bound water retained within the protein and eventual H/D exchange at Q_A binding site. While sensitivity of EDNMR as compared to ENDOR was several orders of magnitude higher, making it the method of choice, the limited resolution of D EDNMR lines might pose disadvantage in future applications. It is perfectly suited for qualitative purposes, like presented sugar rehydration kinetics where no differentiation between coupled and distant water is necessary. This necessity for differentiation between distant and coupled nuclei comes from the fact that they respond differently to mw field amplitude of HTA pulse. When quantitative information is sought, ^{17}O EDNMR can be used instead, taking advantage of high method sensitivity and inherently broader ^{17}O lines that allow for resolving coupled and distant ^{17}O contributions. In this respect W-band EDNMR is a method of choice not only as compared to ENDOR technique, but also to X-band ESEEM which yields the same spectral information but much larger sample volume required makes it impractical.

References

[1] H. Frauenfelder, P.W. Fenimore, G. Chen, B.H. McMahon *Protein folding is slaved to solvent motions*. Proceedings of the National Academy of Sciences of the United States of America **2006,** 103, 15469-15472.

[2] P.W. Fenimore, H. Frauenfelder, B.H. McMahon, F.G. Parak *Slaving: Solvent fluctuations dominate protein dynamics and functions*. Proceedings of the National Academy of Sciences of the United States of America **2002,** 99, 16047-16051.

[3] A.-N. Bondar, J. Baudry, S. Suhai, S. Fischer, J.C. Smith *Key role of active-site water molecules in bacteriorhodopsin proton-transfer reactions*. J.Phys.Chem.B **2008,** 112, 14729-14741.

[4] A. Schweiger, G. Jeschke Principles of pulse electron paramagnetic resonance, Oxford University Press, Oxford, 2001.

[5] G. Feher, J.P. Allen, M.Y. Okamura, D.C. Rees *Structure and function of bacterial photosynthetic reaction centres*. Nature **1989,** 339, 111-116.

[6] M.M. Leonova, T.Yu. Fufina, L.G. Vasilieva, V.A. Shuvalov *Structure-function investigations of bacterial photosynthetic reaction centers*. Biochemistry (Moscow) **2011,** 76, 1465-1483.

[7] T.L. Olson, J.C. Williams, J.P. Allen *The three-dimensional structures of bacterial reaction centers*. Photosynthesis Research **2014,** 120, 87-98.

[8] J.P. Allen, G. Feher, T.O. Yeates, H. Komiya, D.C. Rees *Structure of the reaction center from Rhodobacter sphaeroides R-26: The protein subunits*. Proceedings of the National Academy of Sciences of the United States of America **1987,** 84, 6162-6166.

[9] J.P. Allen, G. Feher, T.O. Yeates, H. Komiya, D.C. Rees *Structure of the reaction center from Rhodobacter sphaeroides R-26: The cofactors*. Proceedings of the National Academy of Sciences of the United States of America **1987,** 84, 5730-5734.

[10] J. Koepke, E.-M. Krammer, A.R. Klingen, P. Sebban, G.M. Ullmann, G. Fritzsch *pH modulates the quinone position in the photosynthetic reaction center from Rhodobacter sphaeroides in the neutral and charge separated states*. Journal of Molecular Biology **2007,** 371, 396-409.

[11] O.G. Poluektov, L.M. Utschig, S. Dalosto, M.C. Thurnauer *Probing local dynamics of the photosynthetic bacterial reaction center with a cysteine specific spin label*. J.Phys.Chem.B **2003,** 107, 6239-6244.

[12] P. Gajula, I.V. Borovykh, C. Beier, T. Shkuropatova, P. Gast, H.-J. Steinhoff *Spin-labeled photosynthetic reaction centers from Rhodobacter sphaeroides studied by electron*

paramagnetic resonance spectroscopy and molecular dynamics simulations. Applied Magnetic Resonance **2007,** 31*,* 167-178.

[13] F. Lendzian, M. Huber, R.A. Isaacson, B. Endeward, M. Plato, B. Bönigk, K. Möbius, W. Lubitz, G. Feher *The electronic structure of the primary donor cation radical in Rhodobacter sphaeroides R-26: ENDOR and TRIPLE resonance studies in single crystals of reaction centers*. Biochimica et Biophysica Acta **1993,** 1183*,* 139-160.

[14] R. Klette, J.T. Törring, M. Plato, K. Möbius, B. Bönigk, W. Lubitz *Determination of the g tensor of the primary donor cation radical in single crystals of Rhodobacter sphaeroides R-26 reaction centers by 3-mm high-field EPR*. Journal of Physical Chemistry **1993,** 97*,* 2015-2020.

[15] R.A. Isaacson, F. Lendzian, E.C. Abresch, W. Lubitz, G. Feher *Electronic structure of Q_A^- in reaction centers from Rhodobacter sphaeroides .I. Electron paramagnetic resonance in single crystals*. Biophysical Journal **1995,** 69*,* 311-322.

[16] E. Bordignon, A.I. Nalepa, A. Savitsky, L. Braun, G. Jeschke *Changes in the microenvironment of nitroxide radicals around the glass transition temperature*. J.Phys.Chem.B **2015,** 119*,* 13797-13806.

[17] U. Ermler, G. Fritzsch, S.K. Buchanan, H. Michel *Structure of the photosynthetic reaction centre from Rhodobacter sphaeroides at 2.65 Å resolution: Cofactors and protein-cofactor interactions*. Structure **1994,** 2*,* 925-936.

[18] E.C. Abresch, M.L. Paddock, M.H.B. Stowell, T.M. McPhillips, H.L. Axelrod, S.M. Soltis, D.C. Rees, M.Y. Okamura, G. Feher *Identification of proton transfer pathways in the X-ray crystal structure of the bacterial reaction center from Rhodobacter sphaeroides*. Photosynthesis Research **1998,** 55*,* 119-125.

[19] M.L. Paddock, G. Feher, M.Y. Okamura *Proton transfer pathways and mechanism in bacterial reaction centers*. Febs Letters **2003,** 555*,* 45-50.

[20] M.H.B. Stowell, T.M. McPhillips, D.C. Rees, S.M. Soltis, E. Abresch, G. Feher *Light-induced structural changes in photosynthetic reaction center: Implications for mechanism of electron-proton transfer*. Science **1997,** 276*,* 812-816.

[21] G. Fritzsch, L. Kampmann, G. Kapaun, H. Michel *Water clusters in the reaction centre of Rhodobacter sphaeroides*. Photosynthesis Research **1998,** 55*,* 127-132.

[22] D. Kleinfeld, M.Y. Okamura, G. Feher *Electron-transfer kinetics in photosynthetic reaction centers cooled to cryogenic temperatures in the charge-separated state: evidence for light-induced structural changes*. Biochemistry **1984,** 23*,* 5780-5786.

[23] B.H. McMahon, J.D. Muller, C.A. Wraight, G.U. Nienhaus *Electron transfer and protein dynamics in the photosynthetic reaction center*. Biophysical Journal **1998,** 74*,* 2567-2587.

[24] G. Palazzo, A. Mallardi, A. Hochkoeppler, L. Cordone, G. Venturoli *Electron transfer kinetics in photosynthetic reaction centers embedded in trehalose glasses: Trapping of conformational substates at room temperature*. Biophysical Journal **2002,** 82*,* 558-568.

[25] F. Francia, G. Palazzo, A. Mallardi, L. Cordone, G. Venturoli *Probing light-induced conformational transitions in bacterial photosynthetic reaction centers embedded in trehalose-water amorphous matrices*. Biochimica et Biophysica Acta **2004,** 1658*,* 50-57.

[26] F. Francia, M. Dezi, A. Mallardi, G. Palazzo, L. Cordone, G. Venturoli *Protein-matrix coupling/uncoupling in "dry" systems of photosynthetic reaction center embedded in trehalose/sucrose: The origin of trehalose peculiarity*. J.Am.Chem.Soc. **2008,** 130*,* 10240-10246.

[27] A. Savitsky, M. Malferrari, F. Francia, G. Venturoli, K. Möbius *Bacterial photosynthetic reaction centers in trehalose glasses: Coupling between protein conformational dynamics and electron-transfer kinetics as studied by laser-flash and high-field EPR spectroscopies*. J.Phys.Chem.B **2010,** 114*,* 12729-12743.

[28] F. Francia, G. Palazzo, A. Mallardi, L. Cordone, G. Venturoli *Residual water modulates Q_A^--to-Q_B electron transfer in bacterial reaction centers embedded in trehalose amorphous matrices*. Biophysical Journal **2003,** 85*,* 2760-2775.

[29] M. Malferrari, F. Francia, G. Venturoli *Coupling between electron transfer and protein-solvent dynamics: FTIR and laser-flash spectroscopy studies in photosynthetic reaction center films at different hydration levels*. J.Phys.Chem.B **2011,** 115*,* 14732-14750.

[30] A. Savitsky, A.A. Dubinskii, M. Plato, Y.A. Grishin, H. Zimmermann, K. Möbius *High-field EPR and ESEEM investigation of the nitrogen quadrupole interaction of nitroxide spin labels in disordered solids: Toward differentiation between polarity and proticity matrix effects on protein function*. J.Phys.Chem.B **2008,** 112*,* 9079-9090.

[31] K.A. Gray, J.W. Farchaus, J. Wachtveitl, J. Breton, D. Oesterhelt *Initial characterization of site-directed mutants of tyrosine M210 in the reaction centre of Rhodobacter sphaeroides*. Embo Journal **1990,** 9*,* 2061-2070.

[32] L.M. Utschig, S.R. Greenfield, J. Tang, P.D. Laible, M.C. Thurnauer *Influence of iron-removal procedures on sequential electron transfer in photosynthetic bacterial reaction centers studied by transient EPR spectroscopy*. Biochemistry **1997,** 36*,* 8548-8558.

[33] K.M. Giangiacomo, D.E. Robertson, M.R. Gunner, L.P. Dutton Stigmatellin and other electron transfer inhibitors as probes for the Q_B binding site in the reaction center of photosynthetic bacteria. in: J. Biggins (Ed.), Progress in Photosynthesis Research, Springer Netherlands, Dodrecht, 1987, pp. 409-412.

[34] M. Malferrari, G. Venturoli, F. Francia, A. Mezzetti *A new method for D_2O/H_2O exchange in infrared spectroscopy of proteins*. Spectroscopy-An International Journal **2012,** 27, 337-342.

[35] M. Malferrari, A. Nalepa, G. Venturoli, F. Francia, W. Lubitz, K. Möbius, A. Savitsky *Structural and dynamical characteristics of trehalose and sucrose matrices at different hydration levels as probed by FTIR and high-field EPR*. Physical Chemistry Chemical Physics **2014,** 16, 9831-9848.

[36] L.B. Rockland *Saturated salt solutions for static control of relative humidity between 5° and 40°C*. Analytical Chemistry **1960,** 32, 1375-1376.

[37] A. Nalepa, K. Möbius, W. Lubitz, A. Savitsky *High-field ELDOR-detected NMR study of a nitroxide radical in disordered solids: Towards characterization of heterogeneity of microenvironments in spin-labeled systems*. Journal of Magnetic Resonance **2014,** 242, 203-213.

[38] N. Cox, W. Lubitz, A. Savitsky *W-band ELDOR-detected NMR (EDNMR) spectroscopy as a versatile technique for the characterisation of transition metal-ligand interactions*. Mol.Phys. **2013,** 111, 2788-2808.

[39] G. Jeschke, H.W. Spiess *NMR-correlated high-field electron paramagnetic resonance spectroscopy*. Chem.Phys.Lett. **1998,** 293, 9-18.

[40] M. Pavone, A. Sillanpää, P. Cimino, O. Crescenzi, V. Barone *Evidence of variable H-bond network for nitroxide radicals in protic solvents*. J.Phys.Chem.B **2006,** 110, 16189-16192.

[41] P. Gast, R.T.L. Herbonnet, J. Klare, A. Nalepa, C. Rickert, D. Stellinga, L. Urban, K. Mobius, A. Savitsky, H.J. Steinhoff, E.J.J. Groenen *Hydrogen bonding of nitroxide spin labels in membrane proteins*. Physical Chemistry Chemical Physics **2014,** 16, 15910-15916.

[42] E.M. Bruch, M.T. Warner, S. Thomine, L.C. Tabares, S. Un *Pulse Electron Double Resonance detected multinuclear NMR spectra of distant and low sensitivity nuclei and its application to the structure of Mn(II) centers in organisms*. The Journal of Physical Chemistry B **2015,** 119, 13515-13523.

[43] K. Möbius, A. Savitsky, A. Nalepa, M. Malferrari, F. Francia, W. Lubitz, G. Venturoli *The magic of disaccharide glass matrices for protein function as decoded by high-field EPR and FTIR spectroscopy*. Applied Magnetic Resonance **2015,** 46, 435-464.

[44] J.F. Carpenter, J.H. Crowe *An infrared spectroscopic study of the interactions of carbohydrates with dried proteins*. Biochemistry **1989,** 28, 3916-3922.

[45] P.S. Belton, A.M. Gil *IR and Raman spectroscopic studies of the interaction of trehalose with hen egg white lysozyme*. Biopolymers **1994,** 34, 957-961.

[46] M.K. Bosch, P. Gast, A.J. Hoff, A.P. Spoyalov, Y.D. Tsvetkov *The primary acceptor quinone Q_A in reaction centers of Rhodobacter sphaeroides R26 Is hydrogen bonded to the $N^{\delta(1)}$-H of His M219. An electron spin echo study of Q_A^{-}*. Chemical Physics Letters **1995,** 239*,* 306-312.

[47] F. Lendzian, J. Rautter, H. Käß, A. Gardiner, W. Lubitz *ENDOR and pulsed EPR studies of photosynthetic reaction centers: Protein-cofactor interactions*. Berische der Bunsengesellschaft für physikalische Chemie **1996,** 100*,* 2036-2040.

[48] M. Flores, R. Isaacson, E. Abresch, R. Calvo, W. Lubitz, G. Feher *Protein-cofactor interactions in bacterial reaction centers from Rhodobacter sphaeroides R-26: I. Identification of the ENDOR lines associated with the hydrogen bonds to the primary quinone Q_A^{-}*. Biophysical Journal **2006,** 90*,* 3356-3362.

[49] M. Flores, R. Isaacson, E. Abresch, R. Calvo, W. Lubitz, G. Feher *Protein-cofactor interactions in bacterial reaction centers from Rhodobacter sphaeroides R-26: II. Geometry of the hydrogen bonds to the primary quinone Q_A^{-} by ^1H and ^2H ENDOR spectroscopy*. Biophysical Journal **2007,** 92*,* 671-682.

[50] G. Feher, R.A. Isaacson, M.Y. Okamura, W. Lubitz Antennas and reaction centers of photosynthetic bacteria - structure, interactions and dynamics, Springer, Berlin, 1985.

[51] J.S. van den Brink, A.P. Spoyalov, P. Gast, W.B.S. van Liemt, J. Raap, J. Lugtenburg, A.J. Hoff *Asymmetric binding of the primary acceptor quinone in reaction centers of the photosynthetic bacterium Rhodobacter sphaeroides R26, probed with Q-band (35 GHz) EPR spectroscopy*. Febs Letters **1994,** 353*,* 273-276.

[52] J. Breton, C. Boullais, J.-R. Burie, E. Nabedryk, C. Mioskowski *Binding sites of quinones in photosynthetic bacterial reaction centers investigated by light-induced FTIR difference spectroscopy: assignment of the interactions of each carbonyl of Q_A in Rhodobacter sphaeroides using site-specific ^{13}C-labeled ubiquinone*. Biochemistry **1994,** 33*,* 14378-14386.

[53] R. Brudler, H.J.M. de Groot, W.B.S. van Liemt, W.F. Steggerda, R. Esmeijer, P. Gast, A.J. Hoff, J. Lugtenburg, K. Gerwert *Asymmetric binding of the 1- and 4-C=0 groups of Q_A in Rhodobacter sphaeroides R26 reaction centers monitored by Fourier transform infra-red spectroscopy using site-specific isotopically labelled ubiquinone-10*. Embo Journal **1994,** 13*,* 5523-5530.

[54] A.Yu. Borisov, M.V. Fok *The polarization model in bacterial photosynthesis*. Biochemistry and Molecular Biology International **1999,** 47*,* 117-125.

[55] J.A. Potter, P.K. Fyfe, D. Frolov, M.C. Wakeham, R. van Grondelle, B. Robert, M.R. Jones *Strong effects of an individual water molecule on the rate of light-driven charge separation in the Rhodobacter sphaeroides reaction center*. Journal of Biological Chemistry **2005,** 280*,* 27155-27164.

[56] H.L. Axelrod, E.C. Abresch, M.Y. Okamura, A.P. Yeh, D.C. Rees, G. Feher *X-ray structure determination of the cytochrome c_2: Reaction center electron transfer complex from Rhodobacter sphaeroides*. Journal of Molecular Biology **2002,** 319*,* 501-515.

[57] M. Plato, K. Möbius, W. Lubitz in: H. Scheer (Ed.), Chlorophylls, CRC Press, Boca Raton, 1991, pp. 1015.

[58] N. Grasmeijer, M. Stankovic, H. de Waard, H.W. Frijlink, W.L.J. Hinrichs *Unraveling protein stabilization mechanisms: Vitrification and water replacement in a glass transition temperature controlled system*. Biochimica et Biophysica Acta (BBA) **2016,** 1834*,* 763-769.

Chapter 8

Preparation of cysteine-34-nitroxide spin-labeled human α_1-microglobulin

This chapter has been partially published as A.I. Nalepa, J.J. Taing, A. Savitsky, M. Knipp *Preparation of cysteine-34-nitroxide spin labeled human α_1-microglobulin*. Protein Expression and Purification **2013,** 88*,* 33-40 and edited for consistency of notation.

8.1 Introduction

α_1-Microglobulin (α_1m) is a 26 kDa plasma and tissue protein belonging to the superfamily of lipocalins [1]. The core structure of the lipocalins is comprised of an 8-stranded antiparallel β-sheet barrel that typically hosts a hydrophobic ligand [2]. In most cases lipocalins contain one or more disulfide bridges. α_1m is mainly expressed in the liver [3], secreted to the blood, and rapidly transported to the extravascular compartment of the peripheral tissues [4;5]. Due to its small size, it is rapidly cleared from the blood by glomerular filtration. Most of the filtrated α_1m is degraded in the kidneys, but small amounts of α_1m are also found in the urine [6], where it is used for diagnostic purposes [7]. The protein is glycosylated with two highly branched *N*-linked and one *O*-linked oligosaccharide [8]. In plasma, about 50% of the α_1m molecules are found in high molecular weight complexes with other serum proteins, mostly with IgA via Cys34 [9], but also with serum albumin and prothrombin [10] and interactions with receptors were found on the surface of different white blood cells [11]. α_1m has a yellow–brown color and reveals charge and size heterogeneity. These features are caused by a set of unidentified chromophores attached to Cys34 [12] and Lys92, Lys118, and Lys130 [13].

In the gene encoding for α_1m, an N-terminal signal peptide is also encoded which leads to the secretion of the protein. At the C-terminal site another sequence is located, that encodes the extracellular protein bikunin, which is the light chain of the plasma protease inhibitor inter-α-inhibitor. The sequences for both proteins are fused in such a way that both proteins are always co-translated as a single polypeptide chain and then cleaved in the Golgi apparatus [3;14;15]. This is surprising since a common physiological function for both proteins is not at hand. The full-length sequence, i.e., signal peptide–α_1m–bikunin is termed protein AMBP (UniProt ID: P02760**)**.

The biological function of α_1m is still unclear. Recent reports point out to a function in heme catabolism and protection against toxicity of hemoglobin (Hb), heme, and free radicals [16-18]. Furthermore, it was shown that reaction of α_1m with the radical 2,2'-azino-bis-(3-ethylbenzthiazoline-6-sulfonic acid) (ATBS) involves Cys34 and results in modification of amino acid side-chains [19]. Generation of a truncated form, t-α_1m, by an interaction with Hb led to degradation of heme [9]. Overall, detailed characterizations of the α_1m-heme interactions are lacking.

The members of another family of lipocalins, termed nitrophorins (NPs), are well-known to bind heme as a cofactor inside their β-barrel structures [20-22]. The almost purely β-strand structure, including two disulfide bridges, is in marked contrast to any other class of heme proteins. Only very

recently, a heme b protein from *Arabidopsis thaliana*, named "nitrobindin", with similar fold was described, although its structure is formed by a 10-stranded β-barrel [23].

By analogy to the NPs, recently a method to obtain a stable heme-α_1m complex was established [24]. For this purpose it was required to modify Cys34 which was achieved through acetamidation with 2-iodoacetamide (IAM). This protein, termed α_1m^{AM}, not only forms a stable complex with heme, but also trimerises, with two heme cofactors being bound per α_1m^{AM} monomer. Thus, a complex $[\alpha_1m^{AM}(heme)_2]_3$ is formed. However, the position and the coordination sphere of the cofactor and the structural details of the complex are not known. Recently, a crystallographic structure of apo-α_1m(C34S) at 2.3 Å resolution was published (PDB ID: 3QKG) [25], which provides a good starting model for following structural investigations.

The expression of human α_1m in *Escherichia coli* as inclusion bodies, the refolding, and purification was achieved in the past [24;26]. α_1m was also previously successfully expressed in baculovirus infected Hi-5 insect cells [27] and in mammalian cells, *i.e.*, COS cells [28]. Although the expression in eukaryotic cells can establish side-chain glycosylation, the bacterial expression provides higher yields and non-glycosylated proteins that are easier to structurally characterize. In this work, the protein production protocol was improved and optimized for the preparation of a tag-free polypeptide. To study the static structure of both the monomeric and trimeric complexes with heme, the modification with nitroxide spin label over IAM is advantageous. In the future perspective, this allows the application of pulsed electron paramagnetic resonance techniques (e.g. 4-pulse PELDOR [29] and Relaxation Induced Dipolar Modulation Enhancement (RIDME) [30]) as a complementary tool to X-ray crystallography to obtain long-range distance information on the structure of formed complex. Dipole-dipole interaction between two nitroxides or between nitroxide and metal porphyrin can be translated into distance information, providing additional constraints to determine the structure of the complex and possible interaction sites. In this work, the quantitative insertion of nitroxide spin label at the position of Cys34 is shown.

8.2 Materials and Methods

Materials

Sequencing grade trypsin from bovine pancreas was obtained from Serva. All reagents were of highest grade commercially available and used as received. Solutions of 3-(2-iodoacetamido)-2,2,5,5-tetramethyl-1-pyrrolidinyloxy (3-(2-iodoacetamido)-PROXYL, Sigma-Aldrich) were always prepared fresh before use and then protected from light.

Construction of the expression plasmid

The previously described expression plasmid with ampicillin resistance was used as a template [26]. To remove the His-tag from α_1m, cloning sites for *Nco*I and *Bam*HI were added to the cDNA at the 5'-end and 3'-end, respectively, as is shown in Scheme 1. The cDNA codes for human α_1m correspond to amino acid residues 20-203 of the human AMBP protein (GenBank ID: X04225), thus lack the signal peptide and bikunin. The gene was then inserted into a pET-28a(+) host vector which contains kanamycin resistance (Novagen). Cloning and sequencing were carried out by GenScript USA, Inc.

Protein expression and folding

Upon transformation of the plasmids into *Escherichia coli* strain BL21(DE3) (Novagen), cells were grown in 1 L cultures in LB medium (1.0% (w/v) tryptone, 0.5% (w/v) yeast extract, 1.0% (w/v) NaCl) containing 0.005% (v/v) Antifoam 204 (Sigma-Aldrich) and 100 µg L^{-1} of ampicillin or 30 µg L^{-1} of kanamycin sulfate, respectively, under vigorous shaking at 37°C. Similar to the previous method [24;26], protein expression was induced at an $OD_{600\ nm}$ = 1.2 by the addition of 1 mM of isopropyl β-D-1-thiogalactopyranoside (IPTG). Culture growth was then continued for 5 h. Subsequently, the cells were harvested by centrifugation (5,000 *g*, 15 min, 4°C). Upon resuspension in 0.9% (w/v) of NaCl, the cells were homogenized in an Emulsiflex C-15 high pressure homogenizer (Avestin). After centrifugation of the homogenate at (5,000 *g*, 20 min, 4°C), inclusion bodies were yielded that were then treated similar to the method established for NPs production [31;32]. Typically, material from an expression volume of 4 L was sequentially washed with 160 mL each of 30 mM Tris/HCl (pH 7.4), 30 mM NaCl, 1 mM EDTA, 2% (v/v) Tween-20, 1 mM 1,4-dithio-D,L-threitol (DTT) (2 times), then with 30 mM Tris/HCl (pH 7.4), 500 mM NaCl, 1 mM EDTA, 1 mM DTT (2 times), subsequently with 30 mM Tris/HCl (pH 7.4), 30 mM NaCl, 1 mM EDTA, 1 mM DTT (2 times), and finally with 10 mM NaH_2PO_4/NaOH (pH 7.5), 1.5 M urea, and 2 mM tris-(carboxyethyl)phosphine hydrohloride (TCEP·HCl). Afterwards, the protein was dissolved in 12 mL of 10 mM NaH_2PO_4/NaOH (pH 7.5), 6 M guanidinium chloride (GdmCl), and 2 mM TCEP·HCl. In the next step, the protein fold was established by the drop-in method where 500 mL of 50 mM Tris/HCl (pH 8.2), 250 mM NaCl, 500 mM sucrose, 500 mM L-arginine, 0.005% (w/v) PEG_{3500}, 1 mM GSH, and 200 µM GSSG were used. After stirring for 1 h at ambient temperature and atmosphere, the solution was transferred into an anaerobic chamber (Coy, Inc.) with Pd catalysts and an atmosphere comprised of 98% N_2/2% H_2. After stirring overnight, $(NH_4)_2SO_4$ was added to a saturation of 20%. After centrifugation (16,000 *g*, 60 min, 4°C) the supernatant was collected and saturation of $(NH_4)_2SO_4$ was increased to 70%. After another centrifugation (16,000 *g*, 60 min, 4°C) the precipitate was collected and dissolved in 20 mL of 100 mM Tris/HCl (pH 8.2).

Modification of Cys34 and size-exclusion chromatography

The protein was kept under anaerobic conditions throughout. The free thiol content was determined using the DTP test described below. Afterwards, the protein preparation was incubated overnight in the dark at ambient temperature with either 1 mM IAM dissolved in H_2O or with ~3 mol equiv of (3-(2-iodoacetamido)-PROXYL dissolved in DMSO. The resulting forms of α_1m are termed α_1m^{AM} or $\alpha_1m^{N-O\bullet}$, respectively. Another DTP test was performed thereafter. The protein was then loaded onto a size-exclusion chromatography (SEC) column (26 × 600 mm) filled with Sephacryl S-100 HR (GE Healthcare) that was equilibrated with 100 mM MOPS/NaOH (pH 7.5), 50 mM NaCl, and 10% (v/v) glycerol.

DTP test

The test was performed under anaerobic conditions to avoid Cys oxidation. Prior to the testing, the buffer was extensively exchanged to 200 mM NaO*Ac* (sodium acetate)/HO*Ac* (pH 4.0), 6 M GdmCl, and 1 mM EDTA using Amicon Ultra-0.5 ultrafiltration units (Millipore Inc.). 100 µL of a stock solution of 2,2'-dithiopyridine (DTP) [33;34] was mixed with 900 µL protein solution inside a quartz

cuvette and the absorbance development at 343 nm was monitored. After the reaction had come to an end (~15 min), the absorbance was read ($\varepsilon_{343\ nm}$ = 7600 M^{-1} cm^{-1}) and used for the determination of the thiol/protein ratio.

Trypsin digest and MALDI-TOF MS

18 µg of protein was dissolved in 30 µL of 50 mM NH_4HCO_3 and 3 µL of CH_3CN were added. Upon addition of 0.5 µL of 0.4 µg of trypsin dissolved in 1 mM HCl, the sample was incubated for 2 h at 37°C. The sample was then dried in a Speed-Vac before analysis on a Voyager-DE PRO Workstation MALDI-TOF-System (Applied Biosystems) with a nitrogen laser (338 nm, maximal pulse energy 32 µJ at 10 Hz). α-Cyano-4-hydroxycinnamic acid (CHCA) was used as a matrix.

CD and MCD spectroscopy

Circular dichroism (CD) measurements were performed using a Jasco Model J-715 spectropolarimeter in quartz cuvettes with 0.1 cm path length at ambient temperature. Four to six spectra were accumulated for each sample between 260 and 186 nm and the values were normalized to the protein concentration upon baseline subtraction. The instrument determines the ellipticity θ, in millidegree, which was converted into the molar extinction by the equation:

$$\Delta\varepsilon = \frac{4\pi \cdot \theta}{180 \cdot \ln(10) \cdot c \cdot l} = \frac{\theta}{32.982 \cdot c \cdot l} \qquad \text{Eq. (8.1)}$$

where c is the sample concentration in mol L^{-1}, and l the cuvette path length in cm. CD spectra were recorded in the UV range (260-185 nm) in 10 mM Tris/H_3BO_3 (pH 8.2) and analyzed by the CDSSTR algorithm [35-37] using DICHROWEB [38-40].

In case of magnetic circular dichroism (MCD) spectroscopy, spectra were recorded in a 1.0 cm quartz cuvette included in a permanent magnet of 1.4 T field strength (Ollis, Inc.). Spectra with both parallel and anti-parallel magnetic field orientation were recorded and the resulting spectrum was calculated as:

$$\theta_M = \frac{\theta_{CD+MCD} - \theta_{CD-MCD}}{2} \qquad \text{Eq. (8.2)}$$

where θ_{CD+MCD} describes the spectrum recorded in parallel and θ_{CD-MCD} the spectrum recorded with anti-parallel magnetic field orientation.

EPR spectroscopy

CW EPR measurements were performed on a Bruker ELEXSYS E580 X-band spectrometer equipped with a Super X FT-EPR bridge, using a dielectric resonator ER 4118X-MD-4W1. The temperature of 170 K was controlled using an Oxford CF935 cryostat with an Oxford ITC4 temperature controller. The low temperature spectra were recorded with the microwave power of 3.8 µW with a modulation frequency of 100 kHz and modulation amplitude set to 0.2 mT. At least 9 spectra were averaged to obtain sufficient signal to noise ratio. For spin counting, the sample volume of 310 µl was applied in quartz capillaries (O.D. 3.8 mm) to ensure that the active volume of the resonator is filled. The room temperature spectra were recorded with a microwave power of 0.95 mW and a modulation amplitude of 0.1 mT.

8.3 Preparation of α_1m^{AM}

A major challenge for the production and handling of α_1m is the presence of 3 Cys of which Cys72 and Cys169 form a disulfide bridge and Cys34 is a highly reactive residue involved in free radical formation [19]. A method that achieves the formation of such a protein form was established in which the Cys34 was carbamidomethylated through nucleophilic substitution of 2-iodoacetamide (IAM), termed α_1m^{AM}, to avoid radical formation for structural and spectroscopic studies [24]. It should be noted that the formation of a bond with Cys34 is of physiological interest because it is well established that the residue allows the formation of covalent complexes with other proteins via disulfide bond formation, for example with IgA [10].

Recently an X-ray structure of α_1m (with mutation C34S) at 2.3 Å resolution was published (PDB ID: 3QKG). In this case, the mutant protein was expressed into the *E. coli* periplasm using an N-terminal OmpA signal peptide and a C-terminal Strep-tag. In this case, the periplasm is able to establish the formation of the Cys72–Cys169 disulfide bond. However, the aim of insertion of a nitroxide spin label into α_1m for distance determination using pulsed EPR spectroscopy requires an increased protein yield. For this purpose, the protein expression protocol was adapted in the following steps:

- The inclusion bodies were dissolved in 6 M GdmCl yielding a higher degree of solvation of inclusion bodies.
- The volume of the refolding buffer relative to the volume of dissolved inclusion bodies was increased.
- Subsequent fractionated precipitation with 20% and 70% saturation of $(NH_4)_2SO_4$ allows the rapid concentration of the protein and further purification in a single step. By these modifications, the yield was increased by approx. 3-fold compared to previous method [24].

Another aim was to remove the His-tag that is located at the N-terminus in the previous construct since the proteolysis of the tag after purification is often not sufficient. Furthermore, for structural biology, for example crystallization experiments, a tag sequence is not supportive. Therefore, a plasmid construct without a tag was prepared, see Scheme 8.1.

T7-promoter ***lac* operator** **ribosome binding site** ***Nco*I**

5'-
...TAATACGACTCACTATAGGGGAATTGTGAGCGGATAACAATTCCCCTCTAGAAATAATTTTGTTT
AACTTTAAGAAGGAGATATACCATGGGCCCTGTGCCAACGCCGCCCGACAACATCCAAGTG...
MetGlyProValProThrProProAspAsnIleGlnVal...

***Bam*HI**

...TGAGGACTCCATCTTCACCATGGCTGACCGAGGTGAATGCAGGAACCAGAGCCCATCTTAATCC
CGAGATGAGGATCCGAATTCGAGCTCCGTCGACAAGCTTGCGGCCGCACTCGAGCACCACCAC...-
3'
...ThrMetAlaAspArgGlyGluCysValProGlyGluGlnGluProGluProIleLeuIleProArgValSTP

Scheme 8.1. *Cloning strategy for the insertion of α_1m into the pET-28a(+) host vector resulting in pα_1m^{Kan}.*

The protein quality and the yields for α_1m both with and without the tag turned out to be very similar. Table 8.1 summarized the yields of the protein throughout the purification procedure. As a result, α_1m was largely enriched by ~65-fold, resulting in a good yield of ~20 mg per L of expression culture.

Table 8.1 *Representative example of the purification steps and enrichment of recombinant human α_1m expressed in Escherichia coli*[a].

	Purification steps	Total protein mass[b] /mg	Volume /mL	Enrichment (-fold)
1	Resuspended *E. coli* cells	1,300[c]	-	1
2	Solubilization in 6 M GdmCl	720	15	1.8
3	Folding	350	520	4.0
4	Reaction with IAM	260	520	5.0
5	Supernatant at 20% $(NH_4)_2SO_4$ saturation	175	540	7.4
6	Precipitation at 70% $(NH_4)_2SO_4$ saturation	38[d]	120	34
7	Size-exclusion chromatography peak *m* (see Fig. 8.1)	20	85	65

[a] Corresponding to a preparation from 1 L of expression culture. [b] Estimated from the absorption at 280 nm ($\varepsilon_{280\ nm}$ = 40,625 M^{-1} cm^{-1}). [c] Wet mass. [d] Upon resolubilization in 100 mM Tris/HCl (pH 8.2).

This is also reflected in the SDS-PAGE in Fig. 8.1 (left) that demonstrates the purity gained during each step and shows, most importantly, that the protein is very pure after the final step of the procedure. As a last step, SEC was performed. With the higher amounts of protein obtained through this protocol, the protein tends to elute to a large fraction as a dimer which is demonstrated in Fig. 8.1(right). SDS-PAGE analysis of the two chromatographic peaks *m* and *d* under reducing conditions (+BME, β-mercaptoethanol) demonstrates that both peaks contain only a single protein of the apparent mass of α_1m (29 kDa). The SDS-PAGE of peak *d* without BME (-BME), however, shows, besides a major fraction of α_1m with the apparent mass of monomer (27 kDa), a small portion occurring at the apparent mass of α_1m dimer (45 kDa).

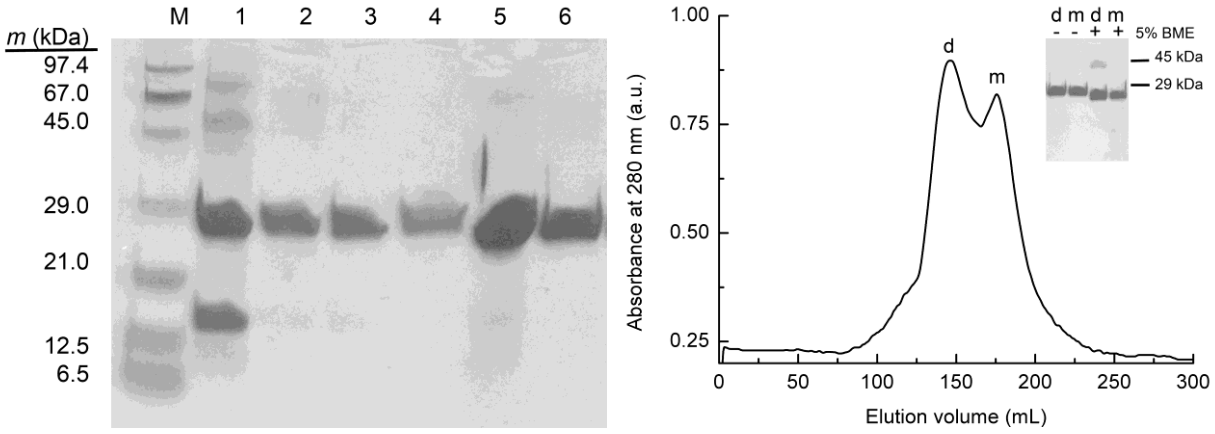

Figure 8.1 *(left) Reducing SDS-PAGE (12.5%) documenting the enrichment during the α_1m preparation. Lane 1, inclusion bodies after washing (dissolved in 8 M urea); lane 2, after refold; lane 3, after the reaction with IAM; lane 4 after 20% $(NH_4)_2SO_4$ saturation; lane 5, after 70% $(NH_4)_2SO_4$ saturation, precipitate after dissolving in 100 mM Tris/HCl (pH 8.2); lane 6, after size-exclusion chromatography. In each case, 10 µL solution were mixed with 10 µL of reducing sample buffer and heated for 4 min at 70°C before application to the gel. Composition of sample buffer: 20 mM Tris/HCl (pH 6.8), 1 mM Na_2EDTA, 20% (v/v) glycerol, 0.025 (w/v) bromphenol blue, 5% (v/v) 2-mercaptoethanol. The following proteins were used as markers (M): bovine*

lung trypsin inhibitor (6.5 kDa); cytochrome c (12.5 kDa); soybean trypsin inhibitor (21.0 kDa); carbonic anhydrase (29.0 kDa); egg albumin (29.0 kDa); bovine serum albumin (67.0 kDa). The gel was stained with Coomassie brilliant blue R-250.
(right) Size-exclusion chromatography of α_1m^{AM} on a Sephacryl S-100 HR column (26 × 600 mm). 20 µL of the main fractions of the two peaks (d = dimer, m = monomer) were analyzed by SDS-PAGE (12.5%, staining with Coomassie brilliant blue R-250) mixed with 10 µL of sample buffer (20 mM Tris/HCl (pH 6.8), 1 mM Na_2EDTA, 20% (v/v) glycerol, 0.025 (w/v) bromphenol blue) with and without 5% (v/v) of α-mercaptoethanol (α-ME). Before loading to the gel, samples mixed with sample buffer were heated for 4 min at 70°C.

As a conclusion, the SEC peak *d* contains mostly non-covalent dimer and a small fraction of dimer covalently linked through an intermolecular disulfide bond. The slight but significant difference of apparent molecular mass in the presence or absence of BME results from the higher compactness of α_1m with the intramolecular disulfide bond Cys72–Cys169 present (-BME) compared to the fully reduced polypeptide (+BME). Because fraction d contains some covalent dimer, only fraction *m* was collected for any further experiments.

8.4 Preparation of $\alpha_1m^{N–O•}$

Insertion of a spin label is typically performed using (1-oxyl-2,2,5,5-tetramethylpyrroline-3-methyl) methanethiosulfonate (MTSSL) as a reagent for the modification of free Cys [41]. Inspection of the X-ray structure of α_1m suggests that Cys34 is positioned at the surface of a cleft that is large enough to accommodate the spin label (see Fig. 8.2). Therefore, the labeling with MTSSL was initiated. The precipitation with $(NH_4)_2SO_4$ allows the efficient removal of the GSH that is required for the successful performance of the reaction.

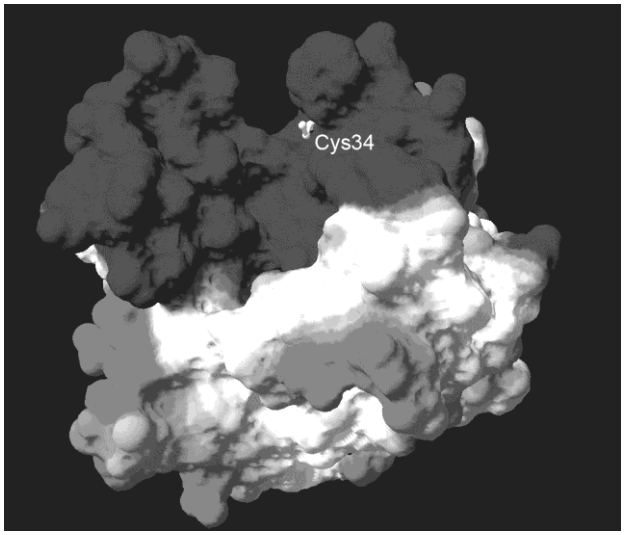

Figure 8.2 *Surface representation of α_1m generated from the X-ray structure (PDB ID: 3QKG, [25]). Positive charges are indicated in dark grey, negative charges in light grey. The position of Cys34 is presented in a ball and stick model. The picture was generated with SWISS-PDBVIEWER 4.04 [42].*

DTP testing was applied to determine the remainder of free thiols before addition of the reagent. However, although reactions with MTSSL were performed at pH conditions between 7.5 and 8.2, where both the protein and the spin probe are stable, and by the addition of 3 to 20 mol equiv of MTSSL, sufficient labeling was not obtained (<15%) as was judged by X-band cw EPR spectroscopy.

The reaction was carried out for up to 24 h and both at room temperature as well as at 4˚C and 37˚C without gain in labeling efficiency.

However, because the crystal structure of α_1m suggests that Cys34 in principle should not be sterically hindered, the spin labeling method was applied using 3-(2-iodoacetamido)-PROXYL nitroxide, that follows the same chemistry as IAM. Labeling was performed overnight at room temperature with 3-5 times molar excess of nitroxide over protein. X-band cw EPR spectroscopy demonstrated that in this case the spin-label was quantitatively inserted. For this purpose it was mandatory to determine an accurate molar extinction coefficient for α_1m, as described below. The modified protein was termed $\alpha_1 m^{N-O\bullet}$.

8.5 Determination of the molar extinction coefficient of $\alpha_1 m^{AM}$ and $\alpha_1 m^{N-O\bullet}$

For the performance of pulsed EPR studies the yield of modification is critical. While the yield of the inserted spin label is quantified by EPR spectroscopy, the protein concentration is determined by UV-vis spectroscopy, typically based on the absorbance of the aromatic side-chains. However, for this purpose an accurate extinction coefficient is required. The amino acid sequence of α_1m contains 4 Trp residues, which, thus, dominate the absorbance spectrum. However, the intensity and energy of the electronic absorbance of the Trp side chain is partly dependent on the environment of the chromophore. It was previously shown that the $\pi \rightarrow \pi^*$ transition into the excited state ^1L_b at 290 nm of L-tryptophan [43;44] is strongly enhanced and well resolved from the excitation into ^1L_a through opposite polarization in MCD spectroscopy.

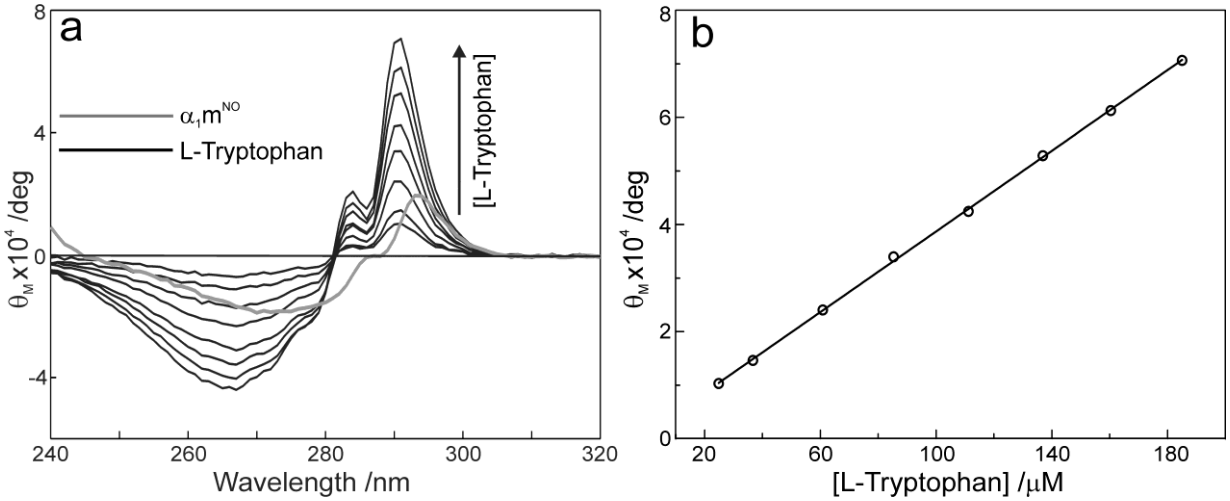

Figure 8.3 *Determination of the $\alpha_1 m^{N-O\bullet}$ extinction coefficient by MCD spectroscopy of the tryptophan. (a) MCD spectra of L-tryptophan at molar concentration of 25, 35, 60, 85, 110, 135, 160, and 185 μM were recorded (black traces). A spectrum of a solution of $\alpha_1 m^{N-O\bullet}$ with an absorbance of 0.495 at 280 nm was also recorded (gray trace). (b) The ellipticity, θ_M, values read out at 291 nm in (a), plotted versus the L-tryptophan concentration. Based on the linear curve fitted (R^2 = 0.99966), the concentration of $\alpha_1 m^{N-O\bullet}$ was obtained for given ellipticity value.*

Furthermore, although the energy of the transition is subject to batochromic or hypsochromic shifts, its intensity is largely independent of the polarity of the environment and thus an excellent tool for extinction coefficient determination of a protein [45;46]. To accurately determine the extinction coefficient of α_1m, a calibration curve of L-tryptophan in 10 mM Tris/H_3BO_3 (pH 8.2) was determined by MCD using a 1.4 T permanent magnet, see Fig. 8.3. An absorption spectrum of α_1m in 10 mM

Tris/H_3BO_3 (pH 8.2) was first recorded, and subsequently an MCD spectrum which allowed the determination of $\varepsilon_{280\ nm}$ = 40,625 M^{-1} cm^{-1}.

8.6 Mass spectrometric analysis

Upon modification with either IAM or 3-(2-iodoacetamido)-PROXYL the protein was digested with trypsin and subjected to MALDI-TOF MS. Most of the signals obtained from α_1m^{AM} were already obtained in the previous study [24]. The mass peaks were assigned as is presented in Table 8.2.

Table 8.2 *Peptides $[M + H]^+$ of α_1m^{AM} and $\alpha_1m^{N–O•}$ after Tryptic Digest.*[a]

	m/*z* (Da)		
	Calculated	Observed	
Peptide		R = AM	R = N–O•
^{25}WYNLAIGSTC^{R}PWLK^{38}	1,710.0/1,851.0[b]	1,710.3 [c]	1,852.6[d]
^{44}MTVSTLVLGEGATEAEISMTSTR^{66}	2,385.7	2,385.0 [c]	2,387.0
^{93}SKWNITMESYVVHTNYDEYAIFLTK^{117}	3,054.5	3,054.3 [c]	3,056.7
^{95}WNITMESYVVHTNYDEYAIFLTK^{117}	2,839.2	2,838.4 [c]	2,839.2
^{122}HHGPTITAK^{130}	961.5	962.4	962.9
^{140}ETLLQDF^{147}	1,022.2	1,022.4 [c]	1,023.0
^{148}VVAQGVGIPEDSIFTMADR^{166}	2,006.3	2,006.2 [c]	-
^{70}GVCEETSGAYEK^{81} | ^{148}VVAQGVGIPEDSIFTMADRGECVPGEQEPEPILIPR^{183} [e]	5,119.4	5,119.3	5,118.7
(^{148}VVAQGVGIPEDSIFTMADRGEC^{AM}VPGEQEPEPILIPR^{183})[f]	(3,919.9)	(3,906.8)	(3,907.1)

[a] Peptides were applied on a CHCA matrix and analyzed by MALDI-TOF MS. [b] Calculated for bothα_1m^{AM} and $\alpha_1m^{N–O•}$. [c] Values taken from [24]. [d] A species with *m*/*z* = 1,833.0 Da was also detected reflecting the radical O depleted nitroxide. [e] The two peptides were covalently linked via the disulfide bridge. [f] This species was only yielded after reduction with TCEP·HCl and subsequent incubation with IAM. Correspondingly, the peak at 5,119.3 or 5,118.7 Da, respectively, disappeared.

The peptides cover 70% over the amino acid sequence. Most importantly, in α_1m^{AM} the peak at 1,710.3 Da reveals the mass of the modified peptide Trp25–Lys38. In case of $\alpha_1m^{N–O•}$, this signal is not obtained but a signal at 1,852.6 Da which corresponds to the modification of Cys34 with 3-(2-iodoacetamido)-PROXYL.When trypsin digested samples of α_1m^{AM} and $\alpha_1m^{N–O•}$ were treated first with 5 mM TCEP and then IAM before subjection to MALDI-TOF MS, the mass peaks corresponding to the peptide Trp25–Lys38 were not changed. However, the mass of the peak at

5,119.3 or 5,118.7 Da, respectively, corresponding to the disulfide linked peptides Gly70–Lys81 and Val148–Arg183, disappeared and a signal at 3,906.8 or 3,907.1 Da, respectively, corresponding to the acetamidated peptide Val148–Arg183, appeared. Thus, in both protein forms the disulfide bond S_{Cys72}–S_{Cys169} is well established.

8.7 Determination secondary structure elements by CD spectroscopy

$\alpha_1m^{N–O•}$ binds heme to the same extent as α_1m^{AM} and triggers the formation of a trimer, which indicates a largely similar fold. CD spectra of the peptide backbone of α_1m^{AM} and $\alpha_1m^{N–O•}$ were recorded between 260 and 190 nm and the content of secondary structure elements was analyzed by the CDSSTR algorithm [35-37]. The results are displayed in Table 8.3 in comparison with the secondary structure elements reported earlier for recombinant α_1m [26] and with the secondary structure elements obtained from the recently releases X-ray structure [25].

Table 8.3 *Comparison of the secondary structure content of recombinant human α_1m^{AM} and $\alpha_1m^{NO•}$ with crystallographic data.*

	α-helix	β-sheet	turn	random	Reference
X-ray structure					
α_1m(C34S)	8%	49%	43%		PDB ID: 3QKG [25]
Secondary structure prediction					
α_1m	9%	39%	52%		UniProtID: P02760[b]
CD spectroscopy					
α_1m	6%	40%	21%	32%	[26][a]
α_1m^{AM}	12%	40%	27%	21%	this work
$\alpha_1m^{N–O•}$	15%	42%	31%	12%	this work

[a] Similar values were reported for the protein isolated from blood and urine. [b] Calculated with PSIPRED v3.0, available at http://bioinf.cs.ucl.ac.uk/psipred/.

Overall, the secondary structure content obtained for both modified α_1m forms is very similar, although not exactly the same. Thus, the insertion seems to introduce slight conformational change. On the other hand, the nitroxides have some absorbance in the UV which might contribute to the CD signal to an unpredictable extend due to the Cotton effect. In comparison to the previous secondary structure estimation, the values are significantly different, but they agree excellently with the secondary structure elements obtained from the crystallographic analysis. The difference with the previous spectroscopic results might originate from the different algorithm used for analysis. The previous analysis was also based on a smaller spectral window down to 200 nm [26]. Because significant structural information is contained in the spectral range <200 nm, spectra were recorded down to 186 nm in this study [47].

8.8 Quantification of the degree of spin labeling in $\alpha_1m^{N-O\bullet}$ preparations

The degree of spin labeling was determined using 55.5 ± 2.5 µM of $\alpha_1m^{N-O\bullet}$ (determined by UV-vis) in 100 mM MOPS/NaOH (pH 7.5) and 20% (v/v) glycerol. The EPR spectrum intensity, which is proportional to the electron spin concentration in the sample, was obtained by double integration of the low-temperature (170 K) X-band cw EPR spectrum. This value was compared to the EPR spectrum intensity of a reference sample, i.e. 3-hydroxymethyl-2,2,5,5-tetramethylpyrrolin-1-oxyl dissolved in 100 mM Tris/HCl (pH 7.5) with 20% (v/v) glycerol, recorded under identical conditions, see Fig. 8.4. From the comparison of double integrals, a total spin concentration of 49.8 ± 5.3 µM was obtained for $\alpha_1m^{N-O\bullet}$. Therefore, a labeling yield of 90 ± 10% was obtained. Because the low-temperature EPR spectrum does not allow to distinguish between free and bound nitroxide, RT X-band cw EPR spectra of the $\alpha_1m^{N-O\bullet}$ protein and of the reference spin probe solution were recorded, see Fig. 8.4(b). The EPR spectrum of the free nitroxide spin label is typical for free tumbling nitroxides in solution with a rotation correlation time of several tens of picoseconds. In contrast, the cw EPR spectrum of $\alpha_1m^{N-O\bullet}$ shows significant immobilization of the spin label. The contribution of the mobile fraction (designated * in Fig. 8.4(b) is estimated to less than 1%. From the line shapes, a rotational correlation time of the immobilized part in the range of nanoseconds is inferred. The mobile fraction is in the sub-nanosecond regime. From the position of Cys34 in the protein structure, a high degree of flexibility is expected, and additionally the spin label has an internal orientational freedom. The distribution of several orientations of the spin label and the flexibility of the protein is also reflected in the low-temperature cw-EPR spectrum in the spectral broadening when compared to the spectrum of the free spin probe (Fig. 8.4(a)). The A_{zz} value extracted from LT cw EPR spectrum for $\alpha_1m^{N-O\bullet}$ is lower, compared to the spin probe. Thus, the average microenvironmental situation of the spin label is shifted toward lower polarity/proticity in $\alpha_1m^{N-O\bullet}$ compared to aqueous environment of the spin probe.

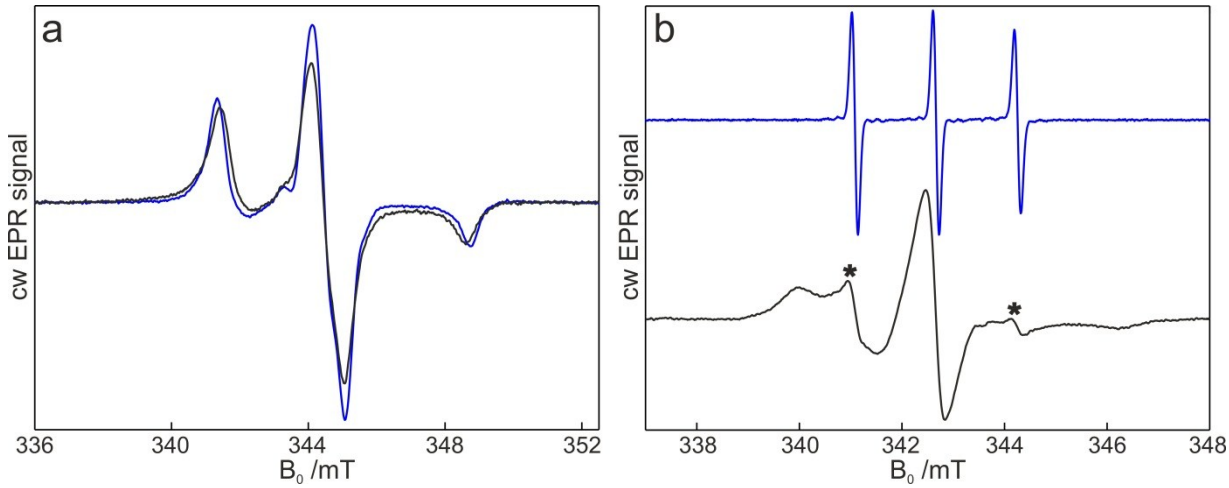

Figure 8.4 *X-band cw EPR spectra of $\alpha_1m^{N-O\bullet}$ solved in 100 mM MOPS/NaOH (pH 7.5) and 20% (v/v) glycerol (black trace) in comparison to that of 3-(2-iodoacetamido)-PROXYL solved in 100 mM Tris/HCl (pH 7.5) and 20% (v/v) glycerol (blue trace). The spectra were recorded at X-band at 170 K (a) at room temperature (b).*

8.9 Conclusions

In summary, a method is presented which improves the yield of the preparation of recombinant human α_1m with Cys34, *i.e.*, α_1m^{AM}, protected. A tag sequence was omitted without compromises in yield or purity. The yields are sufficient even for spectroscopic techniques that require relatively large

amounts of protein like NMR and EPR spectroscopy, so that even isotopic labeling is affordable. Moreover, substitution of IAM with the nitroxide spin label 3-(2-iodoacetamido)-PROXYL resulted in a high degree of nitroxide spin label, *i.e.*, $\alpha_1m^{N-O\bullet}$ at Cys34 with structural and functional features comparable to α_1m^{AM}. Thus, $\alpha_1m^{N-O\bullet}$ can be used for pulsed EPR studies to determine spin-spin interactions for the determination of static properties of the complex (distance) upon insertion of the heme cofactor.

References

[1] S. Pervaiz, K. Brew *Homology of beta-lactoglobulin, serum retinol-binding protein, and protein HC* Science **1985,** 228, 335-337.

[2] D.R. Flower, A.C.T. North, C.E. Sansom *The lipocalin protein family: Structural and sequence overview* Biochim. Biophys. Acta **2000,** 1482, 9-24.

[3] T. Bratt, H. Olsson, E.M. Sjoberg, B. Jergil, B. Akerstrom *Cleavage of the a_1-microglobulin-bikunin precursor is localized to the Golgi apparatus of rat liver cells* Biochim. Biophys. Acta **1993,** 1157, 147-154.

[4] L. Odum, H.W. Nielsen *Human protein HC (a_1-microglobulin) and inter-a-trypsin inhibitor in connective tissue* Histochem. J. **1994,** 26, 799-803.

[5] T. Berggård, T.D. Oury, I.B. Thøgersen, B. Åkerström, J.J. Enghild *α_1-Microglobulin is found both in blood and in most tissues* J. Histochem. Cytochem. **1998,** 46, 887-893.

[6] C. Lopez, A. Grubb, E. Mendez *Human protein HC displays variability in its carboxyl-terminal amino acid sequence* FEBS Lett. **1982,** 144, 349-353.

[7] B. Åkerström, L. Lögdberg, T. Berggård, P. Osmark, A. Lindqvist *a_1-Microglobulin: A yellow-brown lipocalin* Biochim. Biophys. Acta **2000,** 1482, 172-184.

[8] J. Escribano, C. Lopex-Otin, A. Hjerpe, A. Grubb, E. Mendez *Location and characterization of the three carbohydrate prosthetic groups of human protein HC* FEBS Lett. **1990,** 266, 167-170.

[9] M. Allhorn, T. Berggård, J. Nordberg, M.L. Olsson, B. Åkerström *Processing of the lipocalin α_1-microglobulin by hemoglobin induces heme-binding and heme-degradation properties* Blood **2002,** 99, 1894-1901.

[10] T. Berggård, N. Thelin, C. Falkenberg, J.J. Enghild, B. Åkerström *Prothrombin, albumin and immunoglobulin A form covalent complexes with α_1-microglobulin in human plasma* Eur. J. Biochem. **1997,** 245, 676-683.

[11] L. Wester, E. Michaëlsson, R. Holmdahl, T. Olofsson, B. Åkerström *Receptor for α_1-Microglobulin on T lymphocytes: Inhibition of antigen-induced interleukin-2 production* Scand. J. Immunol. **1998,** 48, 1-7.

[12] J. Escribano, A. Grubb, M. Calero, E. Méndez *The protein HC chromophore is linked to the cysteine residue at position 34 of the polypeptide chain by a reduction-resistant bond and causes the charge heterogeneity of protein HC* J. Biol. Chem. **1991,** 266, 15758-15763.

[13] T. Berggård, A. Cohen, P. Persson, A. Lindqvist, T. Cedervall, M. Silow, I.B. Thøgersen, J.A. Jönsson, J.J. Enghild, B. Åkerström *α_1-Microglobulin chromophores are located to three lysine*

residues semiburied in the lipocalin pocket and associated with a novel lipophilic compound Protein Sci. **1999,** 8, 2611-2620.

[14] J. Bourguignon, R. Sesboüé, M. Diarra-Mehrpour, M. Daveau, J.-P. Martin *Human inter-alpha-trypsin inhibitor. Synthesis and maturation in hepatoma HepG2 cells* Biochem. J. **1989,** 261, 305-308.

[15] A. Lindqvist, T. Bratt, M. Altieri, W. Kastern, B. Åkerström *Rat α_1-microglobulin: co-expression in liver with the light chain of inter-□-trypsin inhibitor* Biochim. Biophys. Acta **1992,** 1130, 63-67.

[16] M.G. Olsson, T. Olofsson, H. Tapper, B. Åkerström *The lipocalin α_1-microglobulin protects erythroid K562 cells against oxidative damage induced by heme and reactive oxygen species* Free Radical Res. **2008,** 42, 725-736.

[17] M.G. Olsson, E.J.C. Nilsson, S. Rutardóttir, J. Paczesny, J. Pallon, B. Åkerström *Bystander cell death and stress response is inhibited by the radical scavenger α_1-microglobulin in irradiated cell cultures* Radiat. Res. **2010,** 174, 590-600.

[18] M.G. Olsson, M. Allhorn, J. Larsson, M. Cederlund, K. Lundqvist, A. Schmidtchen, O.E. Sørensen, M. Mörgelin, B. Åkerström *Up-regulation of A1M/α_1-microglobulin in skin by heme and reactive oxygen species gives protection from oxidative damage* PLoS One **2011,** 6, e27505.

[19] B. Åkerström, G.J. Maghzal, C.C. Winterbourn, A.J. Kettle *The lipocalin α_1-microglobulin has radical scavenging activity* J. Biol. Chem. **2007,** 282, 31493-31503.

[20] J.F. Andersen, A. Weichsel, C.A. Balfour, D.E. Champagne, W.R. Montfort *The crystal structure of nitrophorin 4 at 1.5 Å resolution: transport of nitric oxide by a lipocalin-based heme protein* Structure **1998,** 6, 1315-1327.

[21] F.A. Walker *Nitric oxide interaction with insect nitrophorins and thoughts on the electron configuration of the $\{FeNO\}^6$ complex* J. Inorg. Biochem. **2005,** 99, 216-236.

[22] M. Knipp, C. He *Nitrophorins: nitrite disproportionation reaction and other novel functionalities of insect heme-based nitric oxide transport proteins* IUBMB Life **2011,** 63, 304-312.

[23] C.M. Bianchetti, G.C. Blouin, E. Bitto, J.S. Olson, G.N. Phillips *The structure and NO binding properties of the nitrophorin-like heme-binding protein from Arabidopsis thaliana gene locus At1g79260.1* Proteins **2010,** 78, 917-931.

[24] J.F. Siebel, R.L. Kosinsky, B. Åkerström, M. Knipp *Insertion of heme b into the structure of the Cys34-carbamidomethylated human lipocalin α_1-microglobulin: formation of a $[(heme)_2$ (α_1-microglobulin)$]_3$ complex* ChemBioChem **2012,** 13, 879-887.

[25] W. Meining, A. Skerra *The crystal structure of human α_1-microglobulin reveals a potential haem-binding site* Biochem. J. **2012,** 445, 175-182.

[26] A. Kwasek, P. Osmark, M. Allhorn, A. Lindqvist, B. Åkerström, Z. Wasylewski *Production of recombinant human α_1-microglobulin and mutant forms involved in chromophore formation* Protein Expression Purif. **2007,** 53, 145-152.

[27] L. Wester, M.U. Johansson, B. Åkerström *Physicochemical and biochemical characterization of human α_1-microglobulin expressed in baculovirus-infected insect cells* Protein Expression Purif. **1997,** 11, 95-103.

[28] T. Bratt, T. Cedervall, B. Åkerström *Processing and secretion of rat α_1-microglobulin-bikunin expressed in eukaryotic cell lines* FEBS Lett. **1994,** 354, 57-61.

[29] M. Pannier, S. Veit, A. Godt, G. Jeschke, H.W. Spiess *Dead-time free measurement of dipole-dipole interactions between electron spins* J. Magn. Reson. **2000,** 142, 331-340.

[30] S. Milikisyants, F. Scarpelli, M.G. Finiguerra, M. Ubbink, M. Huber *A pulsed EPR method to determine distances between paramagnetic centers with strong spectral anisotropy and radicals: The dead-time free RIDME sequence* J. Magn. Reson. **2009,** 201, 48-56.

[31] M. Knipp, H. Zhang, R.E. Berry, F.A. Walker *Overexpression in Escherichia coli and functional reconstitution of the liposome binding ferriheme protein nitrophorin 7 (NP7) from the bloodsucking bug Rhodnius prolixus* Protein Expression Purif. **2007,** 54, 183-191.

[32] M. Knipp, F. Yang, R.E. Berry, H. Zhang, M.N. Shokhirev, F.A. Walker *Spectroscopic and functional characterization of nitrophorin 7 from the blood-feeding insect Rhodnius prolixus reveals an important role of its isoform-specific N-terminus for proper protein function* Biochemistry **2007,** 46, 13254-13268.

[33] D.R. Grassetti, J.F. Murray *Determination of sulfhydryl groups with 2,2'- or 4,4'-dithiodipyridine* Arch. Biochem. Biophys. **1967,** 119, 41-49.

[34] A.O. Pedersen, J. Jacobsen *Reactivity of the thiol group in human and bovine albumin at pH 3-9, as measured by exchange with 2,2'-dithiodipyridine* Eur. J. Biochem. **1980,** 106, 291-295.

[35] L.A. Compton, W.C. Johnson *Analysis of protein circular dichroism spectra for secondary structure using a simple matrix multiplication* Anal. Biochem. **1986,** 155, 155-167.

[36] P. Manavalan, W.C. Johnson *Variable selection method improves the prediction of protein secondary structure from circular dichroism spectra* Anal. Biochem. **1987,** 167, 76-85.

[37] N. Sreerama, R.W. Woody *Estimation of protein secondary structure from circular dichroism spectra: comparison of CONTIN, SELCON, and CDSSTR methods with an expanded reference set* Anal. Biochem. **2000,** 287, 252-260.

[38] A. Lobley, L. Whitmore, B.A. Wallace *DICHROWEB: an interactive website for the analysis of protein secondary structure from circular dichroism spectra* Bioinformatics **2002,** 18, 211-212.

[39] L. Whitmore, B.A. Wallace *DICHROWEB, an online server for protein secondary structure analyses from circular dichroism spectroscopic data* Nucleic Acids Res. **2004,** 32, W668-W673.

[40] L. Whitmore, B.A. Wallace *Protein secondary structure analyses from circular dichroism spectroscopy: methods and reference databases* Biopolymers **2008,** 89, 392-400.

[41] L.J. Berliner, J. Grunwald, H.O. Hankovszky, K. Hideg *A novel reversible thiol-specific spin label: papain active site labeling and inhibition* Anal. Biochem. **1982,** 119, 450-455.

[42] N. Guex, M.C. Peitsch *SWISS-MODEL and the Swiss-Pdb Viewer: An environment for comparative protein modeling* Electrophoresis **1997,** 18, 2714-2723.

[43] E.H. Strickland, J. Horwitz, C. Billups *Near-ultraviolet absorption bands of tryptophan. Studies using indole and 3-methylindole as models* Biochemistry **1970,** 9, 4914-4921.

[44] J.A. Sweeney, S.A. Asher *Tryptophan UV resonance Raman excitation profiles* J. Phys. Chem. **1990,** 94, 4784-4791.

[45] B. Holmquist, B.L. Vallee *Tryptophan quantitation by magnetic circular dichroism in native and modified proteins* Biochemistry **1973,** 12, 4409-4417.

[46] J.C. Sutherland, B. Holmquist *Magnetic circular dichroism of biological molecules* Annu. Rev. Biophys. Bioeng. **1980,** 9, 293-326.

[47] J.P. Hennessey, W.C. Johnson *Experimental errors and their effect on analyzing circular dichroism spectra of proteins* Anal. Biochem. **1982,** 125, 177-188.

Chapter 9

Summary and outlook

When applying multifrequency and multiresonance EPR techniques to study nitroxide radicals and nitroxide-labeled systems embedded in their specific microenvironments, the success of high-field/high-frequency EPR spectroscopy critically depends on the development of tailor-made instrumentation for optimal detection of the magnetic interaction parameters of interest. This is true not only for rapidly growing fields of EPR application, such as characterization of protein structural changes based on innermolecular nitroxide-nitroxide distances, but also for the characterization of the local environment of the spin probe. The characterization of the nitroxide solvent matrix in terms of polarity and proticity is often the first step in the characterization of spin-labeled biomacromolecules by EPR. This is usually done by using cw EPR. However, in recent years the presence of distinct nitroxide radical populations described by distinct g_{xx} values, has been observed in well-resolved high-field/high-frequency cw EPR spectra of spin-labeled sites, that report on the heterogeneity of the microenvironment. For protonated spin systems, these distinct populations are typically only partially resolved by W-band (94 GHz) EPR techniques. In order to obtain precise g_{xx} values that describe such spin populations, higher field/frequency combinations are required, for instance 275 GHz (magnetic field of 10 T). In the present work the application of an alternative W-band pulsed EPR technique, ELDOR-detected NMR (EDNMR), is presented for characterizing the nitroxide environment heterogeneity. It is shown that the EDNMR technique yields reliable ^{14}N hyperfine coupling parameter, A_{zz}. Similarly to high-field/high-frequency cw EPR spectra, information on the presence of distinct nitroxide radical populations, each described by a different A_{zz} value, can be inferred from the EDNMR spectrum analysis. Importantly, this spectral information is conserved in the EDNMR spectra even when fully protonated systems are studied. This is opposed to W-band cw EPR where the information is lost due to the increased inhomogeneous linewidth. For optimum resolution, the EDNMR technique requires sufficiently long spin-spin relaxation time. This can be easily achieved by admixture of a deuterated cryoprotectant, e.g. glycerol-D_8. The W-band EDNMR technique is particularly well suited for the characterization of the local environment in spin-labeled proteins by means of A_{zz} values. This is because of: (i) the high sensitivity (as compared to ENDOR) and (ii) the superior resolution (as compared to W-band cw EPR).

In subsequent parts of this PhD work, W-band EDNMR was used for a detailed characterization of specific interactions of a nitroxide radical with its local environment in various model systems. By EDNMR it could be unequivocally shown that up to three distinct hydrogen-bonded nitroxide populations are present each one described by a unique A_{zz} value. Their relative fractions depend on the protic solvent used, but are also influenced by the thermal history of the sample. In detail, a different ratio between spin-probe populations was observed in a shock frozen sample and in a sample which was annealed above the glass transition temperature of the solvent. The three hydrogen-bonded nitroxide populations were assigned to: (i) nitroxides lacking specific interactions with the solvent, (ii) nitroxides forming a single H-bond with the solvent, (iii) nitroxides forming two H-bonds with the

solvent. The H-bond formation was subsequently directly confirmed by supplementary W-band ENDOR experiments. While heterogeneity in the g_{xx} spectral region of high-field cw EPR spectra of nitroxide radicals dissolved in protic solvents and in SDSL proteins has been previously reported, this was not the case for the A_{zz} hyperfine coupling parameter.

Up-to-date, A_{zz} was assumed to predominantly depend on the polarity of environment, and the slope of g_{xx} vs A_{zz} plot was proposed to provide a means to differentiate between the two properties, polarity and proticity, of the local environment. In contrast, in this work it was shown that A_{zz} is influenced by H-bond formation to the same extent as g_{xx} is. Hence, each one of these magnetic parameters can be used to characterize the microenvironment of the nitroxide probe in terms of proticity and polarity. From a g_{xx} vs A_{zz} plot, that includes resolved g_{xx} and A_{zz} values for each distinct nitroxide population, it can be concluded, that these magnetic parameters are predominantly sensitive to H-bond formation to the nitroxide radical. The electric field due to polarity of solvent molecules in the second hydration shell appears to have a minor influence on the magnetic parameters of the specific nitroxide radical R1 (3-hydroxymethyl-2,2,5,5-tetramethylpyrrolin-1-oxyl) used in this work. This has important consequences for a meaningful interpretation of polarity/proticity profiles in SDSL proteins and in membranes when using R1 as spin probe.

In addition to the determination of precise hyperfine and quadrupole parameters of nitroxide radicals that report on the microenvironment, EDNMR can also be used to measure the hyperfine interaction with weakly coupled nuclei interacting with the nitroxide moiety. In the present work, this approach was used to provide information on solvent accessibility in the vicinity of paramagnetic cofactor groups of a bacterial photosynthetic reaction center (bRC) – which can be either natural cofactors or nitroxide spin labels. In particular, probing the hyperfine and quadrupole interactions with ^{17}O nuclei proved to be a promising approach for quantitative intra-protein water content studies. Nitroxides possess an obvious advantage over native cofactors, since the electron spin density is mostly localized on the $NO^{\cdot}$ fragment. However, the H-bond formation to the nitroxide complicates the data interpretation, since the contributions of strongly coupled nuclei and matrix water have to be separated for a quantitative comparison between different protein sites. Nevertheless, D_2O exchange experiments allow one to choose those molecular positions that are solvent-accessible. Only then expensive ^{17}O experiments become reasonable to be performed on a number of spin-labeled protein mutants.

In this work only a single example of spin-labeled protein, T4-lysozyme, was studied using W-band EDNMR to characterize the spin-label environment by means of A_{zz}. Two spin probe populations, presumably originating from nitroxide radicals forming different numbers of H-bonds with the protic groups in the vicinity, were observed. However, to estimate to what extent H-bond formation occurs in spin-labeled proteins and to what extent it correlates with the accessibility to water, several spin-labeled proteins would have to be investigated in the future. It would be especially interesting – with regard to a nitroxide rotamer library approach – to differentiate between the H-bonding state of solvent-exposed and buried nitroxides. This information is in principle accessible from high-field/high-frequency cw EPR (preferably at 94 GHz or higher for better resolution). However, EDNMR can provide more reliable information than cw EPR, for which multi-parameter fits are necessary for data analysis. Further studies, including a larger number of spin-labeled proteins, are necessary to determine whether different protein sites, depending on the degree of solvent

accessibility, would respond differently to the thermal history of the sample, reflecting differences in the local glass transition temperature.

To ensure the practicality of local solvent accessibility studies using ^{17}O in conjunction with W-band EDNMR, a study on a number of nitroxide labeled protein variants is also planned for the future. These studies will be performed for a different spin-labeled variant of bRC or, for example, for the α_1m protein to study the trimerization process of the protein. The selection of suitable spin-labeled positions on the protein surface and measuring their solvent accessibility would allow us to specify which protein surfaces interact during the trimerization process. This trimerization will be reflected by a decreased solvent accessibility of the surfaces involved in the process.

Acknowledgements

I would like to thank Prof. Wolfgang Lubitz, for the possibility to perform my PhD work in his group, for his guidance during this time, especially during the final months of my PhD.

I would like to thank Prof. Claus Seidel for being the second advisor of my PhD and for useful discussions.

I would like to thank Dr. Anton Savitsky for his time and effort in teaching me practicalities of pulsed EPR measurements, for innumerable lectures on all intricate details of EPR spectroscopy and for allowing me to get involved in many different projects during my PhD. I'm truly grateful for that opportunity.

I would like to thank Prof. Klaus Möbius, for careful reading of this thesis and useful corrections, but also for serving as an inspiration.

I would like to thank all my collaborators, especially Dr. Markus Knipp with whom I could collaborate on the α_1m project. For letting me work on protein preparation which was an exciting journey.
I would like to thank Dr. Marco Malferrari and Prof. Giovanni Venturoli for the excellent collaboration on local water sensing in bacterial photosynthetic reaction centers and Prof. Enrica Bordignon for providing T4-lysozyme sample for annealing studies.

I would like to thank all colleagues and co-workers from Lubitz group for the pleasant working atmosphere, especially Dr. Agnieszka Adamska-Venkatesh and Dr. Judith Siebel.

I would like to thank Gudrun Klihm, Johanna Taing and Frank Reikowski for excellent technical support.

I thank my family for their unconditional support, being the peaceful harbor no matter where life takes me.

Curriculum Vitae

First name: Anna
Surname: Nalepa
Born in: 7th October 1985
Nationality: Polish

Education:

2000-2004	High school Liceum Ogólnokształcące im. Tadeusza Kościuszki w Busku-Zdroju, Busko-Zdrój, Poland
2004-2009	M.Sc. (Biophysics), Department of Biochemistry, Biophysics and Biotechnology, Jagiellonian University, Cracow, Poland.
2011-2015	PhD student, Max Planck Institute for Chemical Energy Conversion, Mülheim an der Ruhr, Germany; Henrich Heine University, Düsseldorf, Germany

List of publications:

[1] A.I. Nalepa, J.J. Taing, A. Savitsky, M. Knipp *Preparation of cysteine-34-nitroxide spin labeled human α_1-microglobulin*. Protein Expression and Purification **2013,** 88, 33-40.

[2] A. Nalepa, K. Möbius, W. Lubitz, A. Savitsky *High-field ELDOR-detected NMR study of a nitroxide radical in disordered solids: Towards characterization of heterogeneity of microenvironments in spin-labeled systems*. Journal of Magnetic Resonance **2014,** 242, 203-213.

[3] M. Malferrari, A. Nalepa, G. Venturoli, F. Francia, W. Lubitz, K. Möbius, A. Savitsky *Structural and dynamical characteristics of trehalose and sucrose matrices at different hydration levels as probed by FTIR and high-field EPR*. Physical Chemistry Chemical Physics **2014,** 16, 9831-9848.

[4] P. Gast, R.T.L. Herbonnet, J. Klare, A. Nalepa, C. Rickert, D. Stellinga, L. Urban, K. Möbius, A. Savitsky, H.-J. Steinhoff, E.J.J. Groenen *Hydrogen bonding of nitroxide spin labels in membrane proteins*. Physical Chemistry Chemical Physics **2014,** 16, 15910-15916.

[5] S. Razzaghi, M. Qi, A.I. Nalepa, A. Godt, G. Jeschke, A. Savitsky, M. Yulikov *RIDME spectroscopy with Gd(III) centers*. Journal of Physical Chemistry Letters **2014,** 5, 3970-3975.

[6] K. Möbius, A. Savitsky, A. Nalepa, M. Malferrari, F. Francia, W. Lubitz, G. Venturoli *The magic of disaccharide glass matrices for protein function as decoded by high-field EPR and FTIR spectroscopy*. Applied Magnetic Resonance **2015,** 46, 435-464.

[7] E. Bordignon, A.I. Nalepa, A. Savitsky, L. Braun, G. Jeschke *Changes in the microenvironment of nitroxide radicals around the glass transition temperature*. Journal of Physical Chemistry B **2015,** 119, 13797-13806.

Honors and prizes:

2011, poster prize at the 6th International Conference on Nitroxide Radicals (SPIN-2011) for the poster titled: *'High-field ELDOR-detected NMR of nitroxides in disordered solids: Model study of heterogeneity in SDSL proteins'*

2013, poster prize at the 46th Annual International Meeting of the ESR spectroscopy group for the poster titled: *'Local water sensing using high-field ENDOR and ELDOR-detected NMR'*

List of poster presentations:

[1] 25-29.09.2011, Marseille, France
The 6th International Conference on Nitroxide Radicals (SPIN-2011) *'High-field ELDOR-detected NMR of nitroxides in disordered solids: Model study of heterogeneity in SDSL proteins'*

[2] 12-15.12.2012, Schloss Ringberg, Kreuth, Germany
International Symposium on 'Integrating Advanced Spectroscopic Tools for Structure and Dynamics of Biological Macromolecular Complexes *in vitro* and *in vivo*' *'EPR investigation of the proposed [Fe]-hydrogenase conformational change upon catalysis'*

[3] 07-11.04.2013, Warwick, United Kingdom
The 46th Annual International Meeting of the ESR Spectroscopy Group *'Local water sensing using high-field ENDOR and ELDOR-detected NMR'*

[4] 07-10.10.2013, Kraków, Poland
The 9th International Workshop on EPR (ESR) in Biology and Medicine *'Local water sensing using high-field ENDOR and ELDOR-detected NMR'*

[5] 23-25.07.2014, Mülheim an der Ruhr, Germany
International Symposium on 'Catalytic Systems for Chemical Energy Conversion' *'Application of W-band ELDOR-detected NMR to microenvironment characterization and local water sensing in nitroxide-labeled systems'*

List of oral presentations:

[1] 17-22.09.2012, Halle (Saale), Germany
The 34th FGMR GDCh Annual Discussion Meeting, Advanced Magnetic Resonance for the Study of Dynamics in Biomolecules and Materials *'Probing of spin label local environment by W-band ENDOR and EDNMR techniques'*

[2] 28.10-01.11.2013, Leiden, Netherlands
Workshop on 'Responsive Matrices for Solar Fuels' *'The electron transfer in bacterial photosynthetic reaction centers embedded into trehalose matrices – insight from EPR and optical flash-absorption spectroscopies'*

[3] 14-20.09.2014, Zelenogradsk, Kaliningrad region, Russia
The 7th International Conference on Nitroxide Radicals (SPIN-2014) *'Application of W-band ELDOR-detected NMR to microenvironment characterization and local water sensing in nitroxide-labeled systems'*

[4] 10-13.12.2014, Schloss Ringberg, Kreuth, Germany
International Symposium on 'Integrating Spectroscopic and Theoretical Methods to Analyse Molecular Machines' *'Pulsed EPR techniques applied to nitroxide spin probes and nitroxide spin labeled systems'*